Strategies for Detecting DNA Hybridisation Using Surface Plasmon Fluorescence Spectroscopy

Thomas Neumann

MAX-PLANCK-GESELLSCHAFT

Strategies for Detecting DNA Hybridisation Using Surface Plasmon Fluorescence Spectroscopy

Dissertation zur Erlangung des Grades
„Doktor der Naturwissenschaft“

am Fachbereich Chemie und Pharmazie
der Johannes Gutenberg-Universität
in Mainz

vorgelegt von
Thomas Neumann
aus Witten an der Ruhr

Mainz, Juni 2001

CONTENTS

1 Introduction

The number of analysis techniques used in biology, medicine and pharmacy has increased over the past years. Novel detection methods have been developed which combine the specificity of biomolecular recognitions systems with the advantages of instrumental analysis. Biosensoric devices have gained importance is areas like medical diagnostic, quality control and environmental analysis [1,2].

Biosensors

A biosensor is defined as an analytical device which contains a biological recognition element immobilised on a solid surface and an transduction element which converts analyte binding events to a measurable signal [3-5]. Sensors make use of the high specificity of bio-molecules for certain ligands. This specificity permits very similar analytes to be distinguished from each other by their interaction with immobilised bio-molecule (antibodies, enzymes or nucleic acids). Biosensors are valuable tools for fast and reliable detection of analytes and have reached an importance for scientific, bio-medical and pharmaceutical applications [1,6]. The advantages that are offered by the ideal biosensor over other forms of analytical techniques are: the high sensitivity and selectivity, low detection limit, good reproducibility, rapid response, reusability of devices, ease of fabrication and application, possibility of miniaturisation, ruggedness and low fabrication cost. By immobilising the bio-recognition element on the sensor surface one gains the advantage of reusability of the device due to the ease of separating bound and unbound species. By simple washing steps the non-specifically bound molecules may be removed. Some surface sensitive detection formats, such as evanescent wave techniques, even make these washing steps redundant. These techniques are relatively insensitive to the presence of analytes in the bulk solution.

The mere presence of the analyte itself does not cause any measurable signal from the sensor, but the selective binding of the analyte of interest to the biological component. The latter is coupled to a transducer, which responds the binding of the bio-molecule. [7,8]. The three most frequently used transduction devices are electrochemical, piezoelectric and optical detectors. While electrochemical sensors respond to changes in the ionic concentration, redox potential, electron transfer rate or electron density upon analyte binding, piezoelectric sensors monitor

changes in the adsorbed mass on the sensor surface [9]. The large group of optical biosensors are based on the principles of fluorescence, chemi-luminescence or absorption spectroscopy.

DNA Detection

As to date, thousands of different diseases are known to be caused by genetic lesions like single point mutations in the human genome. The sequence specific analysis of the patient's genome has thus reached a high impact in monitoring the progress and prevention of diseases like cancer. DNA analysis is furthermore important for the detection of pathogenic micro-organisms such as bacteria and viruses by their genetic material and the detection of infectious diseases. Due to the increasing amount of genetic information that is to be analysed in routine medical procedures, there is a high demand on efficient screening methods for point mutations in the patient's genome and novel DNA detection schemes. Conventional gel based sequencing methods are relatively time-consuming and expensive in terms of equipment and labour costs. Novel DNA detection formats on surfaces promise to fulfil the requirements for an optimal biosensor. DNA arrays and chips provide the possibility to screen DNA samples for various mutations simultaneously and are widely used for the high throughput analysis of DNA samples.

The commonly applied techniques for DNA detection include the interaction between an immobilised probe DNA sequence on the sensor surface and the target sequences from solution. If fluorescence is involved, the label can either be attached covalently to the target sequence itself or can be added to the sensor after hybridisation. Most of the standard techniques provide a simple yes/no answer, but no kinetic information about the hybridisation process on the surface itself. Kinetic information is important for the improvement of experimental conditions of known detection formats and the characterisation of novel detection strategies. The knowledge of the kinetic behaviour of analytes on the sensor surface helps optimising the sensor architecture and the detection protocols. Surface sensitive detection hence constitutes an appropriate tool to investigate the dynamic processes during DNA hybridisation reactions on the surface. One class of optical techniques that fulfil this requirement are evanescent wave techniques.

Evanescent Wave Techniques

These techniques make use of the exponentially decaying electrical field at the boundary between two media of different optical thickness upon irradiation with electromagnetic waves. Under total internal reflection conditions the decay length of the evanescent field into the optically thinner medium is on the order of the wavelength of the used excitation light. For

visible light the field decays after a few hundred nanometers. Only analyte molecules in the evanescent region are probed, which causes the surface sensitive character of such methods. Basically, three different evanescent wave formats are known: planar waveguides, fibre optics and surface plasmon resonance devices.

A waveguide consists of a planar glass surface with a refractive index higher than the adjacent medium. Under certain conditions light coupled into this waveguide can travel through the sample by total internal reflection. An evanescent field can interact with molecules in the region surrounding the waveguide. Adsorbed analytes change the optical properties of the waveguide and alter the boundary conditions for guiding light in the sample. Hence, the light coupling out of the waveguide can the used to monitor binding reactions at the surface of the waveguide. Fibre optic sensors utilise the same principle as waveguides, but differ in the experimental geometry.

Surface Plasmon Resonance utilises the evanescent field to excite oscillations in the (nearly) free electron gas of the metals. The excitation of the resulting surface waves gives rise to a field enhancement compared to the intensity of the incident electromagnetic field [10]. Illumination by laser light can be used to excite the plasmons in metals. Then the system responds to changes in the optical properties of the medium close to the metal film by altering the intensity of the reflected light. For surface sensitive investigation of adsorption and desorption processes on metallic substrates Surface Plasmon Resonance is the method of choice.

Evanescent Enhancement of Fluorescence

Generally, sensor formats can be divided into direct and indirect sensors. The first group is capable of detecting the presence of the analyte molecule directly, while the indirect schemes detect the presence of an additional signal. In electrochemically based sensors redox-active labels like ruthenium pyridinium complexes bind to the receptor-target complex and may be detected voltammetrically. Surface Plasmon Spectroscopy (SPS) and piezo-electric techniques are sensitive to changes in the adsorbed mass and thickness on the surface. Labels of large molecular weight like proteins can be used to enhance the sensitivity of the system. Finally, the most prominent optical labels are fluorescent molecules. They allow for highly sensitive detection because the excitation and emission wavelength can be separated. Therefore fluorophores are a widely used to detect molecules in a variety of applications.

The development of novel, easy-to-use detection protocols and assay designs rely on the knowledge of kinetic constants of binding reactions. Thus, surface sensitive techniques are essential for the investigation of surface reaction kinetics. Unfortunately, many of the surface sensitive techniques such as Surface Plasmon Spectroscopy lack in their detection limit if low

molecular mass analytes are to be detected. Therefore, combinations of surface sensitive optical techniques with fluorescence detection formats were developed. The excitation of evanescent wave techniques has been demonstrated for waveguides and fibre optic devices [11-14]. Fluorescent molecules close to the sensor surface are excited by the evanescent electrical field. Compared to direct illumination an enhancement of a factor of four can be reached.

Recently surface plasmons were used as intermediate states between the incident light and the excited fluorophore in Surface Plasmon Fluorescence Spectroscopy (SPFS) [15,16]. Depending on the nature of the metal the plasmon field provides the possibility to enhance the fluorescence signal up to a factor of 80. SPFS allows to probe the presence of fluorescent analytes with high sensitivity and simultaneously provides information about the sensor architecture. From the viewpoint of bio-molecular architectures employed for biosensors metal surfaces are important in respect to immobilisation strategies and are irreplaceable for self assembly of thiol tethered lipids, proteins and nucleic acids. The detection formats for DNA investigated in this study are based on controlled and reproducible formation of monolayers of proteins and DNA on gold and silver films. Therefore the SPFS technique was used to characterise the formation of the supporting matrix and the DNA hybridisation.

The excitation of fluorescence in the evanescent field of the plasmons is strongest close to the metal surface. On the other hand the presence of the metal can reduce the observed fluorescence intensity by inducing distance dependent quenching processes like Förster transfer. Excitation and quenching processes exhibit different distance dependencies. An optimal distance to the metal exists at which maximal fluorescence excitation is observed. Therefore, the experimental design of the sensor surface architecture has to be optimised in order to obtain an efficient and sensitive sensor concept.

Aim of the Study

The aim of this study is the development and characterisation of DNA biosensor formats based on evanescent wave techniques such as Surface Plasmon Fluorescence Spectroscopy. The surface plasmon enhanced fluorescence (SPFS) set-up was recently described [16] and the application of this technology for DNA detection on surfaces was shown [17]. However, the excitation of fluorescence on metallic surfaces was not investigated in full detail. Furthermore,

the impact of the SPFS technique on alternative fluorescence detection formats was not evaluated. The aims of this study are defined as follows:

- Investigation of fluorescence excitation and emission on planar and corrugated metallic surfaces. Characterisation of the quenching processes of fluorescence due to the metal surface and determination of the distance dependence of these processes.
- Study of DNA hybridisation reactions on surfaces based on SPFS. Study of the mismatch discrimination sensitivity dependent on the sequence of the probes. Investigation of the influence of secondary structures in DNA probes and targets.
- Development and characterisation of novel detection formats for nucleic acids on surfaces. These studies can include the use of different fluorescence labels and the interaction between proteins and DNA sequences.

The study is thus divided into two parts of different scope: In the first part the physical behaviour of fluorescent dyes near metal surfaces is studied. On the basis of these results the detection of DNA on surfaces using fluorescence techniques is investigated.

In chapter 1 the theoretical background of surface plasmon resonance techniques is reviewed and the concept of fluorescence spectroscopy in solution is discussed. The combination of both techniques in the form of SPFS and the influence of surface plasmon fields on fluorophores close to planar surfaces is discussed in chapter 4. The decay channels for fluorescence on surfaces are identified and alternative measurement modes are compared on a prism set-up. Subsequently, the obtained results are extended to the investigation of fluorescence on corrugated metallic surfaces like gratings. In particular, the excitation and emission of fluorescence in the field of coupled resonances on blazed gratings are investigated in chapter 5.

The use of SPFS for the investigation of DNA hybridisation is discussed in chapter 4. The design of the used sensor format is presented and the measurement principle is explained. The influence of structure and sequence of the DNA probes is studied on the base of theoretical considerations and experimental data. These findings lead to the design of a novel DNA detection format, based on structural changes in the probe sequence (chapter 7). Alternative detection strategies like multiple labelling strategies and energy transfer between labelled DNA strands (chapter 8) as well as DNA/protein interaction (chapter 9) are additionally evaluated.

2 Theory

2.1 Fluorescence

Analytical methods incorporating fluorescence based detection are widely used in chemical as well as biochemical research due to the extraordinary sensitivity and the favourable time scale on which fluorescence occurs. A number of molecular processes can be observed by monitoring their influence on a fluorescent probe during the fluorescence lifetime, which is typically in the range of 10 ns. The impact of this technology in biochemical research has been shown previously. Immunoassays relying on fluorescence detection (fluoroimmunoassays, FIA) may replace established radioimmunoassays if such limitations like relatively high fluorescence background signals can be reduced [18-20].

Several photophysical parameters of fluorescent probes have been exploited to monitor analyte binding events. These include fluorescence polarisation [21], fluorescence quenching [22,23], fluorescence enhancement [24] and resonant energy transfer (RET) [25,26]. Combining one of these fluorescence schemes with other optical or electrical detection methods of interest can lead to an improvement in the sensitivity and detection limit of these methods. Since fluorescence detection has been utilised extensively in this work, the underlying principles shall be explained in the following.

2.1.1 Principle of Fluorescence

Fluorescence is a well characterised phenomenon which describes the emission of photons from molecules that undergo a transition from an electronically excited to the ground state [27]. Fluorophores often exhibit strongly delocalised electrons in conjugated double bonds or aromatic systems. The molecular processes during absorption and emission of photons are illustrated by the schematic Jablonsky energy level diagram shown in Figure 2.1.

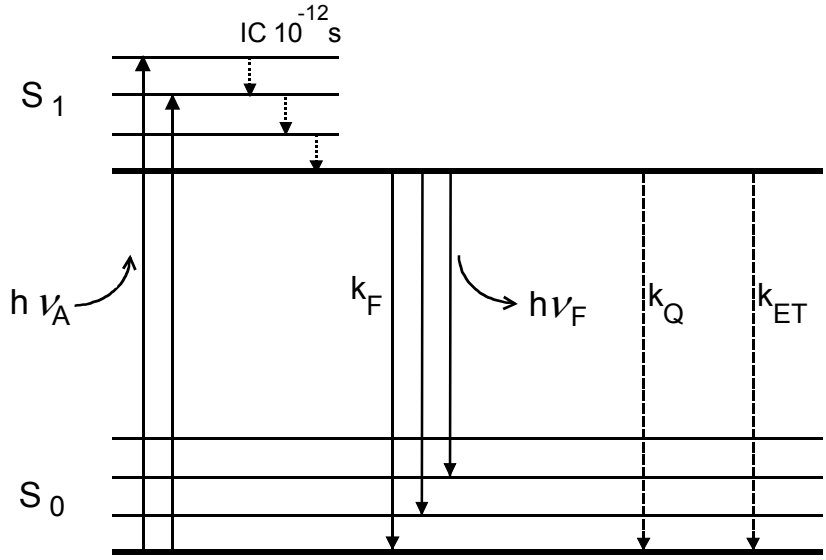

Figure 2.1 : Jablonsky diagram illustrating the electronic and vibrational states of a fluorophore and processes during photon absorption and fluorescence emission.

A fluorophore may exist in several electronic states, two of which are depicted here (S_0 and S_1). These levels are described by the spin multiplicity of the state, so that e.g. singlet and triplet states can be found, depending on how the orbitals of the molecule are populated and how the spins of the electrons are paired. Triplet states are not involved in the fluorescence mechanism itself, so that we concentrate on the singlet levels only. At each of these electronic levels the fluorophore can exist in a number of vibrational levels, which are populated according to the Boltzmann distribution law. Hence, at room temperature and a given energy spacing of the levels most of the molecules will be present in the lowest vibrational level of S_0. Following light absorption, the fluorophore is excited to some higher vibrational levels of S_1 or S_2 (not shown) in the time scale of 10^{-15} s. The absorption spectrum therefore reveals information about the electronically excited states of the molecule. Generally, the system relaxes into the lowest vibrational level of the S_1 state by internal conversion (IC) occurring in about 10^{-12} s. Since fluorescence lifetimes are typically around 10^{-8} s relaxation to the thermally equilibrated ground state of S_1 is complete prior to emission of photons and consequently fluorescence starts from the lowest vibrational level in S_1 (Kasha´s law). From there the molecule can decay to different vibrational levels of the state S_0 by emitting light (with a rate constant k_F). This leads to the fine structure of the emission spectrum by which we can gain information about the electronic ground state S_0. The transition between two states of the same spin multiplicity is a quantum mechanically allowed process and therefore reveals high emissive rates of typically near 10^8 s^{-1}.

Comparing absorption and emission spectra one observes the so called Stokes´ shift of the fluorescence emission to lower wavelength (red shift) relative to the absorption. This shift can be explained by energy losses between the two processes due to the rapid internal conversion in the excited states (S_1, S_2) and the subsequent decay of the fluorophore to higher vibrational levels of S_0. This shift is fundamental to the sensitivity of fluorescence techniques, because it allows the emitted photons to be isolated from excitation photons detected against a low background. In contrast, absorption spectroscopy requires the measurement of transmitted light relative to high incident light levels of the same wavelength. Generally, the fluorescence emission spectrum appears to be a mirror picture of the absorption spectra, because of the same transitions that are involved in both processes and the similarities among the vibrational levels of S_0 and S_1. Often deviations to this mirror rule can occur due to e.g. excited state reactions and geometric differences between electronic ground and excited states.

A fluorescence emission spectrum is recorded by holding the excitation wavelength constant and detecting the fluorescence intensity over a range of emission wavelengths. In contrast to this, an excitation spectrum is recorded by holding the emission wavelength constant and scanning over a range of excitation wavelengths. With a few exceptions the excitation spectrum of a fluorescent species in dilute solutions is identical to the absorption spectrum. Under the same conditions, the fluorescence emission spectrum is independent of the excitation wavelength.

Starting from the excited state S_1 the fluorophore can not only dissipate its energy by fluorescence emission with the rate k_F, but several other radiationless decay channels can be found that lead to a depopulation of S_1. Electronic transition to triplet states by intersystem crossing (ISC, not shown) as well as quenching processes (k_Q) and resonant energy transfer (k_{ET}) consequently result in a decrease of the fluorescence quantum yield, which is defined as

$$\phi = \frac{k_F}{k_F + k_0} \qquad (2.1)$$

This also gives the ratio of the number of emitted photons to the absorbed ones. The rate constant $k_0 = k_{ISC}+k_{IC}+k_Q+k_{ET}$ combines all possible radiationless decay channels including internal conversion losses (k_{IC}).

The fluorescence lifetime τ is defined as the average time the excited molecule spends in the excited state prior to return to the ground state. It is a sensitive measure to parameters influencing the fluorophore in the excited state.

$$\tau = \frac{1}{k_F + k_0} \qquad (2.2)$$

Additionally, the environment of the fluorescent species like the polarity of the solvent or the pH can influence the intensity and the wavelength of emitted fluorescence. The interaction with the fluorophore's dipole moment and chemical reactions between the dye and solvent molecules (hydrogen bonding, acid-base chemistry or charge transfer interactions) can alter the fluorescence intensity. These solvent effects are often used to sense the environment in which the fluorophore exists and have some biochemical impact for e.g. in protein folding studies. In the following sections, the most relevant effects for the present work like quenching and resonant transfer effects are discussed in more detail.

2.1.2 Quenching of Fluorescence

Fluorescence quenching refers to any process that decreases the fluorescence intensity of a fluorescent probe like complex formation, energy transfer, excited state reactions or collisional quenching. In case of the latter one, which is also known as dynamic quenching the quenching species comes into contact with the excited fluorophor during the fluorescence life time and thereby causes the dye to return to the ground state without emitting a photon. With static quenching, the complex formed between quencher and fluorophore is itself nonfluorescent.

Collisional quenching of fluorescence can be described by the Stern-Volmer equation:

$$\frac{Io}{I} = 1 + k_Q \tau_0 [Q] = 1 + K_D [Q] \qquad (2.3)$$

where I_0 and I are the fluorescence intensities in the absence and presence of the quencher, respectively, τ_0 is the lifetime of the fluorophore in the absence of the quencher, k_Q is the bimolecular quenching constant,[Q] is the concentration of the quencher and K_D is the Stern-Volmer quenching constant. Usually quenching data are presented in a Stern-Volmer plot, I_0/I versus the concentration of the Quencher [Q]. This is expected to yield a linear dependence. Deviations from linearity often indicate that two different populations of the fluorophore may exist, one of which is not accessible by the quencher.

Also static quenching processes can lead to linear Stern-Vollmer-plots, since a similar expression as (2.3) can be derived for quenching by complex formation:

$$\frac{Io}{I} = 1 + K_S [Q] \qquad (2.4)$$

where K_S is the association constant for the complex formation,

$$K_S = \frac{[FQ]}{[F][Q]} \qquad (2.5)$$

[F],[Q] and [FQ] are the concentrations of the fluorophor, quencher and formed complex, respectively. Collisional and static quenching can be distinguished by lifetime measurements or temperature dependent experiments, because at higher temperature complexes are expected to be less stable. This would result in a reduced static quenching. As a result, the slope of the linear Stern-Volmer plot is decreased in the case of static quenching and increased for collisional quenching processes.

Combined static and collisional quenching of the same fluorophore finally can be described by the following modified Stern-Volmer equation

$$\frac{Io}{I} = (1 + K_D[Q])(1 + K_S[Q]) \qquad (2.6)$$

which appears to be second order in [Q] resulting in a plot that reveals an upwards curvature towards the I_0/I axis. In order to separate the different origins of quenching, fluorescence lifetime measurements are performed. If these measurements are not available, equation (2.6) can be modified to allow for a graphical separation of K_D and K_S: Multiplication of the term in brackets yields

$$\frac{Io}{I} = 1 + (K_D + K_S)[Q] + K_D K_S [Q]^2 = 1 + K_{app}[Q] \qquad (2.7)$$

with

$$K_{app} = (K_D + K_S) + K_D K_S [Q] = \frac{I_0}{I} - 1 \qquad (2.8)$$

Hence, a plot of K_{app} versus [Q] gives a linear dependence with a slope $S=K_SK_D$ and an intercept $Y=(K_S + K_D)$. From this, the individual values can be calculated by solving the following quadratic equation.

$$K_S^2 - K_S Y + S = 0 \qquad (2.9)$$

By additional considerations is has to be decided which of the two obtained set of solutions reflects the reality most.

2.1.3 Resonant Energy Transfer

An important mechanism to depopulate the excited electronic states of a fluorophore is fluorescence resonance energy transfer (FRET) from a donor to an acceptor molecule [27,28]. This process is a distance-dependent interaction between the electronic excited states of two molecules in which excitation energy is transferred from a donor molecule (D*) to an acceptor molecule (A) without the emission of a photon. The acceptor is thereby excited to a higher electronic state while the donor molecule decays to the ground electronic state:

$$D^* + A \rightarrow D + A^* \qquad (2.10)$$

This radiationless energy transfer differs from simple emission and subsequent re-absorption since it happens before a photon is emitted by the donor. It can be attributed to resonant interaction of the transition dipole moments of donor and acceptor molecules. The rate k_{ET} of energy transfer from D* to A is then given by

$$k_{ET} = \frac{1}{\tau_d r^6}\left\{\frac{9000\ln(10)\kappa^2\phi_d}{128\pi^5 n^4 N}\int_0^\infty \frac{F_d(\tilde{\upsilon})\varepsilon_a(\tilde{\upsilon})}{\tilde{\upsilon}^4}d\tilde{\upsilon}\right\} \qquad (2.11)$$

where ϕ_d is the quantum yield of the donor in the absence of the acceptor, n is the refractive index of the medium, N is Avogadro´s number, r is the distance between donor and acceptor, τ_d is the lifetime of the donor in the absence of the acceptor, $F_d(\tilde{\upsilon})$ is the corrected fluorescence intensity of the donor in the wavenumber range $\tilde{\upsilon} + d\tilde{\upsilon}$ with the total intensity normalised to unity and $\varepsilon_a(\tilde{\upsilon})$ is the extinction coefficient of the acceptor at $\tilde{\upsilon}$ [29],[30]. κ^2 is an orientation factor, describing the relative orientation in space of the transition dipole moments of the donor and the acceptor. It can range from 0 to 4 as illustrated in Figure 2.2. If the orientation of the molecules is random and does not change during the fluorescence lifetime, a value of 0.476 is assumed[31]. In addition to the orientation of the dipoles, there are other factors that control the extent of the energy transfer, such as spectral characteristics of the resonantly coupled molecules.

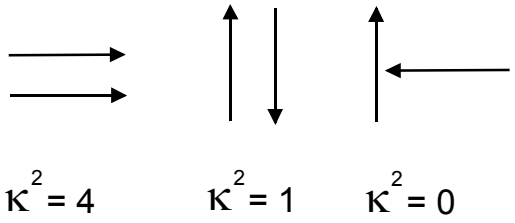

Figure 2.2: Dependence of the orientation factor on the relative orientation of the transition dipole moments of the donor and acceptor

The integral part of (2.11) is called overlap term and expresses the degree of spectral overlap between the donor emission and acceptor absorption. Such a spectral overlap is necessary to transfer energy between both molecules. In this case, a number of emission transitions of the donor can be found, the energy of which matches the absorption transitions in the acceptor. The degree of overlap determines the transfer efficiency. Hence, in case of resonant energy transfer the acceptor is excited to a higher electronic state and is now capable of emitting fluorescence itself. Consequently, successful Förster transfer can be monitored by a decreased donor fluorescence emission and an increased acceptor emission as it is depicted in Figure 2.3.

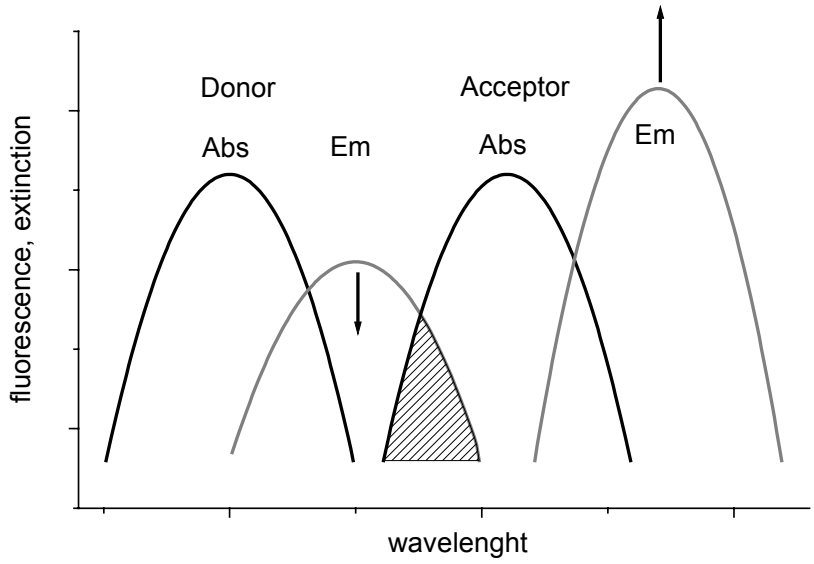

Figure 2.3: Schematic excitation and emission spectra of donor and acceptor fluorophores. Due to the spectral overlap of the excitation and emission spectra of both molecules energy can be transferred from the donor to the acceptor, resulting in a decreased donor fluorescence emission and an increased acceptor emission.

In addition to the orientation of the dipoles and the spectral characteristics, the distance between donor and acceptor controls the degree of transfer as can be derived from (2.11). The term in brackets equals R_0^6, with R_0 being the Förster radius. It characterises a centre to centre distance of donor to acceptor at which the transfer rate k_{ET} is equal to the decay rate of the donor in absence of the acceptor (k_F.+ k_0). Using this definition the transfer rate can be written as:

$$k_{ET} = \frac{1}{\tau_d}\left(\frac{R_0}{r}\right)^6 \qquad (2.12)$$

At the Förster radius R_0 the probability of transferring energy from the donor to the acceptor or loosing it into other decay channels is 50%, and so is the frequently measured energy transfer efficiency, which is given by

$$E = \frac{k_T}{\tau_d^{-1} + k_T} = \frac{R_0^6}{R_0^6 + r^6} \qquad (2.13)$$

This expression represents the proportion of the absorbed photons which are transferred to the acceptor. The direct relation to donor-acceptor distances r can be easily obtained by inserting (2.12) into (2.13). In Figure 2.4 a simulated efficiency curve is shown, which illustrates that below the characteristic Förster radius (here 6nm) most of the donor energy is transferred resonantly.

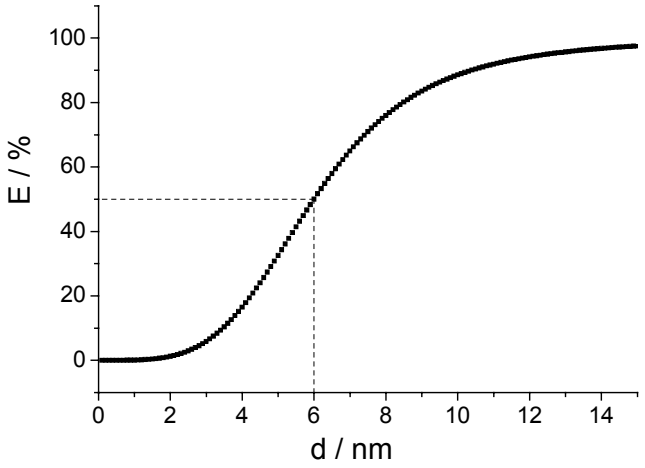

Figure 2.4: Energy transfer efficiency dependent on the donor-acceptor distance. The Förster radius is the distance at which the 50% of the absorbed energy is transferred to the acceptor.

The standard Förster model for dipole-dipole energy transfer has a r^{-6} dependence as discussed above. Other configurations cause different dependencies: If the acceptor takes the form of a line of dipoles rather than a point dipole integration over all possible transfer sites yields a r^{-5} dependence. Similarly, a sheet of acceptors (a surface) yields a r^{-4} dependence.

The distance dependence of the energy transfer has allowed for the sensing of intermolecular distances between Förster transfer pairs in the range of twice the Förster radius. This range of distances is comparable to the thickness of membranes and the diameter of most proteins, so that we find numerous applications in the context of biophysical questions. For example, energy transfer experiments have been used to estimate the distance between binding sites of proteins[32], the lateral association of membrane compounds[33] and the associations reactions between molecules [34] like receptor/ligand interactions [35] to name only a few.

2.2 Langmuir Adsorption

A fundamental part of biosensor operation involves the adsorption of analyte molecules in a gaseous or liquid environment to a surface immobilised probe, with allows the convenient sensing of the binding species. Therefore the understanding of the interaction between molecules with surfaces in general plays a major role for the development of sensoric devices. A characterisation of adsorption processes may lead to an improvement of known detection schemes and the optimisation of reaction protocols.

In order to understand molecular processes on a surface it is assumed that a limited number of binding sites are available, which can be occupied by binding molecules until the complete surface is saturated and all sites are blocked. A common model that describes this behaviour is the Langmuir model[36,37], which assumes that

- all binding sites are equivalent and already occupied sites do not influence the binding reaction in adjacent places.

- the surface is homogenously covered by a monolayer

The processes at the surface can be described by the rate constants of the adsorption k_{on} and the one of the desorption from the surface k_{off} (Figure 2.5). The resulting time dependent surface coverage Θ can be described by the following equation:

$$\frac{\partial \Theta}{\partial t} = c_0 k_{on}(1-\Theta) - k_{off}\Theta \qquad (2.14)$$

where c_0 is the concentration of the binding species in solution. According to this equation the surface will be occupied until all binding sites are blocked. Then $(1-\Theta)$ equals zero and this will occur the fastest when the concentration in solution is high. On the other hand, desorption is only dependent on the rate k_{off} and on the actual number of covered binding sites. Integration of (2.14) with the initial condition $\Theta = 0$ at $t = 0$ leads to

$$\Theta(t) = \frac{c_0 k_{on}}{c_o k_{on} + k_{off}}(1 - \exp(-(c_0 k_{on} + k_{off})t)) \qquad (2.15)$$

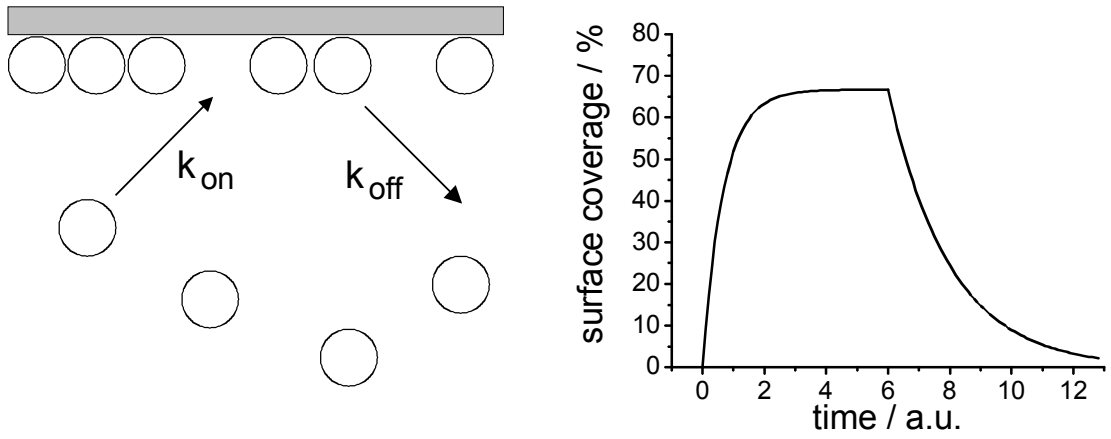

Figure 2.5 : Schematic description of Langmuir adsorption. The surface coverage is dependent on the rate constants k_{on} and k_{off} which characterise the adsorption and desorption process, respectively. A typical Langmuir kinetic curve is depicted: until equilibration, both rate constants contribute to the adsorption process, while upon exchange of the analyte solution only k_{off} determines the desorption behaviour.

A typical solution of this equation is given in Figure 2.5b, where the adsorption process leads to the equilibration of the system at a certain surface coverage, which is dependent on both rate constants. In the case of a real experiment the desorption process can be followed separately by exchanging the analyte solution against pure buffer, since then the concentration c_0 equals zero and the first expression in (2.15) becomes negligible. Thus, the rate constant k_{off} can be determined by considering the pure desorption case and fitting the experimental data according to:

$$\Theta(t) = \Theta_0 \exp(-k_{off} t) \qquad (2.16)$$

where Θ_0 is the surface coverage at the beginning of the desorption process. Here it is assumed that the desorbed molecules are prevented from re-adsorption by continuous rinsing with pure solvent. Practically, the desorption process should be fitted simultaneously with the simulation of the adsorption process. Thus, the desorption constant k_{off} is assured to be identical in both processes.

It is possible to monitor the complete Langmuir-isotherm if the surface is saturated stepwise. For this the sample is immersed in solutions of increasing concentration of the adsorbing species and the system is allowed to be equilibrate before a further increase in bulk concentration. Thus, the starting value of the surface coverage for the individual adsorption curves is larger than zero for the subsequent steps. Therefore (2.14) has to be solved with the initial condition $\Theta = \Theta_0$ at

t=0 with Θ_0 being the surface coverage at the start of the new concentration increase. Integration with these initial values leads to a solution for the single steps as given by (2.17):

$$\Theta(t) = \frac{c_0 k_{on}}{c_o k_{on} + k_{off}} (\Theta_0 - \frac{c_0 k_{on}}{c_o k_{on} + k_{off}}) \exp(-(c_0 k_{on} + k_{off})t)) \qquad (2.17)$$

In case of such stationary surface coverage a simple correlation to the equilibrium constant K of the reaction can be derived from (2.14):

$$\Theta = \frac{c_0 K}{1 + c_0 K} \qquad (2.18)$$

This equation permits the determination of the equilibrium constant K from experimentally determinable concentrations and the surface coverage. In the case of adsorption of fluorescent molecules, the coverage Θ is given by the detected normalised fluorescence intensity scaled to the maximum value at complete surface saturation.

Often it is found that the experimental conditions do not reflect the theoretical assumptions that were made when the model was developed. In some cases the independence of the binding processes does not hold due to the interaction between the binding molecules. The assumption of limiting the adsorption to a mono-layer may be broken by unspecific binding and multi-layer formation. Some effort has been made in developing other models, which take these deviations from the simple Langmuir picture into consideration. For instance the BET isotherm includes multilayer formation like physisorption into the calculations. Others, like the Temkin isotherm consider the adsorption enthalpy and the associated dissimilarity of the given binding sites.

If not mentioned otherwise, the Langmuir simulation was used in this work to calculate kinetic and equilibrium constants. Herein it is assumed that the physisorption of binding species in the used layer systems is negligible. Especially in the case of hybridising DNA strands, highly specific interaction between immobilised probe DNA and target sequences in solution is expected. Special binding model that take cooperative binding effects or replacement reactions are discussed in the corresponding chapter.

2.3 Surface Plasmons

The phenomenon of surface plasmons has been known for a long time. The underlying principles and theories are well understood, so that a number of publications can be found which discuss their properties in detail [10,38,39]. Surface plasmons are surface waves which can be excited at the interface between a metal and a dielectric and the exact excitation conditions strongly depend on the optical properties of the system. It will be derived that changes in these properties will lead to altered experimental excitation conditions. This measurable response of the system permits the sensitive monitoring of processes near this interface. Numerous descriptions of successful surface plasmon based sensors can be found and are discussed later.

A major part of this work is based on the excitation of surface waves and the interaction of the associated electrical field with dielectric thin films. The theoretical background of these processes are described in detail in this chapter, since the understanding of electromagnetic waves in matter and their behaviour at interfaces is essential for the following discussion. Fundamental processes like refraction, reflection, transmission and damping of electromagnetic waves at interfaces are considered in general, followed by a discussion of surface plasmon excitation in a two layer system. Finally, the derived model will be extended to multilayer systems and the connection to experimental surface plasmon spectroscopy is made.

2.3.1 Electromagnetic Fields

The fundamental description of electromagnetic waves in an isotropic, homogenous medium is based on Maxwell´s equations:

$$\nabla \times \vec{H}(\vec{r},t) = \frac{d}{dt}\vec{D}(\vec{r},t) \qquad \nabla \times \vec{E}(\vec{r},t) = -\frac{d}{dt}\vec{B}(\vec{r},t) \tag{2.19}$$

$$\nabla \vec{B}(\vec{r},t) = 0 \qquad \nabla \vec{D}(\vec{r},t) = 0$$

where $\vec{E}$ is the electrical field, $\vec{H}$ the magnetic field, $\vec{D}$ the electrical displacement, $\vec{B}$ the magnetic induction, t is the time and $\vec{r}$ is the spatial vector.

The electrical field of an electromagnetic plane wave can be described in a complex form as:

$$\vec{E}(\vec{r},t) = \vec{E}_0 \cdot \exp(i(\vec{k} \cdot \vec{r} - \omega \cdot t)) \tag{2.20}$$

with $\vec{E}_0$ being the electrical field amplitude, $\vec{k}$ the wave-vector pointing into propagation direction and ω being the angular frequency. The physical field equals the real part of the

complex wave description in (2.20) and the orientation of $\vec{E}_0$ is orthogonal to $\vec{k}$. For each pair $(\omega, \vec{k})$, two mutually orthogonal electrical field amplitudes may exist, corresponding to two possible polarisations. Taking the surface as a reference these polarisations can be characterised by their orientation of the electric and magnetic field vector towards the surface.

The connection between electric and magnetic fields is given by the material equations in combination with Maxwell´s equations and can be calculated by:

$$\vec{D}(\vec{r},t) = \varepsilon\varepsilon_0 \vec{\mathrm{E}}(\vec{\mathrm{r}},\mathrm{t}) \qquad \vec{B}(\vec{r},t) = \mu\mu_0 \vec{\mathrm{H}}(\vec{\mathrm{r}},\mathrm{t}) \tag{2.21}$$

$$\vec{B}(\vec{r},t) = \frac{1}{c}\vec{\mathrm{e}}_{\mathrm{r}} \times \vec{\mathrm{E}}(\vec{\mathrm{r}},\mathrm{t}) \qquad \vec{H}(\vec{r},t) = \frac{1}{\mu\mu_0 c}\vec{\mathrm{e}}_{\mathrm{r}} \times \vec{\mathrm{E}}(\vec{\mathrm{r}},\mathrm{t})$$

where $c = \varpi / k$ is the speed of light, $\vec{e} = \vec{r} / r$ is the unity vector in propagation direction, ε is the dielectric constant, μ is the magnetic susceptibility, ε_0 and μ_0 are the corresponding values in vacuum. According to (2.21) the magnetic field $\vec{H}$ can be calculated from the electrical field $\vec{E}$ and may therefore be used as an alternative description for a electromagnetic plane wave.

2.3.2 Reflection and Transmission of Polarised Light

Consider light of known wavelength, polarisation and intensity that is passed onto a sample consisting of two different optical media. Depending on the optical properties of these materials and the incident angle, part of the light may be reflected at the interface while another part can be transmitted into the adjacent optical medium. In order to obtain information about the optical density of an investigated sample the intensity of reflected and transmitted light as well as the associated angles are measured. These quantities are dependent on the refractive index of the optical material. If the electromagnetic waves travel in the x-z-plane (Figure 2.6) two possible polarisations regarding the surface can be distinguished:

Transversal magnetic (p-) polarisation (TM): Here the magnetic field is polarised perpendicular to the plane of incidence (as schematically depicted in Figure 2.6); the components E_y, H_x, H_z are non-vanishing and the electrical and magnetic field in the three possible direction equals:

$$E_z = E_x = 0; \quad H_y = 0 \tag{2.22}$$

Transversal electric (s-) polarisation (TE): The electric field is polarised perpendicular to the plane of incidence (not shown) and in contrast to p polarised light the field components E_x,E_z and H_y are not vanishing while

$$H_z = H_x = 0; \quad E_y = 0 \tag{2.23}$$

In Figure 2.6 a schematic picture of transversal magnetic light is shown, which is reflected and transmitted at the interface of two optical media of differing refractive index. According to the well known reflection law the reflection angle θ'_1 equals the incident angle θ_1 measured against the surface normal,

$$\theta_1' = \theta_1 \tag{2.24}$$

while the transmitted beam can be detected at an angle given by Snell's law:

$$n_1 \cdot \sin\theta_1 = n_2 \cdot \sin\theta_2 \tag{2.25}$$

where n_1 and n_2 are the refractive indices of both optical media. Although the angles are independent of the polarisation of the light, it has to be considered if the intensity of the electromagnetic waves should be calculated.

The reflection spectrum is the intensity of the reflected wave as a function of the incidence angle. It can be calculated according to Fresnel´s equations if the refractive indices of the optical media are known. If E_i E_r and E_t are the electric fields of the incident, reflected and transmitted wave, respectively, the reflection and transmission is:

$$R = \frac{I_r}{I_e} = \frac{\left|\vec{E}_r\right|^2}{\left|\vec{E}_e\right|^2} \qquad T = \frac{I_t}{I_e} = \frac{\left|\vec{E}_t\right|^2}{\left|\vec{E}_e\right|^2} \tag{2.26}$$

with I_r, I_r and I_t being the measured intensity of the light beams. It is important to note that the analytical expressions for the electrical fields (not shown) are different for s and p polarisation, and so are the reflectivity and transmission.

Total internal reflection

If light is passed through matter with a refractive index n_1, subsequent reflection at a medium with a smaller refractive index n_2 (e.g. in the system glass/air) leads to a experimentally determinable transmission angle θ_2 as given by Snell's law (2.25). Upon increase of the incidence angle θ_1 one finds that the transmission angle θ_2 is increased until the maximum value of θ_2=90° is reached (see also Figure 2.6). Then θ_1 is called critical angle θ_c as given by

$$\sin\theta_c = \frac{n_2}{n_1} \qquad (2.27)$$

Further increase of the incidence angle θ_1 does not change the transmission angle θ_2 to more than 90° since the transmitted light is not able to enter back into the optical dense medium. Therefore it becomes a plane wave which travels along the interface between the two media and causes a so called evanescent field. Since all incident light is reflected for angles $\theta \geq \theta_c$ the reflectivity reaches R=1 and the corresponding sharp increase in R is often referred to as total reflection edge.

The resulting evanescent field decays exponentially perpendicular to the interface (in z direction). Changes in the optical properties that occur within the decay length of this field cause a system response by means of changes in the reflectivity spectrum. The interaction of this field with the environment is therefore fundamental for a number of measurement techniques. These are referred to as attenuated total internal reflection (ATR) methods. The decay length, at which the amplitude of the evanescent field is decreased to 1/e is the penetration depth d. It is in the range of the used wavelength and can be calculated by the following equation:

$$d = \frac{\lambda}{2\pi}\left(\frac{n_1^2}{n_2^2}\sin^2\theta - 1\right)^{-\frac{1}{2}} \qquad (2.28)$$

In Figure 2.7 the calculated reflectivity for p and s polarised light upon reflection at a prism/water interface is plotted as a function of the incidence angle. The plots result from a combination of Fresnel equations (polarisation dependence of the reflected intensity) and total internal reflection conditions (critical angle). By measuring the critical angle and knowledge of one of the refractive indices, the corresponding value of the second medium can be easily calculated by application of (2.27).

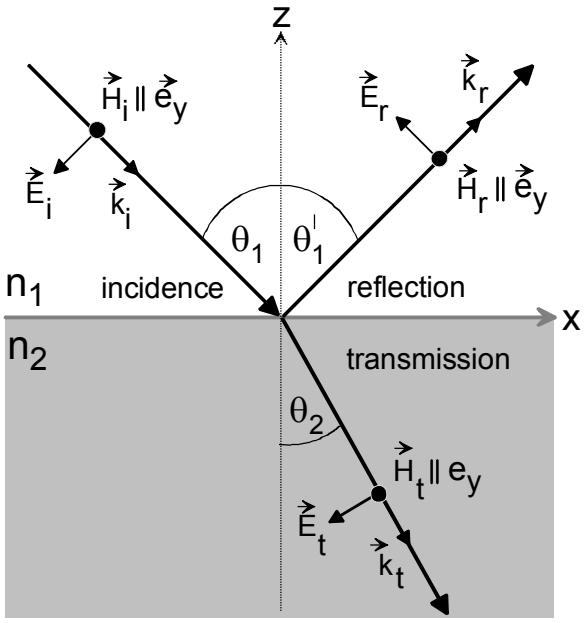

Figure 2.6: Schematic representation of reflected and transmitted p polarised light at the interfaces between two optical media of differing refractive index. The plane of incidence is the x-z plane and the magnetic field is polarised perpendicular to it (transversal magnetic polarisation). Note that the reflection angle equals the incident angle, while the angle of the transmitted beam is determined by Snells' law (see text).

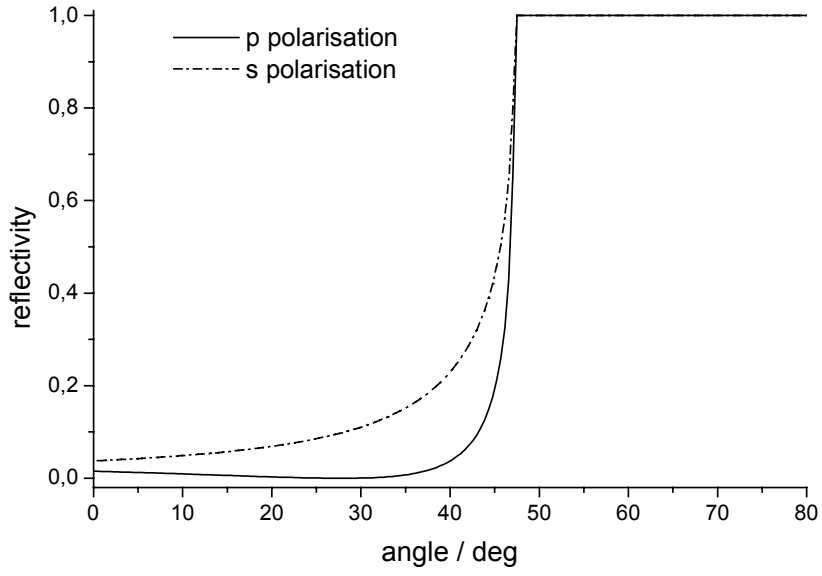

Figure 2.7: Calculated reflectivity for s- and p- polarised light reflected at the interface between a high refractive index $LaSFN_9$ prism (n=1.846) and water (n=1.332) at room temperature and a wavelength of λ=632.8 nm. Note that beyond the critical angle of θ_c=47.48° the reflectivity reaches unity for both polarisations.

2.3.3 Surface Plasmons in a Two Layer System

Surface plasmons are collective oscillations of the quasi-free electron-gas of a metal which propagate along the interface between a metal and a dielectric. These surface waves can be excited by reflecting light at the interface under certain experimental conditions, as discussed in 2.3.4. Plasmons are transversal electromagnetic waves, that are damped by the metal in the propagation direction x as well as perpendicular to the interface. Thereby the field intensity of the evanescent surface wave that is created by the plasmons reaches into both media (Figure 2.8). Before the various excitation mechanisms for surface plasmons are discussed the theoretical background of electromagnetic waves and their interaction with metallic surfaces is discussed in the following.

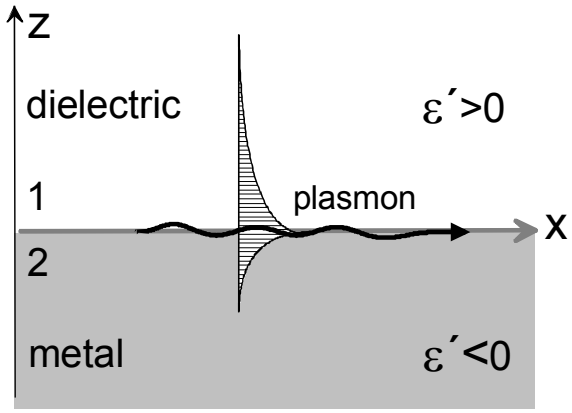

Figure 2.8: Schematic presentation of a surface plasmon at the interface between a metal and a dielectric. Note that the sign of the two media need to be opposite to allow for plasmon excitation.

Maxwell equations

In order to solve Maxwell´s equations for surface plasmons we have to consider an interface between two media. In contrast to 2.3.1 the dielectric constants of both adjacent media are complex:

$$\varepsilon_1 = \varepsilon_1' + i \cdot \varepsilon_1'' \qquad \varepsilon_2 = \varepsilon_2' + i \cdot \varepsilon_2'' \tag{2.29}$$

If we assume that the magnetic permeability equals one, we find the following connection between the dielectric constant ε and the complex refractive index (n+ iκ) of the materials. Both descriptions are equivalent and can be converted into each other:

$$\begin{aligned} (n + i\kappa)^2 &= \varepsilon_1' + i\varepsilon_1'' = \varepsilon \\ \varepsilon' = n^2 - \kappa^2 &\qquad \varepsilon'' = 2n\kappa \end{aligned} \tag{2.30}$$

with n being the refractive index of the material. κ is the absorption coefficient, which describes the damping of propagating electromagnetic waves due to interaction with the material.

In order to describe the electromagnetic wave in both media the Maxwell equations of the following form should be solved:

$$\left.\begin{aligned}\vec{E}_1(\vec{r},t) &= \vec{E}_1 \cdot \exp(i(k_{x1}x + k_{z1}z - \varpi t)) \\ \vec{H}_1(\vec{r},t) &= \vec{H}_1 \cdot \exp(i(k_{x1}x + k_{z1}z - \varpi t))\end{aligned}\right\} \text{ for } z > 0$$
$$\left.\begin{aligned}\vec{E}_2(\vec{r},t) &= \vec{E}_2 \cdot \exp(i(k_{x2}x + k_{z2}z - \varpi t)) \\ \vec{H}_2(\vec{r},t) &= \vec{H}_2 \cdot \exp(i(k_{x2}x + k_{z2}z - \varpi t))\end{aligned}\right\} \text{ for } z < 0 \qquad (2.31)$$

where k_{1z} , k_{2z} , k_{x1} and k_{x2} are the wavevectors for the media 1 and 2 in z and x direction, respectively. Due to the symmetry of the problem a separation of the electromagnetic fields into transversal magnetic (TM) modes with $\vec{H} = (0, H_y, 0)$ and transversal electric (TE) modes with $\vec{E} = (0, E_y, 0)$ is possible. All other solutions are superpositions of these two cases.

Since the electric field vector in s polarisation (TM) has no component perpendicular to the interface no surface polaritons can be induced. Therefore the excitation of plasmons is not possible by s but only with p polarised light. Since the tangential components of $\vec{E}$ and $\vec{H}$ are steady at the interface for p light it follows that

$$E_{x1} = E_{x2} \qquad H_{y1} = H_{y2} \qquad (2.32)$$

and therefore a comparison with (2.31) leads to $k_x = k_{x1} = k_{x2}$. Together with $c_0 = 1/\sqrt{\varepsilon_0 \mu_0}$ and an insertion of (2.31) in the Maxwell equations one obtains:

$$\begin{aligned} k_{z1} H_{y1} - \frac{\varpi}{c_0} \varepsilon_1 E_{x1} &= 0 \\ k_{z2} H_{y2} - \frac{\varpi}{c_0} \varepsilon_2 E_{x2} &= 0 \end{aligned} \qquad (2.33)$$

Finally, insertion of (2.32) leads to the only non trivial solution:

$$\frac{k_{z1}}{k_{z2}} = -\frac{\varepsilon_1}{\varepsilon_2} \qquad (2.34)$$

A closer look onto at last equation reveals that such an electromagnetic wave can only exist at the interface between two materials that have dielectric constants of opposite sign. Therefore

plasmons can be excited at the interface between metal layers (negative ε) and dielectrics. Frequently, silver is used as the metallic layer, but in general gold is preferred due to its high stability against most buffer solutions and environmental influences.

Finally, the dispersion relation of surface plasmons can be derived from the given equations:

$$k_x = k_x' + ik_x'' = \frac{\omega}{c_0}\sqrt{\frac{\varepsilon_1\varepsilon_2}{\varepsilon_1+\varepsilon_2}} \qquad (2.35)$$

The amplitude of the electrical field decays exponentially into both media in z direction as well as into the propagation direction. The propagation length can be calculated by

$$L_x = \frac{1}{2k_x''} \qquad (2.36)$$

and plays an important role for the lateral resolution of methods like surface plasmon microscopy. The length L_x limits the dimensions of the smallest structures, that can still be detected by this method. For an interface between gold ($\varepsilon = -12 + i \cdot 1.3$) and a dielectric and the use of 632,8 nm the propagation length is about 5μm.

2.3.4 Excitation of Surface Plasmons

Although it is known that surface plasmons can be excited by the bombardment of electrons, excitation by incident transversal magnetic (TM) light is the frequently the method of choice, due to the easy experimental handling. In addition to the limitation to p-polarised light a number of additional conditions have to be fulfilled in order to excite surface plasmons.

Consider the dispersion relation of free photons travelling through a dielectric medium with (2.35). Then we find that at a each frequency the impulse of photons is always smaller than the one of surface plasmons propagation along the metal-dielectric interface:

$$k_{ph} = \frac{\varpi}{c}\sqrt{\varepsilon_1} < \frac{\varpi}{c}\sqrt{\frac{\varepsilon_1\varepsilon_2}{\varepsilon_1+\varepsilon_2}} = k_{psp} \qquad (2.37)$$

A graphical presentation of this relation is given in Figure 2.9. Although the dispersion relation of the plasmons (P1) approaches the linear relation of free photons (a) there is no intersect between both lines. The dark grey marked area represents the frequency/wave vector combinations that are accessible by light in vacuum. It is therefore important to note, that surface plasmons are not directly excitable by light in vacuum, unless the impulse of the free photons is increased by appropriate experimental techniques which are described in the following:

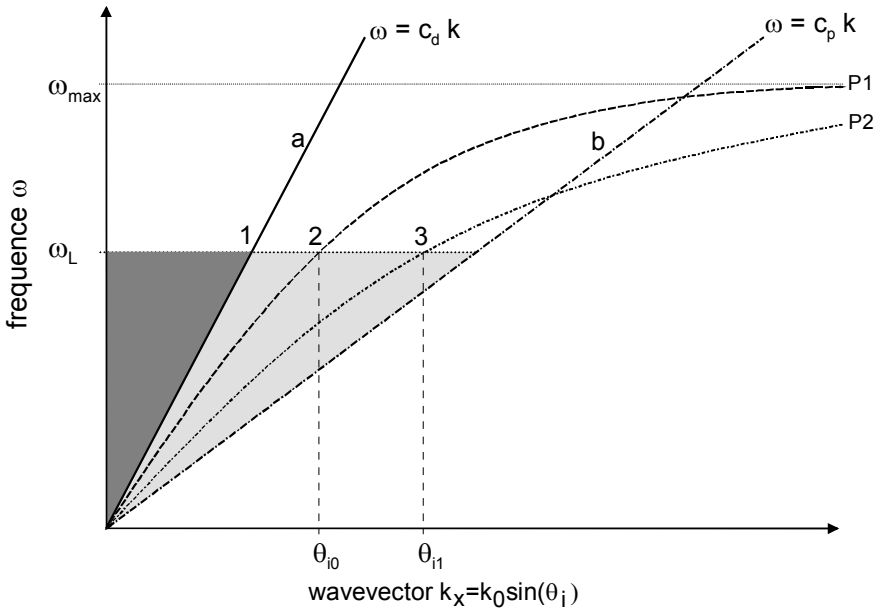

Figure 2.9: Dispersion relation of a) free photons in a dielectric, b) free photons propagating in a coupling prism, compared with the dispersion relation for surface plasmons at the interface between metal and dielectric, before (P1) and after adsorption of an additional dielectric layer (P2). At a given laser wavelength (ω_L) a match of energy and impulse of the photons in the prism (b) and plasmons can be achieved (2,3) due to an increase of the impulse of the free photons (1).

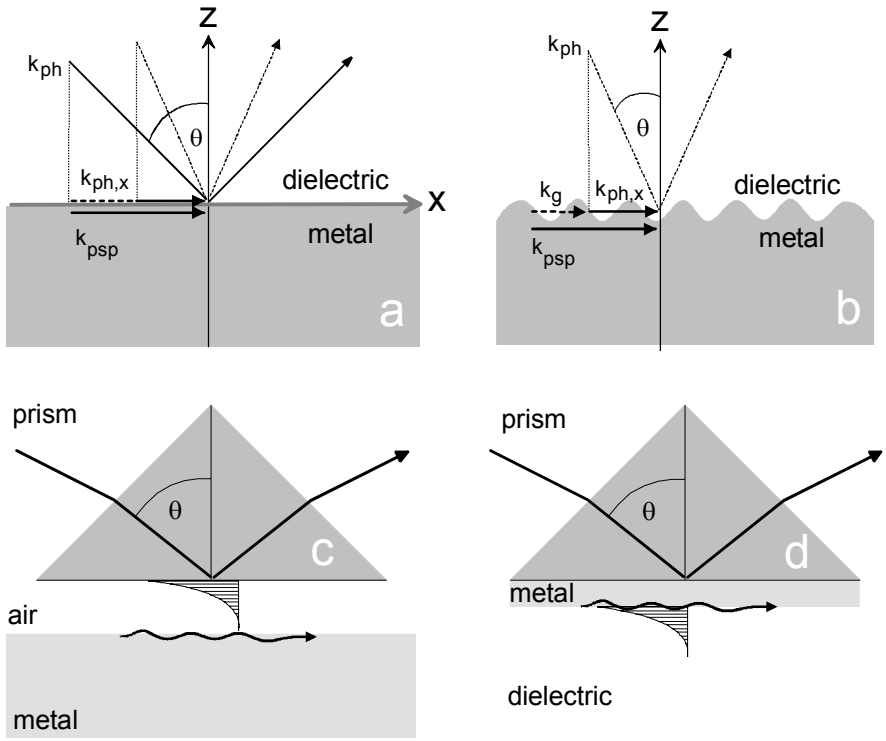

Figure 2.10: Excitation of surface plasmons by light. a) the projection k_x of the light wave vector k_{ph} can be varied by changing the incident angle until it matches one of the plasmon k_{psp}. In case of prism coupling (Otto- c, and Kretschmann configuration d) the wave vector of the light is increased by the interaction with the prism, while in case of grating coupling (b) the grating vector k_g is added to match the plasmon wave vector.

Prism coupling

Although surface plasmons exhibit photonic character a direct coupling of incident light is not possible on a smooth surface, since the impulse of light in a dielectric is too small to couple to the surface. One method to increase the impulse of the photons is to pass the photons through a medium with higher refractive index than the dielectric. This can be done by reflecting the incident light on the base plate of a high refractive index prism (Figure 2.10 c and d). In this so called prism coupling the surface plasmons are excited by the evanescent field of the reflected light under total internal reflection conditions. A detailed description of prism coupling can be found in [10,40-43].

In the case of the Otto configuration (c) the evanescent field bridges a 200nm wide air gap between the prism and the metal and the plasmons are excited at the metal/air interface[44]. Since this configuration is experimentally challenging, an alternative prism coupling set-up is preferred frequently. In the Kretschmann configuration (d) [45] a thin metal film is evaporated directly onto the base plate of the prism and plasmon excitations are found on both sides of the metal film. We only consider the plasmons at the metal/dielectric interface since they can be used to sense changes in the adjacent dielectric. The maximal thickness of the metal film is limited, since metal films that are too thick damp the evanescent field of the reflected beam. Then excitation of plasmons on the opposite site of the film is not possible. On the other hand, losses of the excited plasmon field would occur if the field reaches back into the prism due to an insufficiently thick metal film. Therefore an optimal thickness exists and is in the range of 48nm for gold and excitation by 623,8 nm helium-neon laser light.

As schematically illustrated in Figure 2.9 b, passing the high refractive prism (b) changes the dispersion relation of free photons. The impulse of the photons at a given frequency ω_L is increased compared to photons outside the prism (a). Due to this increase all k values in the light grey marked area are accessible now by the reflected light and a match with the dispersion relation of the surface plasmons occurs.

The wavevector of the light k_{ph} is not important itself for the excitation of surface plasmons, but the projection $k_{ph,x}$ of it onto the propagation direction x of the surface waves. According to the schematic presentation in Figure 2.10a it is possible to tune the system into resonance by changing the incidence angle θ of the incoming laser beam until $k_{ph,x} = k_{ph}\sin(\theta)$. If the projection $k_{ph,x}$ matches the surface plasmon wave vector k_{psp} resonance can occur. This situation corresponds to the intersection 2 in Figure 2.9 where resonant coupling occurs at the

given combination of used frequency and incidence angle. Once the system is in resonance, surface plasmons are excited by the energy of the incident laser light, resulting in a decrease of the reflected intensity. Therefore a resonance minimum is observed by plotting the reflected laser intensity versus the applied incident angle. Such a typical resonance curve of the prism-gold-water system is given in Figure 2.11:

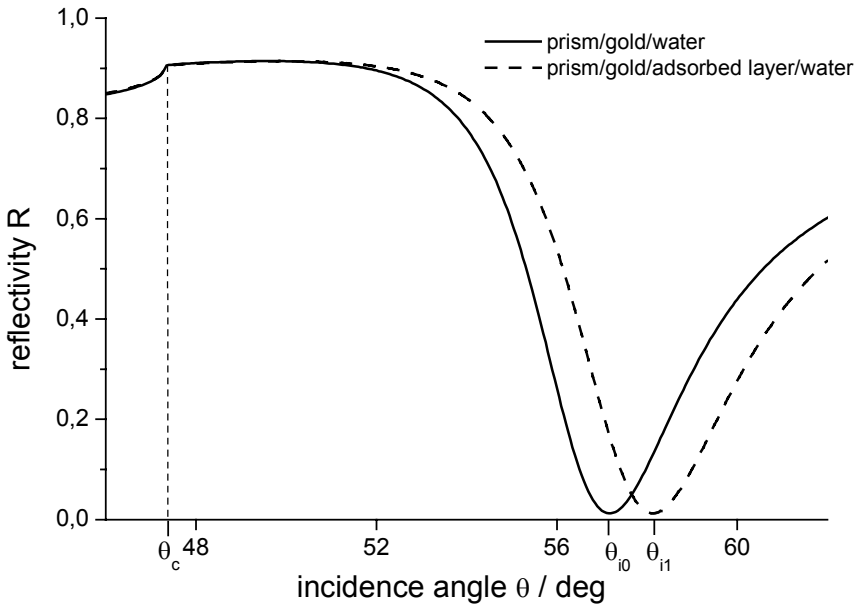

Figure 2.11: Typical resonance curves of two systems are shown: Note that the resonance angle of the system is shifted if an additional layer at the gold is taken into consideration.

Starting from small incidence angles the reflectivity increases until a maximum value is reached at the total reflection edge, θ_c. The reflectivity before the total reflection edge is rather high because the thin metal film acts as a mirror that reflects most of the incoming laser light. Note, that the maximal reflected intensity never reaches unity due to the partial dissipation of photon energy in the metal. According to (2.27) the critical angle θ_c is determined only by the refractive indices of both outer media (prism and water). Further increase of the incident angle increases the impulse incoming photons until the resonance conditions are fulfilled. This results in a decrease of the measured reflectivity until the resonance minimum is reached at θ_{i0}. The resonance dip exhibits a distinct half-width which is dependent on the extent of damping processes in the metal. The resonance angle at which maximal energy transfer occurs is dependent on the dielectric constants of all components and can be derived from the dispersion relation (2.35) and (2.30):

$$\theta = \arcsin\sqrt{\frac{\varepsilon_{metal} \cdot \varepsilon_{dielectric}}{(\varepsilon_{metal} + \varepsilon_{dielectric}) \cdot \varepsilon_{prism}}} \qquad (2.38)$$

2.3.5 Sensitivity of Surface Plasmons to Optical Changes

Since the evanescent field of the surface plasmons decays exponentially into the dielectric medium, changes of the optical properties of the adjacent dielectric will alter the excitation conditions for plasmons. Therefore processes near the metal surface like the adsorption of additional dielectric layers can be sensed by the plasmon field and monitored by the consequences to the resonance angle of the system.

Now we consider the layer system formed by prism-gold-dielectric from the previous paragraph and add another layer of dielectric material onto the gold. Here the dielectric constant of these additional layers is assumed to be higher than the one of the surrounding medium. Then the mean refractive index of the area that is sensed by the evanescent plasmon field is increased. As a result the dispersion relation (P2) is shifted towards larger wavevectors as depicted in Figure 2.9.

$$k_{p2} = k_{p1} + \Delta k \qquad (2.39)$$

where k_{p1} and k_{p2} are the wavevectors of the system before and after the adsorption. It is important to note that the increment Δk depends strongly on the refractive index and the thickness of the adsorbed layer.

At a given frequency ω_L the intersection with the dispersion relation of the photons (3) is therefore shifted towards higher k values. Consequently the connected incidence angle has to be experimentally adjusted to achieve resonance again. This situation is shown in Figure 2.11 where the new resonance angle θ_{i0} of the associated resonance curve (dotted) can be found at higher angles. This resonance minimum shift is fundamental for the experimental application in methods like surface plasmon spectroscopy or microscopy. In case of non adsorbing layers ($\varepsilon'' \geq 0$) the measured shift $\Delta\theta$ is proportional to the change of the optical layer thickness d and refractive index:

$$\Delta\theta \approx \Delta n \cdot \Delta d \qquad (2.40)$$

Since an infinite number of combinations of layer thickness and refractive index exist that lead to the same resonance shift, one of the parameters has to be known in order to calculate the

other one. Therefore at least one of the film parameters is usually determined by other methods or a simultaneous detection of both variables using waveguide spectroscopy is carried out before.

2.3.6 Transfer Matrix Method

The calculation of the reflectivity of a given multilayer system is done considering the field distribution, reflection and transmission at every layer in the system. The mathematical formalism utilising the derived results from 2.3.3 is called the transfer matrix method. This algorithm forms the base for the computer program Winspall2.0 that was used for the analysis of the measured reflectivity spectra. A detailed description of the underlying mathematics of the method can be found in [46].

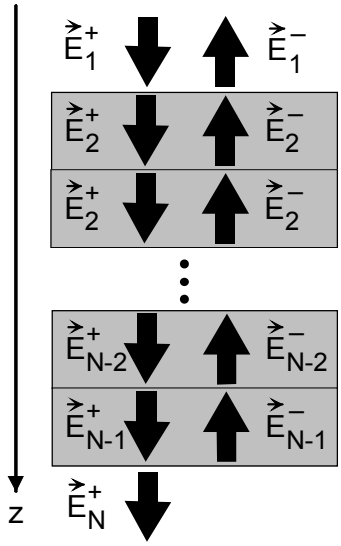

Figure 2.12 : Schematic representation of the reflection and transmission of electric fields in a multilayer system

We consider a multilayer system as depicted schematically in Figure 2.12: In each layer electromagnetic waves can be thought to be superpositions of two partial waves, which are propagating into opposite directions parallel to the surface normal z. The electric field can therefore be described by:

$$\vec{E}(x,z,t) = \vec{E}_i^+ \cdot \exp(i(\vec{k}_x x + \vec{k}_i \cdot z - \omega \cdot t)) + \vec{E}_i^- \cdot \exp(i(\vec{k}_x x + \vec{k}_i \cdot z - \omega \cdot t)) \qquad (2.41)$$

with the components of the wavevectors k_x and k_i:

$$k_x = \frac{\varpi}{c}\sqrt{\varepsilon_1} \cdot \sin(\theta) \quad \text{and} \quad k_i = \sqrt{\left(\frac{\varpi}{c}\right)^2 \varepsilon_i - k_x^2} \qquad (2.42)$$

In the following the calculations are done for the electric field only, since the magnetic field can be calculated by Maxwell´s equations. Values for p and s polarised light are distinguished by

the appropriate indices. The propagation of the field in between layer number i with the thickness d_i in z direction is given by:

$$\begin{pmatrix} \vec{E}_i^{+}(z_i) \\ \vec{E}_i^{-}(z_i) \end{pmatrix}_{p,s} = \begin{pmatrix} \exp(-ik_i d_i) & 0 \\ 0 & \exp(ik_i d_i) \end{pmatrix} \begin{pmatrix} \vec{E}_i^{+}(z_i + d_i) \\ \vec{E}_i^{-}(z_i + d_i) \end{pmatrix}_{p,s} = P_i^{p,s} \begin{pmatrix} \vec{E}_i^{+}(z_i + d_i) \\ \vec{E}_i^{-}(z_i + d_i) \end{pmatrix}_{p,s} \quad (2.43)$$

Here the transmitted and reflected field components at the upper and lower end of the layer are connected by the propagation-matrix $P_i^{p,s}$ that takes into account absorption and phase-shifts. While crossing the interface one finds that due to the steadiness of the tangential components and the normal components of the electric displacement the electrical field is:

$$\begin{pmatrix} \vec{E}_i^{+} \\ \vec{E}_i^{-} \end{pmatrix}_{p,s} = \frac{1}{2} \begin{pmatrix} 1+\kappa^{p,s} & 1-\kappa^{p,s} \\ 1-\kappa^{p,s} & 1+\kappa^{p,s} \end{pmatrix} \begin{pmatrix} \vec{E}_{i+1}^{+} \\ \vec{E}_{i+1}^{-} \end{pmatrix}_{p,s} = Q_{i->i+1}^{p,s} \begin{pmatrix} \vec{E}_{i+1}^{+} \\ \vec{E}_{i+1}^{-} \end{pmatrix}_{p,s} \quad (2.44)$$

with

$$\kappa^p = \frac{\varepsilon_{i+1} \cdot k_i}{\varepsilon_i \cdot k_{i+1}} \quad \text{and} \quad \kappa^s = \frac{k_i}{k_{i+1}} \quad (2.45)$$

The matrix $Q_{i->i+1}^{p,s}$ reflects the amplitudes of the electrical field on both sides of the interface between layer i and i+1 and describes reflection and transmission at this single interface. For the description of the complete system the transfer matrix T is used, which is obtained by multiplication of all matrices P and Q. Thus, the propagation in every layer as well the changes of the field component at the crossing to the next layer is taken into account:

$$T = Q_{1->2} \cdot P_2 \cdot Q_{2->3} \cdot P_3 \cdot \cdots \cdot Q_{N-1->N} \cdot P_2 \quad (2.46)$$

The transfer matrix T combines the field components in the layers on the outside of the multilayer system and can therefore be used to calculate the reflectivity of the complete system if the thickness and refractive index of all layers, the used wavelength and the incident angle are given. Then the reflectivity R can be calculated as the square of the reflection coefficient ρ which is known to be the ratio between incident and reflected intensity:

$$R = \rho^2 = \frac{\left|E_1^{-}\right|^2}{\left|E_1^{+}\right|^2} \quad (2.47)$$

2.3.7 Field Distributions

The electromagnetic field distribution in the layer system may be represented by the magnetic field intensity. The magnetic intensity found in Figure 2.13 is normalized to the incident magnetic intensity and was calculated for the layer system prism (ε=3.4069)/gold (d=50nm, ε=-12.1+i 1.3)/adsorbed layer (d=5nm, ε=2.25)/aqueous solution (ε=1.778) [47]. A look at the calculated intensity at incidence angles near the resonance angle (θ_{i1}) reveals a distinct field enhancement in the metal layer which leads to an increase of the incident field by a factor of about 18 at the metal surface. On both sides of the metal surface the field intensity decays exponentially, resulting in a certain penetration depth into the dielectric medium. This penetration depth is in the order of the used wavelength. It has importance for the surface sensitivity of the surface plasmon spectroscopy, since only processes in the evanescent plasmon field perturb it and are therefore detectable.

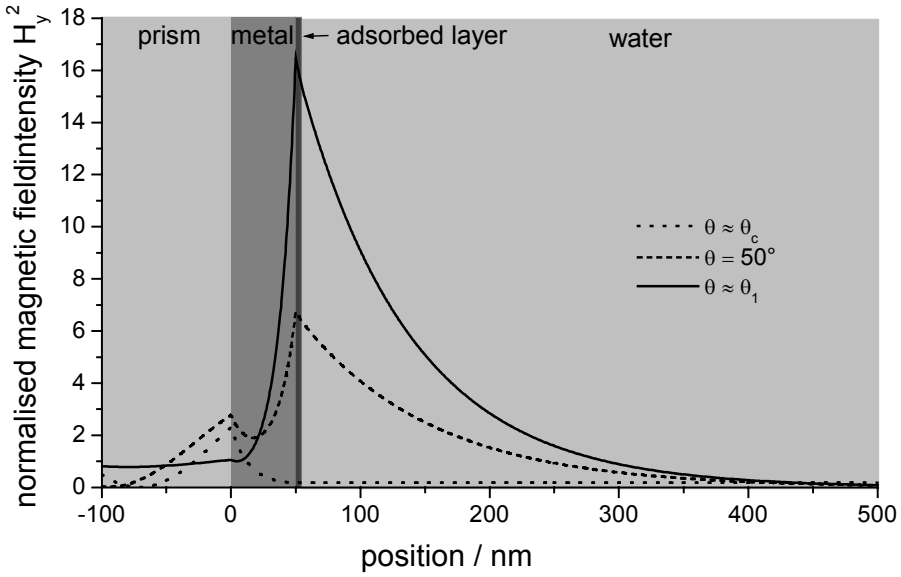

Figure 2.13 : Normalised magnetic field-intensity along a layer system prism/metal/adsorbed layer/water. The exponential decay of the evanescent field into the dielectric is evident. Note that at incidence angles around the resonance minimum for this system θ_1 a distinct field enhancement at the metal surface is noticeable.

In the following the field intensities at the surface for different metallic surfaces and the pure dielectric case of a glass/dielectric interface are considered. The calculated intensities are normalized to the incident intensity and are plotted together with the corresponding reflectivity in Figure 2.14 depending on the incidence angle θ [16].

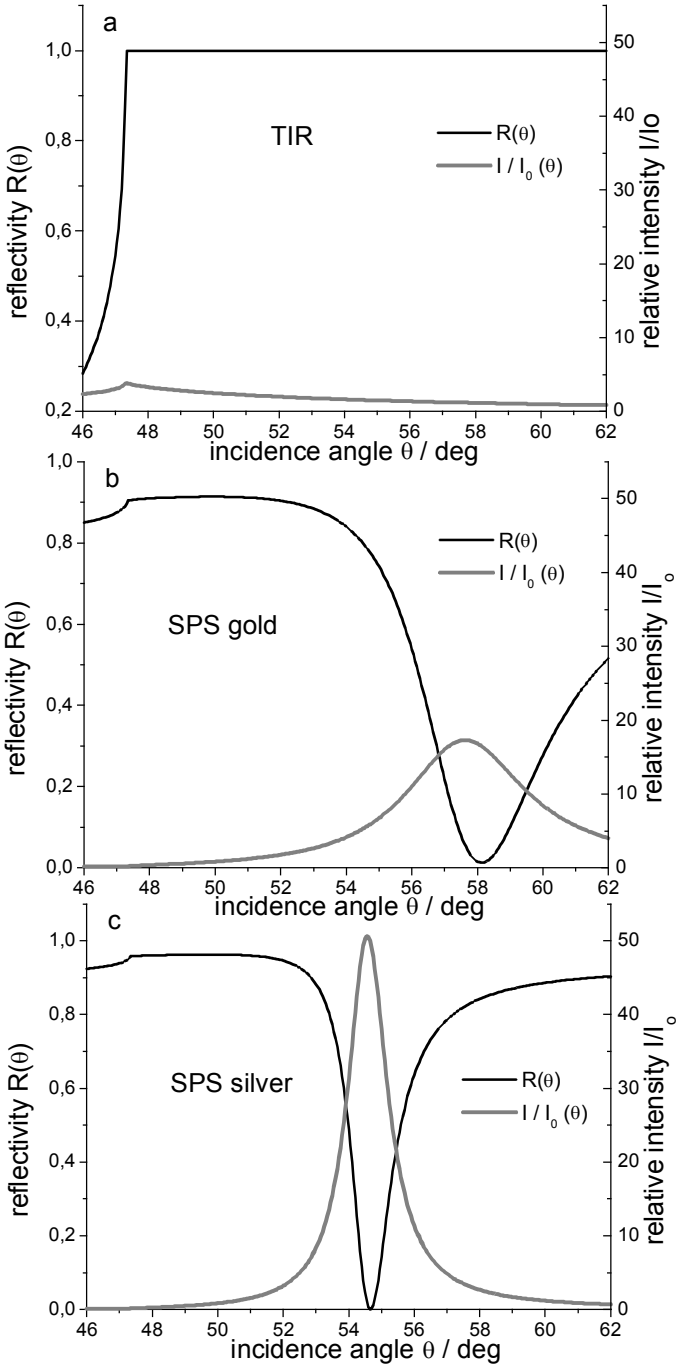

Figure 2.14 : Comparison between TIR and surface plasmon excitation by considering calculated reflectivities R and relative intensities at the surface in the case of a) glass/water interface b) gold and c) silver

In the case of the glass/dielectric interface (a) the total reflection edge is observed in the reflectivity. For angles larger than θ_c the reflected intensity becomes unity. The field intensity at the surface for TIR (total internal reflection) is plotted and a moderate increase of a factor 4 is found at the critical angle. This originated from the constructive interference of the amplitudes of the incoming and reflected electromagnetic field. This moderate enhancement together with the

evanescent character of the light at angles $\theta>\theta_c$ forms the basis for surface sensitive fluorescence spectroscopy [48].

If the glass surface is covered with a thin gold film (b) the total reflection edge is still observed. Additionally the resonance minimum is detectable as described in 2.3.4. Close to the reflection minimum a substantial field enhancement can be found. An enhancement factor of 16 is reached compared to the intensity of the incident electromagnetic field. If silver is used, an even higher factor of about 50 can be obtained (c). These factors as well and the seen half-width of the resonance depend on the real and imaginary part of the dielectric constant. Since the silver film was modelled with (ε=-12.1+i 1.3)[49] the imaginary part ε'' is smaller compared to gold. This results in a narrower resonance dip. Furthermore, the smaller ε'' the lower is the absorption of the sample and the dissipation of optical intensity in the metal, which results in high enhancement factors. This phenomenon is already known from other spectroscopic methods, like surface enhanced Raman scattering [50].

A closer look at the angular positions of the resonance minimum and the maximum surface intensity reveals that the intensity maximum is shifted slightly to smaller incidence angles. This can be explained by considering the system as a resonator that is excited by the incoming laser intensity. If we now sweep through the resonance the phase difference between the surface plasmon mode relative to the driving photon field can be found to behave as follows: in the case of a fictive loss free metal surface the phase would change from 0° to 180° as we cross the angle of resonance, with a sharp step at the resonance. In surface plasmon spectroscopy we observe a coherent superposition of partial waves reflected at the metal/prism interface and a part of the surface mode reradiated into the prism. The observed minimum in the resonance scan can now be explained as the destructive interference between the two partial waves, which are phase shifted by 180° at the resonance angle. Therefore no shift between resonance minimum and intensity maximum would be seen in case of such a loss free metal. In real metallic systems any losses, as described by the imaginary part of the dielectric constant $\varepsilon''>0$, smear out the phase change at the plasmon resonance angle and consequently the resonance minimum and the surface intensity peak. Since the damping in gold is stronger than in silver ($\varepsilon''_{Au}> \varepsilon''_{Ag}$) the difference between these angular positions is larger as for the silver system depicted in Figure 2.14c[16]. Silver is frequently used as metallic layer because of the strong enhancement of the surface mode and the narrow resonance dip. Due to the known stability of noble gold against buffer solution and oxidising agents, the latter is preferred in experiments.

3 Experimental Methods

3.1 Optical Methods

A major part of this work is based on the characterisation of surface processes like adsorption and desorption of analytes onto dielectric thin films of known architecture. Surface Plasmon Spectroscopy (SPS) as a prominent optical method permits the detection of such processes on metal substrates and is therefore described in detail. Furthermore the experimental contribution of simultaneous fluorescence detection in Surface Plasmon Fluorescence Spectroscopy (SPFS) will be discussed. Finally the combination of both methods with microscopy and the resulting possibility to analyse laterally structured samples will be discussed.

3.1.1 Surface Plasmon Spectroscopy (SPS)

Since the theoretical background of surface plasmons was already discussed in chapter 2.3, the measurement modes of SPS are described in the following. The experimental set-up is illustrated in chapter 3.1.1 in combination with fluorescence detection.

Scan curves

As explained, a resonance spectrum (also referred to as scan curve) is obtained by reflecting a polarised laser beam off the base plane of a prism and plotting the normalised reflected intensity versus the incidence angle. The range of the angles measured is important, since the resulting scan should cover the total reflection edge and most of the resonance minimum. The obtained scan curve can then be fitted according to Fresnel formula in order to calculate the thickness of the metallic and dielectric layers. The calculations based on the transfer matrix algorithm are carried out with the computer software Winspall 2.0, which was developed in our group. Parameters that are included in the fitting procedure are the measured reflectivity, the incidence angle, thickness and dielectric constants of the layers as well as the used laser wavelength and the geometry of the coupling prism. By iterative optimisation of the parameters the simulated reflectivity curve is fitted to the measured scan curve and the optical constants of the involved layers are determined.

Since the thickness and dielectric constant of the layers cannot be determined independently, one of the parameters has to be measured by use of other techniques. However, if the refractive

index of the prism is known, the refractive index of a used solvent can be easily calculated by determining the critical angle. The angular position of the total reflection edge is only dependent on the optical constants of both outer media.

The adsorption of an additional layer (e.g. a self assembled monolayer of thiols on gold) changes the optical properties of the dielectric next to the metal and results in a shift of the resonance minimum as schematically depicted in Figure 3.1. This shift can be theoretically considered by introducing an additional layer into the Fresnel simulations while the parameters of the other layers are held constant. Such a comparison between the simulated parameters before and after the adsorption process allows for the determination of the thickness or refractive index of a layer adsorbed to the metal.

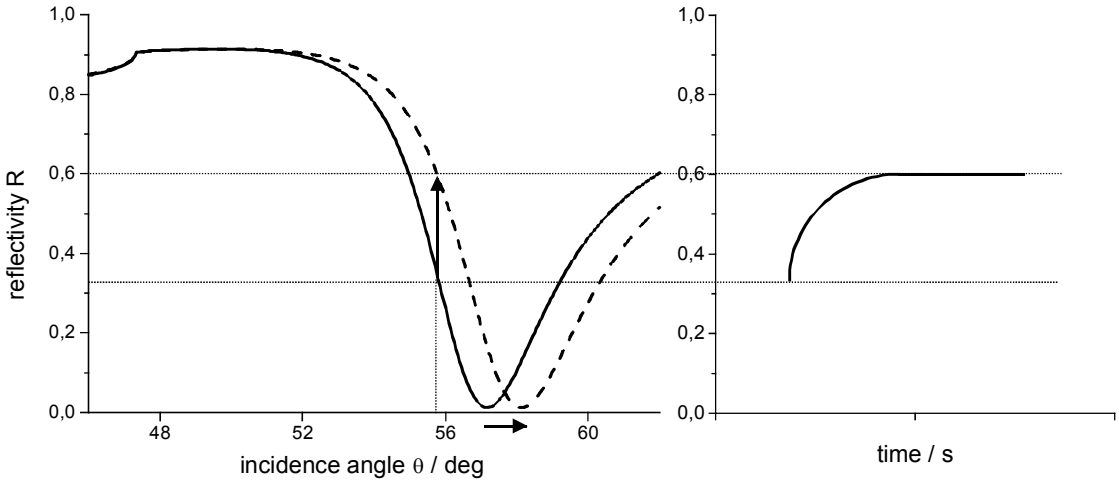

Figure 3.1 : Scan curves and associated kinetics. Note that the reflectivity is increased if the incidence angle is fixed and the resonance curve is shifted.

Kinetics measurement

Not only static measurements of film-thickness and refractive index can be obtained but also the online monitoring of processes near the surface is possible and kinetics of surface reactions can be recorded. For this purpose the incidence angle is fixed at a position where the measured scan curve exhibits a linear slope (e.g. at 30% reflectivity) and the detected reflectivity is recorded with time. The reflectivity at this fixed incidence angle is increased if the resonance is shifted towards higher angles and the detected shift represents a linear time dependence of the optical properties of the investigated system. Here it is assumed that the dependence of the resonance minimum shift on optical changes is linear, too. In addition, it is assumed that the shape of the scan curve in the considered region is not changed upon adsorption of the additional layer. Otherwise the linear response of the kinetic curve would be lost.

3.1.2 Surface Plasmon Fluorescence Spectroscopy (SPFS)

In chapter 4 is will be shown that fluorescent molecules near surfaces can be excited by the evanescent field of surface plasmons. In the following the experimental set-up and the measurement principle will be discussed and the analysis and interpretation of the data will be explained.

Experimental Set-up

The used set-up is a common surface plasmon spectrometer [51] which was modified by fluorescence detection units. As schematically depicted in Figure 3.2, a HeNe laser (Uniphase, 5mW, λ=632.8 nm) and a frequency doubled Nd:YAG laser (λ=532 nm) were used, respectively. The excitation beam passes two polarisers, by which the intensity of the incident light and its TM polarisation can be adjusted. Using a beam splitter and two programmable shutters the incident wavelength can be easily changed by blocking one of laser beams and passing the other laser onto the sample.

The incident laser is reflected off the base plane of the coupling prism (Schott, 90°, $LaSFN_9$) and the reflected intensity is focussed by a lens (L2, f=50mm, Ovis) for detection by a photodiode. In order to allow for noise reduced and daylight independent measurements of the reflected intensity, the photodiode is connected to a lockin-amplifier. This unit filters out all frequencies that are not modulated by the operation frequency of the attached chopper. If working in a lab environment multiple frequencies of 50 Hz should be avoided, since this is the frequency of electric ceiling lamps for example.

The sample is mounted onto a 2 phase goniometer (Huber) which can be moved in 0,001° steps by the use of the connected personal computer. According to the reflection law the angular position of the optical arm holding the detection unit (detector motor) is adjusted during the measurements. The sample is mounted onto two xy-tables and a tilting table, which allow for the optimal adjustment of the set-up. This adjustment is described in detail in the next section.

In order to detect the fluorescence emission of the sample a collecting lens (L1, f=50 mm, Ovis) focuses the emitted light though an interference filter (λ=670 ± 2nm, LOT) into a photomultiplier tube (PM1, Hamamatsu), which is attached to the backside of the sample. Additionally, a second photomultiplier tube PM2 can be placed onto the detector arm. It was used to monitor fluorescence light that was re-radiated and emitted on the opposite side of the coupling prism (see chapter 4). Both photomultipliers are connected to a counter (HP) via a photomultiplier protection unit and a programmable switch box. Thus, the signal of both units

can be alternatively recorded by the on-line personal computer. The protection unit closes the implemented shutter in front of each photomultiplier if the irradiation exceeds a predefined level in order to avoid damage of the sensitive fluorescence detection equipment.

Preparation of the Flow Cell

As schematically shown in Figure 3.3 the flow cell constructed of quartz glass (Herasil, Schott) is placed onto a low-fluorescent quartz glass slide (Herasil, Schott) and sealed by O-rings made of Viton. The glass waver is placed on top of the flow cell, while the evaporated metal film points towards the cell. Finally a high refractive index prism ($LaSFN_9$, n=1.845) is mounted on top of the glass sample. To allow for optimal coupling of incident light into plasmon modes of the metal, a thin film of refractive index matching oil is added in between both glass units. This fluid should have a similar refractive index as prism and glass in order to allow for unperturbed coupling. The higher the refractive index of this fluid the higher the vapour pressure and the easier the fluid is evaporated at room temperature. For practical reasons a less volatile index match liquid is frequently used with the drawback of a lower refractive index and thus non optimal match. The flow cell is equipped with an inlet and outlet and can hold volumes up to ca. 90ul. For the injection of analyte samples one-way plastic syringes are used, but to rinse the cell with pure buffer and to rinse the sample after adsorption processes a peristaltic pump is used.

Practical Alignment Instructions

In order to align the measurement system two apertures are mounted into the incident and reflected beam (Figure 3.4). *Without* having the sample mounted in the set-up the detector arm is moved to 180° to align the height of pinhole 2 and to adjust the position of the photodiode. The incident laser should pass through both apertures and the position of the laser spot on aperture 2 should not change upon movement of the pinhole along the detector arm. Otherwise the height of pinhole 2, the orientation of the photodiode and the angular position of the detector arm have to be optimised.

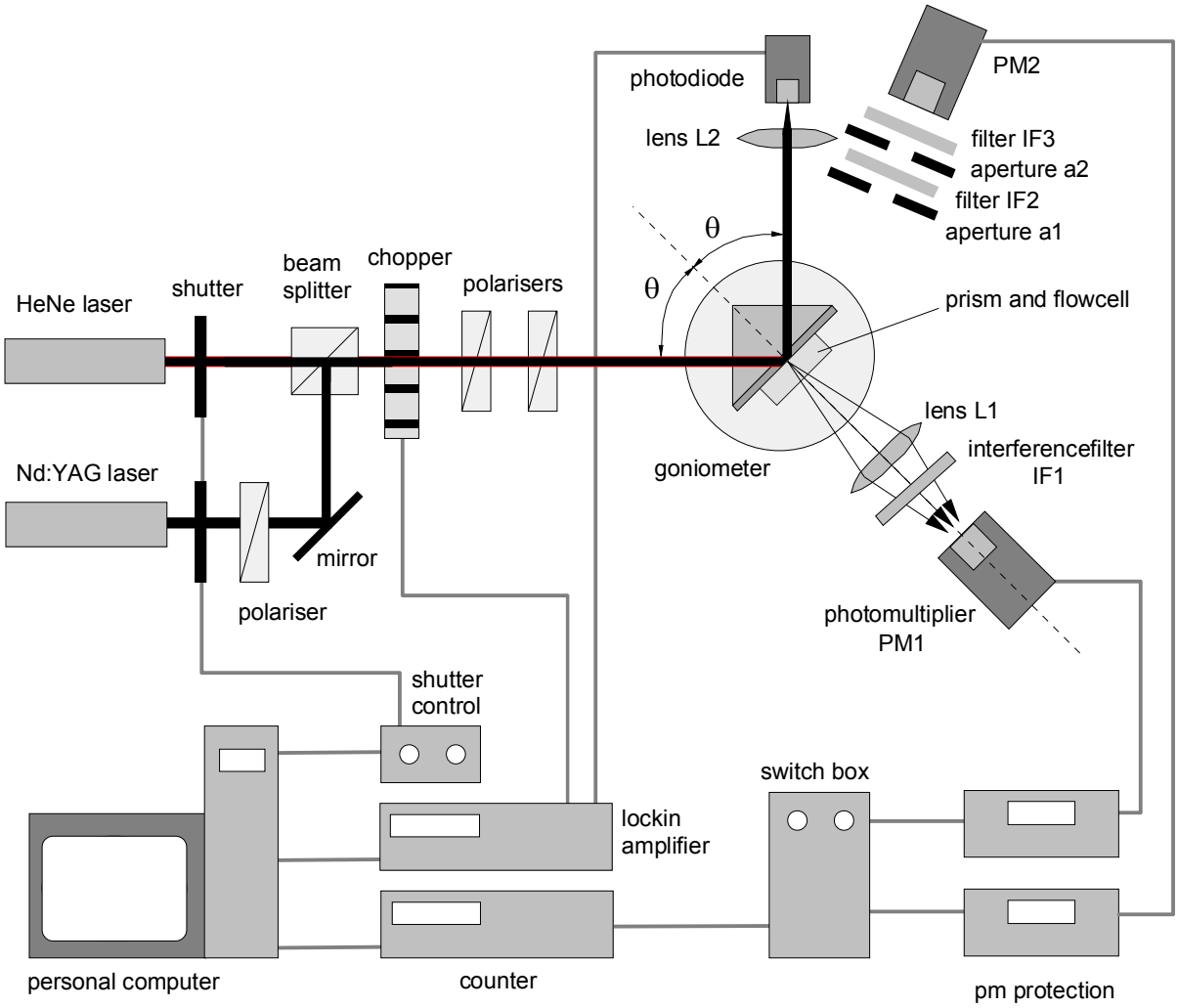

Figure 3.2 : Surface Plasmon Fluorescence Spectroscopy (SPFS) set-up which can be run with two photomultipliers at two different laser wavelength.

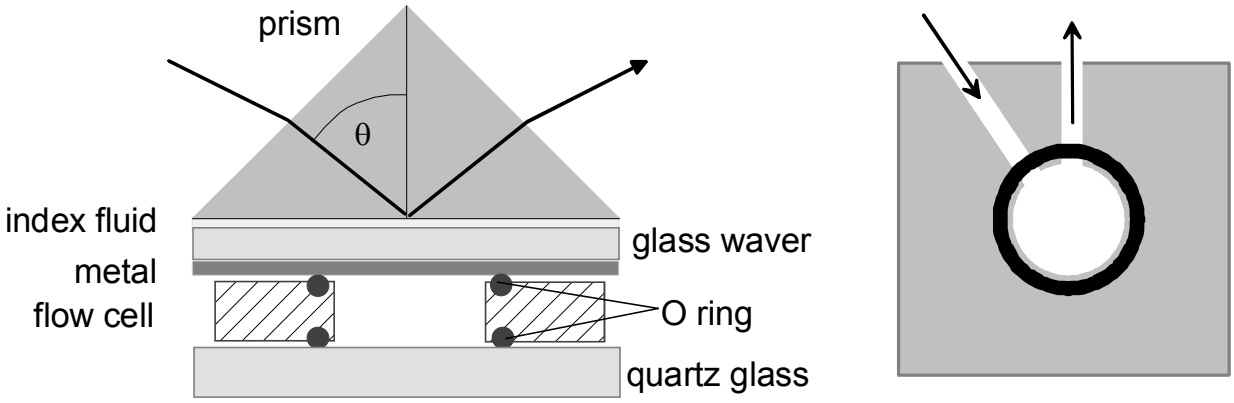

Figure 3.3 : Mounting of the prism, sample and flow cell. The latter is shown on the right side.

The sample is mounted into the set-up and the sample motor moved to 45° while the detector arm moves to 90° according to the reflection law. At this angle, a part of the incident beam should be reflected at the prism-air interface. The back reflex should be directed back into pinhole 1, while the reflection on the prism-gold interface should pass pinhole 2. Sometimes two laser beams are reflected back to aperture 1. Then the light beam that does not change the intensity upon variation of the incidence angle is the one that should be used for the 45° adjustment. The additional beam was caused by multiple reflections inside prism and shows a reflectivity minimum due to reflections on the prism-metal interface. Both tilting tables have to be used in order to align the height of the reflected laser beams on aperture 2 and 1 , respectively.

The beam point of the incident laser light on the gold sample and the reflected light on aperture 2 should be fixed, if sample and detector motor are moved by θ and 2θ, respectively. In case of such a movement of the laser spot during the scan, the prism has to be adjusted in the z direction. Thus the axis of rotation in the prism according to the incident laser beam has to be aligned. Once the beam point is fixed, the prism is moved in x direction in order to hit the centre of the sample. Both apertures are finally opened before the first measurement is started.

In case of simultaneous fluorescence measurements, the lens L1 in Figure 3.2 is adjusted to focus the emitted fluorescence light into the photomultiplier unit P1.

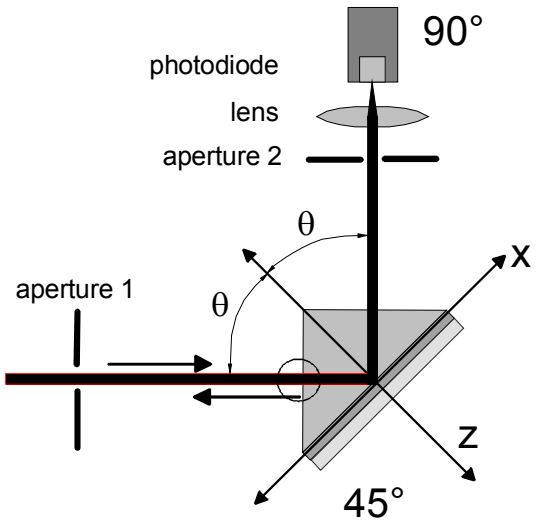

Figure 3.4 : Alignment of the SPS system

Counter-Scans and Kinetics

The simultaneous detection of the fluorescence by the attached photomultipliers during a scan is controlled by a software routine that moves both goniometers in predefined steps, records the actual fluorescence intensity that was measured by the counter and finally collects the reflectivity from the lockin-amplifier. Hence, in the resulting fluorescence scan curve (counter-scan) the measured intensities and reflectivity can be assigned to the same incidence angles. Typical curves before and after adsorption of fluorescent DNA target oligonucleotide are shown in Figure 3.5. Due to the low molecular weight of the used analyte no change of the resonance minimum and of the reflectivity at the fixed angle of 56° is seen.

Before the adsorption of the fluorophores a background signal of about 5000 cps is detected for all angles larger than the critical angle, caused by the intrinsic fluorescence of the used prism. The slight increase of fluorescence before the total reflection edge can be explained by incident light that passed the interference filter IF1 due to its half-width. Additionally, scattered light may influence the measurement signal. For angles larger than the critical angle the incident laser light is reflected completely and does not influence the measured intensities. However, the excitation of the adsorbed fluorophores in the plasmon field leads to a strong fluorescence intensity in the scan. The angular dependence of this intensity follows the already described electromagnetic field intensity. It can be found to be maximal next to the resonance minimum, where the excitation of surface waves is the strongest (chapter 2.3.7).

Starting from the background of ca. 5000 cps the counter-kinetics reflects the increase of the fluorescence emission at the fixed angle of 56°, where the linear part of the reflectivity can be found. At this incident angle no change in the reflectivity was observed. Therefore the time dependent fluorescence measurement reflects changes in the signal under constant excitation conditions. Note, that in case of large shifts of the underlying counterscan curves a deviation has to be considered. The signal needs to be compensated, since the fluorescence would be altered due to changes in the relative position on the fluorescence peak [16]. We assume that no inner filter effects or photo bleaching influence the observed fluorescence signal. However, the measured intensity is not directly convertible into the number of adsorbed fluorophores. This conversion requires the possibility of calibrating the measured fluorescence to an angular resonance shift and hence to a measurable layer thickness. In cases where SPS alone is not sensitive alone to detect the adsorption of low molecular fluorescent dyes, a theoretical calibration approach is rather difficult.

However, the difference between the observed fluorescence increase during the adsorption of the labelled molecules and the virtually unchanged reflectivity demonstrates the sensitivity enhancement of surface plasmon spectroscopy (SPS) by the additional fluorescence detection in SPFS.

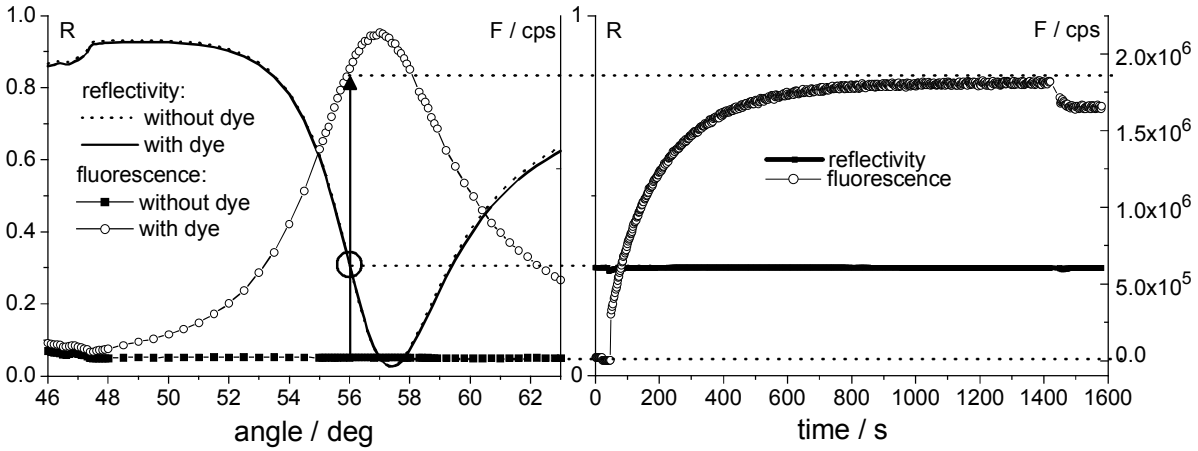

Figure 3.5 : Fluorescence scan curves and corresponding fluorescence kinetics before and after adsorption of fluorescent labelled DNA targets onto the sensor surface described in chapter 1. Due to the low molecular weight of the analyte no change in reflectivity is seen at 56°, while the excited fluorescence causes a clear signal increase in both scan and in the kinetics.

Measurement Sequence

The experiments carried out in this work may vary in the used materials and samples. In general the following measurement sequence was used frequently to monitor ad- and desorption processes on the surface.

1. Scan curve: To determine the thickness of the used metal film and to obtain a measure for the fluorescence background of the sample a counter scan is recorded. Eventually, the cell was filled with the pure buffer, which was used to dissolve the analyte of interest.

2. Kinetic run: The analyte to be tested is dissolved and injected into the flow cell after the observed baseline was found to be stable. After the adsorption process is finished, the sample is rinsed with pure buffer, so as to remove bulk analytes and unspecifically bound molecules from the sample surface.

3. Scan curve: In comparison with the reference scan the change in thickness, refractive index and fluorescence signal is determined as explained before.

This sequence has to be carried out for every single layer on the sample so that each additional layer can be characterised separately.

3.1.3 Surface Plasmon Microscopy (SPM)

Surface Plasmon Microscopy (SPM) is used to carry out surface plasmon spectroscopy studies on structured samples, since this technique provides resolution of laterally structured coatings on metal films [40,51-53] [54]. The technique has already been proven to be applicable for sensing interfacial binding and recognition reactions [55-57].

Experimental Set-up

As in surface plasmon spectroscopy the sample is irradiated with TM polarised light in order to excite surface plasmons on the interface between metal and dielectric coating. Instead of passing a focussed laser beam onto the sample, the diameter of the laser beam is expanded to about 1 cm using a spatial filter. By doing so, an illumination of the entire sample area is possible (Figure 3.6). This spatial filter consists of a microscopy objective (10x) that focuses the laser beam onto a pinhole (25 μM) of defined diameter in front of it. Upon correct alignment, the laser beam is expanded and can now be caused to form a parallel beam by placing a collecting lens (f=150 mm) into the beam path. Note, that the lens-pinhole distance equals the focal length of the used lens. Additionally the spatial filter removes static fluctuations in the laser light caused by refraction at dust particles.

The obtained parallel laser beam is reflected on the base plane of the coupling prism as described in the previous chapter. The reflected light is then observed by means of a zoom objective (EHD, Zoom70 or Rodenstock f=50mm) which focuses the reflected light onto a CCD camera (Hamamatsu, C5405-01). In contrast to SPS, an image of the whole sample area (768x512 pixels) is obtained here, rather than averaging the reflectivity signal over the usual 2mm diameter of the laser spot. This observed picture contains laterally resolved information about the reflectivity at all positions on the sample.

Measurement Principle

To illustrate the basis of the SPM mechanism, a structured gold sample is considered. Onto this three layers of silicon oxide of different thickness were prepared by thermal evaporation. The thickness of the SiO_x in the four resulting areas is assumed to be 0, 5, 15 and 30 nm, respectively. The incidence angle of the incoming p-polarised laser is fixed at an angle θ and the reflected intensity observed by means of recording CCD camera images. Depending on the particular thickness, some areas fulfil the resonance conditions given by Fresnel's equations. For these areas the incident laser intensity excites surface plasmons and hence the reflected intensity is

minimised. Therefore these areas on the surface appear virtually dark compared to the non resonant domains where more light is reflected. This situation is depicted in Figure 3.7 where theoretical pictures of the prepared SiO_x stripes on gold are shown for two different incidence angles θ_a and θ_b. According to the increasing thickness from layer 1 to 4 the single resonance scan curves are shifted to higher angles with increasing thickness. At angle θ_a the intersection with the scan curves for the four layers is found at different reflectivity, which results in the observed contrast in the obtained surface plasmon microscopy picture. For the same reason the contrast is changed if we take a picture at incidence angle θ_b. Analogous to surface plasmon spectroscopy (SPS) the incidence angle is varied over the range of interesting angles in predefined steps, as to drive one surface area after the other into resonance. At each of these angles a CCD camera picture is recorded via a frame-grabber card (Stemmer, ICP-AM-VS) and a connected personal computer.

The picture series can now be analysed by software routines that determine the grey values of defined sample areas. Due to optical difficulties in reflecting the whole light bundle over a large angle range the assigned structures might move on the observed picture upon changing the incidence angle. Additionally, an angle dependent distortion of the pictures has to be considered. This movement is taken into account by two different analysis options: Either adapted software (Stemmer) is used to recognise defined structures in each recorded picture [55] or a manual definition of lateral movement of the resulting structures in all recorded pictures in used. The software for the latter one was developed in the MPI. A linear interpolation between the position of the investigated structures in the first and last picture was used to evaluate the probable position in the intervening pictures. By plotting the calculated grey values for the separate areas versus the incidence angle the scan curves of the single coating areas are finally obtained. Kinetic measurements are carried out by fixing the incidence angle and pictures are recorded with time.

The minimal observable structures of an investigated sample strongly depend on the used metal, since the decay length of the plasmon governs the imaging resolution. For gold this decay length is about 5 μm at λ=633 nm. In the case of silver the smaller imaginary part of the dielectric constant leads to reduced losses in the metal and hence the decay length is extended. Since only structures larger than this decay length can be observed by surface plasmon microscopy (SPM), gold is frequently the metal of preference. Furthermore, gold is used due to its stability against most of the commonly used solvents. Surface plasmon microscopy is capable of sensing the thickness of observed layers in the magnitude of a few angstroms up to hundreds of nanometers.

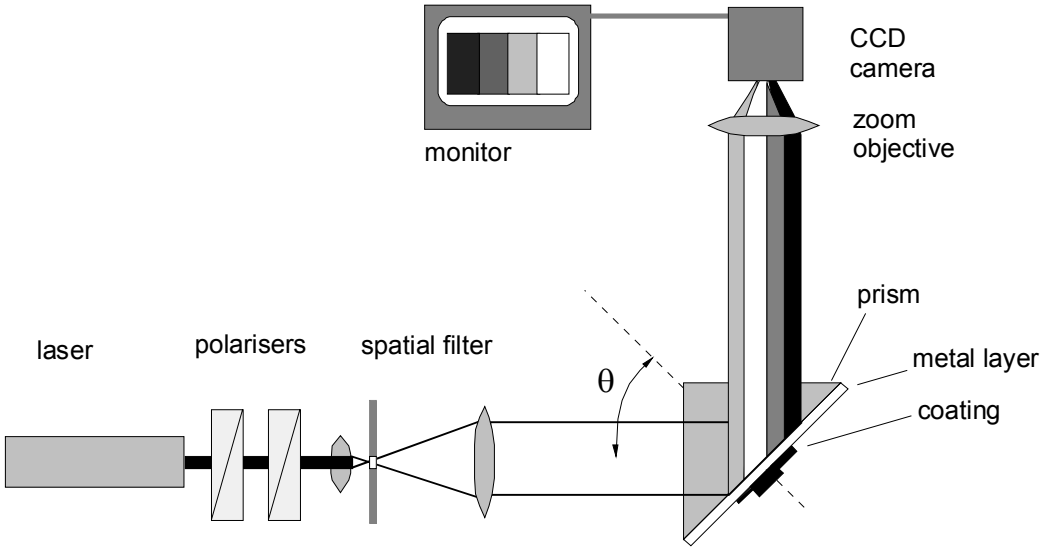

Figure 3.6 : Experimental set-up of Surface Plasmon Microscopy (SPM).

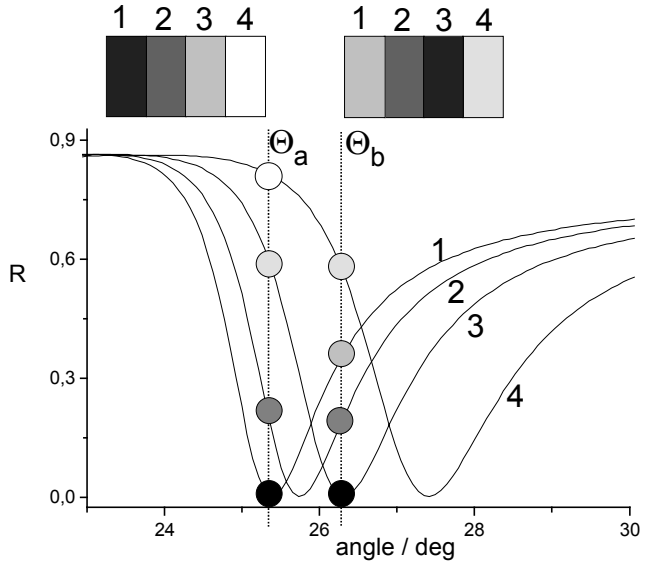

Figure 3.7 : Schematic presentation of the surface plasmon microscopy response to layers of different film thicknesses but identical refractive index. The layers 1-4 correspond to silicon oxide layers of 0,5,15,30 nm on gold, respectively. The surface plasmon microscopy pictures of the structured sample shows a contrast change between the different areas due to the different reflectivity at the given angles θ_a and θ_b.

Practical Alignment Instructions

The practical alignment of the surface plasmon microscopy system is described in the following: First the system is aligned by the methods in 3.1.2. Thus, the 45-90° alignment is finished after the basic configuration at a detector angle of 180° was checked.

After the basic alignment of the system according to the position of the prism and sample is correct, the set-up is changed from the spectroscopy mode towards a microscopy mode. For this

purpose the spatial filter is placed into the laser beam in a distance of about 2 cm behind the chopper. In order to align this filter, several parameters have to be considered like the x-y-z position of the microscopy objective relative to the incident beam and to the pinhole in front of it. The microscopy objective is aligned by the attached x-y-screws such that the incident beam passes in the centre of the objective. Subsequently, the pinhole is aligned in the same way in order to be in the focal point of the beam. Thus, starting from a large distance between objective and pinhole the microscopy objective is moved stepwise towards he pinhole (in z direction) and the x-y position of the latter is adjusted. The spatial filter is aligned until an extended, diffuse laser beam is obtained, free of any interference fringes.

If such optimal position is reached, the expanded laser beam is caused to form a parallel beam bundle by placing a collective lens into the beam path. The lens needs to be placed at a distance from the spatial filter that equals its focal length. Practically, the lens can be moved in z direction until the extended laser beam does not change its diameter upon movement of a piece of paper in front of the lens.

Now that the beam is confirmed to be parallel, the alignment can be verified by placing a pinhole after the expanded beam. If this aperture is closed, the back-reflection of the air-prism interface should be hitting the pinhole like the unmodified laser beam in 3.1.2. Since the position of the prism has been already aligned before to 45° the collecting lens in front of the spatial filter has to be adjusted now. A movement perpendicular to the optical bench allows for a correct back-reflection into the placed pinhole.

The CCD camera is placed into the beam path of the reflected beam. To check for the correct position of the camera the pinhole in front of the spatial filter is almost closed and the reduced laser spot is observed as a bright spot in the recorded CCD camera picture. As the camera is moved along the detector arm, the position of the bright observed on the monitor should not change the position. In case of a movement, the angular position of the detector arm and the tilt of the camera-objective needs to be adjusted.

Finally, the pinhole is opened and the brightness of the incident laser light is adjusted to observe the contrast change of the observed features near the resonance minimum. If the difference between the maximal reflected intensity and the low intensity resonance positions is too large to be detected by the dynamically limited CCD camera, two scans at different laser intensity have to be recorded in order to complement each other.

In addition to the movement of the observed structures due to angularly dependent distortions, additional movement due to the misalignment of the system may occur. Therefore, a

fine tuning of the prism position is necessary to avoid such movements in the investigated angular range.

Frequently, interference lines are observed in the recorded pictures which change position upon altering the incidence angle. Such perturbations need to be excluded from the grey value determination. The collective lens as well as the z-position of the sample should be adjusted in order to obtain a undisturbed reflection of the sample. Frequently, additional reflections at the prism-glass waver interface can cause such distortions, based on non ideal index matching fluids. For $LaSFN_9$ prism high refractive index are recommended. However, these fluids are often volatile and have to be avoided in long term kinetics.

3.2 Surface Modification Techniques

In the following the applied techniques that were used to modify surfaces with metallic and dielectrics films are described. The well known self-assembly of organic material onto metallic surfaces and the principle of other surface modification techniques like spin-casting, thermal evaporation and formation of sol-gel based silicon oxide layers are illustrated.

3.2.1 Cleaning of Glass Samples

If not mentioned otherwise high refractive $LaSFN_9$ glass wavers (20x20x2.5 mm, n= 1.8458) Helma, Germany) were used for the optical experiments. These were cleaned according to the following procedure prior to further treatment: Old metal films were removed by mechanical rubbing with smooth optical paper and water or ethanol. Chromium films were removed by a treatment with an aqueous solution of ammonium cerium (IV) nitrate (Aldrich, 99%). In case of resistant gold films the treatment with aqua regia (HCl and HNO_3 in a ratio of 3:1) was used. The samples were sequentially sonified for 15 min each in a) 2% alkaline detergent solution (Helmanex, Helma, Germany; sonification apparatus Super RK510, Sonorex, Germany), b) MilliQ water and c) 15 min sonification in ethanol (Chromasolv, Riedel-de Haehn, Germany). In between the sonification steps the samples were rinsed in MilliQ water. Finally the samples were blown dry in a stream of nitrogen and placed directly into the evaporation apparatus for further processing.

3.2.2 Thermal Evaporation of Metals and Silicon Oxide

For standard SPS measurements, 47nm gold or silver (99.99%, Balzers) were deposited onto clean $LaSFN_9$ wavers by thermal evaporation [58] at a deposition rate of 0.1 nm/s under UHV conditions ($5 \cdot 10^{-6}\, mbar$) in an evaporation apparatus (Edwards, FL400 or Balzers, model BAE 250). To improve the adhesion of the gold film to the glass substrate a 3 nm thin chromium film was evaporated first, if the planned experiment required extremely stable gold films. Silicon oxide (SiO_x) films were deposited at a rate of < 0.1 nm/s using the same technique.

3.2.3 Self Assembled Monolayers (SAM) on Gold

Self assembled monolayers are known to be molecular assemblies that are formed spontaneously by the immersion of an appropriate substrate into a solution of an active surfactant in an organic solvent [37]. As an alternative to Lagmuir-Blodgett films SAM's are easy to prepare and thermodynamically relatively stable [59]. From a thermodynamic point of view several processes are known to promote the assembly process on surfaces: Chemisorption of the head group of a surfactant (like the sulphur in an alkanethiol SAM on gold) leads to a strong attractive and exothermic interaction to the surface. As a result molecules try to occupy every available binding site on the surface. In addition, van der Waals interactions between alkyl chains of the molecules are a further attractive force and bulky polar groups in the chain can give rise to electrostatic interactions.

The most common SAMs are alkanethiols on gold, silver and copper, several sulfides on gold, alcohols on platinum and carboxylic acids on aluminium oxide. However, in this work the adsorption of thiols onto silver and gold was frequently used. Here the sulphur groups are known to be bound to the gold surface while the alkyl chains of the thiols are oriented uniformly at an angle of 30° (relative to the surface normal) to form a close packed assembly of the thiols.

If not mentioned otherwise, a 0.1 mM solution of thiols was prepared in PBS buffer and the gold or silver samples were immersed into this solution for 30 minutes. The samples were rinsed by PBS buffer (0.01M phosphatebuffer: 0.0027 M KCl, 150 mM NaCl, pH 7.4, Sigma) prior to further self assembly steps. The self assembly kinetics of the individual steps were monitored by SPS as described before.

In case of subsequent streptavidin adsorption a 9:1 mixture of biotinylated thiols and OH-terminated thiols was used. The latter served as lateral spacers for the biotin moieties to allow for optimal streptavidin binding. The exact composition of the thiol-streptavidin architecture is discussed in detail in the results section.

3.2.4 Spin Coating

This well established technique was used to prepare films of variable thickness (nm-mm). The film material was dissolved in an appropriate solvent of different concentrations. After the sample was placed onto the spin coater its surface was completely covered with the solution followed by spinning the sample at a moderate speed (2000-4000 rpm). After 60 seconds the sample could be removed from the apparatus to be stored under Argon until further use.

The resulting layer is a function of the used concentration, the used solvent, the rotation speed and the process duration. For polyvinyl alcohol (PVA) a concentration of 10mg/ml in water was used and the sample was spun for 60 seconds, while varying the rotation speed systematically to test the influence of the speed on the resulting film thickness. The latter parameter was determined by a surface profiler (α-stepper) afterwards and plotted in Figure 3.8. According to this calibration a rotation speed of 2000 rpm was chosen in order to obtain a Polymer film of about 20 nm PVA on gold.

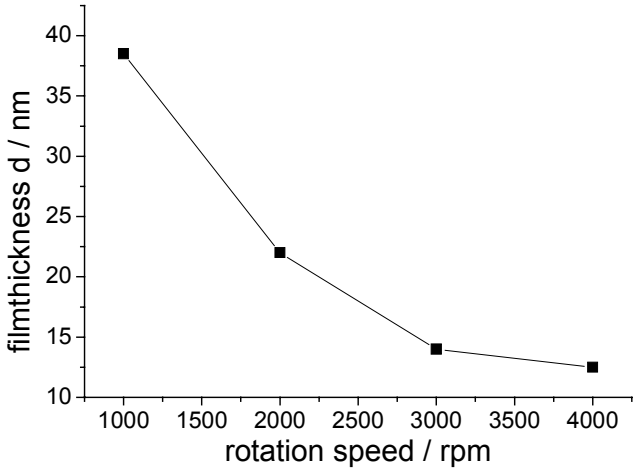

Figure 3.8 : Dependence of the film thickness on the rotation speed during the spin coating procedure for PVA at 10mg/ml in water.

3.2.5 Sol-gel Procedure for the Deposition of Silica Film

As an alternative to thermal evaporation of SiO_x films the following sol-gel procedure was used to deposit silicon oxide films on silver and gold samples:

1. A solution of 20 mM 3MPT (distilled 3-(mercaptopropyl)trimethoxysilane) in anhydrous ethanol was prepared.
2. The clean Ag or Au samples were immersed in the 3MPT solution for 2 hours to allow for SAM formation of the thiols on the metal. Caution was taken to avoid water

contamination during these steps. Therefore the used glass-ware was dried in an oven and the reactions were carried out under Argon atmosphere.

3. After 2 hours the samples were rinsed with ethanol to remove unbound 3MPT followed by rinsing with MilliQ water.

4. In order to activate the surface the samples were placed in 0.1 M HCl for 1 hour

5. The sol-gel solution is prepared 30 min before spin-coating: Water and HCl are mixed. Then TMOS is added and the solution vigorously shaken. The mixture was allowed to react for 30 minutes and shaken or stirred periodically meanwhile. The final thickness of the sol-gel layer is determined by the rotation speed and the amount of TMOS in the solution. Typical mixtures are given in Table 3.1 :

Table 3.1 : Typical spin coating solutions for sol-gel film of different thickness

thickness / nm	µl water	µl 0.1 M HCl	µl methanol	µl TMOS
3	183	81	55	2
8	163	81	55	5
15	163	81	55	10
30	163	81	55	20

6. The 0.1 M HCl solution was removed from the samples by rinsing with MilliQ water subsequently and the samples were placed onto the spin-coating apparatus.

7. Ca. 45ul/cm^2 sol-gel solution was applied to the samples, in order to cover its surface completely prior to spinning. The surfaces were spun at 3.4 rpm for 1 minute and placed into an dessicator for 2 days prior to use.

3.2.6 Preparation of Silane Layers on Silicon Oxide Films

In order to immobilise streptavidin molecules onto silicon oxide films or glass surfaces a layer of biotinylated silanes was immobilised by the following procedure. Since it is known that the adsorption of the biotin-binding protein needs a certain distance between the biotin sites for proper binding, the biotinylated silanes were diluted on the surface by using a lateral spacer silane. An amino-terminated short silane (aminopropyl-trimethoxy-silane, $C_6H_{17}NOSi$, MW= 179.29) was used in a ratio of 9:1 to the biotinylated silane ($C_{22}H_{44}N_4O_5SSi$, MW=504.76). The biotinylated silane (a) was synthesised at the MPI (workgroup Knoll, Dr. Ossi Prucker). Both structure formulas are shown in Figure 3.9.

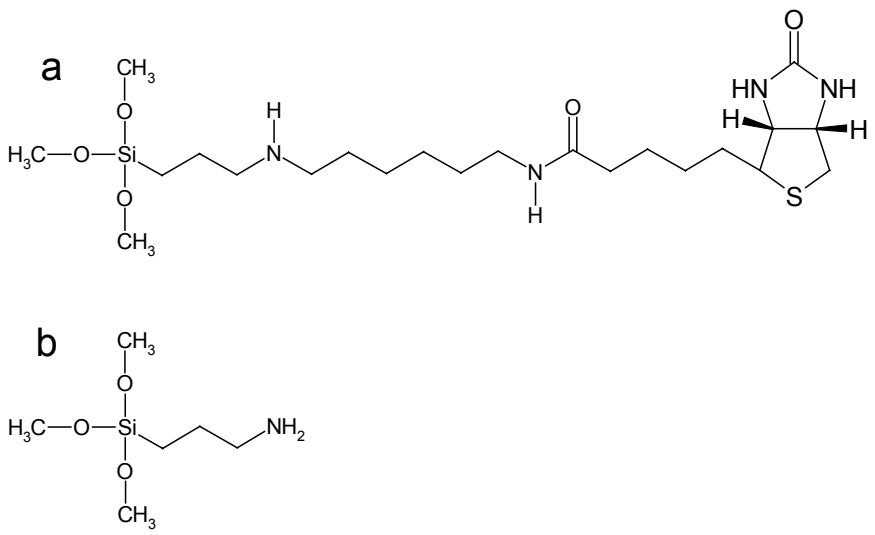

Figure 3.9 : Structure formulas of the a) biotinylated silane and b) amino-terminated spacer silane

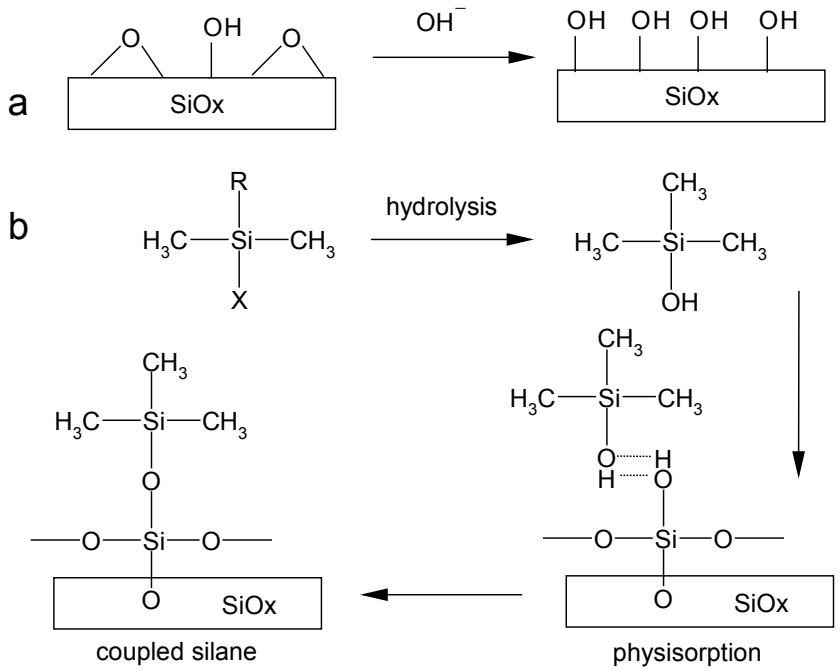

Figure 3.10 : Mechanism of the activation of the SiOx surface (a) and silane coupling of a monofunctional silane(b): After hydrolysis of the silane and physisorption of the silane onto the surface the coupling reaction can take place. For a tri functional silane in Figure 3.9 the mechanism is analogous, but additional coupling between the silanes occurs.

In case of experiments which required a amino-terminated surface the same procedure was carried out using the short amino-silane, exclusively.

The process of the silane adsorption is shown schematically in Figure 3.10. Before coupling silanes to the SiOx surfaces most of the siloxane groups had to be oxidised to silanol groups by the activation with alkaline solution (a). Subsequently, the silanes in solution could be hydrolysed

and coupled to the silanol groups on the surface after physisorption (b) [60,61]. The silane coupling was realised by done by the following protocol:

1. An alkaline activation buffer solution of 0.1M KH_2PO_4/K_2HPO_4 in a 1:9 mixture was prepared and adjusted to an pH of 9.4 by adding aqueous KOH solution.
2. Onto the sample a silicon oxide layer were deposited by thermal evaporation or sol-gel technique. The surface was activated by immersing it in the activation solution for 30 minutes.
3. The samples were rinsed with MilliQ water and dried in a nitrogen stream and then in a vacuum-oven at 50°C for 2 hours to remove bound water.
4. The samples were immersed in a 0.2 mM solution of the silanes in dry methanol and allowed to react overnight.
5. The samples were rinsed with methanol and dried by nitrogen.
6. Finally the modified samples were dried in a vacuum-oven at 120°C for 2 hours. Caution was taken not to decrease the temperature too fast but to allow for a cooling period of ca. 2 hours. The samples could be stored for weeks in a dust free dry environment.

3.2.7 Labelling of Surfaces with Fluorescence Labels

Three different methods were used to label surfaces with fluorophores such as Cy5 and MR121:

Adsorption of Fluorescently Labelled Streptavidin (SA-F)

If a surface was available by self assembly of biotinylated thiols or silanes was available, Cy5 labelled streptavidin (Amersham Pharmacia) molecules were immobilised on the modified surface by immersing the surface into a 5µM solution of the fluorescent species in PBS. The self assembly product was allowed to proceed for 45 minutes and the sample was rinsed by pure PBS buffer. The adsorption was follow by SPFS as described before. Cy5 is a well known cyanine dye with an absorbance maximum at $\lambda_{abs} = 649nm$ and maximal emission at $\lambda_{em} = 670nm$.

Adsorption of Streptavidin and Binding of Biotinylated MR121

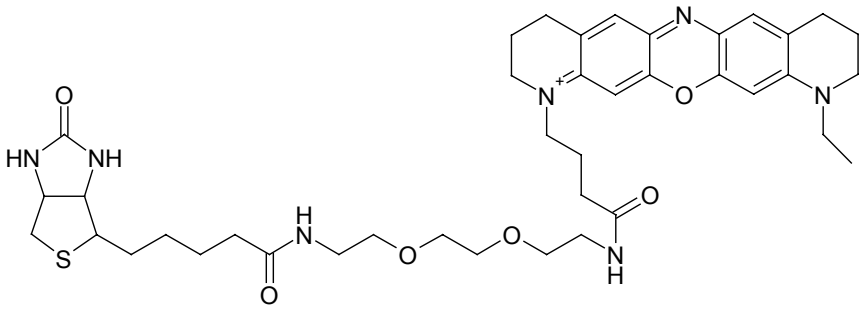

Figure 3.11 : Structure formula of the biotinylated MR121 dye

MR121 is a synthetic fluorophore (Boehringer Mannheim) with an absorbance maximum of $\lambda_{abs} = 610nm$ and an emission maximum at $\lambda_{em} = 660nm$ that can be excited by helium-neon laser light of $\lambda = 633nm$. The structure formula of the biotinylated dye is given in Figure 3.11. Under experimental conditions where a fluorescently labelled streptavidin surface was required but the use of directly labelled streptavidin (see above) was not appropriate, the thiol-streptavidin surface mentioned above was prepared by using unlabelled streptavidin. Subsequently biotinylated MR121 was applied at a concentration of 5uM to bind by interaction of the biotin moiety and the binding pockets of the streptavidin.

NHS Coupling of Fluorophores to Amino-Terminated Surfaces

In order to label SiO_x surfaces with a fluorescent dye, the silane procedure of 3.2.6 was applied. After obtaining a surface covered with a certain density of amino-groups a monofunctional NHS-ester of Cy5 was used to couple the fluorophores to the surface. N-hydroxy-succinimide esters are known to react with free amino groups as shown in Figure 3.12. The technique is suitable for labelling biopolymers like DNA, proteins and antibodies [62,63]. The actual coupling leads to the formation of an amide bound between the carboxylic group of the Cy5 and the free amino group of the amino-terminated silane (surface).

Practically the active ester (1 vial of monofuctional dye pack by Amersham Pharmacia) is dissolved into 1 ml of PBS and 0.2 ml of this solution is applied onto the dry amino-silane surface. In order to cover the surface a thin glass slide (used in optical microscopy) is placed on top to spread the applied droplet. After 30 min the samples were rinsed by PBS, dried in a stream of nitrogen and stored in the dark until the fluorescence of the sample was measured.

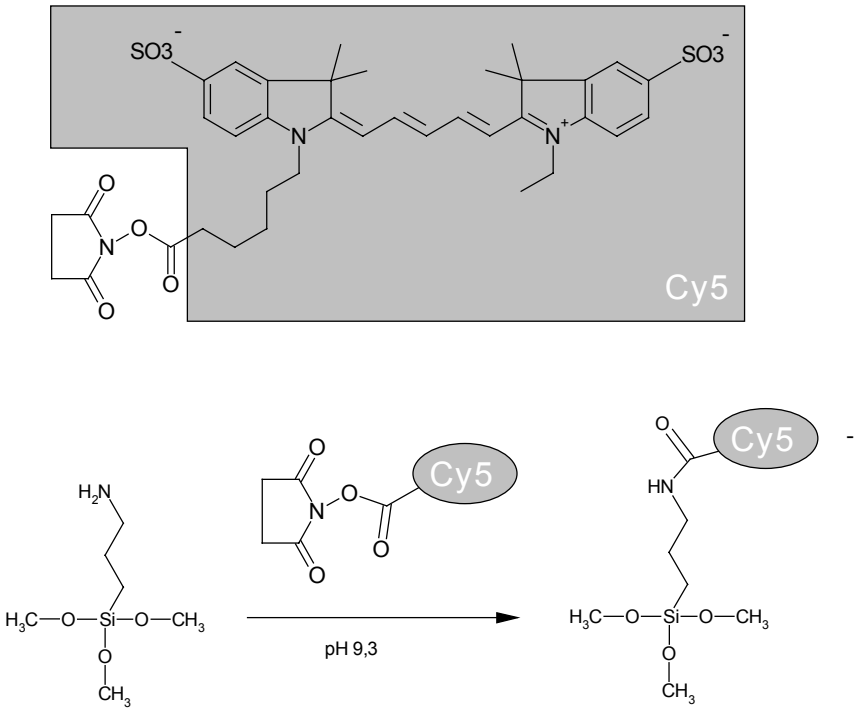

Figure 3.12 : Structure formula of the NHS ester of Cy5 (top) and the reaction scheme with amino-terminated silanes.

3.3 UV Spectroscopy of DNA

DNA absorbs light in the rage of λ=260 nm and UV spectroscopy is therefore an appropriate technique to determine the concentration of DNA in solution. In double-stranded DNA the interaction between the bases leads to an extended electron system and results in a certain absorbance at 260 nm at a given concentration. Denaturation of the DNA causes the absorbance at this wavelength to be increased by 40%, which is known as the hyperchromic effect [64]. Thus, the denaturation temperature, at which 50% of the material is denatured, can be follow by measuring the signal at 260nm versus the temperature.

Considering single stranded oligonucleotides in solution the absorbance at 260nm can be calculated according to the extinction coefficient. If the optical density OD_{260} is measured in a 1 cm light path in a 1 ml cuvette the concentration of oligonucleotides is therefore given by

$$\mu\text{mol of oligo/ml} = \frac{OD_{260}}{10 \cdot \text{length of oligo}} \qquad (3.1)$$

A more accurate calculation of the oligonucleotide concentration also considers the extinction coefficient of the individual bases [65] :

$$\mu\text{mol of oligo/ml} = \frac{OD_{260}}{\text{extinction coefficient for entire oligo } \varepsilon_{\text{Oligo}}} \qquad (3.2)$$

$$\varepsilon_{Oligo} = (A \cdot 15.4) + (C \cdot 7.3) + (G \cdot 11.7) + (T \cdot 8.8)$$

4 Fluorescence Enhancement and Emission near Metallic Surfaces

In recent years much effort has been made to develop optical biosensors. While direct sensors are capable of monitoring the presence of the analyte without use of labelling agents the group of indirect sensors exploit the signal enhancement caused by bound marker molecules. Surface Plasmon Spectroscopy (SPS) as a direct detection method is known to lack sensitivity for the detection of low mass analytes. In order to enhance the sensitivity and to improve the detection limit the technique was combined with fluorescence methods in Surface Plasmon Fluorescence Spectroscopy (SPFS) as described recently [16]. The theory of plasmon excitation and the experimental realisation of SPFS was already introduced in chapter 2.3 and chapter 3.1.2.

From the view point of biomolecular architectures metal surfaces are very important in respect to the immobilisation of molecules and for the self assembly and self organisation of lipids, proteins and nucleic acids. For instance, the detection of DNA on surfaces as described in chapter 4 is based on the preparation of immobilised multilayers on thiol tethered gold surfaces. Furthermore, the presence of a metal surface is essential for the SPFS technique since fluorescent dyes in the proximity to the surface can be excited by the evanescent surface plasmon field. The various decay channels for fluorescence near metal surfaces are distance dependent and have a strong impact on the measurable fluorescence intensity. The various ways of detection in this study are entirely based on the interaction of fluorophores with surface fields. Thus, understanding the behaviour of dyes in the proximity to a metal surface was of great importance for the development of these detection schemes. Both, excitation and emission of fluorescence will be discussed on the basis of theoretical considerations and experimental data.

In the following, plane metal surfaces are considered. The SPFS experiments were performed using the prism coupling set-up as introduced in chapter 3.1. Later on in chapter 5 the influence of structured surfaces, like blazed gratings was discussed.

4.1 Surface Plasmon Field Enhanced Fluorescence

First a short review of the theoretical field distribution at the surface under total internal reflection (TIR) conditions and upon surface plasmon resonance excitation is given. Then measurements of surface plasmon enhanced fluorescence close to a silver film will be presented.

4.1.1 Theoretical Considerations

As outlined in chapter 2.3 the electrical field at the surface when exciting plasmons in a metal film depends on factors like the optical properties of the layer system, the metal and the incidence angle of the exciting laser beam. In the case of total internal reflection (TIR) conditions (for instance a plain glass prism in contact with a dielectric) only a moderate field enhancement by a factor of 4 is obtained at the critical angle due to constructive interference between the incoming and reflected electromagnetic field (compare Figure 2.14). The presence of a thin (noble) metal film on the prism changes the situation dramatically. The evanescent field at the glass-metal interface can be used to resonantly excite surface plasmons in the metal and thus the incident electrical field is enhanced close to the resonance minimum. In the case of gold a maximum enhancement factor of about 20 is found while less damping of electromagnetic waves in silver leads to a factor of as high as 80 (Figure 2.14).

In the past, it has been shown that fluorophores close to the metal surface experience this enhanced evanescent plasmon field and consequently will be excited resonantly [66,67] [15,68]. Such excitation of fluorescence via surface plasmons has been observed for planar systems using prism coupling [15,69] as well as for grating coupling [67]. Only a few studies are know which use the surface sensitive enhancement for sensing purposes [15,17] As discussed in chapter 2.3 the evanescent field decays exponentially into the dielectric layer adjacent to the metal film. The penetration depth into the dielectric, at which the surface field intensity drops down to 1/e of the interface value, is in the order of the used wavelength. Thus, surface sensitive fluorescence measurements are possible, since only dyes in the proximity to the metal film contribute significantly to a measurable signal. Fluorophores further away from the metal surface cannot be excited due to a negligible evanescent field.

4.1.2 Experimental Verification of the Surface Field Enhancement

In Figure 4.1 the fluorescence signal under TIR and SPS conditions is given for a random distribution of fluorophores (MR121, Boehringer Mannheim) in a 20nm thick polyvinyl-alcohol (PVA) film. In order to ensure identical experimental conditions half of a high refractive index $LaSFN_9$ waver was covered with a 50 nm thin silver film, such that TIR and SPS experiments

could be performed on the same sample. After spin coating the MR121/PVA film SPFS scan curves of both domains were recorded as described in chapter 3.1.2 using p-polarised HeNe laser light of λ=632.8 nm. While for TIRF (total internal reflection fluorescence) only moderate enhancement was observed for angles larger than the critical angle of θ_c=22.1°, a strong signal enhancement was evident close to the resonance minimum for plasmon excitation at θ =29.8°. Note that the angular dependence of the sharp fluorescence peak was found to follow the calculated field distribution as discussed in Figure 2.1. When the polarisation of the incident electromagnetic waves was changed from p- to s-polarisation (not shown) no surface plasmons were excited anymore and the fluorescence signal did not exceed the background level for all angles.

Compared to conventional TIRF the excitation of fluorescence via plasmons is favourable due to the following considerations: It is desirable to maximise the surface field intensity to enhance fluorescence emission while simultaneously reducing the field penetration depth in order to avoid excitation of bulk dyes in solution. If a 'figure of merit' is defined as the ratio between enhancement to penetration depth TIRF and SPFS can be compared. For TIRF a compromise has to be made, since both penetration depth and enhancement factor reach a maximum at the critical angle (at θ_c the penetration depth is infinite, the enhancement factor is four). No such compromise is necessary for SPR enhancement and the figure of merit is always 20 times greater than for TIR. Furthermore, tests with fluorescent labelled antibodies proved that fluoroimmunoassays based on SPR excitation are at least 5 times more sensitive than the TIR technique [15].

The drawbacks of TIRF are the following: If prism coupling is used for TIRF enhancement, strong background fluorescence can occur due to the intrinsic fluorescence of the $LaSFN_9$ prism. If the difference between the excitation and emission wavelength of the dye is small, the exciting laser light can interfere with the Stoke's shifted fluorescence due to a finite bandwidth of the interference filters. The additional metal film in SPFS samples acts as a mirror and helps to reduce background fluorescence.

Summarising, SPFS is a valuable tool that allows for a surface sensitive investigation of fluorophores. Due to various advantages over common TIRF detection the SPFS technique is the method of choice if the environment of fluorescent species in the vicinity of metal surfaces shall be investigated. The influence of the metal on the fluorescence intensity is discussed in the following.

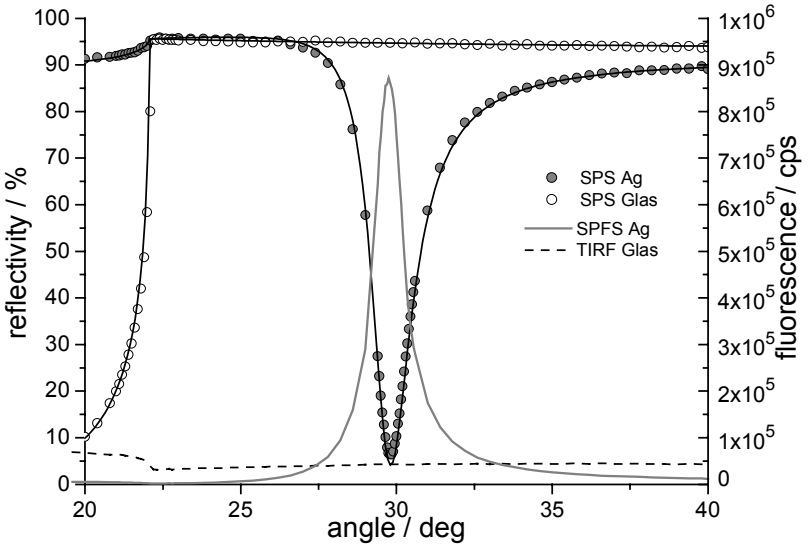

Figure 4.1 : SPFS scan of MR121 in a polyvinyl–alcohol film spin coated on silver and $LaSFN_9$ glass, (and Fresnel fits for the reflectivity) respectively. Due to plasmon excitation a clear fluorescence maximum is seen near the resonance minimum at θ=29.8°, while under TIR conditions (glass) no such maximum was found for angles larger than the critical angle at θ_c =29.8°.

4.2 Energy Transitions for Fluorescence near Metal Surfaces

Consider a fluorophore that is excited by either direct illumination or evanescent surface plasmon fields in front of a planar metallic surface. Since the metal film serves as a mirror the reflected field interferes with the emitting dipole. If the reflected field is in phase with the dipole oscillations, it will be excited by the reflected electromagnetic wave. The dipole will be driven harder and consequently the emission will be enhanced. If the reflected field is out of phase, the emission will be hindered. Thus, the dipole can be considered as a forced, damped, dipole oscillator [70]: it is forced in the way that the field reflected by the boundary provides a driving term for the oscillation of the dipole and it is damped because the oscillator radiates power. With increasing distance between the dipole and the metal surface the phase difference between incident and reflected light alters, which results in an oscillating emission rate of the dipole. Furthermore, with increasing distance of the dye to the metal the strength of the oscillation will decrease. The radiation field of the dipole at the surface weakens with increasing distance to the surface and thus the strength of the reflected field will also decrease. These predicted features were verified the measuring the lifetime of Eu^{3+} ions in front of a Ag mirror [71,72]. In addition to these features a strong quenching of the fluorescence light was found for small emitter-surface

separations. This phenomenon could not be explained by simple interference and was attributed to direct coupling between the dipole field and the surface plasmon modes as discussed in the next paragraph.

In this study mainly metal-dye distances up to 100 nm are considered. Therefore, individual decay channels for fluorescence in this distance range are summarised below and experimentally identified for the particular prism set-up used for the investigations.

4.2.1 Theoretical Considerations of the Major Decay Channels

Mainly three different decay channels for fluorescence near the surface may be considered as schematically presented in the cartoon in Figure 4.2:

(a) Non Radiative Transition and Exciton Coupling: Very close to the metal surface up to 10 nm from the surface electron-hole pairs (excitons) can be excited by the near field of the dipole and thus the interaction is of dipole-dipole nature. For very small metal-dye distances d the dipole field is dominated by the near field the strength of which decreases with d^{-3}. The classical Förster model for the interaction between two individual dipoles involves the distance dependence of both acceptor and donor and thus results in a d^{-6} dependence. However, integrating over all possible sites of an entire surface of acceptors will yield a d^{-4} dependence. A d^{-3} dependence is obtained if the excitation of excitons in the bulk of the substrate is considered. The interaction with electron-hole pairs on the surface of the sample will lead to the d^{-4} dependence. The transferred energy is dissipated in the metal and thus lost for fluorescence detection.

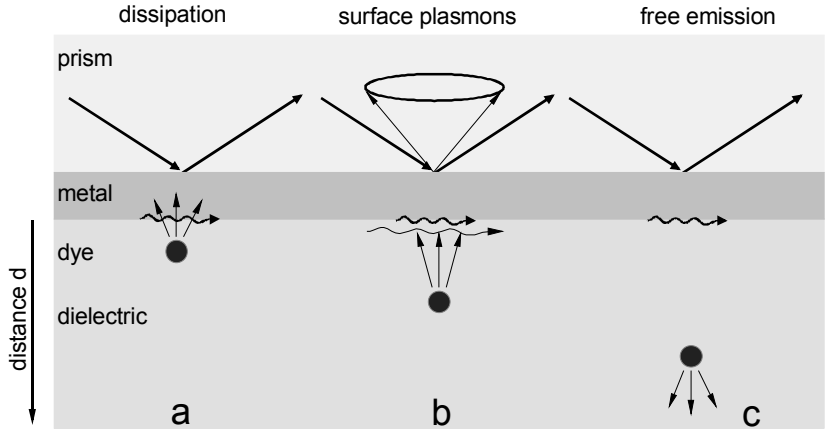

Figure 4.2 : Major decay channels for fluorescence near metallic surfaces (from [16]). While at close distances quenching due to the metal layer is found (a), the excitation of plasmons by the red-shifted fluorescence light is dominating the fluorescence intensity up to distance of about 20 nm (b). This new PSP mode reradiates via the prism in a cone at angles corresponding to the dispersion relation at the Stoke's wavelength. Finally at large distances to the metal the free emission of photons can be found (c).

(b) Coupling to Surface Plasmon Modes: Consider the dipole being located a few nanometers away from the surface up to 20 nm. An excited dipole close to a metal surface can excite surface plasmon modes at the Stoke's shifted wavelength. This again can couple to light if momentum matching via prism or grating occurs [73]. This type of excitation typically becomes dominant at dye-metal distances of about 20 nm [74]. The angular distribution of this plasmon coupled fluorescence emission is determined by the fluorophore emission spectrum and the surface plasmon dispersion[70]. The back radiation through the prism will lead to an emission cone [68], since the wavevector of the excited plasmons is fixed, but no plane of incidence can be defined anymore because the fluorophores emit into random direction.

(c) Emission of Photons: At rather large metal-dye distances free emission of photons in the bulk is dominant over the other modes of excitation discussed above. The emission rates might be predicted by considering the classical picture of a dipole, which is influenced by the back reflected field caused by its image dipole. It is important to take the orientation of the dipole into account. Consider the reflecting surface to produce an image dipole, which interacts with the original dipole. Then it can be assumed that a dipole parallel to the surface and its image will be cancelled out, while a perpendicular one will be enhanced. Any dipole orientation can be considered as a combination of parallel and perpendicular dipole moments, for which certain decay rates can be calculated. For dyes in solution and for the layer systems under investigation a random distribution of dipole orientations was assumed.

4.2.2 Experimental Set-up

In order to identify the above mentioned decay channels in the employed prism setup a model system consisting of the following layers was prepared as described before (chapter 3.2.7):

Au/SiOx/biotinylated silanes/Cy5-labelled streptavidin

The formation of the layer architecture was monitored by SPS and the optical thickness of the individual layers (Au: 47nm, SiOx-Silane: 9nm, streptavidin: 5nm) was determined by Fresnel simulations.

In order to compare the excited fluorescence via free emission and via plasmon radiation back into the prism, the experimental prism set-up in Figure 4.3 was used. At the backside of the prism, adjacent to the metal film and the dye layer, a lens (not shown) was mounted to collect the radiated free emission into photomultiplier A. Simultaneously the intensity of the reflected laser beam was recorded by photodiode B in order to record the SPS signal. Additionally, the emission

cone of the plasmon coupled fluorescence on the front side of the prism was sampled by photomultiplier C. The position of the latter one was determined by the emission angle θ_{rel}, the distance to the prism d and the distance to the plane of incidence h as defined in Figure 4.3. Both photomultipliers were equipped with an interference filter (λ=670nm) in order to block all wavelengths different from the emission of the Cy5 dye.

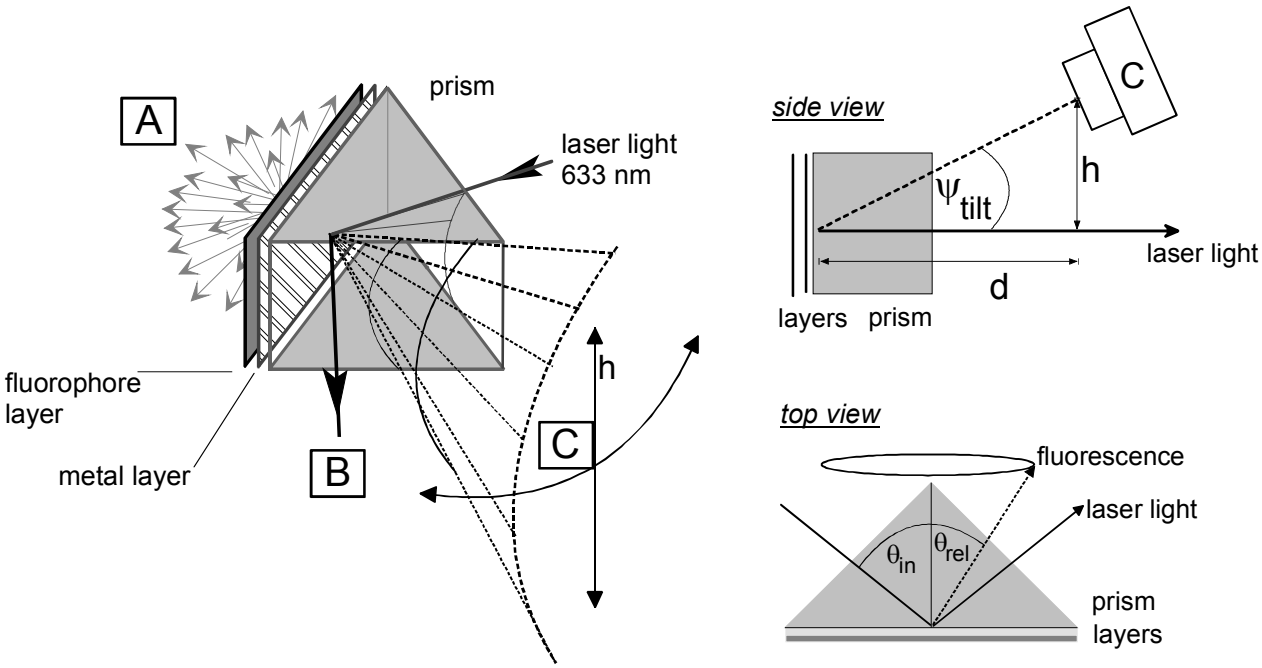

Figure 4.3 : Schematic illustration of the prim set-up. The reflected laser light is monitored by detector B. Photomultiplier A detects the randomly oriented free emission of photons from the backside of the sample, while unit C is used to sample the emission cone of the plasmon coupled fluorescence at the opposite side of the prism. The position of photomultiplier C is determined by Θ_{rel}, d and h as defined in the top and side view of the set-up.

4.2.3 Experimental Verification of the Decay Channels

Free Emission of Photons

The SPFS scan curves as measured by detectors A and B before and after adsorption of Cy5-labelled streptavidin on the silane functionalised surface are presented in Figure 4.4. Due to the adsorption of the molecules on the surface the resonance minimum was shifted to higher incidence angles as discussed before (chapter 2.3.7). Compared to the low fluorescence background a strong signal enhancement was observed near the resonance minimum after the immobilisation of the labelled proteins. Two important features need to be emphasised here: although for the measurements on silver in Figure 4.1 another layer architecture was investigated, comparison of systems with silver and gold metal layer reveals a much broader peak in case of the gold, resulting from the stronger damping of electromagnetic waves. The maximum of the

fluorescence can be detected close to the resonance minimum of the surface plasmon for HeNe laser light but was shifted slightly to smaller incidence angles. This was also considered as a result of the damping in the metal (chapter 2.3.7).

Due to the SiO_x and the protein layer a minimum metal-dye distance of not smaller than 14 nm was achieved. The rather high fluorescence signal of the free emission process at the base sensed by the detector proves that quenching processes are already largely reduced at this distance.

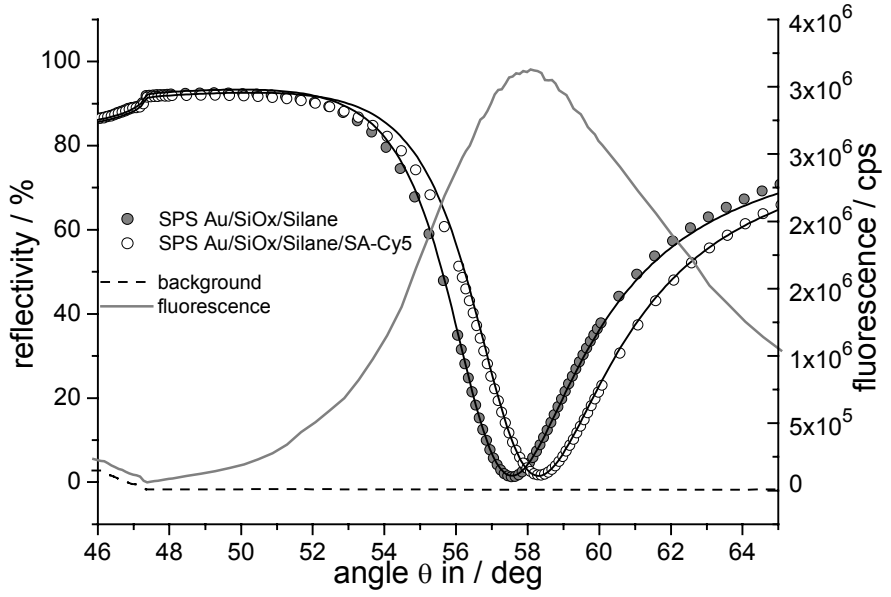

Figure 4.4 : SPFS scan (free emission of photons) of the layer system Au/SiOX/Silane/SA-Cy5 before and after adsorption of the CY5 labelled streptavidin onto the silane functionalised surface as measured with detector A in Figure 4.3. The fluorescence maximum at 58° was slightly shifted to smaller angles compared to the resonance minimum as explained in chapter 2.3.7.

Surface Plasmon Modes

Emission characteristics of the plasmon coupled fluorescence process were obtained by increasing the angle of incidence Θ_{in}=46-64° stepwise ($\Delta\Theta_{in}$=1°) and performing scans with detector C around the 'frontside' of the prism (Θ_{rel}=15-85°) at each incidence angle. The position of the photomultiplier was given by the angle Ψ_{tilt} which can be expressed in terms of the distances h=4cm and d=10cm. The angular resolution was determined by the pinhole (2 mm) in front of detector C and was thus calculated to be 0.76°. Figure 4.5 summarises the obtained scans and reveals that depending on both the excitation angle Θ_{in} and the emission angle Θ_{rel} an intensity maximum can be found for the plasmon coupled fluorescence.

The maximum at Θ_{in}=58° was already observed in Figure 4.4 for the free emission of photons and results from sweeping through the resonance minimum of the layer system. The more the plasmon resonance is excited the higher is the field at the surface. Therefore a fluorescence maximum is found close to the plasmon resonance minimum of Θ_{in}=58°. Since the excitation rate of the dyes is independent of the processes by which the fluorophore goes back to the ground state. Thus, it is easily understood that the same excitation maximum at Θ_{in}=58° was observed. Scaling the fluorescence peak in Figure 4.4 (detector A) and comparing with the peak at Θ_{in}=58° in Figure 4.5 revealed identical curve shapes (not shown).

The maximum at Θ_{rel}=55° corresponds to the detector crossing the emission cone sketched in Figure 4.3. and proves that the plasmon coupled fluorescence light was emitted into a narrow angular range. Due to the red shift of the fluorescence light from λ_{ex}=632.8 nm to λ_{em}=670 nm the fluorescence maximum and the corresponding resonance minimum at this wavelength appears at smaller incidence angles as measured for the exciting HeNe laser light (Θ_{rel}=58°). According to the dispersion relation, surface plasmon light of λ=670 nm excites a plasmon mode at a different incidence angle as light of λ=632.8 nm. The small peak around Θ_{rel}=35° is considered to be caused by multiple reflections of the fluorescence light in the prism and can be neglected.

In order to sample the shape of the emission cone two more scans with detector C were performed at different heights h=2,4,6 cm, while the distance d=15 cm was kept constant. An increase in the distance h between detector C and the plane of incidence causes the photomultiplier to cross the emission earlier. This results in a shift of the maximum fluorescence to smaller angles Θ_{rel} for increasing heights h (Figure 4.6). Note, that the intensity variation in this set resulted from experimental difficulties in aligning the detector and is of no importance here. However, when the angles of maximal intensities were converted to the inner wavevectors k_{in} all three maxima appeared to be superimposable and thus proved the measured fluorescence to be identical in its origin.

The intensity of the measured free emission and plasmon coupled fluorescence cannot be compared directly, since only a cross section of the emission cone was recorded. Due to experimental uncertainties based on the difficulties in aligning detector C a simple evaluation of the total back radiated emission by integrating over the complete cone is not possible. An experimental configuration, which allows collecting the intensity of the entire emission cone is

recommended. However, not the absolute intensities were under investigation, but rather the presence of the individual decay channels were to be verified for the used prism set-up.

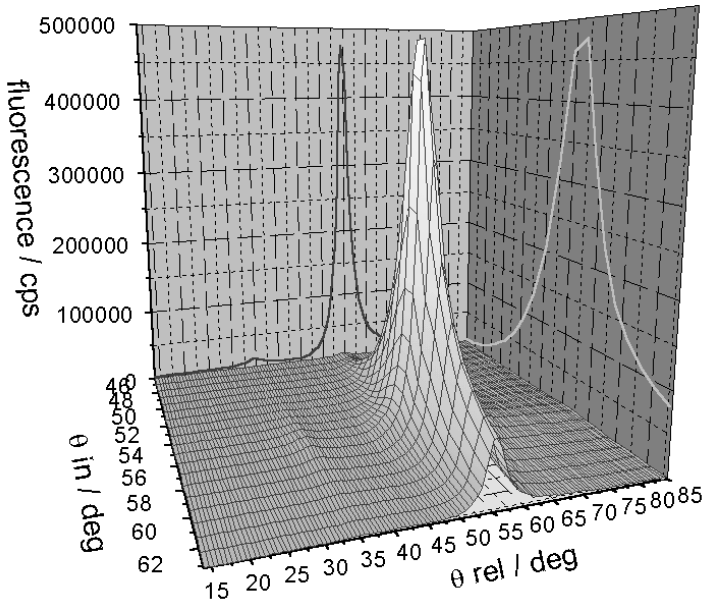

Figure 4.5 : Emission characteristics of plasmon coupled fluorescence depending on the incident angle Θ_{in}=46-64° and the emission angle Θ_{rel}=15-85° as measured by detector C in Figure 4.3. Maximal fluorescence can be found at Θ_{in}=58° (=maximum in Figure 4.4) and Θ_{rel}=55°.

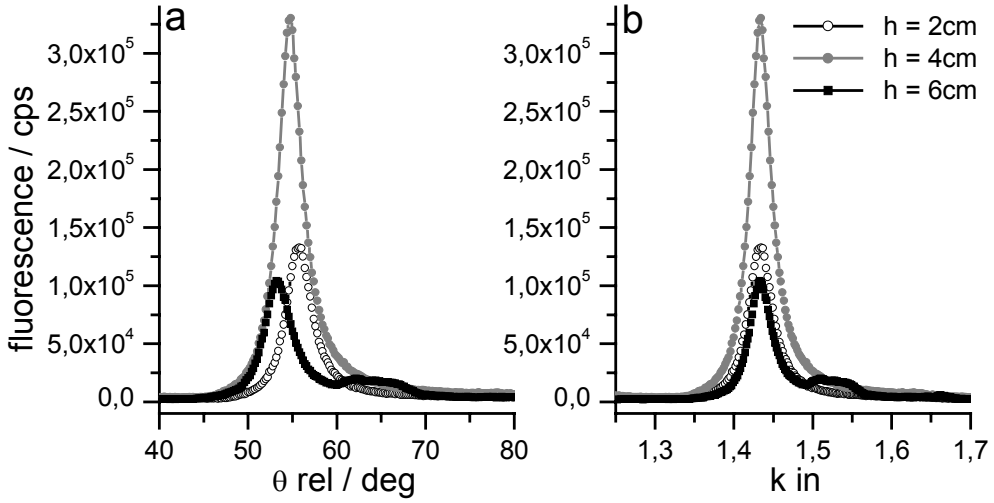

Figure 4.6 : Plasmon coupled fluorescence emission at a fixed excitation angle of Θ_{in}=56°. Scans around the prism with detector C revealed a fluorescence emission in a narrow range of angles Θ_{rel}. a) Scans at increasing distances h=2,4,6 cm to the plane of incidence (and a detector-prism distance of 15cm) revealed a peak shift to smaller angles, corresponding to the earlier cross-point between detector and emission cone. b) Conversion of Θ_{rel} into inner wavevectors proved that all maxima belong to the same k_{in}.

Although the measurement of back coupled fluorescence has been employed by other researchers for sensing purposes already [15] the detection of the free emission in SPFS as described in chapter 3.1.2 is a much simpler experimental approach and is therefore favoured in the following investigations. Additionally, the extension to fluorescence microscopy is possible only by employing measurements of the fluorescence from the 'backside' of the prism.

4.3 Distance Dependence of Decay Channels

The dominance of the above mentioned decay channels strongly depends on the dye's distance to the metal surface. Shifting the molecule away from the surface may lead to an emission enhancement by orders of magnitude. This dependence is of major importance for the optimisation of surfaces that are used to support the immobilisation of fluorescent species. Furthermore, the distance dependent quenching profile is the base for a novel DNA detection scheme as introduced in chapter 7 which makes use of the conformational change of an immobilised probe strand upon hybridization. The quenching profile of fluorophores close to a gold surface was determined experimentally and compared to theoretical predictions in the following.

4.3.1 Theoretical Consideration of the Quenching Profile

Although a detailed description of the theoretical model would go beyond the scope of this study the procedure of calculating the quenching profile is outlined in the following: In order to calculate the distance dependent quenching profile for the following layer system, the probability of exciting dyes in the exponential decaying evanescent field and detecting the fluorescence emission of these excited species was calculated. It was assumed that the free emission of photons and the plasmon induced photon excitation are the dominant decay processes. The investigated layer system is summarised in Table 4.1 together with the optical constants and the assumed layer thickness.

Table 4.1 : Optical constants of the investigated layer system Au/gold/SiOx/air

layer no.	type	d / nm	ε'	ε''
1	air	∞	1.000	0
2	SiOx spacer	d_2	2.123	0
3	gold	51.5	-12.3079	1.2071
4	prism	∞	3.4069	0

It is not possible to model the behaviour of dyes sitting exactly at an interface between two media. The dyes have to be shifted into one of the medium by a small distance. The dyes are considered to be placed just above the spacer/air interface. If not mentioned otherwise, the calculations were performed at an angle of incidence of optimal resonance excitation. The fluorescence intensity due to the free emission of photons at the backside of the prism setup (detector A in Figure 4.3) as well as the plasmon coupled fluorescence (detector C) will be evaluated for an excitation wavelength of the HeNe laser of λ_{ex}=632.8 nm and a fluorescence emission wavelength of λ_{em}=670 nm.

Absorption Process

The probability P_{abs} of adsorbing a photon by a dipole in the orientation **d** is given by

$$P_{abs} \propto \left|\mathbf{d}\cdot\mathbf{E}\right|^2 = d_x{}^2\left|E_x\right|^2 + d_y{}^2\left|E_y\right|^2 + d_z{}^2\left|E_z\right|^2 \qquad (4.1)$$

with E_x, E_y and E_z being the components of the electromagnetic field in all directions. For the definition of the coordinates refer to Figure 5.2. The transfer matrix algorithm from chapter 2.3.6 was used to calculate the square values $|E_n|^2$ for a fixed spacer thickness d_2 and variable wavevector of the plasmon k_{psp}. The latter can be converted into inner incident angles θ by:

$$\sin(\theta) = \frac{k_{psp}}{n_4 \cdot k_0} \qquad (4.2)$$

with n_4 being the refractive index of the used prism. The k_{psp} at every thickness d_2 was calculated for which the corresponding $E_x{}^2$ and $E_z{}^2$ reach a maximum. These maximum values are plotted in Figure 4.7 in dependence on the spacer thickness. The plotted $E_z{}^2$ (perpendicular to the surface) corresponds to the exponential decay of the evanescent plasmon field.

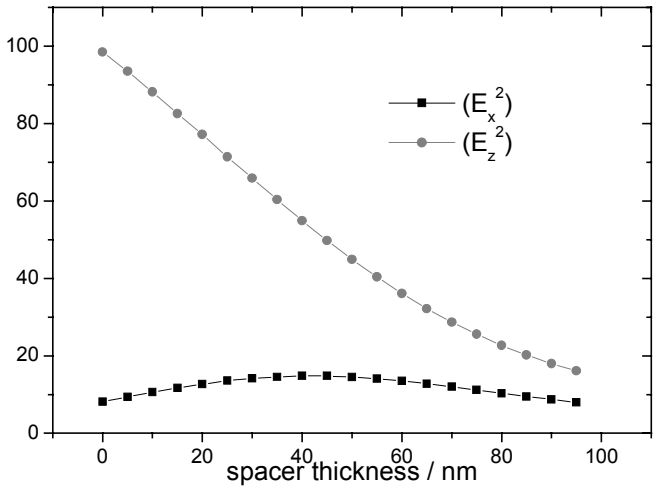

Figure 4.7 : Maximum E_x^2 and E_z^2 dependent on the spacer thickness as calculated for the excitation of dyes in the layer system in Table 4.1.

Emission Process

The following three emission probabilities were considered:

1.) Fluorescence light of the dye is emitted in the direction in which coupling to plasmons and re-radiation into the prism can occur (detector C)

2.) The dye emits freely into the air (detector A)

3.) Fluorescence is emitted into all directions other than the above mentioned ones.

Plasmon Coupled Emission (Detector C)

The calculation of process 1 is analogous to the adsorption process if the wavelength is adjusted to λ=670 nm and if the dielectric constants are fixed. The probability of a dipole emitting its radiation via plasmon excitation into detector C can be evaluated best by considering the inverse process: illumination of the sample with light of the wavelength λ=670 nm under the angle Ψ_{tilt} given by the position of the detector d and hypothetical direction of excitation of the dyes. Both considerations are equal due to the reciprocal theorem. The probability of detecting emitted light is dependent on the electrical field and given by:

$$P_{\det C} = \left|d_x \cdot E_x\right|^2 + \left|d_y \cdot E_y\right|^2 + \left|d_z \cdot E_z\right|^2 = d_x^2 \cdot \left|E_x\right|^2 + d_y^2 \cdot \left|E_y\right|^2 + d_z^2 \cdot \left|E_z\right|^2 \qquad (4.3)$$

E_x and E_z could be assumed to be caused by p-polarised light, while E_y corresponds to illumination with s-polarised light. The calculated electrical fields for maximal emission are

illustrated in Figure 4.8. The x and z component was found to behave like in the case of the excitation as shown above, while the y component appears to be negligible.

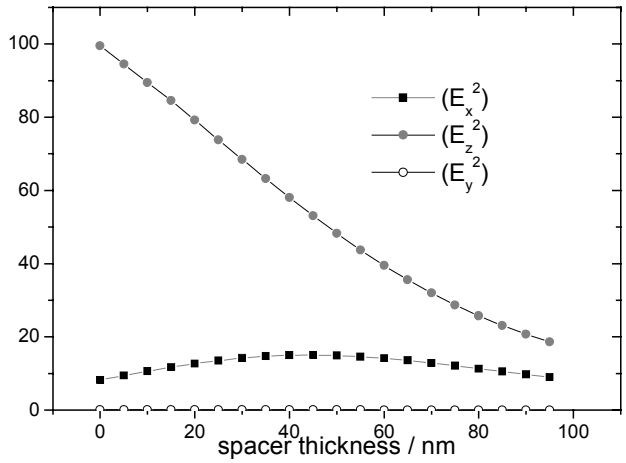

Figure 4.8 : Maximal E_x^2, E_y^2 and E_z^2 for the plasmon coupled emission process dependent on the spacer thickness as calculated for the layers system in Table 4.1.

Free Emission (detector A)

The probability of detecting the free emission of photons with detector A can again be calculated according to the reciprocal theorem. For the calculation a fixed dipole moment is considered to be excited by light originating from all angles which can be covered by the detector A. Thus, integration over all possible angles leads to:

$$P_{\det A} = \int_{\theta<\theta\max} \left(\left| d_x \cdot E_x \right|^2 + \left| d_y \cdot E_y \right|^2 + \left| d_z \cdot E_z \right|^2 \right) = d_x^2 \cdot \int_{\theta<\theta\max} \left| E_x \right|^2 + d_y^2 \cdot \int_{\theta<\theta\max} \left| E_y \right|^2 + d_z^2 \cdot \int_{\theta<\theta\max} \left| E_z \right|^2$$
$$= d_x^2 \left\langle E_x^2 \right\rangle + d_y^2 \left\langle E_y^2 \right\rangle + d_z^2 \left\langle E_z^2 \right\rangle \qquad (4.4)$$

The problem is symmetric and the x-axis of the coordinate system is defined as the direction parallel to projection of the dipole onto the surface. Then E_x and E_y correspond to dipoles oriented parallel to the surface and E_z presents perpendicular dipoles. The calculated values in Figure 4.9 illustrate that perpendicular oriented dipoles barely contribute to the detectable free emission (note the different scale). This small contribution is reasonable since detector A is placed nearly in the direction of the axis of dipoles perpendicular to the surface. The larger contribution to the detectable emission by dipoles parallel to the surface (E_x and E_y) is decreasing for small distances from the surface. This effect has been discussed above as destructive interference with the back radiation field caused by the image dipole.

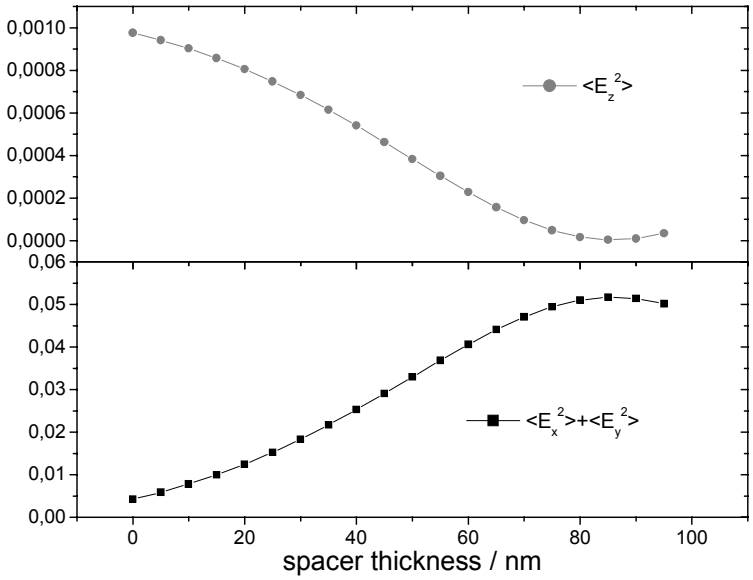

Figure 4.9 : Calculated $<E_x^2>+<E_y^2>$ (dipoles parallel to the surface) and $<E_z^2>$ (dipoles perpendicular to the surface) for the free emission process dependent on the spacer thickness as calculated for the layers system in Table 4.1

Fluorescence Intensity

Finally the measurable fluorescence intensity can be calculated knowing the probability of excitation and emission. The dipole moment of the fluorophore is considered to be fixed but arbitrary and the orientation of the dipole is assumed to be randomly distributed. Thus, the orientation is averaged over all possible angles Ω and the detected intensity is calculated to:

$$I_{\det} = \int d\Omega \, P_{ex} \frac{P_{\det A,C}}{P_{ges}} \qquad (4.5)$$

with P_{ges} being the total probability for photon emission. This probability can be calculated from the local electromagnetic fields at the dipole. Non radiating processes were neglected in the probability conditions. Using equation (4.5) the fluorescence intensities as measured by detector A and C were calculated and are plotted versus the spacer thickness in Figure 4.10. Although the absolute intensities cannot be compared, the preferential emission of light in different directions depending on the dye-metal distance is seen clearly. At relatively small spacer distances below 20 nm (compare 4.2.3) both processes with the two different emission directions are found to contribute to the decay but the plasmon process is dominating. For large spacer thickness free emission is the main contribution.

In the following, the simulated quenching profile will be compared to experimental data in order to confirm the predicted quenching behaviour for the distances regime up to 50 nm.

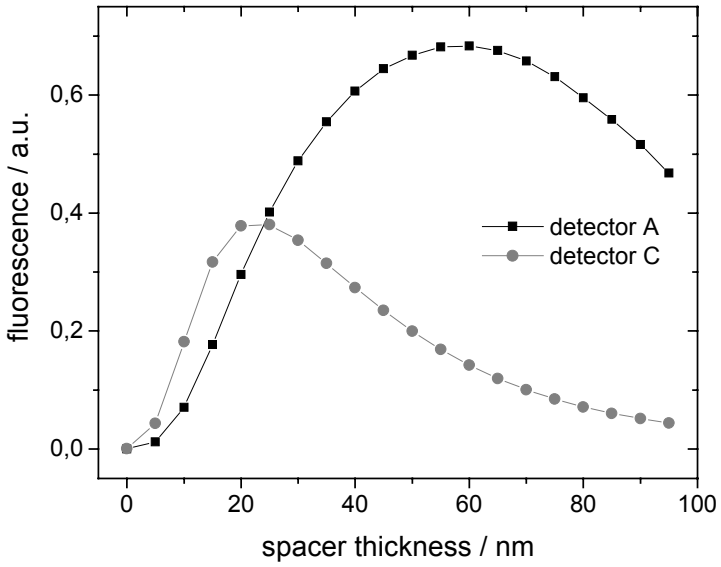

Figure 4.10 : Simulation of the fluorescence intensity of the free emission of photons and the plasmon coupled process which can be measured by detector A and C, respectively.

4.3.2 Experimental Set-up and Sample Preparation

Due to the experimental ease of preparing silicon oxide films on metal surfaces by thermal evaporation, SiOx films of various thickness were used as spacers to separate the dye molecules from the metal surface. The silicon oxide was modified by amino-terminated silanes as described before. Subsequent treatment with (NHS) activated Cy5 labels lead to a coupling between dyes and functionalised amine surface (chapter 3.2) to obtain a Au/SiOx-Silane/Cy5 layer architecture. Due to the aggressive treatment of the SiOx surface during silane adsorption it is not possible to distinguish the individual thickness for the SiOx and the silane layer. So a single layer with a dielectric constant of $\varepsilon'=2.123$ for (SiOx-silane) was used in the Fresnel simulations.

In order to avoid varying dye intensities in different samples, structured samples were considered by evaporating 16 different SiOx steps on one and the same gold sample. The steps were obtained in 4 subsequent evaporation steps with different evaporation rates using aluminium masks in order to control the thickness of the individual steps. Figure 4.11 illustrates in a cartoon the idealised silicon oxide steps illustrates the dimensions of the applied structure.

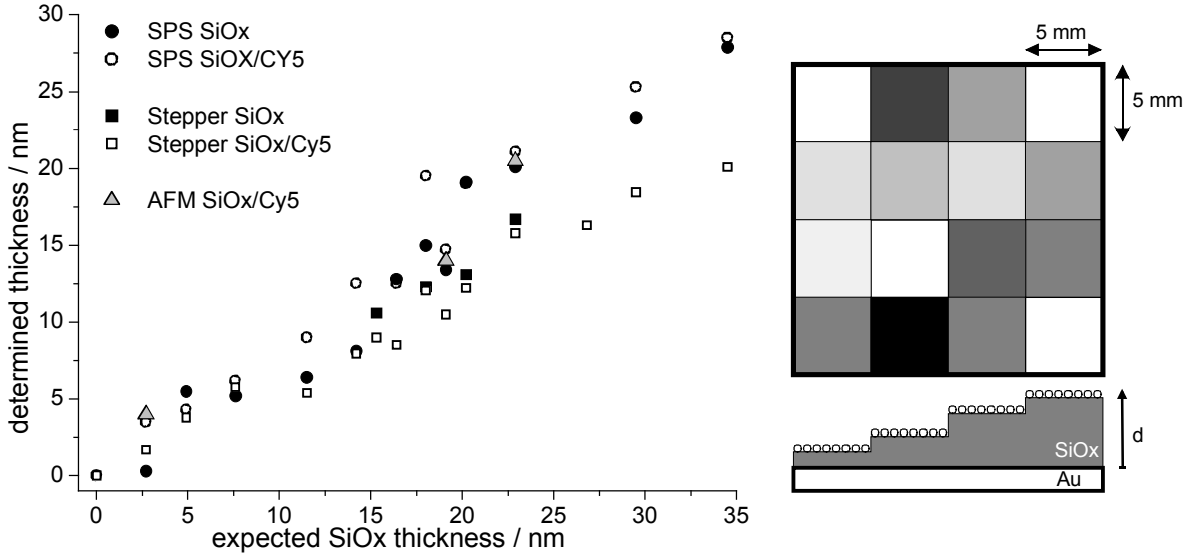

Figure 4.11 : By thermal evaporation of silicon oxide using masks 16 different SiOx thicknesses were obtained on the same sample. After silanisation and Cy5 coupling a layer system Au/SiOx/silane/Cy5 was prepared. The thickness of the individual areas was determined by SPS, α-stepper and AFM. The obtained values were plotted versus the expected silicon oxide thickness, which were calculated from the deposition rate and time.

The silicon dioxide structure on the sample was investigated using Surface Plasmon Microscopy (SPM) in air. A sequence of pictures of six different steps is shown in Figure 4.12 together with the corresponding scan curves of the three upper steps. The scans were obtained by plotting the averaged grey values of the individual areas versus the applied incidence angle. Note, that depending on the actual film thickness plasmon resonance is excited successively at the areas of different thickness. This is indicated by the change in reflectivity/grey value. The dotted lines indicate the incident angles at which the pictures were taken and illustrate the contrast change with increasing angle of incidence.

In order to verify the measured spacing between the Cy5 dyes and the gold surface the 4x4 array was investigated by SPS and surface profiler (α-stepper) before and after silane/Cy5 treatment. Additionally, the gold thickness and three selected domains were measured by AFM. In Figure 4.11 the obtained values were plotted versus the SiOx thickness that was expected due to the combination of evaporation rate and mask position.

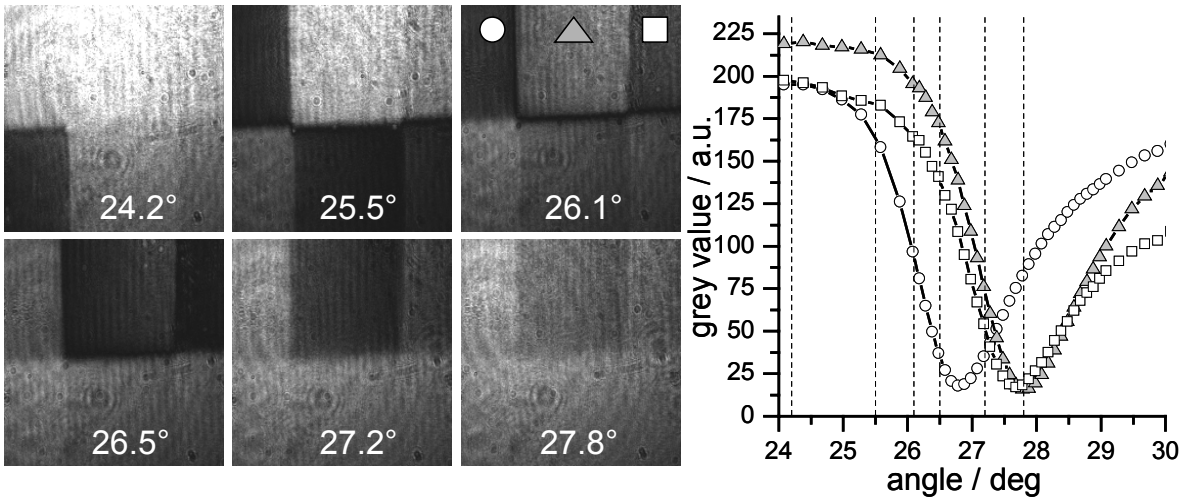

Figure 4.12 : Surface Plasmon Microscopy (SPM) pictures of the same silicon oxide steps at different incident angles. The averaged grey values of the individual areas were plotted versus the incident angle to obtain the resonance curves as shown for the three upper areas. Note that with increasing angle one after the other areas turns into resonance, according to the thickness of the silicon oxide step (circles: 8.1nm, triangles:13.4nm, squares:12.8nm)

Generally, the experimental thickness was smaller than predicted due to variations in the evaporation rate. The thickness of the underlying gold film of d=48.5 nm measured by SPR, α-stepper and AFM was found to be in very good agreement. Regarding the adjacent dielectric films it is noticeable, that the thickness measurement performed with the surface profiler (squares) deviated from the optical measurements by SPS (circles) for both the bare SiOx and the silane covered surface. The smaller values in the case of the mechanical characterisation can be explained by the SiOx-silane-surface being too soft to be measured accurately by the applied force during the α-stepper process. The error in both the mechanical measurement by surface profiler and the surface plasmon measurement is about 1 nm. Due to the high accuracy in determining surface features the data points obtained from AFM are believed to be the most accurate. Since for the three steps under investigation (d=4, 14, 20.5) the agreement with Fresnel simulations (using a dielectric constant of ε'=2.123) are excellent, it is assumed that the SPS thickness of the other steps is reliable, too, and will be used for further considerations.

4.3.3 Experimental Conformation of the Simulated Quenching Profile

SPFS scan curves of all steps were recorded by moving the prism laterally and hence focussing the incident HeNe laser beam onto the area of interest. In order to take photo bleaching of the dyes into account control measurements were taken before and after the scan series but there was no bleaching evident. The fluorescence intensities at angles of maximal field enhancement were plotted against the step thickness measured with SPS in Figure 4.13a (white circles). The

measurement was repeated for smaller step-width (black circles) up to a maximal SiOx thickness of 30 nm.

The experimental signals were scaled so that maximal agreement with the predicted quenching profile from 4.3.1 (black line) was obtained for the investigated thickness range. The experimental and simulated quenching profile was found to be in good agreement for distances below 30 nm, but a strong deviation was observed beyond this thickness limit. The steep increase in the experimental profile could not be verified by the simulation, which predicts a rather moderate increase of the fluorescence signal until a fluorescence maximum at about 60 nm is reached (compare Figure 4.10).

One way to account for the overestimation of the experimental fluorescence particular at large metal-dye distances is to consider a high roughness and pore formation in the SiOx layer. Also, not only a single dye layer on top of the SiOx step would give rise to a fluorescence signal but the dye solution was assumed to seep into the step and form a thick dye layer. This contribution was modelled by integrating the simulated curve in Figure 4.13a over variable thickness. When a general roughness of 18% was assumed for all steps and the experimental values were rescaled a good agreement over the complete distance range was observed (Figure 4.13b). However, in both models the simulation seemed to describe the distance-dependence of the fluorescence intensity very well up to a distance of 30 nm. Since in the further experiments the maximal employed metal-dye distance is noticeably below this level (up to 20nm), the simulated quenching profile can be used to evaluate distance changes on the base of relative fluorescence measurements.

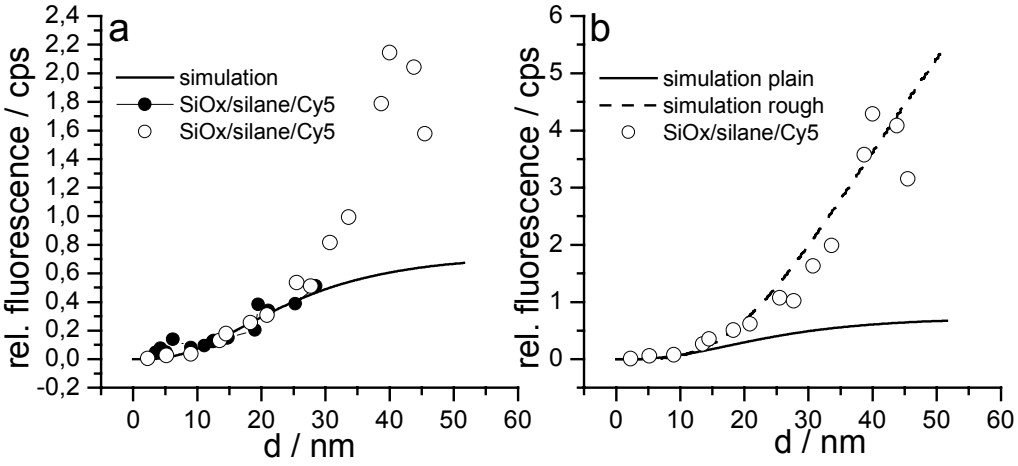

Figure 4.13 : Experimental and theoretical quenching profile of immobilised Cy5 dyes at increasing distance to the gold surface. The simulated quenching profile fit the experimental data only up to a distance of 30 nm (a). If a general roughness of 18% at every thickness is assumed a much better fit can be obtained until d=50 nm(b).

4.4 Conclusion

It could be shown that fluorescent dyes can be excited by the evanescent surface plasmon field close to metallic surfaces. It was discussed that the enhancement factor is strongly dependent on the optical properties of the metal. For maximal fluorescence emission it is necessary to chose the optimal spacing between dye and metal surface. For small distances between dye and metal the exponentially decaying evanescent field exhibits a maximum, and so does the probability of exciting the fluorophore by the surface field. On the other hand the proximity to a metal surface gives rise to quenching effects which reduce the measurable fluorescence intensity. Since most of the measurements in the following chapters were performed at distances below 50 nm the quenching profile of the frequently employed Cy5 dye on gold was determined experimentally. Comparison with the simulated curve revealed a deviation for dye-metal distances larger than 30nm. However, up to this limit the experimental data could be confirmed by the simulated quenching profile and can thus be used as a calibration curve for the analysis of distance dependent fluorescence measurements in this regime.

It could be shown that both the free emission of photons as well as the plasmon coupled fluorescence can be measured by using the prism set-up shown before. Furthermore, the plasmon coupled fluorescence could be successfully employed to record fluorescence kinetics (not shown). Compared to the experimental comfort of detecting the fluorescence from the 'backside' of the prism (detector A) more effort has to be made to align the spatial and angular position of detector C. Since no clear advantage of measuring the plasmon coupled fluorescence was seen, the common SPFS measurements using detector A are preferred for further experiments. Additionally, the extension of the existing set-up towards fluorescence microscopy is only possible from the position of detector A at the prism set-up. Measuring the plasmon coupled fluorescence might be applicable for special applications which make use of the distance dependent quenching profile but it was not found to be an alternative to the free photon detection.

5 Fluorescence on Blazed Gratings

In the last chapter excitation and emission of fluorescence close to plane metal surfaces were discussed and prism coupling was employed to excite the evanescent plasmon field. Now the obtained results are extended to structured surfaces like metallic gratings. The excitation of fluorophores in the evanescent field and the decay channels are identical to the ones discussed for prism coupling. Not the investigation of symmetric gratings is the aim of this chapter but special emphasis is laid on the influence of coupled surface resonances. These can occur in the case of blazed grating structures. An important feature of coupled resonances is strong localisation of the electrical field along the grating period. This localisation can be sampled by fluorescent probes on top of the grating by using SPFS.

The work in this chapter was carried out in collaboration with M. Kreiter [75] and has been published recently [76].

5.1 Coupled Resonances on Blazed Gratings

After a short review on surface plasmon grating coupling and the definition of the investigated grating structure, the existence of coupled resonances is discussed to the extent necessary to understand the experimental results in this chapter.

5.1.1 Grating Coupling

The coupling between light and surface plasmon resonances is not only possible using a high refractive prism (chapter 3.1.1), the momentum of the incident photons can be adjusted alternatively by a grating [10]. In this case the characteristics of a periodically modulated surface is used to couple reflected laser light to surface waves.

Grating profile

A grating structure can be modelled as a Fourier sum, specified by the amplitude A_m and the phase ϕ_m:

$$z(x) = \sum_{m=0}^{\infty} A_m \sin(mk_g x + \phi_m) \qquad (5.1)$$

with z and x being the Cartesian coordinates and $\mathbf{k}_g = 2\pi / \Lambda$ being the grating vector. Λ is the grating constant. In case of a symmetric 'normal' grating as illustrated in Figure 5.1 the surface profile can be modelled as a pure sinusoidal modulation and no higher Fourier components than the fundamental sine are necessary. The special case of asymmetric profiles, which are under investigation in this chapter, require the introduction of a second harmonic component to describe structures which are called 'blazed' gratings [77].

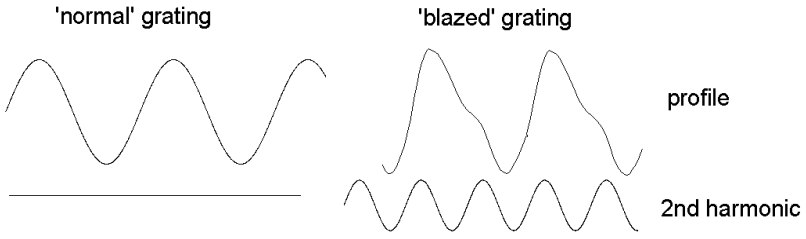

Figure 5.1 : Surface profiles of a ‚normal' grating (left) and a ‚blazed' grating (right) together with the second harmonic component in the Fourier representation of the profile

Excitation of Plasmons

Consider a sine-like periodically modulated surface, which can be prepared e.g. by embossing processes. Then the momentum $\hbar\mathbf{k}_g$ can be added to the momentum of the incident photons so that resonant coupling is possible if following condition is fulfilled:

$$\mathbf{k}_{psp} = \mathbf{k}_{x,light} \pm m \cdot \mathbf{k}_g = \mathbf{k}_{x,light} \pm m \cdot \frac{2\pi}{\Lambda} \qquad \text{with} \qquad \mathrm{m} = \pm 0,1,2,3,... \qquad (5.2)$$

with $\mathbf{k}_{x,light}$ being the wavevector of the incoming photons and m being the order of refraction. At a fixed grating constant the wavevector of the incident light is adjusted by choosing the incidence angle θ. For matching momenta optimal resonance conditions are achieved and the reflectivity reaches a single minimum similar to the typical resonance scan curve for prism coupling (chapter 2.3)

Experimental Geometry

The response of the grating upon irradiation is strongly dependent on the experimental geometry of the grating and the orientation and polarisation of the incident electromagnetic waves. In Figure 5.2 the electromagnetic wave is characterised by its polar angle θ, the azimuthal angle Ψ, its wavelength λ and the wave vector $\mathbf{k}_{light}$. The polarisation (TE, TM) of the incident light is defined by the polarisation angle φ. The azimuthal angle Ψ describes the counter

clockwise rotation of the plane of incidence relative to the x-axis (which is perpendicular to the grating grooves). In a classical resonance experiment normal incidence at an azimuthal angle of $\Psi=0$ is chosen and the polar angle θ of TM polarised light (p) is varied to change the in-plane component $\mathbf{k}_{x,light}=\mathbf{k}_{light}\sin(\theta)$ until the resonance condition in (5.2) is fulfilled. However, in the 'conical mount' azimuthal angles larger than $\Psi=0$ lead to a tilt of the plane of incidence. It will be shown that the resonances in this tilted configuration differ strongly from the classical behaviour at $\Psi=0$.

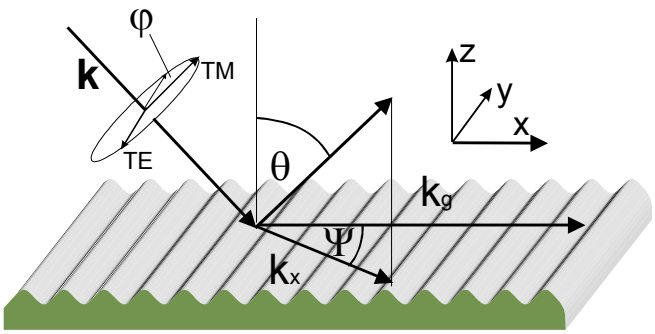

Figure 5.2 : Definition of angles for polarisation, incidence and diffraction in respect to the grating structure [76].

5.1.2 Coupled Resonances and Localised Electric Fields

In the following, the effect of the second harmonic component of blazed grating upon irradiation with polarised light is discussed and the electric field distributions along the metal gratings are characterised.

The sample under investigation consists of a blazed metal grating as schematically depicted in Figure 5.3, which was prepared by thermal evaporation of an optically thick, 150nm gold film onto a silica grating. Subsequently, a 20 nm thin polyvinyl-alcohol layer (PVA) was spin coated onto the sample, assuming that the polymer film follows the grating structure.

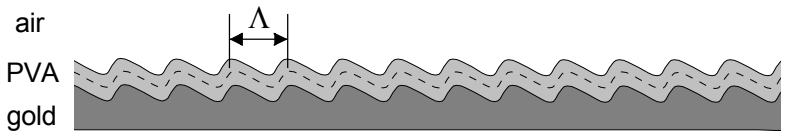

Figure 5.3 : Schematic presentation of the investigated grating structure

In Figure 5.4 the reflectivity of $\lambda=632.8$ nm TE polarised light ($\varphi=90°$) is presented as measured with the introduced blazed grating [75] in Figure 5.3. When both the azimuthal angle Ψ and the polar angle θ were varied, two different stripes of reflectivity can clearly be observed. They can be attributed to the excitation of surface plasmon resonances by $+1^{st}$ and -1^{st} order of

diffraction. Far away from Ψ=90° each of the stripes can be independently described by the momentum matching condition in equation (5.2). However, at Ψ=90° a deviation of the stripe's continuity is seen. For symmetric grating profiles (without second harmonic Fourier component) the m=+1 and the m=-1 resonance are expected to cross each other (modelled as the thin black line), resulting in a single resonance minimum as introduced above. Instead, a splitting between the resonance braches is seen and two different minima are obtained. The obtained coupled resonances appear at different incidence angles as compared to unperturbed plasmons and show an altered width. The narrower one is called 'long range surface plasmon' (LRSP), while the broader one is referred to as 'short range surface plasmon' (SRSP) according to their different coherence length [78]. The distance between these minima is referred to as 'photonic band gap' [79-82] and can be interpreted as follows: At this certain combination of polar and azimuthal angle both resonances are excited simultaneously and can mutually couple to each other via the additional momentum which is provided by the second harmonic component of the grating.

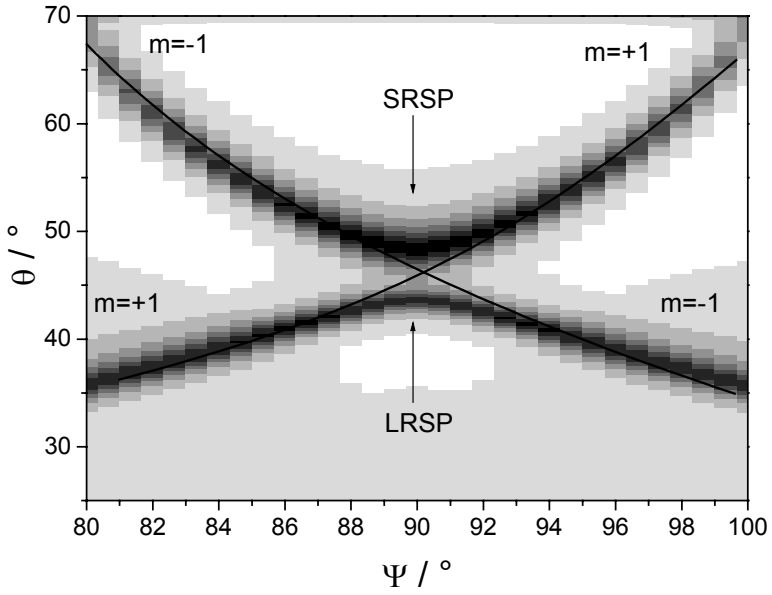

Figure 5.4 : Experimentally determined reflectivity of a gold grating with dielectric coating for TE polarised light of λ=632.8nm in dependence on the polar angle θ and the azimuthal angle Ψ. The grey values represent the reflectivity from 1 (white) to 0 (black) [76].

If the same experiment is repeated with a different wavelength of λ=670nm a similar reflectivity behaviour is observed. The modelled reflectivity in Figure 5.5 differs in the angular position of the resonances but still exhibits the described band gap structure at Ψ=90°. For four different angular positions (a-d) the electrical field strength over the grating profile was calculated

as given in Figure 5.6. Combinations b and c correspond to the two coupled resonances, for which a strong lateral localisation of the electrical field strength is observed. Comparing b and c the simulations reveal a coincidence of the minima of LRSP (b) with the maxima of the SRSP (c) and vice versa. For normal surface plasmons outside the bandgap (c,d) a moderate modulation is seen, but the lateral variation is much weaker than for the coupled resonances. The observed behaviour was expected for the latter cases, since surface plasmons are electromagnetic waves travelling along the interface.

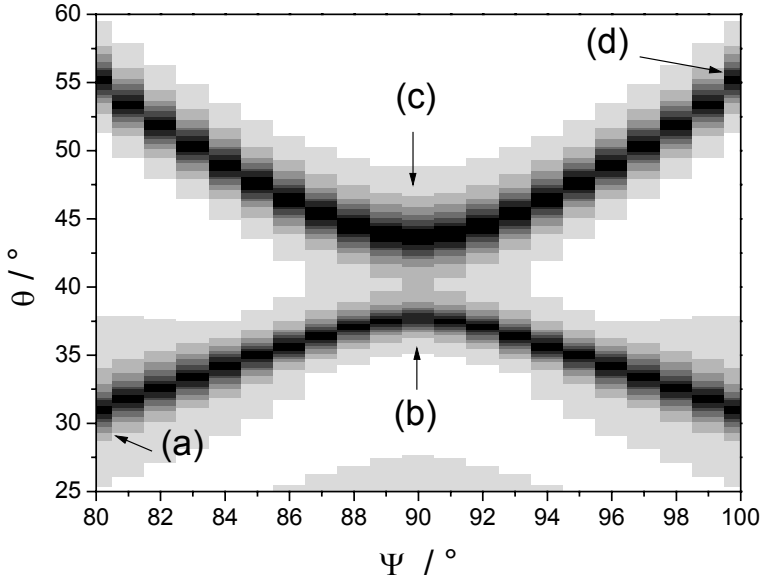

Figure 5.5 : Modelled reflectivity of a gold grating with dielectric coating for TE polarised light of λ=670nm in dependence on the polar angle θ and the azimuthal angle Ψ. The grey values represent the reflectivity from 1 (white) to 0 (black) [76]

The contrast between the electric field distributions and the correlation to the grating profile is clearly seen, if the field strength for all four cases is plotted for a distance of 10 nm above the metal surface (in the middle of the applied poly-vinyl-alcohol film). The second harmonic of the grating profile (dotted line) determines the positions of the maxima of the electrical field [83]. It is worth noticeable, that the maxima of the electrical field of SRSP coincide with the maxima of the second harmonic of the grating profile, while the LRSP has its minima there. Both coupled resonances exhibit sinusoidal like field distributions. The maxima of the field distributions appear to be phase shifted by 180° with respect to each other. As explained before the correlation of the free plasmons to the grating structure is again very weak.

Summarising, the field distribution over the blazed metal grating can be controlled by choosing the appropriate incidence angle θ_{in}. The field strength shows a strong modulation that is half the wavelength of the period of the grating. Thus, experimentally two different (resonance) incidence angles can be found which have complementary field distribution along the metal surface.

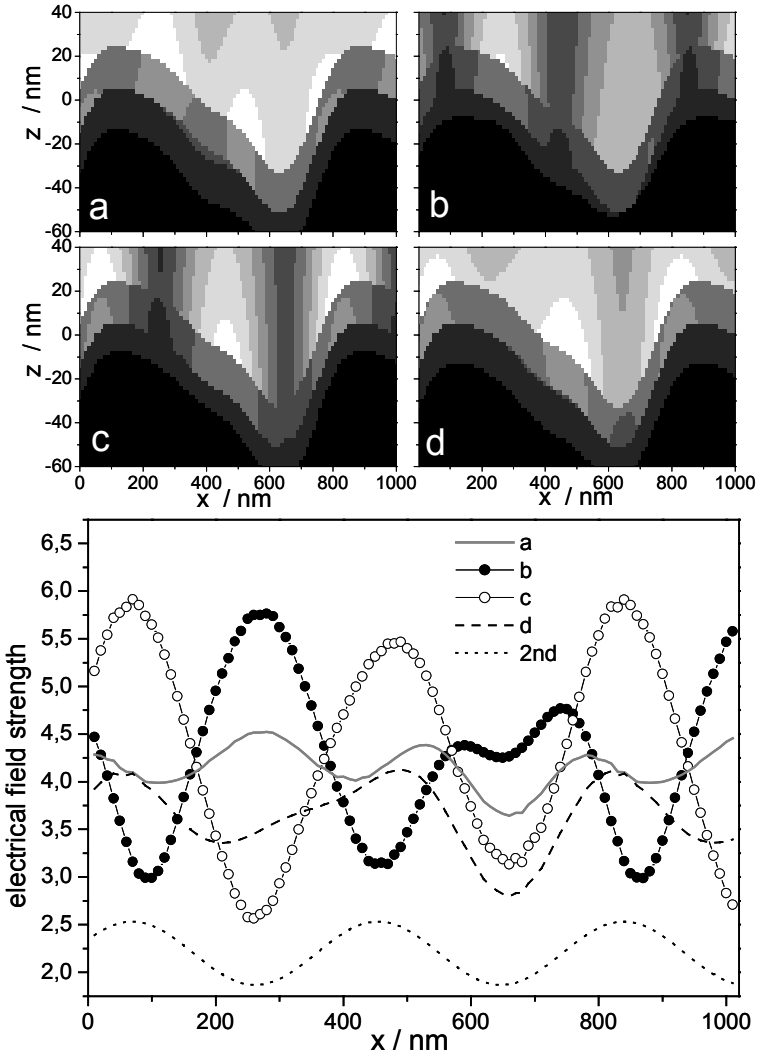

Figure 5.6 : (top):Calculated electrical field strength over the grating illuminated for the angular positions as characterised in Figure 5.5: a) Ψ=80°, θ=31.1° (m=+1); b) Ψ=90°, θ=37.7° (LRSP); c) Ψ=90°, θ=43.7° (SRSP); d) Ψ=100°, θ=55.1° (m=+1); white represent high field strength. (bottom): the electrical field for the cases a-d was calculated at a distance of 10 nm above the metal surface. a) straight line (free plasmon, m=+1); b) full circles (LRSP); c) open circles (SRSP); d) (free plasmon, m=+1); dotted line: second harmonic of the grating profile

5.2 Excitation and Emission of Fluorescence

The behaviour of fluorescent molecules above plane metal surfaces was subject of a number of experiments in chapter 4. The importance of surface plasmon modes for both the excitation and emission of the fluorescence was discussed for the Kretschmann configuration. For the case of metallic gratings it was similarly reported that fluorophores could be excited via the evanescent field of surface plasmons [66]. Furthermore, it has been proved for silver gratings that surface plasmon as intermediate states play an important role for coupling the chromophore's excitation energy to light. [84]. As discussed in chapter 4 the plasmon mode provides an additional decay channel for the fluorophore, so that the lifetime of the excited state is reduced if the dye is placed closer than 20nm to the interface.

Kitson [66] and Andrews[81] have performed experiments on silver gratings, in which the band gap structure was observed in the reflectivity and the emitted fluorescence of dyes was found to reflect this band gap. This proves that in addition to free plasmons also coupled resonances can effectively enhance the fluorescence intensity. In further experiments [82,85] emission maxima were observed in certain directions, which correspond to reflectivity minima if the excitation experiment was performed at the Stokes' shifted fluorescence emission wavelength. Thus, the band gap structure not only plays a role in the excitation but also in the decay of fluorescence over metal gratings.

In this chapter the excitation and emission of fluorophores via surface plasmons on silver gratings will be investigated. Special emphasis will be laid on the influence of coupled resonances and the effect of the strong field localisation in the case of blazed gratings. While in the case of free plasmons only moderate modulation of the surface field is seen, the choice of the right excitation angle allows to produce strong field intensities at different positions along the metal grating (Figure 5.6). Thus, the excitation and emission probability of a dye is expected to vary strongly with the dye's position along the grating pitch. In a simplified view two sets of chromophores can be distinguished: One group being placed in the field of the LRSP and the other placed in the electrical field of the SRSP. By choosing the right excitation angle θ in Figure 5.4 one of these two sets can be selectively excited.

Since the optimal excitation angle depends on the molecules position on the grating it is expected that the same holds for the angle under which optimal emission is observed. Excited fluorophores at positions were LRSP fields are predominant should leave their energy predominantly into these resonances; the other set of chromophores is expected to prefer the

SRSP resonances. Both groups of fluorophores are defined according to the field of LRSP and SRSP resonances, which are found either in the maxima or minima of the second harmonic of the grating (Figure 5.6). The grating pitch is very small for the investigated grating structure, and so is the distance between the centre of both groups (< 200nm). The selective excitation via coupled resonances therefore allows the manipulation of dye molecules on a sub-micron scale.

5.2.1 Simulation of the Excitation and Emission Process

The comprehensive theoretical description of the physical processes can be found elsewhere [76] but the basic concept of underlying model may be outlined in the following: It is assumed that the fluorophores are randomly distributed in the polymeric layer over the metal grating as depicted in Figure 5.3. First, the excitation and emission probability for a single dye molecule was evaluated and then the total fluorescence intensity could be obtained by averaging over all fluorophores.

Single molecules

First the excitation probability for a single molecule at a fixed position with a certain dipole moment was determined. The exciting light is defined by its wavelength, the direction of incidence and its polarisation. The absorption process can be described as the excitation of an electrical dipole with fixed oscillation axis by the incident electrical field. The calculated transition probability P_{ex} is based on Fermi's golden rule. This describes the transition between two states, dependent on the intrinsic properties of the fluorophore (characterised by the transition moment V_{mk}) and the surrounding (characterised by the density of states σ_{mk}):

$$P_{ex} = \frac{4\pi^2}{h} |V_{mk}|^2 \sigma_{mk} \qquad (5.3)$$

with h being Planck's constant. For a fixed direction of the dipole, the transition matrix element is given as

$$V_{mk} = -r_{ex} \cdot E \qquad (5.4)$$

with r being the transition dipole moment and E being the electrical field.

In the second step the emission process has to be modelled theoretically. A complete description of the processes would include a calculation of the electrical field caused by the dipole in the boundaries given by the grating. Then the probability of emitting light from the

dipole into the detector could be calculated. Unfortunately, this problem cannot be solved by standard mathematic algorithms, so that an alternative approach was chosen: The dipole and the detector are considered as systems that exchange energy via photons. We cannot calculate the direction of energy transition from the dye to the detector. But the coupling strength for the energy transfer is equal for both directions. Therefore we can consider the reverse process: an emitter at the position of the detector, which transfers its energy to a dye molecule at the grating surface. This problem has been already solved in 5.1.2 and can easily adapted to the emission wavelength of the fluorophore.

Averaging procedures

The average is taken over the orientations of all randomly distributed molecules in the polymeric film by two alternative strategies:

a) **fixed dipole model :** The transition dipole moments for excitation and emission are assumed to be identical and the molecules do not rotate between absorption and emission. Then the average has to be taken over the combined process as well. The probability for this process is obtained by averaged over all possible directions.

b) **rotating dipole model :** Due to rotation of the chromophore or on the molecular level the transition dipole moment can be different for excitation and emission. The average over the orientations have to be taken for each process separately. The emission probability is then proportional to the product of the independently calculated probability of both emission and excitation.

Finally, the calculated emission probabilities can be spatially averaged over all possible positions of the dyes in the polymeric film. This leads to the expected fluorescence intensity. Both averaging procedures are compared with experimentally determined data later.

5.3 Results and Discussion

After the characterisation of the sample by reflectivity measurements the fluorescence of the Cy5 dyes in the polymeric film was measured and the angular dependence of the emission was investigated. For this purpose fluorescence scans were recorded at varying incidence and relative emission angle. Additionally the effect of leaving the plane of incidence was investigated. The obtained experimental data were compared to the theoretical models of fixed and rotating dipoles as introduced before. Finally, the selective bleaching of the dyes by LRSP and SRSP was investigated and a possible application for determining diffusion coefficients was proposed.

5.3.1 Experimental

Sample Preparation

The grating sample in Figure 5.3 was prepared by thermal evaporation of an optical thick 150 nm gold film onto a blazed silica grating, the manufacturing of which was described elsewhere [75]. Cy5-labelled Streptavidin (Molecular probes) was dissolved in a solution of poly-vinyl-alcohol in water (1 weight% polymer) and spin-coated onto the metal film at 4000 RPM. The streptavidin (compare chapter 6.3.1) was used as an anchor for the Cy5 dye but its chemical or biological properties are of no importance.

Experimental Set-Up

The used experimental set-up in Figure 5.7 is similar to the SPFS set-up from chapter 3.1.2. A HeNe laser beam passes a set of polarisors in order to ensure s-polarisation and to control the intensity of the incident laser light. A programmable shutter protects the fluorescent sample when no data are taken in order to reduce photo bleaching of the fluorophores. All additional wavelength components other than λ=633nm are filtered out in front of the grating sample. The grating was mounted into the set-up in Ψ=90° geometry (grating grooves in the plane of incidence) in order to investigate the coupled resonances from Figure 5.5. The probe is mounted onto a goniometer in order to control the incidence angle θ_{in}. Two different measurement modes are possible:

a) **reflectivity measurement:** A photodiode was mounted onto a second goniometer and moved around the sample. According to the reflection law the photodiode was moved by an angle of $2*\theta_{in}$ in order to follow the reflected laser beam. During the measurements the detector is kept in the plane of incidence.

b) **fluorescence measurement:** The photodiode is exchanged by a photomultiplier tube (PMT). The emitted fluorescence of the grating is probed by moving the PMT around the sample by an angle θ_{rel}. The angular resolution is defined by the distance between the sample and the PMT of d=15cm and the diameter of 2mm of the pinhole in front of it. A combination of pinholes and interference filters blocks out all other wavelength than the emission wavelength of λ_{em}=670 nm. Similar to the experiments with the prism set-up in the last chapter, the detector can be moved out of the plane of incidence (which equals the drawing plane in Figure 5.7) by a height h. The detection system (PMT, filter, pinhole)

was aligned such that its optical axis was always pointing towards the centre of the grating sample. There the incident laser beam hit the grating. The applied tilt is then defined by:

$$\Psi_{tilt} = \arctan(h/d) \qquad (5.5)$$

Note, that the angles θ_{rel} and Ψ_{tilt} for this experimental set-up are not necessarily equal to the polar angle θ and the azimuthal angle Ψ from Figure 5.2. They can be converted into each other by simple trigonometry (not shown). Only if the PMT is in the plane of incidence (Ψ_{tilt}=0°) the azimuthal angle corresponds to Ψ=90° and then θ_{rel}= θ.

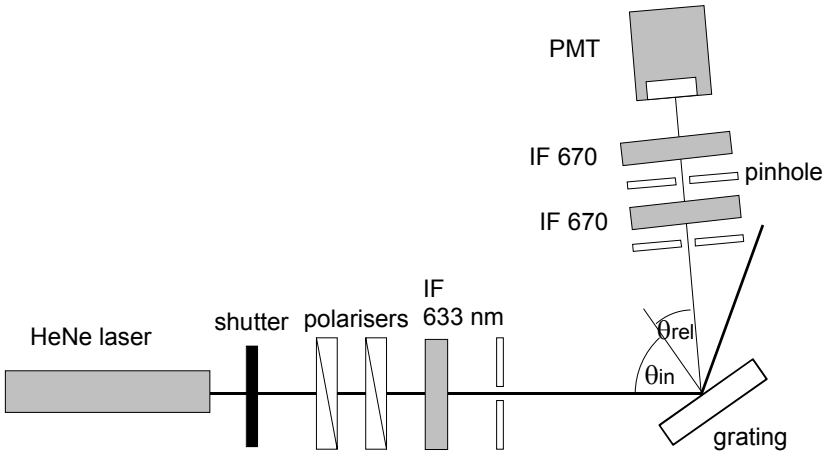

Figure 5.7 : Schematic illustration of the experimental set-up as described in the text.

5.3.2 Reflectivity Measurements

The sample in Figure 5.3 was mounted into the set-up in Ψ=90° geometry and the reflectivity was measured with TE polarised HeNe light of λ=632.8 nm wavelength. Measurements were performed before and after spin-coating the polymeric layer onto the metal film. The obtained scan curves could be simulated by taken into account the shape of the grating, the dielectric properties of the gold and the polymeric film, the polarisation and wavelength of the used laser light [76]. In Figure 5.8 the obtained scan for the polymer covered grating is presented together with the simulation based on the parameter set given in the legend. Two resonances are clearly seen at incidence angles θ_{in}=44.8° and θ_{in}=51°, respectively, which can be assigned to the excitation of LRSP and SRSP resonances. The obtained scan curve corresponds to a cross-section of the reflectivity map in Figure 5.4 at Ψ=90°.

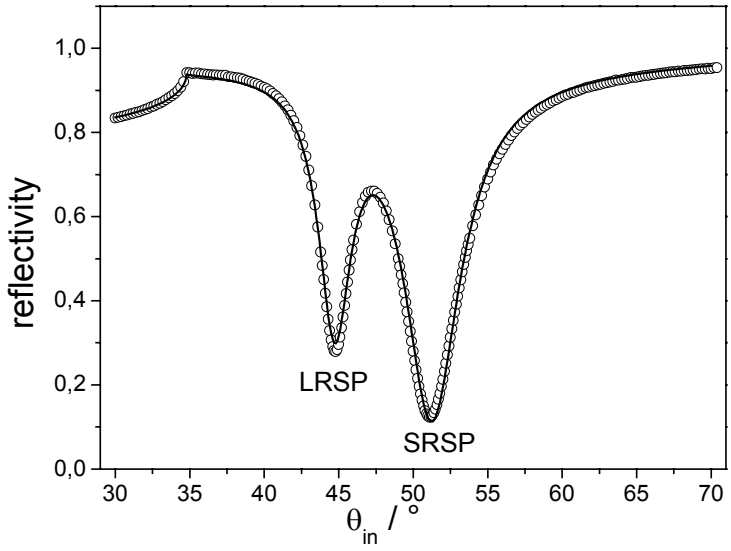

Figure 5.8 : Reflectivity of the investigated sample at Ψ=90° geometry for 632.8nm TE polarised HeNe laser light. The two minima can be attributed to the excitation of LRSP and SRSP resonances. The scan corresponds to a cross-section of the reflectivity map in Figure 5.4 at Ψ=90°. For the simulation the following parameter set was used: grating pitch Λ=770.35 nm, Fourier components: A_1=25.6nm, A_2=7.62nm, φ=63°, metal: ε_{Au}=-11.2+i1.17, polymer: ε_{PVA}=-11.2+i1.17, thickness 19.1nm

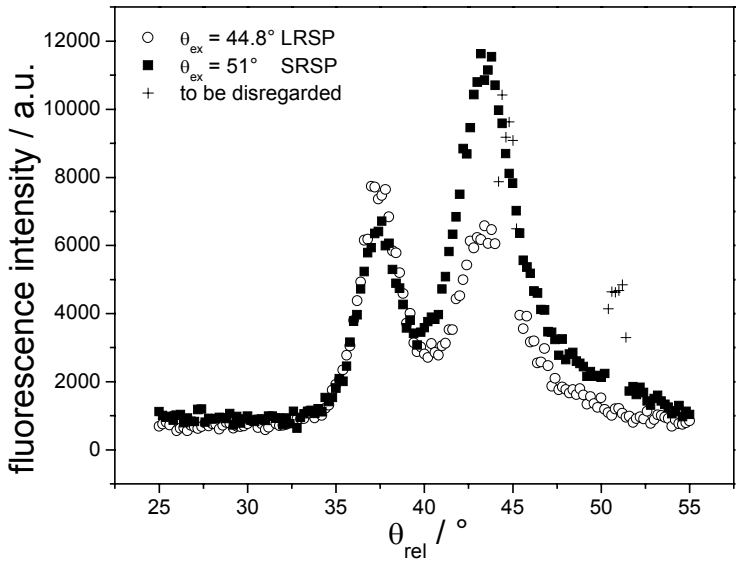

Figure 5.9 : Fluorescence signal dependent on the emission angle θ_{rel} at Ψ=90° measured at the two plasmon resonance angles θ_{ex}=44.8° (LRSP) and θ_{ex}=51.0 ° (SRSP) from Figure 5.8. The perturbations due to the laser stray light are to be disregarded.

5.3.3 Fluorescence Measurements in the Plane of Incidence

The fluorescence excitation and emission under the influence of LRSP and SRSP coupled resonances from Figure 5.4 and Figure 5.8 was investigated at Ψ=90°. During the measurements the photomultiplier was in the plane of incidence. The incidence angle θ_{in}=40-62° was increased stepwise ($\Delta\theta$=1°) and a fluorescence scan with the PMT at θ_{rel}=25-55° was performed at each angle. The Cy5 dye were excited at λ=632.8 nm and the Stoke's shifted emission maximum was observed at λ=670 nm. The shutter blocked incidental light when no data points were taken but the photo bleaching was not negligible. All fluorescence values in one experimental series were thus corrected for bleaching using a set of control data points taken before and after the actual measurements.

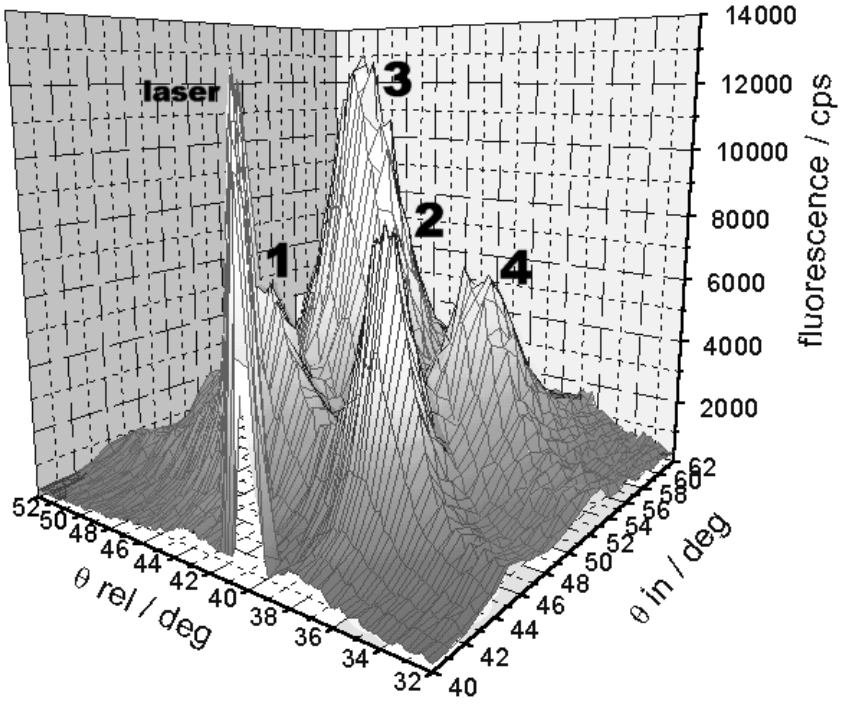

Figure 5.10: Fluorescence of the grating sample as a function of the incident angle θ_{in} and the relative emission angle $\theta_{rel.}$ Four emission peaks can be clearly seen which are obtained by sweeping through both the LRSP and SRSP resonances. Both excitation and emission are mediated by the plasmon resonances. Note that the maximum intensity of all four peaks is different, as discussed in the text. The coordinates of the peaks (θ_{in}/θ_{rel}) are: 1: (44.8°/43.5°), 2:(44.8°/37.5°), 3:(51.0°/44.8°), 4:(51.0°/37.5°)

Four different fluorescence maxima are observed in Figure 5.10. This can be explained by employing the LRSP and the SRSP resonances for both the excitation and the emission process: Increasing the incidence angle θ_{in} results in a successive excitation of the LRSP and SRSP

resonances in Figure 5.8. At θ_{in}=44.8°(LRSP) and θ_{in}=51.0°(SRSP) the fluorophores in the corresponding localised field are excited, resulting in an enhanced fluorescence emission at both excitation angles. The cross sections at these angles along the θ_{rel} axis are given in Figure 5.9. Clearly two emission peaks are found at θ_{rel}=37.5° and θ_{rel}=43.5°, respectively. This behaviour can be explained as follows: Once the fluorophores are excited by either the LRSP or the SRSP field they loose their energy via the surface plasmon decay channel as discussed for plane metal surfaces in chapter 4. The electrical field on the surface is modulated and the strong localisation in case of coupled resonances was discussed before. Depending on the localisation of the excited fluorophore along the grating the fluorescence decay will involve either the LRSP or SRSP resonance to couple the fluorescence energy to photons. The angles of maximum emission θ_{rel}=37.5° and 43.5° coincide with the positions at which reflection minima were observed in the modelled reflectivity map for λ=670 in Figure 5.5. This proves that the emission process is mediated by the coupled resonances.

By comparing the maximum fluorescence intensities in Figure 5.9 a clear difference between the peak intensities for both excitation angles θ_{ex}=44.8° (LRSP) and θ_{ex}=51.0 ° (SRSP) was observed. Upon excitation LRSP excitation (θ_{ex}=44.8°) the peak at θ_{rel}=37.5° is more pronounces than the one at θ_{rel}=43.5°. This relation is reversed for SRSP excitation (θ_{ex}=51.0°). This can be explained as follows: the fluorophores are fixed in their position on the grating during excitation and emission. Fluorophores, which are excited by the LRSP will predominantly loose their energy via LRSP resonances due to the field localisation. The same arguments hold for the SRSP case. However, the field distribution of LRSP and SRSP field are partially overlapping (Figure 5.6) and consequently the separation of the two sets of dyes is not strict. Fluorophores in the intersection of the surface fields will involve both resonances for excitation and emission and thus leading to the smaller maxima denoted as peak 1 and 4 in Figure 5.10.

In order to quantify the site specific enhanced excitation and emission the unit-less 'correlation number' C is defined as:

$$C = \frac{I_L^L / I_S^L}{I_S^S / I_L^S} \qquad (5.6)$$

where $I_{emmision}^{excitation}$ denotes maximum emission that was obtained for the excitation and emission via either LRSP(L) and SRSP(S). These values can be read out from the plots in Figure 5.9. For the case discussed above a correlation number of C=2.12 was found.

Model Calculations

Calculations based on the introduced 'free rotating dipole' and 'fixed dipole' model were performed for excitation and emission in the plane of incidence. The obtained simulations are compared with experimental results from Figure 5.9 and presented in Figure 5.11. Generally, the simulated trend was found to be in agreement with the experimental values. Correlation numbers were calculated from the simulations in Figure 5.11. The correlation number C_{rd}=1.79 for the rotating dipoles model is smaller than the experimental value C=2.12, while the fixed dipole model yields a higher value of C_{fd}=2.93. Both models represent extreme cases, and hence it is not surprising that the experimental values can be find in between these limits. All possible experimental uncertainties (roughness of the sample, smearing out of the signal at large and small angles) may lead to decreased correlation. Since the simulated value for the rotating dipole was smaller than the experimental one, this model doesn't seem to be appropriate. To summarise, the absolute correlation of fluorescence excitation and emission could not be mirrored by neither of the model simulation. However, the approximate values were sufficient to understand the underlying processes.

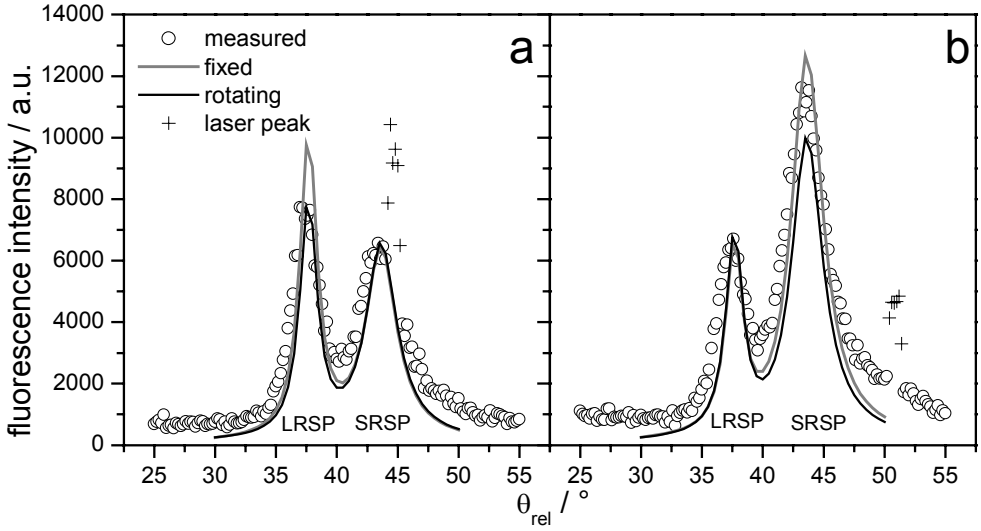

Figure 5.11 : Model calculations for the excitation via a) LRSP(θ_{ex}=44.8°) and b) SRSP (θ_{ex}=51.0°) based on the 'fixed dipole' (grey line) and the 'rotating dipole' model (black line).

5.3.4 Fluorescence Emission Outside the Plane of Incidence

In the experiment mentioned above the influence of coupled resonances on the excitation and emission on fluorescence was investigated. In the following experiments the dyes was still excited by the coupled LRSP and SRSP resonances. The emission process was tracked in their evolution from coupled resonances (Ψ_{tilt}=0° equals Ψ=90°) to unperturbed resonances at higher tilt angles ($\Psi_{tilt} \neq 0°$, $\Psi \neq 90°$). This transition from coupled to free resonances is clearly seen in the modelled reflectivity map for λ=670 nm in Figure 5.5. If the plane of incidence is left stepwise ($\Psi_{tilt} \neq 0°$, $\Psi \neq 90°$) the influence of the coupled resonances is decreasing and unperturbed free resonances are dominating. In the case of free resonances only weak field localisation along the grating profile was found in Figure 5.6. Therefore it is expected that no emission channel is preferred anymore for large tilt angles (free plasmons).

The experimental fluorescence curves for two different tilt angles are presented in Figure 5.12. Two features are noteworthy here: Compared to the experimental data for Ψ_{tilt}=0° in Figure 5.9 the distance between the emission maxima was increasing for higher tilt angles as predicted by the reflectivity plot in Figure 5.5. The correlation to the SPRS and LRSP channels was found to weaken as we proceeded from coupled resonances at Ψ_{tilt}=0° (C=2.12) over Ψ_{tilt}=1,6° (C=1.96) to free plasmons at Ψ_{tilt}=5.5° (C=1.024). At the largest tilt angle of Ψ_{tilt}=5.5° the resonances could be regarded as free plasmons.

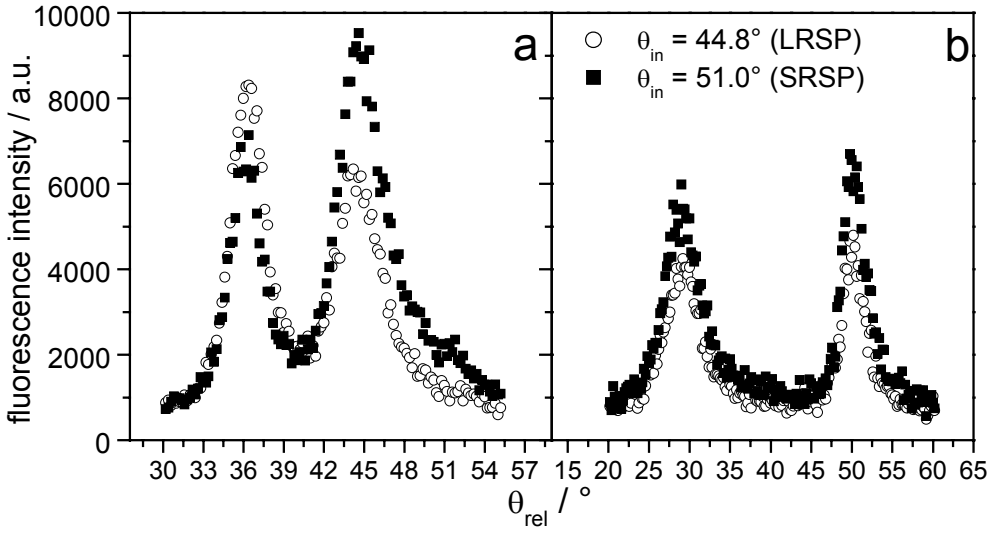

Figure 5.12 : Experimental fluorescence intensities at a) Ψ_{tilt}=1.6° and b) Ψ_{tilt}=5.5° for the two excitation angles of the LRSP and the SRSP.

In Figure 5.13 experimentally determined correlation numbers for further tilt angles were plotted together with simulations based on the models of free and rotating dipoles. As expected the correlation exhibited a maximum in the plane of incidence (Ψ_{tilt}=0°) due to the strong field localisation of the coupled resonances. When the detector was moved out of the plane of incidence the free plasmons more and more dominated the emission process until at Ψ_{tilt}=5.5° the correlation number reached unity.

Both of the models described the trend in correlation qualitatively. The predicted valued for the correlation in the plane of incidence were not satisfactory. Furthermore, both models predicted a finite correlation (C >1) for large tilt angles that could not be verified experimentally. It has to be concluded that none of the models are capable of reflecting the physical processes quantitatively. However, modelled correlation was appropriate to understand the underlying physics.

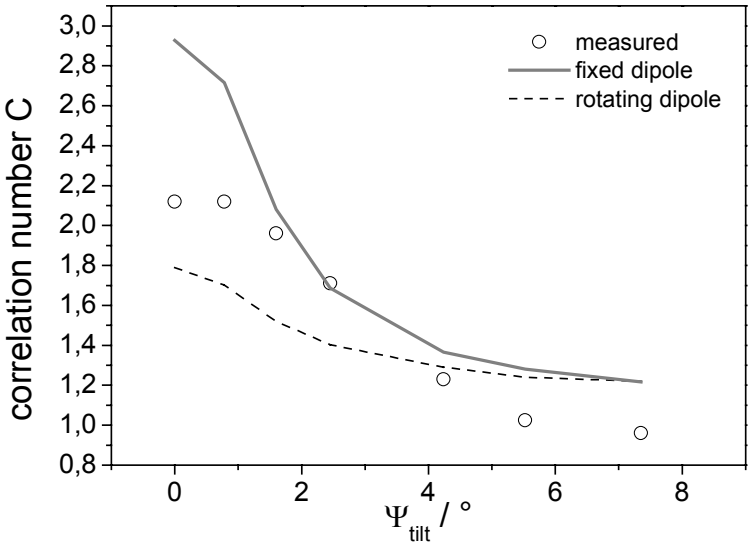

Figure 5.13 : Measured and calculated correlation numbers C as a function of the tilt angle Ψ_{tilt}.

5.3.5 Bleaching by the Field of Coupled Resonances

It was shown that mainly two sets of chromophores can be defined on top of the blazed grating depending on their position relative to the localised fields. By the choice of the appropriate excitation angle either the dyes in the LRSP or the SRSP field could be excited. While a shutter was used to avoid photo bleaching in the previous experiments the selective bleaching of the fluorophores was investigated in this chapter.

Selective Bleaching

In order to study the selective bleaching of the dyes, the time dependent fluorescence intensity was measured as a function of the excitation angle and emission angle. All measurements were performed in the plane of incidence. To assure maximal coupling to the fields of SRPS and LRSP two excitation angles θ_{ex}=44.8° (LRSP) and θ_{ex}=44.8°(SRSP) and two emission angles θ_{em}=37.5° (LRSP) and θ_{ex}=43.5°(SRSP) were chosen for the time dependent observation. After bleaching the sample with λ=632.8 nm light at the incidence angle θ_{bleach} for a defined period of time (5 minutes) the fluorescence at all excitation and emission angles were measured successively. By repeating this cycle the dyes were bleached stepwise. When θ_{bleach} was chosen to excite the sample at one of the resonance minima (e.g. θ_{ex}=44.8°, LRSP) the corresponding emission could be observed online (e.g. LRSP emission). However, both sample and detector had to be moved to monitor the fluorescence at the other angles. Then the bleaching process was interrupted for a short time and during the measurement the sample was bleached under the 'wrong' angle for about 10 seconds per cycle. Bleaching of the 'wrong' fluorophores could not be avoided but the extent was reduced by choosing a ratio of 5minutes bleaching / 10 measuring. Additionally the laser was blocked during the movement of the goniometers.

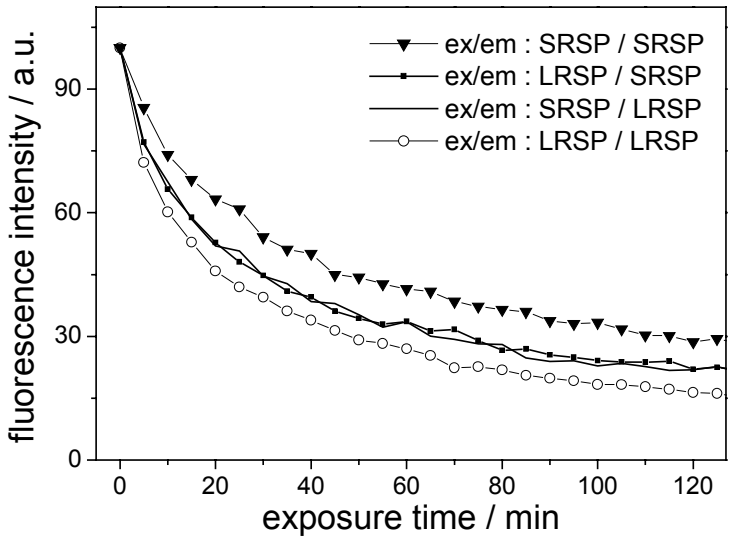

Figure 5.14 : Fluorescence intensities of all peaks in Figure 5.10 as a function of time upon bleaching by the LRSP field. The notation ex/em indicates which of the resonances was responsible for excitation and emission of the dye. Note that the LRSP/LRSP fluorescence is bleached the strongest.

In Figure 5.14 the time dependent fluorescence intensities of all four fluorescence peaks from Figure 5.9 and Figure 5.10 was measured upon bleaching the sample at θ_{ex}=44.8° (LRSP). A clear difference in the bleaching rate of the peaks was found. The notation (ex/em) indicates with resonance was mainly responsible for excitation and emission of the fluorescence. The dyes under the influence of the LRSP field are bleached the most (LRSP/LRSP). The signal denoted as (SRSP/SRSP) was attributed to fluorophores in the field of the SRSP resonance. Since illumination at θ_{ex}=44.8° excited mainly LRSP the (SRSP/SRSP) signal is bleached only moderately. Finally (LRSP/SRSP) and (SRSP/LRSP) represent fluorophores in the intersection between both fields. These dyes experience the field of both resonances and thus moderate but identical bleaching rate was observed. Due to the finite width of the resonances in Figure 5.8 it was not possible to excite only fluorophores in the field of the LRSP; the illumination at one resonance angle also involved the partial excitation of the other resonance. Thus, all fluorophores were bleached slightly with time. However, selective bleaching of one set of fluorophores could be proven.

A New 'FRAP' Method

The selective bleaching of dyes can lead to a strong modulation of non bleached fluorophores on the grating surface. Due to the grating structure a period of the modulation of about 400nm was reached. The strong modulation was investigated for the use as a novel 'FRAP' method.

Fluorescence Recovery After Photo-Bleaching (FRAP) [86] is used to determine diffusion coefficients of labelled molecules in and on thin films. By focussing high laser intensity onto the sample of interest, all chromophores in the focal point of the laser are bleached. After switching off the bleaching laser, the fluorescence of this spot is measured as function of time. From the recovery kinetics the diffusion coefficients of the molecules in the environment can be deduced. In analogy to this technique the fluorophores on the blazed grating were bleached selectively. Diffusion of not bleached chromophores into bleached regions should lead to a recovery of the bleached signal. The distance between maximal and minimal fluorescence on the surface is very small (200nm). There the proposed technique is expected to be advantageous in particular for the observation of very small diffusion coefficients.

In the following, the mobility of Cy5-labelled streptavidin in a poly-vinyl-alcohol (PVA) film was investigated. The sample was prepared as described above. In Figure 5.15 the time dependent fluorescence intensities of the LRSP and SRSP fluorescence signal are monitored upon bleaching at the SRSP resonance angle.

After bleaching for 20 minutes, the laser was blocked and both intensities were monitored with time. The slight decrease in both signals could be attributed to photo bleaching during the measurement process. After 35 minutes the sample was treated with humid air for a few seconds such as to increase the humidity at the sample to 100%. An increase in SRSP fluorescence was observed simultaneously with a decrease in the LRSP signal. This can be attributed to a redistribution of the dye molecules in the polymeric film. PVA is known to be a hydrophilic polymer and thus takes water up from the surrounding which leads to a swelling of the polymer. As a result the proteins' mobility in the film was enhanced and an exchange of bleached and intact dyes between the sets of chromophores could occur. The identical (scaled) relative intensity of both peaks after diffusion indicated a final random distribution of bleached and intact chromophores in the film.

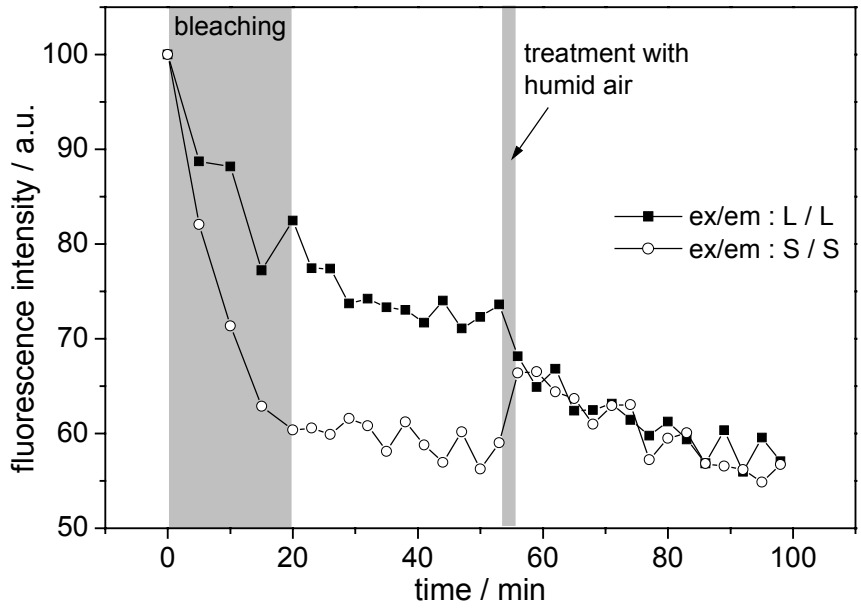

Figure 5.15 : Time dependent fluorescence intensity of LRSP and SRSP coupled fluorescence upon bleaching under the SRSP excitation angle. Note, that after treatment with humid air the mobility of the proteins in the polymer film was enhanced, such that the fluorescence could be recovered due to diffusion.

This experiment proves the potential impact for measuring diffusion coefficients by coupled resonances on gratings. The diffusion kinetics of the proteins in the swollen polymer film were to fast to be detected. For slower diffusion reactions the proposed technique might be an appropriate tool for the observation of dynamic processes on metal surfaces. Once the experimental conditions are optimised, it is no longer necessary to follow the fluorescence of both groups of fluorophores. The restriction to one species allows the detection at fixed

excitation and emission angles. Therefore the number of data points in the interesting region can be increased.

5.4 Conclusions

In the last chapters it was shown, that structured metal surfaces can influence the excitation and emission properties of fluorophores due to the electric field distribution of surface plasmon resonances. In the case of coupled resonances a strong field localisation was found along the grating surface. This led to a inhomogeneous excitation and emission behaviour. It could be shown that both the excitation and emission process involve coupled resonances as intermediate states. A quantitative description was not possible due to uncertainties in both experiment and theory. However, the model simulation could qualitatively describe the physical processes satisfactory. As predicted by modelled reflectivity maps at the emission wavelength of the fluorophore, the specific coupling to either LRSP or SRSP was lost when the plane of incidence was left. Then the fluorophores didn't experience the localised fields of the coupled resonances anymore and the emission process involved the weakly modulated free plasmon field.

Furthermore it could be shown that fluorescent dyes on the surface can be bleached selectively according to their lateral position along the grating. Upon increase in the relative humidity a recovery of the selectively bleached signal was observed due to enhanced diffusion in the swollen polymer film. This proves that coupled surface plasmon resonances may be the basis for a proposed novel 'FRAP' method.

In analogy to the experiments in chapter 4 surface plasmon fields were found to be an important decay channel for fluorescence at close distances to a metal surface. This constraint has to be kept in mind if surface architectures on metal films are designed for the sensing of fluorescently labelled molecules by optical techniques.

In the following chapters surface plasmon excitation is used for the detection of bio-molecules like DNA on metal surfaces. In this chapter it has been shown that gratings can be used to excite labelled molecules. However, the use of gratings involves experimental difficulties such as the alignment of the sample and the measurement against other media than air is challenging. The measurement of fluorescence adsorption kinetics is difficult, since the exciting laser beam has to pass the analyte solution, resulting in high background fluorescence. Therefore, prism coupling is preferred in the following experiment.

6 DNA Hybridisation on the Sensor Surface

To date, thousands of different genetic lesions such as point mutations or deletions are known which are correlated to human diseases [87]. A prominent example is the tumour suppressor gene p53, which is one of the most commonly mutated genes in human tumours [88]. Sequence specific analysis of this gene has thus become very useful to assist in monitoring cancer progress and patient therapy. In addition, driven by the human genome project (started in 1990), researchers are currently working on the sequencing of the complete genome of organisms. Due to the enormous number of base-pairs that need to be analysed, sensitive and efficient screening methods are needed that are capable of processing DNA samples in a convenient way. Most of the detection formats include the interaction of immobilised DNA probes and targets with surfaces. The analysis of the kinetic behaviour of oligonucleotides at the sensor surface is hence of major importance for the improvement of known detection schemes. Furthermore, the characterisation of DNA structure on surfaces can lead to the development of novel detection formats. In this study surface sensitive fluorescence detection by SPFS was used to investigate hybridisation reactions between oligonucleotides at a surface. In particular, the influence of sequence and secondary structure of immobilised probe sequences on the mismatch discrimination sensitivity of DNA probes will be discussed.

6.1 Nucleic Acid Structure

The function of deoxyribonucleic acid (DNA) is to carry the genetic information in living organisms from generation to generation and to allow for the expression of that information under appropriate conditions. The information that is stored in DNA is transcribed into RNA sequences and translated into amino-acid sequences. Thus, DNA serves as a blue-print for the synthesis of proteins and is of fundamental importance for living cells.

Structure

DNA is a biopolymer which is formed from nucleotide units [89,90]. These monomers consist of either a purine base (adenine, guanine) or a pyrimidine base (thymine, cytosine), deoxyribose and a phosphate moiety. The deoxyribose is in a cyclic furanoside form and is connected by a β-glycosyl linkage with one of the four heterocyclic bases. The 3' and 5' hydroxyl group of the sugar is phosphorylated. If nucleotides are coupled together by phosphodiester linkages the

typical sugar phosphate backbone of single stranded DNA is formed as shown in Figure 6.1. Due to the numbering of the atoms in the deoxyribose unit one can distinguish the 5' and the 3' end of a DNA strand.

Two single strands can bind to each other in an ordered manner and form double stranded DNA. This process is referred to as hybridisation. The two polynucleotide chains are of opposite polarity in the way that the terminal nucleotide of one strand has a 5' end, while the complementary one exhibits a 3' end on the same terminus. The strands are running in opposite directions and are said to be anti-parallel. Different forms of DNA helixes can be formed but the B form of DNA is the preferred one. It is a right handed helix with a pitch of 3.4 nm and 10 bases per each turn of the helix, such that the distance between on base pair is 0.34 nm. Figure 6.1 shows that there is a minor and major groove running along the helix. The diameter of the B helix is 2nm.

Stability

According to Chargaff's rule the sum of the purine bases (A, G) in a duplex equals the sum of the pyrimidines (T, C). The reason for this is the characteristic Watson-Crick base pair formation between adenine-thymine and guanine-cytosine in DNA duplexes [91]. This pairs are based on hydrogen bond formation between the heterocycles. Because G-C base pairs have one more hydrogen bond than A-T pairs, the regions in DNA rich in G and C are more stable than regions rich in T and A.

Upon base pairing, the net hydrogen bonds that are formed and cleaved between water and the bases is zero. Therefore the contribution of forming hydrogen bonds itself is negligible. The only stabilising contribution if the associated inductive effect. This inductive effect results from the aromatic system formed between two paired bases in a duplex (compare Figure 6.1). The alternating increase and decrease in the electron density among the hydrogen bonds results in a delocalisation of the electron density in the pseudo six-membered ring system. A decrease in the enthalpy stabilises the overall stability of the duplex.

Since the base pairs are flat they may stack one above the other like a pile of plates. Therefore the double strand is represented as a spiral staircase, with the base pairs forming the stairs. The double helix is stabilised by such stacking interactions in the duplex. The stability of the duplex is known to be sequence dependent since stacking interactions between the bases are nearest neighbour dependent. However, the major contribution to duplex stability comes in due to entropic considerations[90]. This effect refers to the tendency of hydrophobic substances to minimise interaction with water molecules and to maximise interactions with them self. The

number of water molecules around the strand is reduced if the double helix is formed from two single strands. Therefore duplex formation is preferred in an aqueous medium.

Experimental Factors Influencing the Stability

If double stranded DNA is subjected to extreme temperature, pH, low ionic strength or chaotropic agents the hydrogen bonds or the hydrophobic interactions are disrupted. As a result the DNA is said to denature and changes from a double strand to a random coil of single strands. In the case of denaturation by temperature the process is called melting. The temperature at which 50% of all strands are separated into ssDNA is called the melting temperature T_m. The bases in the DNA strands absorb light at 260nm. This absorption is partially suppressed in double stranded DNA due to stacking interaction of the bases. The increase in absorbance upon melting is referred to as hyper-chromic effect and can be used to monitor DNA melting quantitatively by UV spectroscopy.

The stability of duplex DNA and hence the melting temperature is dependent on several factors:

- (C+G) content of the DNA: Since a G-C pair has three hydrogen bonds and T-A only two, the stability of the duplex is influenced by the content of cytosine and guanine
- Length L of the sequence: with increasing chain length Tm increases and the slope of the melting curve at Tm becomes steeper. This is resulting from an enhanced cooperativity at higher temperatures.
- Sequence dependent nearest neighbour and end effects: the stacking interaction between two neighboured bases along the chain is dependent on their identity. Therefore the melting temperature for short strands is dependent on their sequence. The identity of the closing base pairs at both end of the duplex can additionally influence T_m.
- Presence of hydrogen bond disrupting agents like formamide or urea.
- Mismatches: If a double strand contains one or more non-complementary base pair combinations like AA, AC, GG, CT etc. the stability of the duplex is reduced. The number of hydrogen bonds is reduced and the cooperative stacking effect is influenced. Hence the stability of the whole strand is affected. The destabilising effect of a single mismatch decreases as the chain length increases. As a rule of thumb, 1% mismatch causes a decrease of about 1°C in T_m for duplexes < 100 bp.

- Ionic strength and pH of the solvent: At high salt concentrations, the negative charges in the DNA backbone are screened; the melting temperature is increased and the melting curve shows a sharp transition.

With respect to the introduced factors, the melting temperature is determined empirically by:

$$T_m = 81.5° + 16.6 \log M + 41(\%G + C) - 500/L - 0.62(\%\,formamide) \qquad (6.1)$$

with M being the concentration of monovalent cations and L being the strand length in bp [92].

The dependence of the duplex stability on the number of mismatched base pairs forms the basis for many biological applications. Fully complementary and mismatched sequences can be distinguished if the experimental parameters are optimised. The number of mismatched base pairs that can still be tolerated between two strands of a still stable duplex is defined as stringency. In various assays low stringency conditions are chosen to allow for the formation of complementary double strands while the hybridisation of mismatched sequences in suppressed.

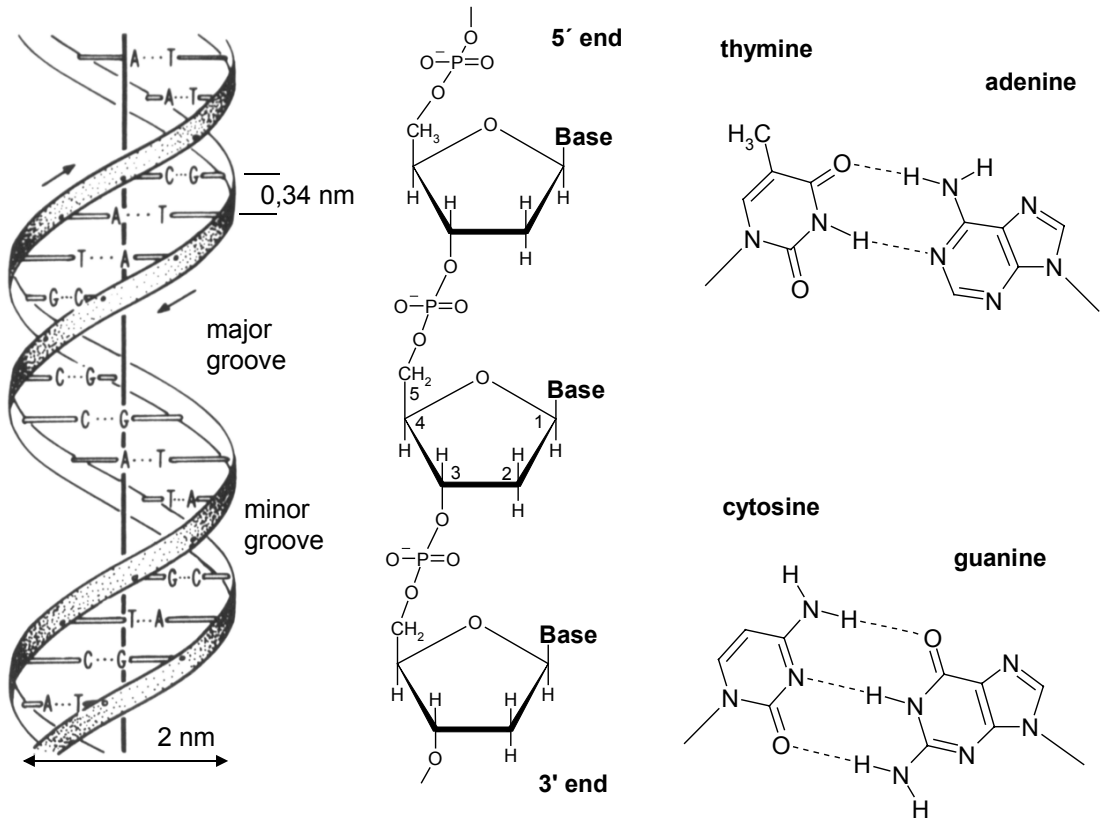

Figure 6.1 : A cartoon presentation of the double helix (B form) showing the major and minor grooves, a fragment of the phosphate-sugar backbone and the hydrogen bonding between the base pairs A-T and C-G

6.2 DNA Sequencing and Detection

In conventional gel-based sequencing methods, like the enzymatic Sanger chain-termination technique [93] or the chemical-cleavage method of Maxam and Gilbert [94], DNA samples are generally treated by agents which produces a mixture of dye or radio-labelled sequences of successive length. These fragments are separated by gel electrophoresis and the sequence of the analyte-DNA can finally be deduced from the obtained gel pattern. Modern gel-based methods can be used to sequence DNA strands up to 1000 bases long in several hours, but they are still slow. Furthermore, these techniques are expensive (several dollars per sequenced base pair) by means of costs of running the equipment and labour. Often they require the inconvenient use of radioactive material or toxic ethidium-bromide. Therefore a variety of alternative methods have been developed in the past years, which promise to overcome these drawbacks and are suitable for high-throughput analysis.

Especially modern DNA detection schemes on surfaces are actively investigated. The consequent development of DNA sensors and so called DNA chips or multi-spot arrays allows for the automation of the analysis process and the recycle of the used sensor surface. Most, if not all such nucleic acid detection schemes are designed in a sandwich format. They exploit the specificity of base recognition between DNA strands and the high binding constants of the resulting duplex. The sensor surface is usually modified with probe DNA of known sequence and is exposed to an aqueous solution of the target sequence. Successful monitoring of hybridisation of the target to the modified sensor surface indicates the complementary of probe and target. Thus, from the analysis of the binding processes the target sequence can be deduced. In particular in the case of DNA chips thousands of different probes are immobilised and analysed simultaneously. This process is called sequencing by hybridisation (SBH) and relies on the discrimination between fully matched and mismatched oligonucleotide pairs [95,96]. The DNA sequence can be thought of as an assembly of overlapping sequences. In some formats the target DNA is hybridised to short overlapping sequences of probes on the sensor surface. The continuous sequence of the original target can then be reconstructed from the sequence of positively scored probe oligos.

For many pharmaceutical and biomedical applications it is not always necessary to analyse a complete unknown DNA target by means of deciphering every single base as in sequencing approaches. In particular, in the analysis of point mutations of genes the corresponding genomic sequence and the position of pathogenic genetic lesions are known. Thus, the task is either to screen DNA samples for the defective gene itself or to test specifically for single base mutations

in a given DNA sequence. The detection of a base mismatch can then be used to evaluate the probability of developing the associated disease. Therefore the ability of a sensor system to distinguish between fully complementary and mismatched target sequences is essential for mutation analysis. The stringency of hybridisation reaction on surfaces depends on a variety of factors. These have to be optimised for each detection format in order to provide reliable and reproducible results.

Techniques

Independent of the surface architecture of the sensor a variety of different techniques can be applied to detect DNA on surfaces. Some piezoelectric methods like quartz crystal microbalance (QCM) [97,98] are capable of detecting a change in mass upon hybridisation, while others analyse the optical properties of the sensor surface. Examples are surface plasmon spectroscopy [99-107], waveguide spectroscopy [108] or fibre optic evanescent wave spectroscopy [109]. Other techniques require the labelling of the target sequence. Electrochemical techniques [110,111], fibre optic fluorescence spectroscopy [112] and electro-chemiluminescence [113] are frequently used. The choice of the appropriate detection technique is often a compromise between the high sensitivity of labelling techniques and the convenience of detecting unlabelled samples.

Recently, it was reported that Surface Plasmon Fluorescence Spectroscopy (SPFS) could be successfully applied to detect fluorescently labelled oligonucleotide sequences with high sensitivity [17,114]. A clear advantage to common non evanescent fluorescence techniques is the possibility to monitor online hybridisation kinetics. Due to the surface sensitivity the target fluorescence on the surface can be measured in the presence of fluorophores in the bulk. In many fluorescence formats only a simple yes/no is obtained, while SPFS provides information about the ongoing processes. The SPFS technique was already introduced in chapter 3.1.2. In the following the analysis of DNA/DNA interactions using modified sensor surfaces is discussed.

The work conducted in this study is based on the published preliminary results of Liebermann. Thus, the reported detection strategy is reviewed in the following. Own experimental results are compared to those published by Liebermann. The data are discussed based on the knowledge of the sequence dependent secondary structure of the probes. Thus, an attempt is made to elucidate the strong sequence dependence of the published kinetic constants in the chosen set of probes and targets.

6.3 DNA Immobilisation Architecture

As in Liebermann, the utilised sensor-architecture consists of multiple layers as schematically depicted in Figure 6.2. The base substrate is a $LaSFN_9$ high refractive index glass which allows the unperturbed coupling of laser light into the sensor multiplayer architecture. A coupling prism of the same refractive index was used in the Kretschmann configuration (chapter 3.1.1). A 47 nm thick gold film was evaporated thermally on top of the glass sample as described in chapter 3.2.2. Subsequently, a self assembled monolayer of a binary mixture consistent of two different thiols was formed on the gold layer from an aqueous solution of both thiols. The biotin moieties on the surface were used as anchors for the streptavidin protein. The latter formed the basis for a universal binding matrix, onto which biotinylated probe oligonucleotides were immobilised. The formation of the multi-layers was monitored by means of thickness determination using SPS. Finally, the binding reaction of the fluorescently labelled targets (a→c and b→c) could be monitored by SPFS. The biophysical characteristics of the individual layers will be discussed in the following.

6.3.1 Biotin-Streptavidin

In order to immobilise the probe oligonucleotide sequence, a universal binding matrix of streptavidin was prepared on the gold surface. Herein, the strong binding between the protein and biotin (vitamin H) was utilised.

Streptavidin

Streptavidin is a tetrameric protein (molecular weight 4 x 15 kDa) which was isolated from the actinobacterium *Streptamyces avidinii* .It is known for its ability to bind up to 4 molecules of d-biotin with an extraordinary high binding affinity and an exceptionally slow dissociation rate in solution ($K_d=10^{-15}M^{-1}$) [115,116]. This protein and the homologous avidin serve as natural antibiotics by depleting the environment (in e.g. egg clear) of the essential vitamin biotin. Since both proteins are able to bind derivatised forms of biotin as well, the biotin/streptavidin system has gained a wide spread importance for diagnostic purposes [117-120]. It is applicable for various assay formats that require an essentially irreversible binding between biological macromolecules. In the case of oligonucleotides and PCR products the biotin-moiety can be introduced during the synthesis process using biotinylated primers. Alternatively standard activation chemistry (e.g. NHS active esters) can be used to couple the carboxylic function of biotin to amino groups in other bio-molecules.

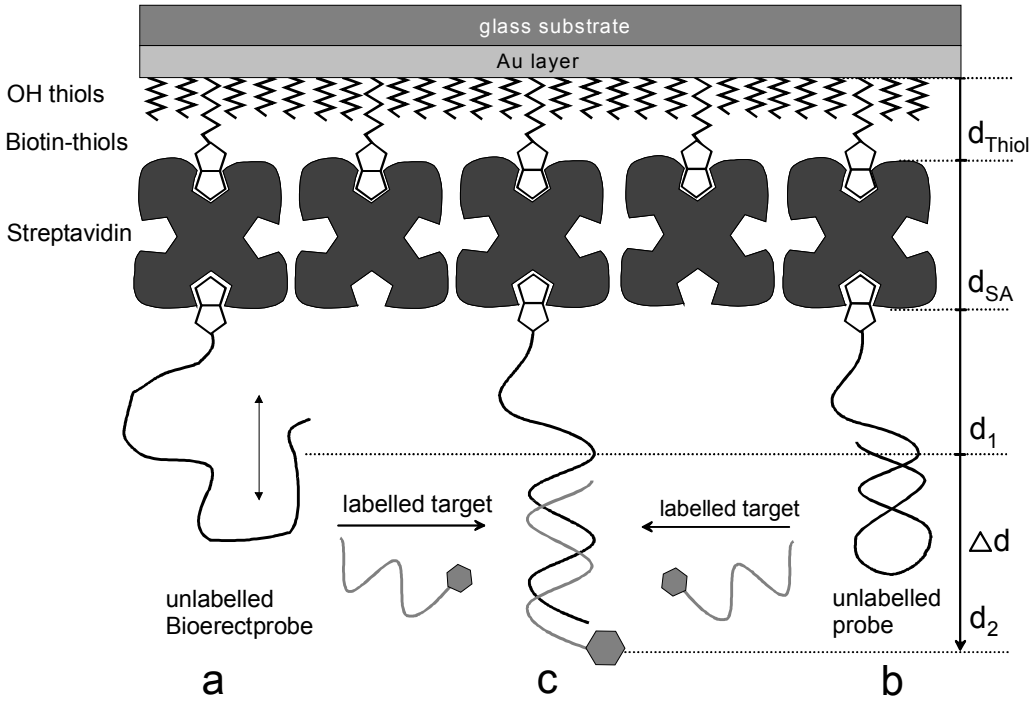

Figure 6.2 : Schematic presentation of the sensor surface architecture: Onto an evaporated gold film a binary SAM of two thiols (hydroxylated thinner thiols and biotinylated moieties) was formed, which supported a streptavidin protein layer. Biotinylated oligonucleotides were finally immobilised and the hybridisation reaction was monitored by measuring the fluorescence signal of the labelled target (c). While in a→c a random-coil probe was used, the probe sequence in b) exhibits a hairpin. This secondary structure alters the stability and accessibility of the probe. The thickness of the thiol and the streptavidin layer were 1.6nm and 4 nm, respectively. Therefore the marked distances to the gold were assumed as d_{Thiol}=1.6nm, d_{SA}=5.6nm, d_1~10nm, d_2~15nm.

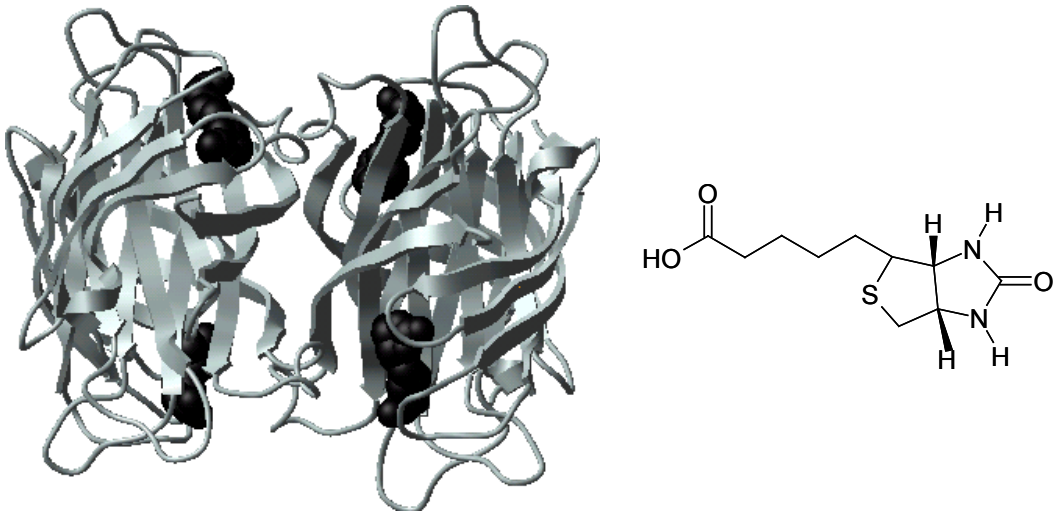

Figure 6.3 : Tetrameric Streptavidin (left) can bind up to 4 biotin molecules (black) with high affinity. The structure formula of biotin (right) exhibits a carboxylic function which can be used to couple biological molecules to the ligand.

The structure of streptavidin is depicted in Figure 6.3 together with the four binding pockets and the bound biotin (black). The dimensions of the protein were determined by Xray-scattering [115,121] to be 5.6nm x 4.2nm x 4.2nm [122]. The biotin moieties are bound by the binding pockets of the protein by hydrogen bonds and reach into the host by 1-2 nm. The carboxylic function of the biotin is still accessible from the surrounding of the protein. Therefore it is possible to bind biotinylated molecules like DNA, peptides, proteins and lipids to streptavidin.

It was reported [123], that bulky biotin derivatives had binding affinities much less than those found for the underivatised biotin ligand. The strength of the biotin-streptavidin bond has been attributed to extensive hydrogen bonding between the carboxylic oxigens and the protein groups. Functionalisation of the ligand leads to a loss of one oxygen and hence destabilises the binding. However, the major loss in affinity is likely to arise from the steric bulk[121] that inhibits a proper binding of the biotin by the pocket. Streptavidin has D_2 symmetry and adjacent binding sites are separated by approximately 2 nm [124]. Hence bulky ligands are not able to cover all four binding pockets of the protein. Nevertheless, the biotin streptavidin system can be used to construct nano architectures on surfaces [102,125-127].

Thiol-SAM

Although streptavidin can adsorb directly onto gold surfaces in an unspecific way, such relatively disordered physisorbed protein layer should be avoided. Rather, the formation of the complex organised sensor architecture must be controlled using appropriate sub-layers. A very convenient way of providing binding sites for the streptavidin on the surface is the use of biotinylated thiols. Thiols are known to form SAMs very facile onto gold (chapter 3.2.3) and the biotin-moiety assures binding of the adjacent protein layer in specific ordered and controlled way.

An optimal protein self assembled protein layer is obtained only, when the distance between the biotin-moieties corresponds to the distance of the streptavidin binding pockets in the protein layer. A too high biotin density was found to inhibit the formation of proper protein layers [102]. Thus, the biotin sites on the surface were diluted with a thiol of identical core structure, in which the biotin was exchanged by a hydroxyl end group. By varying the ratio of both thiols in solution the density of the biotin-moieties on the surface can be controlled. If the lateral dilution of the biotinylated thiol is too small, the accessibility of the binding sites is reduced and improper protein layer formation is observed. Contrasting, if the surface concentration of the biotin sites is too small, the consequent density of the bound streptavidin molecules is decreased and the

formation of a complete monolayer is hindered. In previous studies, a mixture of 10% biotinylated thiol (Biotinamino-capronacid-amidodioctyl-mercaptopropion-amid) and 90% OH-terminated thiol (2-Mercaptopropionacid-[2-(2-hydroxyethoxy)]ethylamid) in the binary mixture was reported to be optimal [128,129] [47]. If not mentioned otherwise this ratio of thiols was used for further studies. The structure formulas of both molecules are given in Figure 6.4.

The streptavidin layer provides a defined and stable binding matrix that can be used to immobilise a variety of biotinylated molecules for sensing purposes. As has been discussed in chapter 4, the fluorescence intensity of fluorophores near metal surfaces is strongly dependent on the metal-dye distance. It is important to note that in the used architecture the protein matrix separates the DNA bound fluorophore from the gold surface. SPFS can hence be conducted with only moderate losses of the fluorescence signal. From the results in chapter 4.3 an even higher fluorescence yield is expected if additional spacing would be introduced between the DNA strands and the metal. Alternative (and thickness variable) spacers like evaporated silicon oxide layers in combination with silane chemistry often lead to less organised and instable sensor architectures. Therefore the reported biotin/streptavidin system was the architecture of choice.

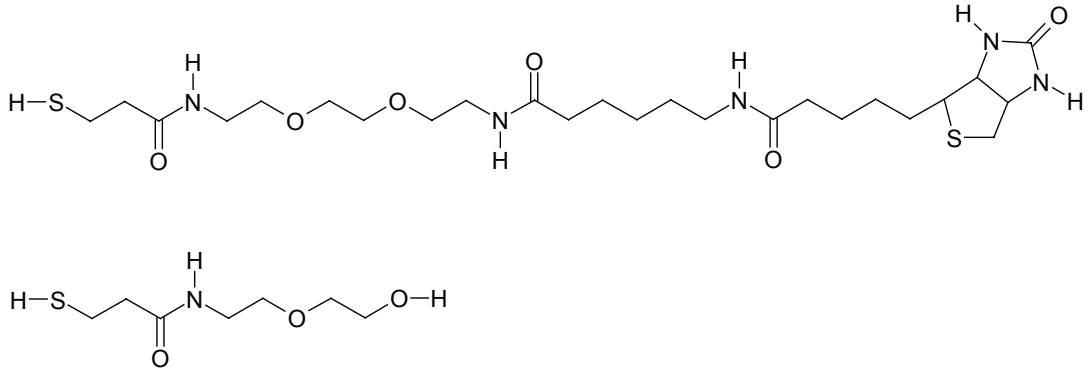

Figure 6.4 : Structure formulas of the biotinylated (top) and OH-terminated (bottom) thiols.

6.3.2 DNA Probe and Targets

A probe is defined as a short sequence of nucleic bases that can bind to a specific region of a target sequence [92]. The length of the probes can range from 10 to several hundred bases, but the common size is 14-40 bases [130]. From statistical considerations the minimum size of a probe that is unique, is 20 bases. The length of the probe influences the specificity and sensitivity of the assay. Short probes hybridise faster than long ones, but are limited in specificity.

Secondary structures and self complementary regions can influence the hybridisation kinetics. In order to investigate this effect, probes with and without secondary structures are compared: In

Table 6.1 the sequences of probe and target oligonucleotides that were studied experimentally are summarised (PHF, THF1, PHF2). These sequences were designed to be free of hairpin structures. In contrast to this the sequences used in Liebermann's studies are capable of forming hairpins and self annealed complexes [47].

The probe sequences are all biotinylated on the 5´end in order to permit immobilisation onto the streptavidin matrix (Figure 6.2). The first 15 bases in all probe sequences were chosen to be thymine residues, which served as a spacer between the actual 15 bases long recognition sequences and the protein surface. It has been reported [131] that the length and type of such spacer groups can influence the hybridisation efficiency strongly (up to an 150 fold increase). Steric hindrances during the hybridisation process can thus be reduced. For disulfide bound oligonucleotides on bead surfaces, an increasing length of the poly(dT) spacer was found to linearly increased the hybridisation efficiency [132]. On the other hand a spacer of large length can result in crowding effects. This in turn causes steric hindrances itself, such that an optimal spacer thickness exists. For SPFS it is important to note that the thymine spacer separates the target fluorophore from the surface after hybridisation. The fluorescence losses due to quenching by the metal surface are reduced.

Table 6.1 : Sequences of the unlabelled probe and labelled target oligonucleotides. Differences in the base sequences in each series are underlined.

name	type	bases	sequence	hairpin	selfanneal.
P1	probe	30	5´-*Biotin* -T_{15} TGT ACG TCA CAA CTA -3´	yes	yes
P2	probe	30	5´-*Biotin* -T_{15} TGT ACA TCA CAA CTA -3´	yes	yes
P3	probe	30	5´-*Biotin* -T_{15} TGT ACG TGA CAA CTA -3´	yes	yes
T1	target	15	5´- *Cy5* -TAG TTG TGA CGT ACA -3´	yes	yes
T2	target	15	5´- *Cy5* -TAG TTG TGA TGT ACA -3´	yes	yes
T3	target	15	5´- *Cy5* -TAG TTG TCA CGT ACA -3´	yes	yes
PHF	probe	30	5´-*Biotin* -T_{15} TGT ATC TCA GTT CTA -3´	no	no
THF1	target	15	5´- *Cy5* - TAG AAC TGA GAT ACA -3´	no	no
THF2	target	15	5´- *Cy5* - TAG AAA TGA GAT ACA -3´	no	no

The three probes P1-P3 used in Liebermann's studies exhibited a particular base sequence differing in one and two bases (underlined in Table 6.1), respectively. The 15 bases long target sequences T1-T3 were fully complementary to the corresponding probes P1-P3. Fully complementary duplexes such as (P1-T1; P2-T2; P3-T3) are referred to as MM0 (mismatch 0). Duplexes, which contain single non complementary bases are analogous named mismatched (MM1,MM2). These combinations can be constructed by cross hybridisation such as P2-T1 (MM1), P2-T3 (MM2) etc. The target sequences were labelled with a fluorophore on the 3´, which could be excited by HeNe laser light (λ=632.8nm) in SPFS experiments. In Liebermann's studies the used dye was MR121 (Boehringer Mannheim), while in our experiments the cyanine dye Cy5 (Molecular Probes) was chosen. The spectral properties make this fluorophore a suitable dye for our purposes (λ_{abs}=649nm, λ_{em}=670nm). All oligonucleotide sequences were commercially available (MWG Biotech, Germany).

Thermodynamically Stability of Sequences

Accurate prediction of the thermodynamic stability of DNA and RNA is important for several biomolecular techniques such as PCR, sequencing by hybridisation [95], anti-sense targeting [133] and techniques that rely on the hybridisation between nucleic acids. The choice of non-optimal conditions or sequences can lead to the detection or amplification of undesired sequences. Furthermore, the sequence dependent stability of helices has importance for the understanding of molecular processes like DNA unwinding and replication. Historically, a widely used method to predict thermodynamic properties of duplexes is the nearest neighbour model. The stability of a base pair is assumed to be governed by its identity (G-C, A-T, hydrogen bonds) and the identity and condition (paired or unpaired) of its neighboured base pairs (stacking energy). It has been reported that the trend in nearest neighbour stability (in one strand) is given by

GC>CG>GG>GA~GT~CA>CT>AA>AT>TA

Thus, both sequence and base composition are important for DNA duplex stability [134]. Increments of thermodynamic values can be assigned to these combinations such that the free energy of the system can be calculated by summarising these stacking parameters. At least 12 different nearest neighbour parameter sets are available in the literature [135-137] and were compared according to their accuracy in predicting melting temperatures and free energies [138-141]. Additional factors that have to be considered are the salt concentration, helix nucleation energies, mismatches, end effects (closing base pair in contact with the solvent) and the formation of secondary structures in the duplex. The calculated energies in this study are based on the parameter set published by SantaLucia [142].

The thermodynamic stability of the probe-target duplexes was represented by the free energy ΔG, which was calculated using freely available software routines [143] [144]. To evaluate the results published by Liebermann the theoretical equilibrium constant K of the hybridisation reactions was then calculated by

$$K = \exp(-\Delta G / R \cdot T) \qquad (6.2)$$

with R=8.31441 $JK^{-1}mol^{-1}$ being the gas constant and T=293.15K being the room temperature.

Hairpin Formation and Self Complementary

If an oligonucleotide exhibits intra-molecular complementary sequences by means of Watson-Crick pairs, secondary structures such as hairpins may be formed. These structures contain a double stranded part of at least 3-4 bases called the stem. Both complementary strands are connected by a single stranded loop sequence. Hairpin structures can be found frequently near functionally important regions such as regulation and promotion sites in genomic sequences [145]. For biotechnology applications, e.g. in the anti-sense strategy, the 3´end of oligonucleotides can be protected hairpin structures. For instance, the short sequences GCGAAGC forms extraordinary stable hairpin structures that protect oligonucleotides from degradation by heat or nucleases [146].

The thermodynamic properties of hairpins, bulges and dumbbells (two loops connected by a stem) have been the subject of many studies [147-149]. It is known, that the stability of hairpins is dependent on the structure of the stem as well as on the length and sequence of the loop region. It has been reported, that the stability of loop sequences follows the relation T loop > C loop > G loop > A loop [150] and that the identity of the closing base pair in the loop influences the properties of the hairpin[151].

In the detection scheme that is reviewed here, 30bases long oligonucleotides are used as immobilised probes. Thus, it is important to check the probe and target sequences for the probability of forming secondary structures. The formation of hairpins would stabilise the strand and the intramolecular hybridisation would compete with the binding of the target DNA. As a result, the measured kinetic constants would deviate from the bimolecular case, in which completely unperturbed binding in assumed. On the other hand, structured probes have been reported to show an enhanced specificity in hybridisation reactions. The difference in the melting temperatures for MM0 and MM1 target sequences with these structured probes is larger than those for the structure free ones [152]. By appropriate design of the stem length and content the

discrimination sensitivity of such hairpin probes can be optimised [153]. A novel probe design known as molecular beacons [154] consists of a hairpin probe, the ends of which are labelled with a fluorophore and quencher, respectively. Opening of the hairpin due to hybridisation to a target removes the quencher from the dye and thus the quenched fluorescence signal is recovered. High rates of hybridisation were also reported for probes in which the hairpin was used to tether the recognition sequence on the surface [155]. The above discussion points out that it is essential to control the structure of the utilised DNA capture probes. Structural constraints must be taken into consideration if hybridisation data are interpreted on the basis of kinetic measurements.

All probe and target sequences were analysed with respect to potential hairpin formation and then the thermodynamic properties of these structures were calculated. Furthermore, the probability of self annealed sites in the probes and targets due to complementary base sequences had to be considered. Such probe-probe or target-target combinations could compete also with the hybridisation between immobilised probes and targets. The prediction of the secondary structures was based on free energy minimisation calculations, carried out with the previously mentioned software bundle [143].

The analysis of the sequences revealed numerous secondary structures for an individual sequence, but only the most stable structures on the basis of free energies were considered here. In Table 6.2 self-complementary regions and potential hairpin candidates are indicated for the probes P1-P3 and the targets T1-T3 and the calculated free energies for these structures are given. The probe sequence PHF and the targets THF1 and THF2 were designed to be free of secondary structures. In Figure 6.5 the secondary structures of the duplex between P2 and all targets T1-T3 are shown schematically. Additionally the hairpins and self annealed complexes of probes and targets are illustrated. In some cases the calculated secondary structure was the same for more than one species and only differed in the base sequence. Here only a single structure was drawn representative for the other sequences. For example, the hairpin of the probes differed only in the sequence of the loop but not in the structure of the overall stem-loop.

As a result of the determined secondary structures the following probe formats will be discussed in this chapter: Structured probes (like P1, P2, P3), the hairpin of which can compete with the hybridisation reaction (see Figure 6.2 b→c) and a random coil probe (PHF) without any

secondary structure (see Figure 6.2 a→c). In comparison to the reported equilibrium constants, it will be discussed how this loop sequence may influence the binding constant. It will be evaluated if these structural differences are able to explain the strong sequence dependence of the experimental equilibrium values. Experimentally determined equilibrium constants for the hairpin free system PHF/THF will be compared with the literature values.

Table 6.2 : Potential hairpin formation and self complementary in probes and targets. Complementary regions are indicated as black boxes. The free energy was calculated using a software bundle as explained in the text.

name	type	complementary sequences	ΔG/ kcal/mol
P1	hairpin	5' TTTTTTTTTTTTTTTTGTACGTCACAACTA 3'	-1.3
	self comp.	5' TTTTTTTTTTTTTTTTGT ACGTCACAACTA 3' 3' ATCAACACTGCA TGTTTTTTTTTTTTTTT5'	-8.0
P2	hairpin	5' TTTTTTTTTTTTTTTTGTACATCACAACTA 3'	-1.3
	self comp.	5' TTTTTTTTTTTTTTTTGTACATCACAACTA 3' 3' ATCAACACTACATGTTTTTTTTTTTTTTTT 5'	-6.9
P3	hairpin	5' TTTTTTTTTTTTTTTTTGTACGTGACAACTA 3'	-1.4
	self comp.	5' TTTTTTTTTTTTTTTTGT ACGTCACAACTA 3' 3' ATCAACACTGCA TGTTTTTTTTTTTTTTT5'	-9.0
T1	hairpin	5' TAGTTGTGACGTACA 3'	-0.5
	self comp.	5' TAGTTGTGACGT ACA 3' 3' ACA TGCAGTGTTGAT 5'	-5.8
T2	hairpin	5' TAGTTGTGATGTACA 3'	-0.2
	self comp.	5' TAGTTGTGATGTACA 3' 3' ACATGTAGTGTTGAT 5'	-5.4
T3	hairpin	5' TAGTTGTCACGTACA 3'	-0.2
	self comp.	5' TAGTTGTCACGT ACA 3' 3' ACA TGCACTGTTGAT 5'	-5.8

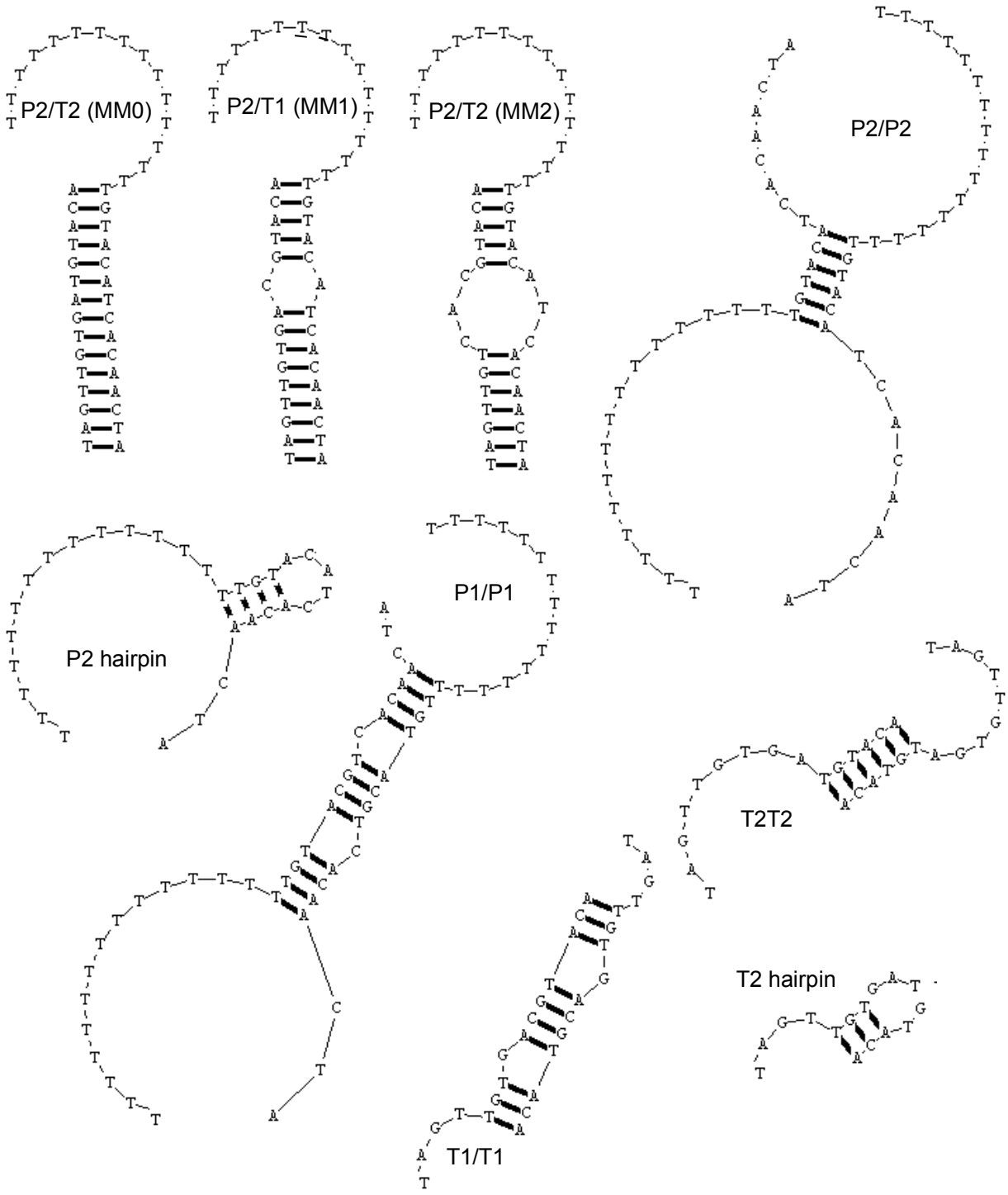

Figure 6.5 : Schematic presentation of some of the probe(P2)-target(T1,T2,T3) duplexes and potential secondary structures that are probable to occur in the oligonucleotides. The shown structures resulted from free energy minimisation calculations based on nearest neighbour thermodynamics and were carried out using software routines described elsewhere [144].

6.3.3 Experimental Results

First the experimental results on the formation of the streptavidin matrix are discussed in this chapter. The characterisation of these layers were described elsewhere, but the streptavidin layer is fundamental for all investigated detection schemes in this study. It seemed reasonable to describe their characterisation by SPS before discussing typical hybridisation kinetics between probes and targets.

Streptavidin Matrix

After the preparation of the gold film on cleaned high refractive index $LaSFN_9$ glass (chapter 3.2), both thiols (Boehringer Mannheim, Germany) were dissolved in PBS buffer in the given ratio to a concentration of $5 \cdot 10^{-4} M$ and applied to the gold surface. During the self assembly process the film thickness of the growing SAM was measured by SPS kinetics. After equilibrium was reached, unspecific bound and bulk material was removed by rinsing the flow cell with analyte free PBS buffer. The obtained optical film thickness was calculated by fitting the SPS scan curves before and after the adsorption process. Streptavidin (Boehringer Mannheim, Germany) was dissolved in PBS buffer to a concentration of $5 \cdot 10^{-6} M$, applied to the prepared thiol surface and was typically allowed to self assemble for about 30 minutes.

In Figure 6.6a typical adsorption kinetics of all individual layers are given. Before and after each adsorption process the surface architecture was characterised by means of thickness determination using the simulation software WINSPALL2.0. The underlying scan curves and the corresponding simulations are depicted in Figure 6.6b and c. The used optical constants and the resulting optical thickness of the layers are summarised in Table 6.3. As seen from the plots, all adsorption steps appeared to be in equilibrium after a time of max. 15 minutes.

Table 6.3 : Optical constants and determined thickness of all layers in the sensor architecture. For the DNA target no thickness increase was observed by SPS.

layer	d /nm +- 0.1 nm	ε′	ε′′
gold	47	-12.380	1.38
thiol	1.6	2.2500	0
streptavidin	4.0	2.1025	0
DNA probe	1.7	1.8903	0

The determined thickness of the thiol and streptavidin layers were 1.6nm and 4.0 nm, respectively and were in agreement with previous studies. By application of the following relation the adsorbed amount A of protein per area can be calculated [102]:

$$A = d \cdot \frac{(n - n_0)}{\partial n / \partial c} \qquad (6.3)$$

with n_0 and n being the refractive index of the solution, respectively, d the measured thickness and $\partial n / \partial c$ being the refractive index increment of the dissolved molecule (streptavidin). The latter was determined by refractometric measurements to be $\partial n / \partial c =$ 0.212g/ml. With the thickness of 4.0nm, n=1.45 and n_0=1.33 the maximal adsorbed mass of $A = 2.0 \cdot 10^7 \, g/ml$ was calculated. This corresponds to an area/protein of 44nm^2. Since x-ray determination of the protein structure lead to an area of 5.6nm x 4.2nm = 23.5nm^2 per protein, a surface coverage of streptavidin in an optimised protein layer can be deduced to be 53%. By ellipsometric measurements of a streptavidin monolayer on a biotinylated lipid interface and in two-dimensional streptavidin crystals a coverage of 65% and 66% was found, respectively. Therefore we have to assume that the streptavidin layer in our architecture is not as highly ordered as in a crystal and that defects in the layer structure are apparent.

In this study we make use of the streptavidin-matrix as supporting layer for measuring binding reactions between probe and target oligonucleotides. In addition to the stable immobilisation of the probe DNA, the use of the streptavidin platform assures that the immobilised probes are diluted on the surface. It is assumed that due to steric constraints only one of two neighbouring binding pockets can be occupied by a biotinylated DNA strand. From the above calculations we can derive a density of one probe strand per 44 nm^2 or a density of $4.2 \cdot 10^{12}$ probes/cm^2. A double-helix can be calculated to occupy 3.1nm^2 on the surface (2nm in diameter). Thus, the obtained dilution is large enough to permit duplex formation. Furthermore, interactions like crowding effects between the probes are reduced by this high lateral dilution of the immobilised oligos on the surface.

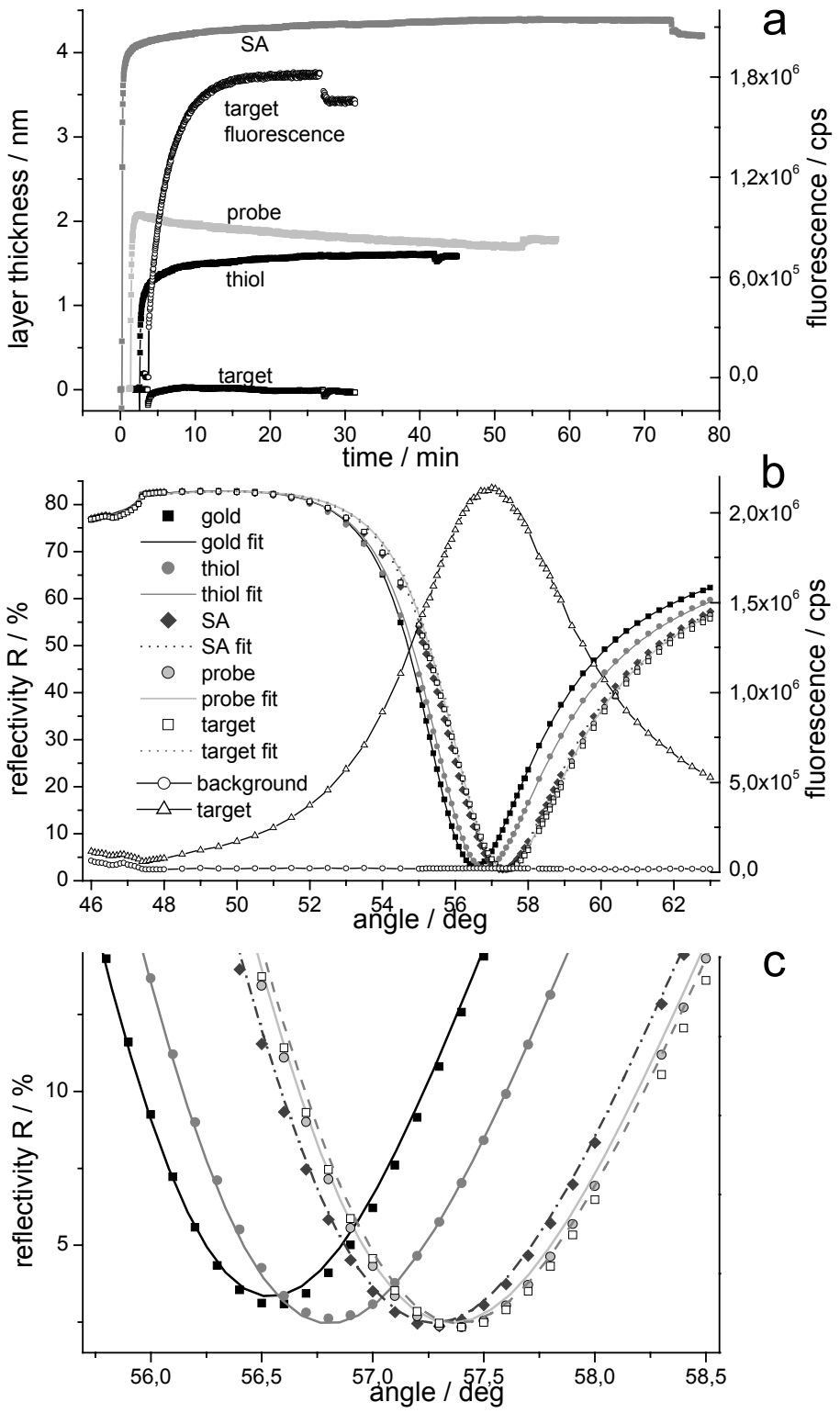

Figure 6.6 : a) Experimental adsorption-kinetics of all immobilised layers and b, c) corresponding scan curves. Note that the hybridisation of the target can be monitored by means of the fluorescence signal while no minimum shift is seen in the SPS resonance curves.

Probe-Target layer

After successful preparation of the streptavidin matrix the probe oligonucleotides were immobilised by adding a $5 \cdot 10^{-6} M$ solution of DNA in PBS buffer to the surface and allowing to sit for 30 minutes. The corresponding adsorption kinetic is given in Figure 6.6a. After rinsing off unspecific bound material the thickness was determined to be 1.7nm by assuming a refractive index of d=1.5 [156]. The thickness of all underlying layers were characterised by the corresponding scan curves in Figure 6.6b and c. The Fresnel simulation and the measured data appeared to be virtually identical. Note that the determined thickness is an optical thickness, which includes the thickness and refractive index of the layer. Furthermore the dilution of the probe on the surface influences this optical thickness. In the B form of a DNA helix, 10 bases occupy a length of 3.4 nm. Hence, in the case of the 30 bases long probe a maximum length of about 10 nm can be expected. The same value was assumed for the probe-target duplex, although it might be smaller due to the flexibility of the single stranded thymine spacer. However, prior to hybridisation the probes are single stranded and the end-to-end distance of the oligonucleotide is not equal to the duplex length. In the case of the random-coiled probe an average value of the 3´end to the streptavidin surface is assumed to be 5 nm (chapter 7). The probes P1-P3 were shown to form hairpins, such that the recognition region of the probe is folded back (Figure 6.5). Due to uncertainties in the actual length of the flexible single stranded thymine spacer a distance of the 3´end to the streptavidin was estimated to be ~5nm, too. The change Δd as depicted in Figure 6.2 was estimated to be 5nm for both probes.

When a $1 \cdot 10^{-6} M$ solution of a MM0 fluorescently labelled target in PBS was applied to the probe loaded sensor surface effectively no change in the SPS kinetic could be detected (Figure 6.6a). No shift in the resonance minimum was observed before and after the hybridisation step as seen in Figure 6.6c. According to this observation common SPS detection was not sensitive enough to monitor the binding event of the target sequence. Accounting for the fact, that the target is only half of the length in bp and mass of the probe, the expected signal change upon maximum hybridisation would be only one half of the obtained SPS signal obtained for the probes. The hybridisation efficiency is assumed to be smaller than 100% for the investigated reaction, which reduces the expected minimum shift even more. It was not possible to detect even a slight signal change and to detect whether hybridisation had occurred by analysing the resonance signal alone. Considering these arguments a hybridisation efficiency of not more than 40% was calculated [47].

However, if the fluorescence signal of the attached fluorescent label was measured by SPFS during the hybridisation step, a fast rise in the fluorescence kinetics was seen and the signal stabilised after about 15 minutes. Rinsing the sample by pure buffer removed bulk fluorophores and led to a small drop in the fluorescence signal as seen in Figure 6.6a. This result demonstrated that the sensitivity of surface plasmon spectroscopy was enhanced by introducing the simultaneous measurement of surface enhanced fluorescence. A relatively high fluorescence signal was obtained by hybridisation of a $1 \cdot 10^{-6} M$ target solution. This permits the detection of target even at small surface coverage as will be shown in the following chapter.

Compared to the small angle independent fluorescence background the fluorescence signal is increased strongly after binding of the fluorescent labelled targets to the surface. As explained before (chapter 2.3.7) the measured fluorescence signal exhibits a maximum near the resonance minimum and follows the calculated electrical field strength at the surface.

The shown results prove that SPFS is a sensitive tool to monitor binding events between immobilised and fluorescent labelled partners under conditions at which label free detection schemes like the investigated SPS are not suitable to sense such marginal changes in optical thickness.

6.4 DNA Hybridisation and Mismatch Discrimination

In this chapter the detection scheme of unlabelled probe/labelled target is evaluated in the used SPFS sensor format. It will be discussed how the secondary structure of probes and targets can influence the discrimination sensitivity in a given set of structured probes and targets. The data set of the structured probes P1-P3 can be found in the literature [114] but so far these results were not discussed on the basis of structural constraints. The results are reviewed now taking into account hairpin stability and thermodynamic considerations. The experimental equilibrium constants of hybridisation reactions with hairpin free probes from this study will be compared with the published results. The conclusions of this discussion will have an impact on the studies in chapter 7 where a novel class of DNA probes is the basis of these investigated probe sequences.

6.4.1 Hybridisation with Hairpin Probes and Targets

After the preparation of the streptavidin matrix biotinylated probe strands were immobilised and the hybridisation reaction to targets could be monitored by SPFS. First the results for the probe sequence P2 are discussed. Then the results are compared to the probes P1 an P3

Hybridisation of the Hairpin Probe P2 with T1-T3

In Figure 6.7 fluorescence kinetics of hybridisation reactions of probe P2 with fully complementary (T2=MM0) and mismatched targets (T1=MM1, T2=MM2) at a target concentration of $1 \cdot 10^{-6} M$ are shown[17]. The adsorption and desorption steps in all cases were fitted by simple Langmuir simulations according to chapter 2.2. The visually apparent differences between the individual targets of different complementary are described as follows: In the case of MM0 a fast rise is seen upon injection of the fluorescent labelled target, resulting in a constant stable signal. Constant flow rinsing of the flow cell at 1ml/min with analyte free PBS buffer barely altered the fluorescence signal, indicative of a small desorption constant. When the same experiment was repeated with a MM1 target a similar signal strength was reached in the adsorption process. However, upon rinsing the signal decreased until the starting value close to the fluorescence background was reached after several hours. Finally, the MM2 target caused only a slight increase in fluorescence and the subsequent exchange with pure buffer resulted in a stepwise drop to the fluorescence background signal.

These findings are reflected by the kinetic constants in Table 6.6: while the association constant k_{on} decreases with increasing number of mismatches, the dissociation constant k_{off} increases. The equilibrium constant K=kon/koff is reduced upon introduction of each mismatch and reaches over several orders of magnitude. According to the Langmuir picture, the observed kinetics can be explained by considering the half saturation concentration c=1/K at which 50% of the surface is occupied with the binding species.. These values are $2 \cdot 10^{-10} M$ for MM0, $4 \cdot 10^{-8} M$ for MM1 and $1 \cdot 10^{-4} M$ for MM2. Performing the hybridisation reaction at a working concentration of $1 \cdot 10^{-6} M$ results in high surface saturation for MM0 and MM1, while the applied concentration is not sufficient to bind the MM2 targets. If the flow cell is rinsed by pure buffer, the target concentration in the cell is reduced by at least two orders of magnitude. Hence, the concentration in the cell falls under the half saturation constant for MM1 and material is desorbed from the surface. However, in the fully complementary case the new concentration is still above this limit and the equilibrium is still on the side of the surface bound targets. Note,

that if the target concentration in the cell would be reduced to zero (which is technically difficult for the given geometric flow cell set-up) also the fully complementary targets would desorb, but very slowly.

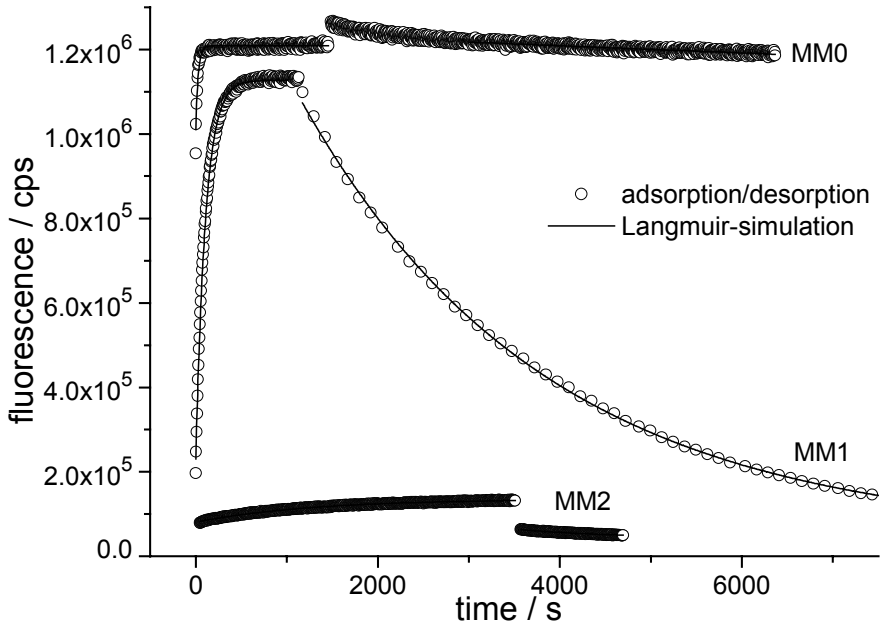

Figure 6.7 : Hybridisation kinetics (circles) of probe P2 with targets T1(MM1), T2(MM0) and T3(MM2)at a target concentration of 1uM together with the corresponding Langmuir-simulations (lines). Note, that upon rinsing with analyte free PBS buffer MM1 can be desorbed while the MM0 duplex is stable. In the case of MM2 barely no hybridisation is detectable. Data were taken from literature with the permission of the author [17].

From the thermodynamic point of view the introduction of mismatches into a fully complementary double strand corresponds to an energetic penalty, likely to destabilise the duplex. In the case of long sequences the influence of a single mismatch becomes negligible, but on the level of 15 base long strands an exchange of one base has a considerable effect. For DNA sequences it is known as a rule of thumb that 1% of mismatched base pairs causes a drop in the melting temperature of the duplex of 1°C. Thus, at a given reaction temperature targets of different complementary can be distinguished. The sensitivity of a system (at a particular temperature) is given by the difference in the melting curves of the fully complementary and the mismatched target. More simply the mismatch sensitivity is the greatest in the region of the melting temperatures of both targets, while extreme reaction temperatures will cause an 'all or none' situation and the discrimination sensitivity is lost.

Hybridisation of the Hairpin Probes P1 and P3 with T1-T3

The experimental results for the probe P2 are explained by the Langmuir picture and a discrimination between MM0, MM1 and MM2 targets was possible under the given reaction conditions (T=25°C, target concentration $1 \cdot 10^{-6} M$). However, the analogous datasets derived from experiments with the probes P1 and P3 were not as consistent with the unperturbed binding model as in the case of P2. The literature values for the equilibrium constants of both probes hybridised with the targets T1-T3 can be found in Table 6.6. Between P2, P1 and P3 only one and two bases were different (Table 6.1), respectively. However, the mismatch discrimination ability changed drastically compared to P2. In the case of P1 little difference is seen between MM0 and MM1 (note that in this combination no MM2 can occur). With P3 fully complementary targets still exhibit a larger equilibrium constant than MM1, but the latter case exhibits no difference to MM2.

6.4.2 Hybridisation With Hairpin Free Probes and Targets

The formation of secondary structures like hairpins and self annealing of complementary sequences is known to influence the hybridisation kinetics and the resulting equilibrium constants. In order to investigate the influence of such structural constraints hybridisation experiments were performed with the probe sequence PHF and the targets THF1 and THF2. These oligonucleotides were designed to be free of secondary structures and cannot form self annealing complexes.

The equilibrium constants of the PHF hybridisation with THF1 (MM0) and THF2 (MM1) were determined experimentally by recording the Langmuir isotherm as explained in chapter 2.2. The surface was saturated stepwise and the resulting equilibrium values were fitted using a steady-state solution of the Langmuir equation (equation (2.18)). In Figure 6.8 the measurements for the MM0 case are shown together with the Langmuir-simulation. It should be emphasised that all individual saturation steps and the rinsing step in Figure 6.8 (top) were fitted using the same $k_{on} = 2.2 \cdot 10^{4} M^{-1} s^{-1}$ and $k_{off} = 3.5 \cdot 10^{-4} M^{-1} s^{-1}$ values. However, the step at 0.05 µM deviated from the simulated curve if these k_{on} and k_{off} constants were used. This is likely to be the result of mass transfer effects and diffusion controlled delivery of the target to the surface. This led to a reaction slower than predicted. The same arguments hold for the measurements in Figure 6.9.

The equilibrium constant for the MM0 case was calculated to $K = k_{on} / k_{off} = 6.3 \cdot 10^{7} M^{-1}$. This value was identical to the one obtained by analysing the Langmuir isotherm in the steady state model (bottom). The same analysis was performed for the MM1 case in Figure 6.9.

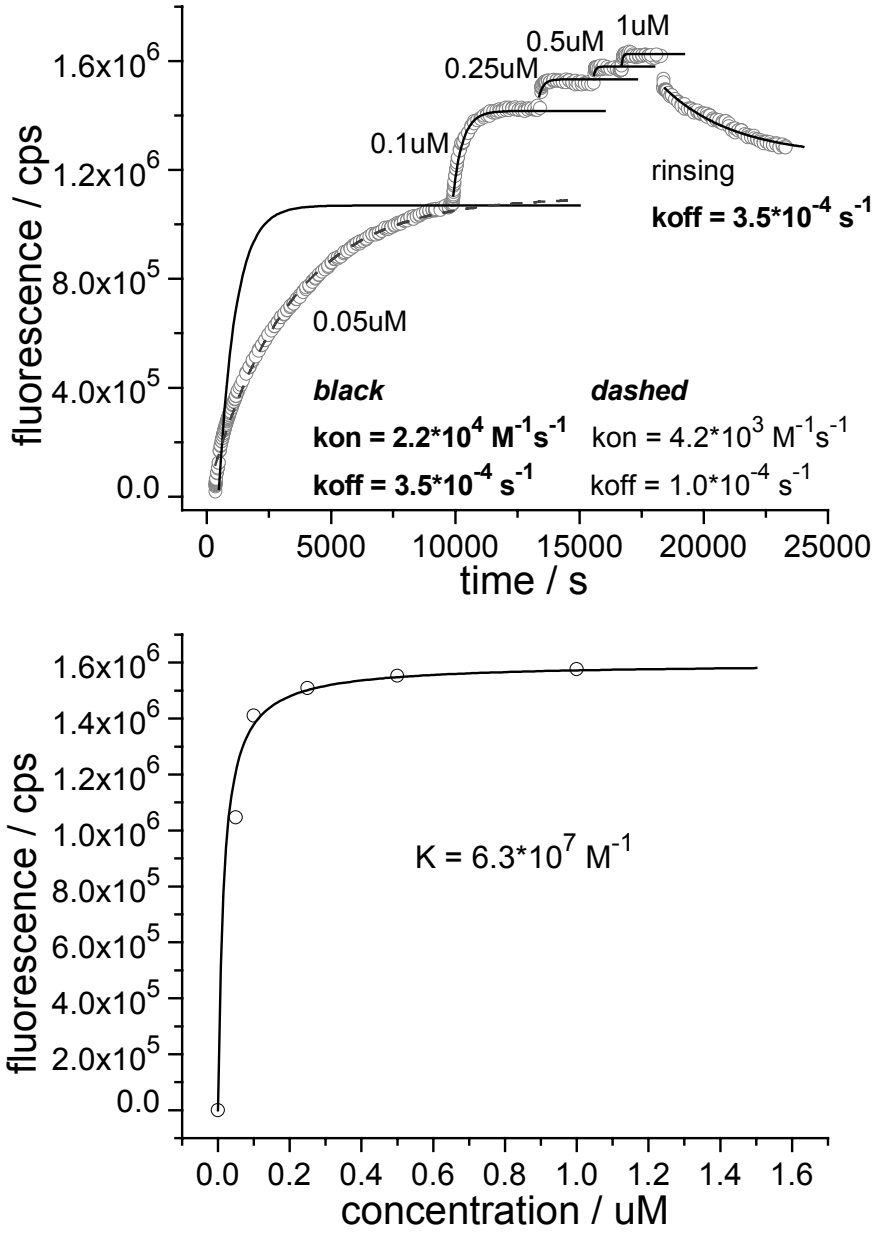

Figure 6.8 : Langmuir-isotherm of the hairpin free MM0 system PHF/THF. Top: The surface was saturated stepwise by injecting increasing target concentrations (circles) and the kinetics were simulated by a Langmuir model (line) . Note that all individual kinetics could be fitted with the same set of kinetic constants ($k_{on} = 2.2 \cdot 10^4 M^{-1}s^{-1}, k_{off} = 3.5 \cdot 10^{-4} s^{-1}$) except for the 0.05 uM step for which a satisfactory simulation could only be reached by applying an other set of parameters (dashed curve). The equilibrium constant $K = 6.3 \cdot 10^7 M^{-1}$ that could be derived from the kinetic constants (kon/koff) is identical to the equilibrium constant that was calculated by fitting the individual equilibrium values with a stationary Langmuir-isotherm (bottom).

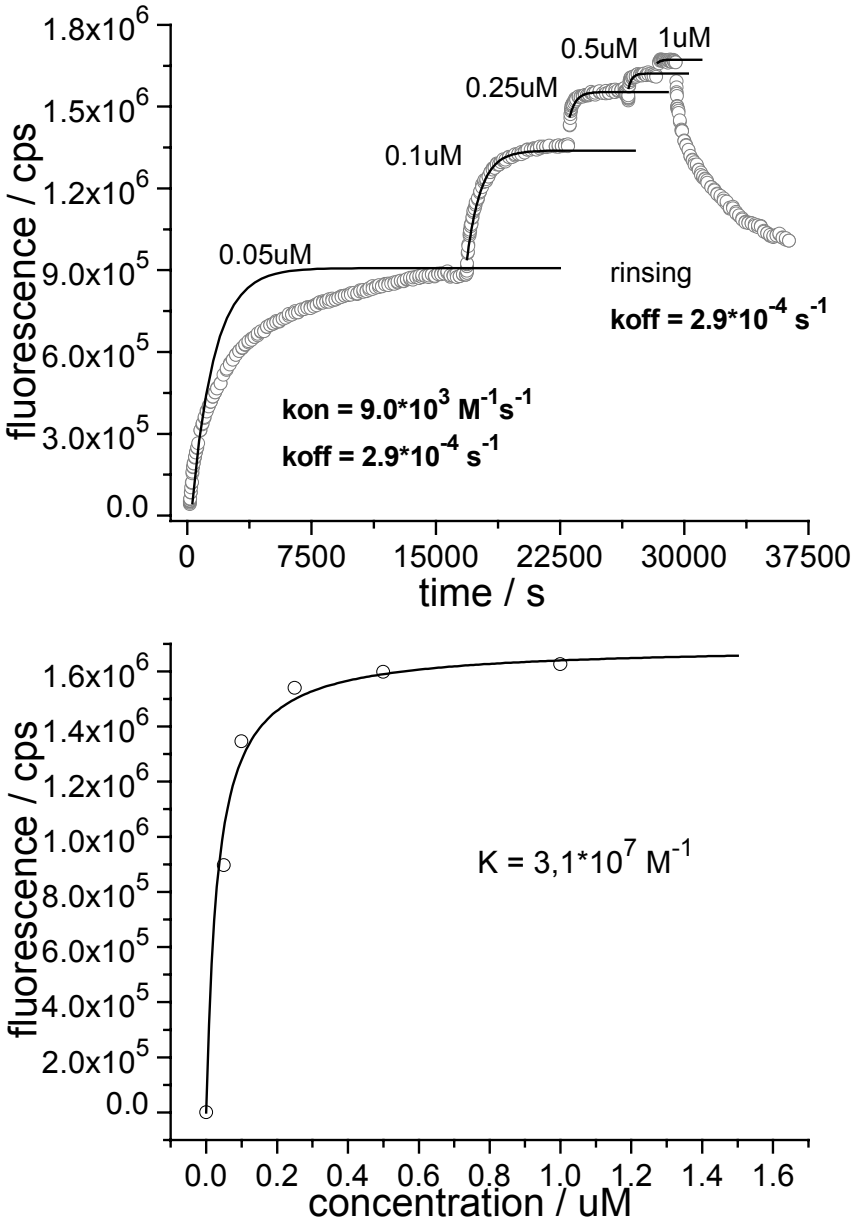

Figure 6.9 : Langmuir-isotherm of the hairpin free MM1 system PHF/THF2. Top: The surface was saturated stepwise by injecting increasing target concentrations (circles) and the kinetics were simulated by a Langmuir model (line). All individual kinetics could be fitted with the same set of kinetic constants ($k_{on} = 9.0 \cdot 10^3 M^{-1}s^{-1}, k_{off} = 2.9 \cdot 10^{-4} s^{-1}$) except for the 0.05 uM step. The equilibrium constant was calculated to be $K = 3.1 \cdot 10^7 M^{-1}$ (=kon/koff) and was identical to the one determined by fitting the individual equilibrium values (bottom).

A comparison of the determined equilibrium constants in Table 6.6 revealed only a slight difference between the complementary THF1 and the mismatched target THF2. The constants k_{on} for both cases appeared similar to those for MM0 and MM1 of P2, respectively. The k_{off} constants in PHF both equal the P2-MM1 case and so do the equilibrium constant.

6.4.3 Discussion

In Table 6.6 the experimental kinetic constants for the hairpin free probe PHF are compared with those published for the hairpin probe P1-P3. The mismatch sensitivity of all probes is discussed in the following: According to the equilibrium constants K, the probe sequence P2 shows the best mismatch discrimination. The K values for MM0, MM1 and MM2 differ by several orders of magnitude and permit the mismatch discrimination under the applied experimental conditions. For P1 no difference is observed between MM0 and MM1, while P3 did not differentiate between MM1 and MM2.

First consider the nature of mismatches (CG, AT) in these cases. A broken GC pair (3 hydrogen bonds) destabilises the duplex more than an A or T mismatch (2 hydrogen bonds) due the reduction in hydrogen bonds. All duplexes have the same length of 15bp. Therefore the change in the net number of cleft hydrogen bonds for all mismatch situations can be compared (Table 6.4). This simple consideration did not explain the lack in mismatch discrimination sensitivity. For all probes a destabilisation of the duplex was predicted that should be sufficient to permit the mismatch discrimination.

Table 6.4 : Comparison of the net number of hydrogen bonds broken in the transition from fully complementary to mismatched targets. For G and C mismatches the number of hydrogen bonds in the duplex are reduced by 3, for A and T only 2.

	MM0	**MM1**	**MM2**
P1	0	GT: **3**; CC : **3**	---
P2	0	AC : **2**	AC + CC : **5**
P3	0	GG : **3**	GT + GG : **6**
PHF	0	AA : **2**	---

Secondary Structures and Thermodynamic Constraints

The destabilisation of a helix by a mismatch is dependent on the neighbouring base pairs along the strand. The thermodynamic stability of complementary and mismatched sequences can be considered using the nearest-neighbour model [157-159].

In Table 6.6 the kinetic constants for the probes P1-P3 and the hairpin free oligonucleotides PHF and THF are summarised. To compare the experimental constants with simulated data the free energy ΔG_{exp} was calculated using (6.2). For comparison, free energies ΔG_{sim} were simulated for every duplex by considering nearest neighbour interactions [142] using a freely

available software routine [160] [161]. The software was capable of considering salt effects, dangling ends, mismatches and temperature effects. Thus, the given dataset ΔG_{sim} was calculated for the temperature T=25°C and a salt concentration c(Na^+)=0.16M (=PBS).

Secondary structures in the sequences can compete with the hybridisation between probe and target and alter the observed equilibrium constants. These structures are (compare Figure 6.5):

- self annealed probes
- self annealed targets
- hairpin in the probe
- hairpin in the target

In order to evaluate the influence of these structures, ΔG values for all sequences were simulated (Table 6.5). The loop sequence in hairpins can influence the stability of the entire structure. However, only a slight difference in ΔG_{hair} was found for the hairpins of probes P1-P3. The stability of the hairpin structures in between the set of targets T1-T3 was found to be slightly different. Furthermore, moderate differences in the free energies for self annealed complexes ΔG_{self} in one set of oligonucleotides were calculated.

The complexes between biotinylated immobilised and dissolved probes (probe-probe) can be neglected here. Probes, which are not bound by the streptavidin, are removed due to rinsing with pure buffer. These structures are hence not interfering in the subsequent hybridisation step. The formation of probe/probe complexes on the surface with are dissociating due to competitive formation of a probe/target complex upon hybridisation are not likely, due to the following considerations: in chapter 7 analogous experiments with labelled probe/unlabelled targets were performed. A replacement of loosely bound labelled probes by the hybridising unlabelled target would have caused a decrease in the fluorescence signal. This effect was not observed.

Table 6.5 : Calculated free energy ΔG_{hair} and ΔG_{self} in kcal/mol for secondary structures such as hairpins and self annealing structures in the probes P1-P3 and targets T1-T3. The sequences PHF and THF1-2 exhibited no secondary structures.

	P1	**P2**	**P3**	**T1**	**T2**	**T3**	**PHF**	**THF**	**THF**
ΔG_{hair} / kcal/mol	-1.3	-1.3	-1.4	-0.5	-0.2	-0.2	--	--	--
ΔG_{self} / kcal/mol	(-8)	(-6.9)	(-8)	-5.8	-5.4	-5.8	--	--	--

In order to account for the competing effect by hairpin structures in probe and target the simulated free energy ΔG_{sim} was corrected in ΔG_{hp}. Additionally the self annealed target structures were taken into account in ΔG_{tsa}:

$$\Delta G_{hp}=\Delta G_{sim}-\Delta G_{hair} \;; \quad \Delta G_{tsa}=\Delta G_{sim}-\Delta G_{hair}-\Delta G_{self} \qquad (6.4)$$

Table 6.6 : Kinetic constants for the hybridisation between P1-P3 and T1-T3 and the hairpin-free sequences PHF and THF1-THF2. Experimental data for P1-P3 are literature values [47] while data for PHF were determined in chapter 6.4.2. The experimental free energies ΔG_{exp} are compared to the simulated values ΔG_{exp}. ΔG_{hp} and ΔG_{tsa} were corrected for hairpin formation and target self annealing, respectively. All values were determined for T=25°C, PBS buffer.

probe	target	mm	k_{on} / $M^{-1}s^{-1}$	k_{off} / s^{-1}	K / M^{-1}	ΔG exp kcal/mol	ΔG sim kcal/mol	ΔG hp kcal/mol	ΔG tsa kcal/mol
P1	T1	0	$1.26\cdot10^{4}$	$0.014\cdot10^{-3}$	$9.0\cdot10^{8}$	**-12.01**	-17.17	-15.26	-10.39
	T2	1	$3.29\cdot10^{4}$	$0.034\cdot10^{-3}$	$9.6\cdot10^{8}$	**-12.04**	-13.60	-11.88	-7.21
	T3	1	$2.01\cdot10^{4}$	$0.125\cdot10^{-3}$	$1.6\cdot10^{8}$	**-11.00**	-11.38	-9.66	-4.60
P2	T2	0	$3.69\cdot10^{4}$	$0.007\cdot10^{-3}$	$5.3\cdot10^{9}$	**-13.04**	-15.81	-14.09	-9.41
	T1	1	$8.94\cdot10^{3}$	$0.370\cdot10^{-3}$	$2.4\cdot10^{7}$	**-9.89**	-11.22	-9.32	-4.41
	T3	2	$1.0\cdot10^{1}$	$0.770\cdot10^{-3}$	$1.3\cdot10^{4}$	**-5.51**	-5.44	-3.72	+1.34
P3	T3	0	$1.05\cdot10^{4}$	$0.008\cdot10^{-3}$	$1.3\cdot10^{9}$	**-12.21**	-17.17	-15.36	-10.30
	T1	1	$1.43\cdot10^{4}$	$0.370\cdot10^{-3}$	$3.9\cdot10^{6}$	**-8.84**	-12.91	-10.92	-6.04
	T2	2	$1.05\cdot10^{4}$	$0.440\cdot10^{-3}$	$2.6\cdot10^{6}$	**-8.60**	-9.35	-7.54	-2.86
PHF	THF1	0	$2{,}2\cdot10^{4}$	$0.350\cdot10^{-3}$	$6.3\cdot10^{7}$	**-10.43**	-15.4		
	THF2	1	$9\cdot10^{3}$	$0.290\cdot10^{-3}$	$3.1\cdot10^{7}$	**-10.05**	-11.8		

Mismatch Discrimination of Hairpin Probe P2

The comparison between the experimental free energy ΔG_{exp}(-13.04, -9.89, -5.51 kcal/mol) and the simulation ΔG_{hp} (-15.81, -11.22, -5.44 kcal/mol) in Table 6.6 reveals good agreement for all targets. The introduction of self annealed target in ΔG_{tsa} led to simulated values smaller than the experimental ones. Considering hairpin formation in ΔG_{hp} did not alter the relative energetic difference between MM0, MM1 and MM2. This results from the fact, that ΔG_{hair} is very similar

in one set of oligonucleotides. Summarising, the experimentally mismatch discrimination for P2 was in good agreement with the predicted discrimination sensitivity at this temperature.

Mismatch Discrimination of Hairpin Probes P1 and P3

The distance between the simulated thermodynamic values for duplexes between P3 and T1-T3 is large enough to allow for a discrimination of all three cases (ΔG_{sim}=-17.17; -12.91; -9.35 kcal/mol). Taking into account hairpin formation and self annealing in ΔG_{hp} and ΔG_{tsa} did not alter this relation. The experimental values for ΔG_{exp} confirm a discrimination between complementary (−12.21kcal/mol) and single mismatched targets (-8.84 kcal/mol). However, no difference was observed to the MM2 case (-8.60 kcal/mol). Also in the case of P1 a deviation of the experimental from the simulated values was found. No distinction could be made between MM0 (ΔG_{exp}=-12.04) and MM1 (ΔG_{exp}=-12.01; 11.0kcal/mol) although the energetic differences in ΔG_{sim}, ΔG_{hp} and ΔG_{tsa} predicted a clear difference between these cases.

As discussed above an enhanced discrimination ability is expected for probes that can form secondary structures like hairpins[152,153]. Generally, the free energy ΔG_{sim} for duplex formation from the random coiled state is reduced if competition of secondary structures is taken into account. (compare to ΔG_{hp} ΔG_{tsa} in Table 6.6). All probes and targets were found to be capable of forming hairpins of the same secondary structure. (Figure 6.5, Table 6.2). The mismatched bases could be found in the loop part of the hairpin. The relative stability of such hairpins is dependent on the loop sequence [150]. However, the calculated energetic differences ΔG_{hair} (probes: -1.3; -1.3; -1.4 kcal/mol, targets:-0.5; -0.2; -0.2 kcal/mol) and ΔG_{self} (-5.8; -5.4; -5.8 kcal/mol) in one set of secondary structures (like probe hairpins) was small compared to the absolute ΔG_{sim} values in Table 6.6. Accounting for secondary structures did not alter the simulated discrimination ability of the systems and could not explain the lack in experimental mismatch sensitivity for P1 and P3.

Mismatch Discrimination of Hairpin Free Probe PHF

For the hairpin probe P2 a difference of several orders of magnitude between the equilibrium constants for MM0 and MM1 was measured. Such a difference was not experimentally found for the random oligonnucleotides PHF and THF. As described in 6.4.2, only a slight difference was observed in the experimental equilibrium constants for duplex formation with the complementary target THF1 ($K = 6.3 \cdot 10^7 M^{-1}$, ΔG_{exp}=-10.43 kcal/mol) and mismatched target

THF2 ($K = 3.1 \cdot 10^7 M^{-1}$, ΔG_{exp}=-10.05 kcal/mol). The free energies for duplex formation ΔG_{exp} were comparable to the values found for MM1 in P2 (ΔG_{exp}=-9.9 kcal/mol).

PHF and P2 are similar in the sequence and identical in the G+C content. Therefore the absolute simulated ΔG_{sim} values for MM1 (PHF:-15.4, P2: -15.81 kcal/mol) and MM0 (PHF: -11.8, P2: -11.22 kcal/mol) are similar, too. These values predict a substantial mismatch discrimination for both PHF and P2, but this behaviour was only confirmed for the probe containing hairpins. From this it has to be concluded, that indeed the competing secondary structure in the probe P2 was partially responsible for the mismatch discrimination at the used experimental conditions (room temperature, PBS).

The simulated thermodynamic values ΔG_{sim} and the corrected values $\Delta G_{hp}$and ΔG_{tsa} were calculated on the basis of reactions in solution. The absolute simulated values may differ for surface based reaction that were investigated here. On the surface, additional steric hindrance effects such as crowding of the probes and interaction with the streptavidin matrix may influence the equilibrium constant. For instance, the immobilisation of one DNA terminus may alter the change in entropy upon duplex formation compared to the reaction in solution. On the other hand the probe sequences are very similar in length and structure. These surface factors are assumed to alter the conditions for all probes to the same extent. This consideration justified the above discussion of surface reactions on the basis of solution based constants.

6.5 Conclusion

In this chapter the detection of DNA hybridisation on sensor surfaces using Surface Plasmon Fluorescence Spectroscopy (SPFS) was discussed. The applied detection format exploited the specific recognition between immobilised unlabelled probe sequences and fluorescent labelled target sequences.

The investigated sensor architecture was characterised on the base of Surface Plasmon Spectroscopy measurements. A metal surface was modified with a SAM of biotinylated thiols in order to form a streptavidin layer. This was used as a binding matrix for the biotinylated probe sequences. Due to the distance between the streptavidin binding pockets the probe sequences were laterally diluted on the surface and steric interactions between the probes were thus reduced. Furthermore the protein layer separated the probes from the metal surface, which reduced losses in the fluorescence signal due to quenching by the gold.

Due to the small mass of the targets and the hybridisation efficiency below unity, Surface Plasmon Spectroscopy was not sensitive enough to monitor the hybridisation event. Contrastingly, the binding of the labelled targets could easily be monitored by measuring the fluorescence signal using SPFS. The sensitivity of SPS was thus enhanced by introducing simultaneous fluorescence detection.

Already published results from Liebermann were compared with experimental results obtained in this study. In particular, the mismatch discrimination sensitivity of hairpin and random coiled probe sequences was investigated. On basis of experimental and simulated thermodynamic quantities the competing influence of secondary structures in the probe was discussed. For the probe P2 the reported good mismatch discrimination was in agreement with the carried out simulations. These results were compared to a probe sequence (PHF) free of secondary structures. This hairpin free sequence was not capable of discriminating between fully complementary and mismatched targets. The enhanced sensitivity of P2 was at least partially attributed to the presence of the hairpin in the probe structure.

Further probes P1 and P3 were investigated in previous studies. Although the probe sequences were similar to P2, a lack in mismatch sensitivity was reported for these sequences. In this study the published results were discussed on the basis of their thermodynamic properties. The influence of the hairpin stability in these probes was analysed. The stability of the secondary structures in probes P1-P3 were found to be similar and thus not be responsible for the differing mismatch sensitivity in the group of hairpin probes P1-P3.

No straight forward solution to the discrimination problem in P1 and P3 could be provided by comparing experimental and simulated thermodynamic quantities. The experimental values for ΔG_{exp} were obtained from experimental Langmuir isotherms at room temperature. It is recommended to determine the thermodynamic parameters of all probe and target combinations by alternative methods. Measuring the melting curves of all duplexes can help to elucidate the differences in mismatch discrimination sensitivity. As pointed out before the reaction temperature influences the hybridisation efficiency strongly. Thus, an increase in temperature may cause a better discrimination also for probes P1 and P3.

The probe sequence P2 showed the best mismatch discrimination. The development of the novel labelled probes in the next chapters will be hence based on this sequence.

7 A Novel Detection Scheme for Unlabelled Targets Based on Structural Changes in the Probe

During the past years strong efforts have been made to investigate the behaviour of DNA on surfaces and consequently to develop new techniques that are capable of detecting DNA with high specificity at even small analyte concentrations. Frequently, fluorescence techniques are used for this purpose and a variety of assays have been developed so far [162]. By including fluorescence formats the detection limit and the sensitivity of optical methods like Surface Plasmon Spectroscopy can be improved[16,17]. Most, if not all nucleic acid detection schemes are designed as sandwich formats. In a common strategy, fluorescently labelled analyte DNA targets are detected by monitoring their fluorescence upon hybridisation to surface immobilized unlabelled probes. Alternative transduction mechanisms include intercalating agents (like ethidium bromide) that bind preferentially to double-stranded DNA. However, these dyes are often hazardous. Others formats make use of competitive binding assays in which fluorescent nucleotides are replaced by unlabelled analytes[13]. In spite of the multiple advantages of fluorescence detection several researchers are currently studying the possibilities of label-free detection in order to avoid the time consuming and expensive attachment of fluorescent labels to the analyte DNA. As mentioned in chapter 6 a variety of different techniques were developed which are sensitive to optical, electrical or mechanical changes of a sensor surface. Unmodified analytes can be detected by the device (e.g. DNA arrays) without further modification. However, these techniques often lack sensitivity and cannot replace the well established fluorescent techniques, yet. Thus, there is a need for novel detection schemes, which are capable of detecting unlabelled targets with high sensitivity.

7.1 Introduction

The aim of this study is the development of a new detection scheme that combines the benefits of fluorescence detection on surfaces with the opportunity of sensing unlabelled DNA targets. One approach based on the design of a novel class of oligonucleotide probes was reported[154,163] [164]. Molecular beacons can sense the presence of unlabelled targets in homogenous solutions by switching from a quenched to a fluorescent state. The probes consist of a double stranded stem part that is formed by intra-molecular hybridisation of complementary

parts in the probe and of a loop part. The latter contains the actual recognition sequence and is hence complementary to the target sequence. Either ends of the molecular beacon are labelled with a fluorophore and quencher, respectively, such as to quench the fluorescence in the hairpin state. Upon hybridisation with the target the hairpin opens up and the dye is separated from the quencher, leading to a recovery of the fluorescence. This concept was then adapted to surface sensitive fluorescence detection by immobilising the molecular beacon onto a fibre optical evanescent wave sensor [164,165]. Despite of the advantages of such probes, the probe synthesis includes three different modifications and is thus time consuming and expensive. The position of the biotin-anchor in the probe sequence and the choice of appropriate fluorophores complicate the design of the probes.

It this study a novel fluorescence detection strategy is presented, which is based on conformational changes of a fluorescently labelled probe sequence upon hybridisation with the unlabelled target. These novel probes are investigated by surface plasmon enhanced fluorescence spectroscopy (SPFS) on metallic substrates. The mismatch discrimination ability of this novel probes is investigated and factors that influence the fluorescence of the probes are discussed.

It is well known that double stranded DNA may exhibit a helix like structure with characteristic properties. The diameter of B-DNA, a predominant form of DNA helix, exhibits a diameter of 2 nm and one helical turn of 10 nucleotides 3,4 nm in length (see chapter 6.1). The stiff double stranded helix differs from a single strand of the same length (in bases) in its flexibility. The persistence length characterises the distance along the DNA backbone over which a strand behaves as a rigid rod. This length was determined to be ~1.0 nm for single stranded DNA[166] but is much longer for dsDNA [167]. In case of the investigated 15 bases long recognition sequences the contour length of the strands is much smaller (5.1 nm) than this persistence length, so that they are considered as rigid cylinders. Studies have shown that the sugar-phosphate backbone appears to be more conformationally flexible than usually expected [168] and that the elastic properties of dsDNA and ssDNA are sequence dependent [169,170]. Furthermore the flexibility and curvature of duplexes was found to be dependent on the presence of mismatches in the helix[171]. However, compared to the flexible random-coil structure of single stranded DNA, helical structures in duplexes can be regarded as stiff rods. Therefore the end-to-end distance in an oligonucleotide probe is increased if the transition between the random coil and the helix is made by formation of the duplex.

Neutron reflectivity studies of DNA monolayers on gold have indicated that hybridisation of immobilised probes leads to double strands that tend to prefer an orientation towards the surface normal after hybridisation [172]. A loose helix-like but flexible structure is assumed in the single stranded state. An increase of the distance between the free terminus of the probe and the surface is seen upon hybridisation. As discussed in chapter 4 the fluorescence of dyes in close proximity to metal surfaces is influenced by the distance dependent quenching profile. Thus, one can exploit the "standing-up" effect of the probe during hybridisation by labelling the probe strand at the free end. Any change in the metal-dye distance can then be followed by measuring the relative fluorescence. An increase in fluorescence indicates reduced quenching due to the formation of the helix and can thus be used to sense hybridisation events at metallic surfaces.

7.2 Probe Sequences

7.2.1 Probe Design

Principally two alternative ways of immobilising DNA probes are frequently used: many reported studies utilise covalent linkage in form of thiol-tethered probe strands immobilised on gold substrates. In this study the well established alternative coupling via the strong interaction between 5' biotinylated strands and streptavidin surfaces is preferred. The preparation and characterisation of the underlying streptavidin matrix was already discussed in chapter 6.3. The used probe and target sequences are introduced in the following:

In Table 7.1 the investigated probe sequences are summarised. In analogy to chapter 6.3.2 the probe sequences were biotinylated at the 5´end in order to be immobilised on the streptavidin matrix. They exhibited a spacer unit consisting of 15 thymine residues. This unit separates the recognition sequence from the surface and increases the hybridisation efficiency by reducing steric hindrances during the hybridisation. In order to investigate the influence of the initial distance of the recognition sequences from the gold, two spacers of differing length (T_{15} and T_{30}) were used. The fluorescence yield may be increased due to the increased distance in the case of the T_{30} spacer. On the other hand, only a third of the BioCy5T30 probe sequence will exhibit a rod like structure after hybridisation. The still flexible spacer unit may reduce the expected fluorescence increase due to the 'standing up' effect.

The actual recognition sequence in BioCy5T15 and BioCy5T30 was the probe sequence P2 from chapter 6.3.2 which allowed for the best mismatch discrimination. In contrast to the usual "unlabelled probe/labelled target"-scheme all probe sequences were Cy5 labelled on the 3´end.

The oligonucleotide sequences were modified with an amino-group at the 3' terminus followed by a coupling step with NHS active-ester bound Cy5 (CY5 mono functional dye pack, Amersham Pharmacia). These reactions were carried out by the provider of the oligonucleotide sequences (MWG Biotech, Germany).

It was pointed out before that the probe sequences P1-P3 can form secondary structures such as hairpins, which may influence the hybridisation kinetics and the mismatch sensitivity. Thus, the hairpin free sequence PHF was investigated additionally in a 3' labelled form in sequence BioCy5HF in order to investigate the effect of secondary structures in the probe. The signal change in these experiments is based on the dye/surfaces distance and hence depends on the initial distance d_1 in Figure 7.1. The cartoon shows the expected conformational change of the probes upon hybridisation. Both, the random coil sequence BioCy5HF (a) and the hairpin probe BioCy515 (b) will form a 15 base long double helix with the unlabelled target. The duplex is then connected to the streptavidin layer via the biotinylated spacer unit (T15 or T30). The conformational change in the probes causes the dye to be stretched out into surrounding medium by the distance Δd. Hence a change in the fluorescence signal is expected due to reduced quenching by the gold.

The labelled probe sequences were used in hybridisation experiments with unlabelled targets, the sequences of which were adapted from T1-T3 and THF1-THF2 in chapter 6.3.2.

Table 7.1 : Sequences of the Cy5 labelled probes

name	bases	sequence
BioCy5T15	30	5´-*Biotin* -T_{15} TGT ACA TCA CAA CTA - *Cy5*-3´
BioCy5T30	45	5´-*Biotin* -T_{30} TGT ACA TCA CAA CTA - *Cy5*-3´
BioCy5HF	30	5´-*Biotin* -T_{15} TGT ATC TCA GTT CTA - *Cy5*-3´

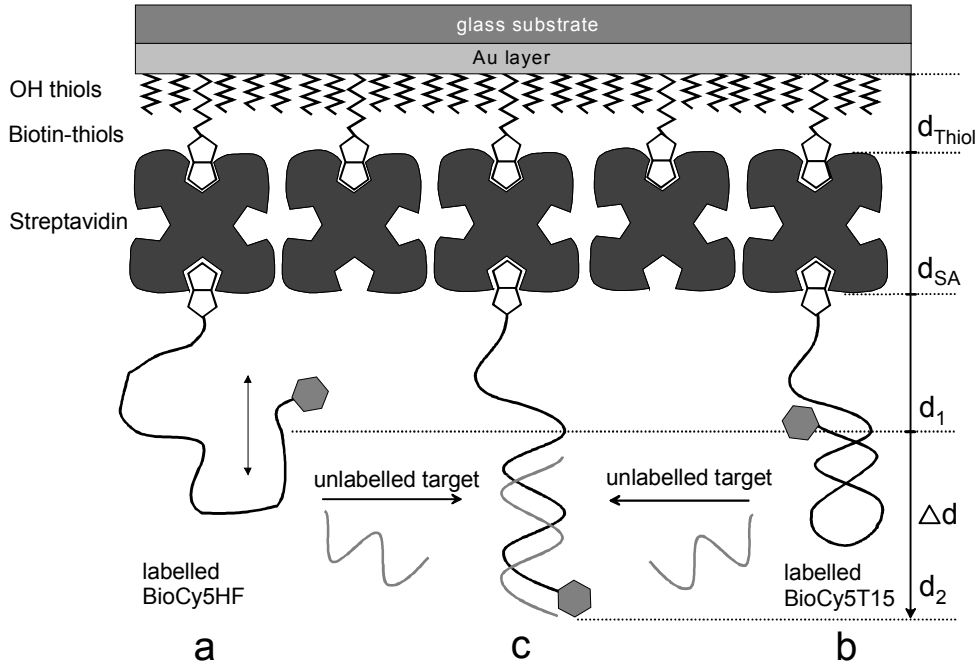

Figure 7.1 : Conformational change of the biotinylated Cy5 labelled probes upon binding of the unlabelled target and formation of a stiff helical structure in the duplex (c). Consequently, the distance of the bound dye to the metal surface is altered by Δd. As a result a change in the fluorescence intensity is seen due to reduced quenching by the metal. Note, that the probe BioCy5T15 exhibits a hairpin, while BioCy5HF is free of secondary structures. The probes differ in the initial conformation, but the final distance d_2 in the duplex is the same for both probes.

7.2.2 Photobleaching

In order to build the layer system

Au/thiols/streptavidin/Cy5 labelled probe sequence (7.1)

the streptavidin matrix was prepared as explained in chapter 6.3. Subsequent immobilisation of BioCY5probeT15 from a 1 uM solution onto the streptavidin matrix (Figure 7.1) led to a strong initial fluorescence as observed by SPFS. The signal was then starting to decrease immediately due to photo bleaching of the surface bound fluorophore. The extent of bleaching could be minimised in the following experiments by blocking the incident laser by the automated shutter system described in chapter 3.1.2 (Figure 7.2). Furthermore the laser power was reduced to avoid photo bleaching and to allow for measurements in the linear range of the photo multiplier system (up to $2 \cdot 10^6$ cps). As a compromise between the number of available data points and the reduction of photo bleaching, the period of data acquisition was chosen to be 1-3 minutes if not mentioned otherwise. When the laser intensity was reduced a decrease of the signal-to-noise-ratio was found but was considered to be acceptable.

Interestingly, the strong bleaching effect was not found in the case of experiments in chapter 6.4. There, Cy5 labelled targets were bound to the surface by hybridisation to immobilised unlabelled probes in the layer system:

Au/thiols/streptavidin/unlabelled probe sequence/Cy5 labelled target (7.2)

The fluorescence of these labelled targets appeared to be stable for hours during the hybridisation steps if the same experimental conditions (laser intensity, exposure time, sublayer system au/thiol/streptavidin) were assured[47,173]. Since the dye-gold distance is equal in both systems (compare Figure 7.1 c and Figure 6.2 c) the extent of photo-bleaching of the bound Cy5-fluorophores is comparable. The stability of the fluorescence signal in the hybridisation of labelled targets can be explained by the equilibrium constants of both reactions. The equilibrium constant of the system unlabelled probe/labelled target was measured to be in the range of $5 \cdot 10^{-9} M^{-1}$ to $2 \cdot 10^{-7} M^{-1}$ depending on the presence of mismatches [17]. Therefore a steady exchange between already bleached targets on the surface and fresh unbleached ones from solution is possible by competitive replacement. If this exchange is faster than the bleaching process the signal of the bound fluorophores seems to be virtually stable.

In the case of labelled probes the coupling between the biotinylated Cy5 labelled strand and the streptavidin is too strong to allow for an exchange with fresh labelled probes from solution. Thus, the number of active species on the surface is reduced by photo-bleaching and a decrease in fluorescence signal is observed (Figure 7.2).

In order to prove this exchange mechanism, a layer system as in (7.2) was prepared by hybridising labelled MM0 and MM1 strands to unlabelled probe sequences, respectively. Subsequently, a replacement reaction was induced by injecting a solution of unlabelled targets of identical sequence and complementarity as the labelled ones. Figure 7.3 shows the time dependent fluorescence signal after adding the unlabelled targets for both cases. A steady exchange between initially hybridised labelled targets on the surface and fresh targets from solution was observed. In the case of fully complementary sequences (MM0) the exchange is rather slow due to the stability of the formed hybrid on the surface. In the case of MM1 the signal decreases relatively fast due to the lower higher k_{off} rate, which allows for an easier replacement of the bound species.

In summery, it may be noted that the used Cy5 dye is sensitive to photo bleaching. This effect has to be taken into account if a high laser power is applied without protecting the sample by appropriate chopping of the excitation source. In cases where the target solution provides a reserve supply of unbleached dye molecules, this bleaching effect might be negligible. However, in case of irreversibly bound fluorescent molecules, the bleached dyes stay at the surface and reduce the fluorescence yield of the sample. In rinsing steps the analyte solution is replaced by pure buffer. Therefore no recovery of the bleached species can occur and bleaching might be misinterpreted as desorption processes.

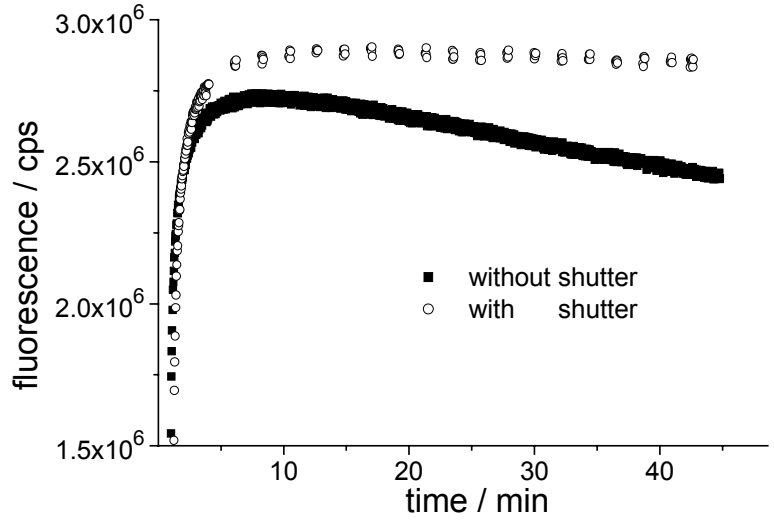

Figure 7.2 : Immobilisation of BioCy5T15 with and without using an automated shutter system in order to prevent the Cy5 dye from being photo bleached during the measurements.

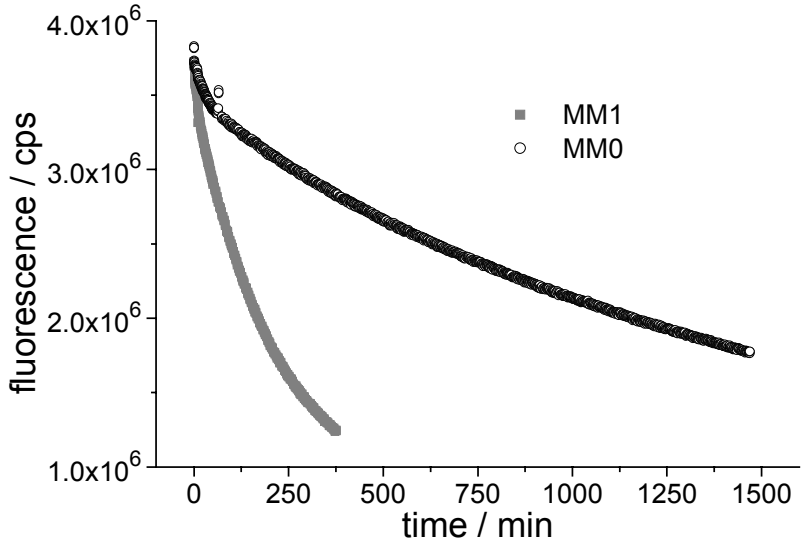

Figure 7.3 : Replacement of Cy5 labelled targets by unlabelled targets of the same sequence and complementarity as the unlabelled probe sequence.

7.2.3 Secondary Structure of Probes and Interaction with the Matrix

Biotinylated fluorescently labelled probes (BioCy5T15) were immobilized on the described layer system from a 1uM solution in PBS buffer, leading to a stable fluorescence signal after 10 minutes. After rinsing with analyte free PBS buffer (Figure 7.4) the signal decreased by about 70% of the initial signal. This decrease was not constantly observed in all experiments but could be frequently for labelled probe.

In chapter 6 the possible secondary structures of all oligonucleotides are discussed as schematically depicted in Figure 6.5. The probe sequences BioCy5T15 and BioCY5T30 (P2) were not only found to form hairpin structures but are also capable of forming self annealed complexes with each other. Due to self complementary parts in the probe, it is assumed that probe-probe complexes were formed during immobilisation onto the streptavidin matrix. The additional fluorophores then lead to a high initial fluorescence. The free binding energy of such complexes is low (Table 6.5) and hence the equilibrium constant is small. Therefore the additional probes can be rinsed away by pure buffer. The removal of these loosely bound labelled probes leads to the observed drop in the fluorescence signal. This drop is not evident in the reflectivity (not shown). From this one may conclude that not all possible binding sites on the surface were covered with self annealed probes. Such difference in adsorbed mass would be detectable by SPS. Further investigation is necessary to determine the extent of initial probe-probe complex formation. An experimental comparison between probes pre-incubated before immobilisation and heat denaturised samples can help to characterise this effect.

In the case of probe BioCy5HF (not shown) no drop in the fluorescence signal was observed upon rinsing, since this sequence did not contain self complementary sites. The only decrease was due to the removal of a small amount of background fluorescence from the bulk solution.

It is widely known, that streptavidin can bind a variety of ligands with different binding constants[174]. Biotin is know to exhibit an extraordinary dissociation constant of $K_d=10^{-15}\,M^{-1}$ and is often cited as one of the strongest non-covalent protein-ligand interaction. Fluorophores such as fluorescein are among the possible ligands which can bind to streptavidin. It has been reported that their fluorescence is quenched when the dyes are bound in the binding pockets of the protein. In the case of fluorophores that are immobilised onto streptavidin surfaces via a linked biotin moiety (like in BioCy5T15) an ostrich like quenching process can be found. According to a metaphor, the ostrich is believed to hide its head in the sand and believe itself to be unseen. Similarly, the backbone of the biotinylated construct can bend over and the dye can

be loosely bound in a neighboured binding pocket [175]. Once native biotin is added the fluorescence was reported to be recovered completely, likely due to competitive replacing of the bound fluorophore moiety by the biotin ligand.

In order to confirm that the quenching of Cy5 in our experiments is due to the energy transfer to the gold and not due to streptavidin binding, a 10μM solution of native biotin was added to the immobilised BioCy5T15 probes. As depicted in Figure 7.4 no signal change was seen upon biotin injection, indicating that the dyes were not bound in the streptavidin pockets. It was reported that the described quenching effect is dependent on the surface coverage of the ligand. At low coverage the receptor to fluorophore ratio is high enough to allow for Cy5 dye binding. However, used probe concentration of 1uM caused high surface coverage in our experiments. Therefore all binding pockets are occupied by the biotin moiety and fluorophore binding is hindered. Hence, no change in fluorescence signal was seen after applying the native biotin solution.

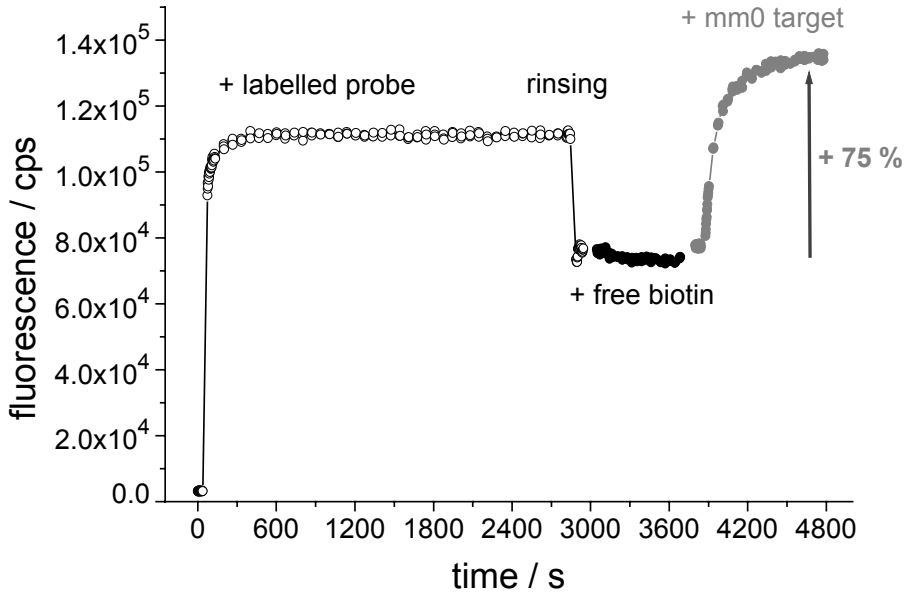

Figure 7.4 : Immobilisation of BioCy5probeT15 and hybridisation to unlabelled mm0 target: An increase of the fluorescence signal was detected after adding unlabelled target. This change can be attributed to conformational changes of the probe strand upon hybridisation and a resulting increase of the dye-metal distance that leads to reduced fluorescence quenching. The intermediate injection of free biotin indicates that the fluorophores are not bound in the streptavidin pockets.

7.3 Detection of Unlabelled Targets

7.3.1 Hybridisation on the Surface

Subsequent to preparing the BioCy5T15 probe layer, a 1μM solution of unlabelled targets (mm0) was added in order to hybridise to the immobilised probes. When the fluorescence signal was monitored by SPFS an increase of about 75 % of the initial fluorescence was seen (Figure 7.4). In chapter 4 it has been shown that the fluorescence of a dye close to a metal surface is strongly dependent on the distance to the surface. Furthermore it is known that stiff helical parts are formed in the duplex due to hybridisation. Since this stiff parts orient normal to the surface, the distance of the bound dye to the metal is increased upon hybridisation (see Figure 7.1). Hence, the fluorescence increase upon hybridisation can be attributed to a reduction in quenching due to the separation of the bound Cy5 dye from the gold surface. The distance change upon duplex formation was evaluated to be about 3 nm will be discussed in chapter 7.4.3.

When the experiment was repeated with BioCy5T30, which contains a longer spacer unit, a maximal increase in fluorescence upon hybridisation of 25% was observed. This is easily understood by considering the flexibility of the strand after duplex formation. While in BioCy5T15 one half of the probe is still single stranded, in BioCy5T30 two thirds of the probe is still occupied by the flexible spacing unit. A conformational change in the recognition site due to duplex formation has the largest effect in the 30mer probe, while the long 45mer probe is only slightly affected.

7.3.2 Hybridisation in Solution

The hybridisation experiment between labelled probe and unlabelled targets (mm0) was repeated in a solution experiment using common fluorescence spectroscopy. Here no energy transfer to the metal can effect the fluorescence of the dye and the influence of the unlabelled probe strand on the probe fluorescence can be investigated. The labelled probe BioCy5T15 was excited at λ=633nm in PBS at a strand concentration of 1uM. After adding unlabelled target (final concentration 1uM), emission spectra were recorded over 40 minutes. The fluorescence intensity at 670 nm was plotted versus time in Figure 7.5. Compared to the solid phase experiments no change in the fluorescence was observable upon hybridisation. This indicates that not a change in the local environment of the dye (local pH, salt concentration) due to the hybridisation was responsible for the signal increase in Figure 7.4. More likely the fluorescence increase in 7.3.1 results from reduced quenching to the metal surface.

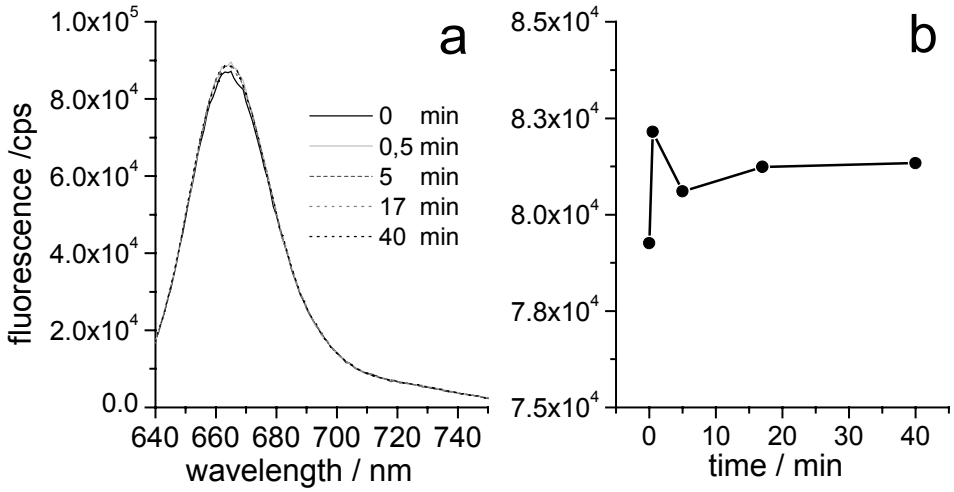

Figure 7.5 : a) Hybridisation of unlabelled target to fluorescent labelled probe BioCy5probeT15 in solution at an excitation wavelength of 633 nm; b) no considerable signal change was seen at the maximum of the emission spectrum during hybridisation over the time range of 40 minutes.

7.3.3 Mismatch Discrimination Using Labelled Hairpin Probes

It has been reported that DNA binding kinetics to unlabelled surface bound probe strands can be observed by labelling the targets with fluorescent dyes e.g. [11,17,47]. The analysis of these kinetics can lead to the determination of association- dissociation- and equilibrium constants by fitting the experimental results to an appropriate binding model.

Our experiments prove that alternatively the use of labelled probes can be used to discriminate between complementary and mismatched unlabelled target sequences. In separate experiments BioCy5T15 probes were immobilized onto the streptavidin matrix and hybridisation kinetics with MM0, MM1 and MM2 sequences were recorded by SPFS at a 1µM target concentration. After equilibrium was reached the flow cell was rinsed with analyte free PBS buffer at a constant flow of 1 ml/min in order to desorb the hybridised strands from the surface. The observed kinetics are given in Figure 7.6 together with the corresponding Langmuir simulations.

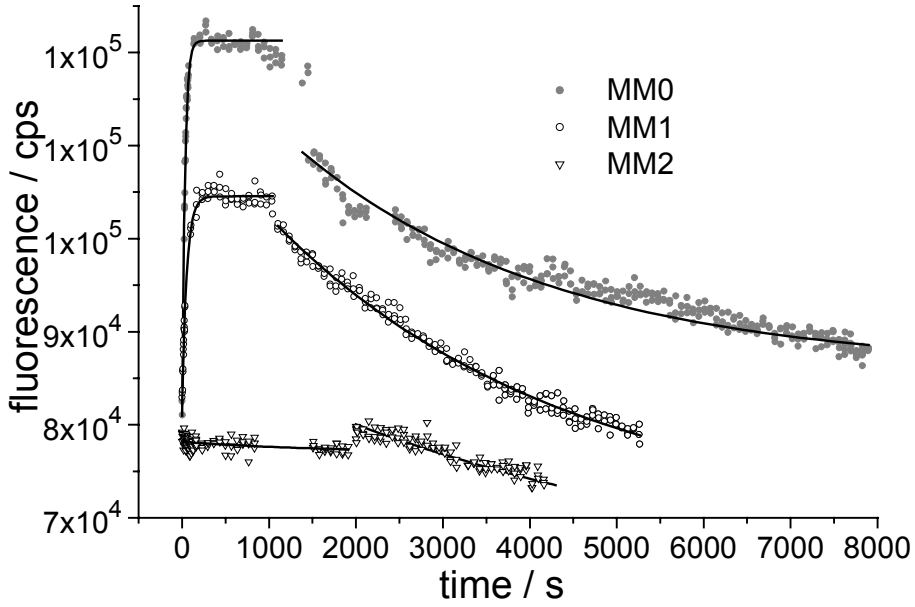

Figure 7.6 : Experimental hybridisation kinetics of unlabelled targets to the labelled probe BioCy5T15 together with the corresponding Langmuir simulations. The obtained kinetic constant are summarised in Table 7.2.

As presented in Figure 7.6 the hybridisation kinetics of MM0, MM1, and MM2 targets can be distinguished by qualitative considerations. While in the case of two mismatching base pairs in the target sequence no significant hybridisation can be detected, a clear increase of fluorescence in seen during binding of the MM1 and the fully complementary MM0 targets. Similar to the analogous unlabelled probe/labelled target experiments in chapter 4 a single mismatch destabilises the duplex. Therefore, the mismatched target can be desorbed by extensive rinsing with pure buffer.

In case of labelled MM0 targets the recorded desorption kinetics differ from the expected behaviour. In chapter 6.4 it was demonstrated that the fully complementary duplexes between unlabelled probe/labelled target are quite stable. The labelled MM0 target could not be removed by rinsing under the same experimental conditions (PBS, 25 C). However, in our experiments with labelled probes and unlabelled MM0 targets a substantial desorption of the target strand is detectable (Figure 7.6). This difference is not fully understood. The described behaviour is reflected in the kinetic constants, which were derived from the Langmuir simulations and are summarised in Table 7.2.

7.3.4 Mismatch Discrimination Using Hairpin Free Labelled Probes

Analogous to the experiments in chapter 6.4.2 the influence of secondary structures in the probe sequences was investigated. Experiments were carried out with probes that were not capable of forming secondary structures. The probe sequence BioCy5HF was immobilised on the streptavidin layer and the fluorescence was followed by SPFS. In contrast to BioCy5T15, these probes did not contain self complementary sequences. Therefore no probe-probe complexes could be formed in the immobilisation step and hence no drop in fluorescence upon removal of self annealed probes was seen (not shown).

The obtained hybridisation kinetics are given in Figure 7.7 together with the Langmuir simulations. In the case of the fully complementary target an increase of 83% was observed, a value that is comparable to the 75% increase for BioCy5T15 in chapter 7.3.1. While for the hairpin probes in Figure 7.6 a strong desorption was observed for MM0 and MM1 targets, the duplexes with BioCy5HF appeared to be more stable. Only moderate desorption of the targets could be obtained upon rinsing. Qualitatively, this can be thought to be the result of the missing competition in the hairpin free structures. The derived kinetic constants are summarised in Table 7.2.

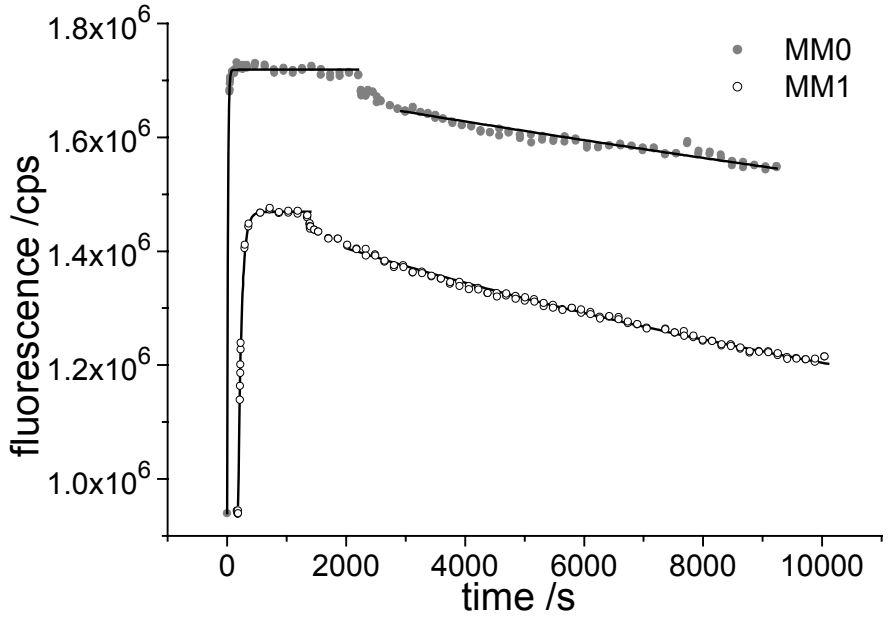

Figure 7.7 : Hybridisation kinetics of unlabelled targets to the hairpin free probe BioCy5HF. The kinetic constants resulting from the shown Langmuir simulations can be found in Table 7.2.

7.3.5 Comparison of Structured and Hairpin Free Labelled Probes

The kinetic constants of the labelled probes BioCY5T15 and BioCy5HF are compared with the values for the corresponding unlabelled sequences P2 and PHF in Table 7.2 as follows: As pointed out in chapter 6.4 part of the mismatch discrimination sensitivity of the structured probes is based on the competitive hairpin formation in the probe sequences. While the equilibrium constants for complementary and mismatched sequences in P2 vary over several orders of magnitudes, almost no difference between MM0 and MM1 with the hairpin free probe PHF was detectable. For P2, the calculated free binding energies ΔG_{exp} were in acceptable agreement with the simulated values ΔG_{sim}; PHF showed hardly any difference in the energies (-10.43 kcal/mol, -10.05 kcal/mol), although a clear distinction was predicted by ΔG_{sim} (-15.4 kcal/mol; -11.8 kcal/mol).

The base sequences of labelled and unlabelled probes are identical. The software was not capable of taking into account energetic constraints caused by the additional label in BioCy5T15 and BioCy5HF. Thus, identical energetic predictions were made as for the unlabelled probes.

In the case of BioCy5T15 the transition from MM0 to MM1 and MM2 targets caused a decrease in K by an order of magnitude each ($K=10^8M^{-1},10^7M^{-1},10^6M^{-1}$) and permitted the discrimination of all three cases. However, the difference is neither as distinct as in the analogous unlabelled P2 nor as predicted by ΔG_{sim}. For the hairpin free probes no MM2 target was available during the experiments, so only complementary and single mismatches are compared.

The ratio $r_{0-1}=K_{MM0}/K_{MM1}$ of the equilibrium constants is considered as a measure for the mismatch discrimination ability. For the probes the following trend in sensitivity is obtained:

$$\text{P2 } (r_{0-1}=220) \;>>\; \text{BioCy5HF } (r_{0-1}=15) \;>\; \text{BioCy5T15 } (r_{0-1}=5) \;>\; \text{PHF } (r_{0-1}=2)$$

As discussed above, the higher sensitivity of P2 over PHF is based on the loss in secondary structure. Note, that the mismatch sensitivity is reduced in the case of labelled BioCy5T15 compared to unlabelled P2 but still is capable of distinguishing complementary and mismatched sequences. It may be postulated, that the hairpin formation in the labelled BioCy5T15 probe is partially hindered due to steric constraints of the attached Cy5 dye. Hence the extent of secondary structure is reduced and so is the mismatch sensitivity.

It is questionable why the labelled hairpin free probe BioCy5HF shows a higher sensitivity than BioCY5T15 as given by the ratio r_{0-1}. While for unlabelled probes a hairpin enhanced the mismatch discrimination, the opposite effect is found for labelled probe sequences. A possible explanation is provided by the postulation of a secondary structure in BioCy5HF introduced by the Cy5 label. This could compete with the hybridisation reaction of the targets and therefore enhance the discrimination sensitivity. A secondary structure based on the capture of the dye by the streptavidin binding pocket is not likely, since the surface was treated with native biotin before hybridisation. The strong ligand would have replaced any loosely bound Cy5, but this effect was not observed (compare Figure 7.4).

However, the difference between the labelled probes is small (r_{0-1}=5 → 15) compared to the strong loss in sensitivity if the hairpin is removed in unlabelled probes (r_{0-1}=220 → 2). The similarity between the labelled sequences points toward weak secondary structure formation. Furthermore, a conformational similarity is underlined by the ionic strength experiments in the next chapter, in which both probes appeared virtually identical.

Table 7.2 : Comparison of kinetic constants of unlabelled and labelled probes. The values for the unlabelled probes were taken from Table 6.6. The ratio r_{0-1} is a measure for the mismatch sensitivity of the probes. Note the difference between the sensitivity of the unlabelled probe P2 (r_{0-1}=220) and the labelled probes (r_{0-1}=5; 15) and unlabelled hairpin free probe PHF (r_{0-1}=2).

probe	MM	k_{on} / $M^{-1}s^{-1}$	k_{off} / s^{-1}	K / M^{-1}	ΔG exp kcal/mol	ΔG sim kcal/mol	r_{0-1}= K_0/K_1
labelled probe / unlabelled target							
BioCy5T15	0	$3.10 \cdot 10^4$	$1.2 \cdot 10^{-4}$	$2.6 \cdot 10^8$	-11.29	-15.81	5
	1	$1.77 \cdot 10^4$	$3.5 \cdot 10^{-4}$	$5.1 \cdot 10^7$	-10.34	-11.22	
	2	$5.62 \cdot 10^2$	$1.2 \cdot 10^{-4}$	$4.6 \cdot 10^6$	-8.92	-5.44	
BioCy5HF	0	$7.95 \cdot 10^4$	$2.0 \cdot 10^{-6}$	$3.8 \cdot 10^9$	-12.85	-15.4	15
	1	$1.17 \cdot 10^3$	$7.0 \cdot 10^{-6}$	$2.54 \cdot 10^8$	-11.25	-11.8	
unlabelled probe / labelled target							
P2	0	$3.69 \cdot 10^4$	$7.0 \cdot 10^{-6}$	$5.3 \cdot 10^9$	-13.04	-15.81	220
	1	$8{,}94 \cdot 10^3$	$3.7 \cdot 10^{-4}$	$2.4 \cdot 10^7$	-9.89	-11.22	
	2	$1.0 \cdot 10^1$	$7.7 \cdot 10^{-4}$	$1.3 \cdot 10^4$	-5.51	-5.44	
PHF	0	$2.2 \cdot 10^4$	$3.5 \cdot 10^{-4}$	$6.3 \cdot 10^7$	-10.43	-15.4	2
	1	$9.0 \cdot 10^3$	$2.9 \cdot 10^{-4}$	$3.1 \cdot 10^7$	-10.05	-11.8	

7.4 Ionic Strength and Conformational Change

It was shown in the previous chapters that immobilised probe strands can be stretched by formation of double stranded helical structures. DNA is a biopolymer, which exhibits a negative backbone at physiological pH due to the negative phosphate groups (Figure 6.1). Inter- and intra-molecular repulsion between these groups is expected at low ionic strength. The persistence length of a polymer p is used to characterise the distance along the backbone that can still be regarded as a stiff rod. It is dependent on the ionic strength I as given by [166].

$$p = 6.42 \cdot 10^{-8} + 4I^{-0.5} \qquad (7.3)$$

The persistence length can be described as the sum of two terms: a bare persistence length p_i, which results from the intrinsic rigidity of the strand, and an electrostatic contribution p_e, which is dependent on the ionic strength of the medium If the ionic strength is increased the persistence length decreases to the intrinsic persistence length p_i. Typically values for p_i between 0,8 and 1,3 nm are found for ssDNA. Hence, the flexibility of single stranded DNA is expected to increase at high salt concentrations in solution.

7.4.1 Probes in Solution

The fluorescence intensity of dyes in solution can be dependent on the ionic strength of the medium. This dependence of the intrinsic fluorescence of the Cy5 labelled strand dye on changes in the ionic strength in solution was thus investigated first. The BioCy5T15 probe was dissolved in 10nM NaCl solution and the salt concentration was increased stepwise to a value of 1M NaCl. Fluorescence spectra were obtained by fluorescence spectroscopy in solution at each concentration and can be found in Figure 7.8. The signals at λ_{em}=670nm (analogeous to the SPFS experiment) were plotted versus the applied NaCl concentration. Except for slight fluctuations at small salt concentrations, no change in fluorescence signal was seen upon increasing the salt concentration. This result proves that any signal change of immobilised labelled targets in the surface experiments can be attributed to a salt dependent flexibility of the strands and an altered quenching behaviour.

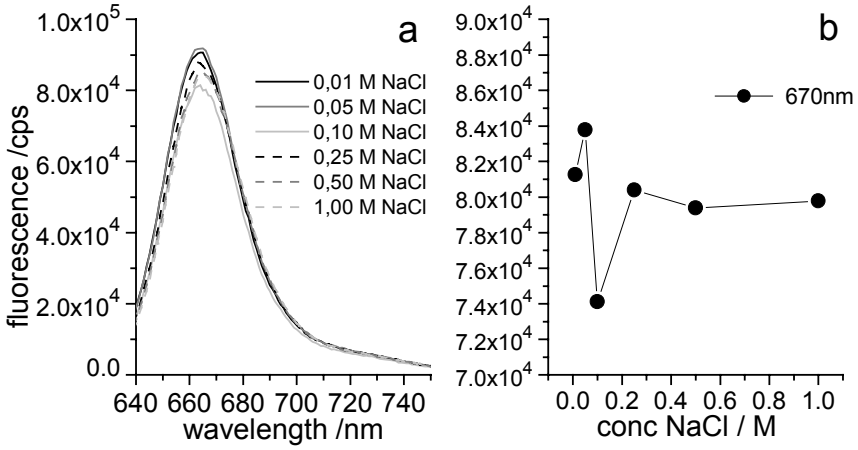

Figure 7.8 : Fluorescence of the BioCy5T15 probe as measured by fluorescence spectroscopy in solution at different NaCl concentrations. a) Emission maximum measured at λ_{ex}=633nm, b) fluorescence emission at λ_{em}=670nm. Except for fluctuations no change in fluorescence was observed upon increasing the salt concentration in the cell.

7.4.2 Immobilised Probes

A less flexible probe strand should separate the attached dye farther away from the surface. Therefore an increase in the fluorescence signal of immobilised labelled probes is expected with decreasing salt concentration. In two separate experiments, BioCy5T15 and BioCy5HF were immobilised on the streptavidin matrix in PBS buffer, followed by an exchange to 10nM NaCl in 18kΩ MilliQ water. The sodium chloride concentration in the cell was increased stepwise up to 1M and the equilibrated fluorescence was measured by SPFS at each concentration. Due to the changed refractive index the SPFS scan curves were shifted with respect to each other (not shown). In order to obtain a quantitative measure for the fluorescence at each concentration, the maximum fluorescence in all SPFS scan curves was considered and plotted versus the salt concentration in Figure 7.9.

As predicted, a decrease in fluorescence is seen with increasing NaCl concentration for the hairpin probes BioCy5T15 as well as for the random coil probes BioCy5HF. Both curves were normalised to maximal fluorescence at the lowest ionic strength. Note, that no difference in the salt dependence of hairpin and random coiled probes is seen.

The fluorescence of BioCy5HF could be recovered with a slight hysteresis effect by reducing the salt concentration again to 10 nM. However, the initial value at 100% could not be recovered, but only 70% at 0.005 M could be reached. This was likely due to experimental difficulties in rinsing off all salt in the flow cell.

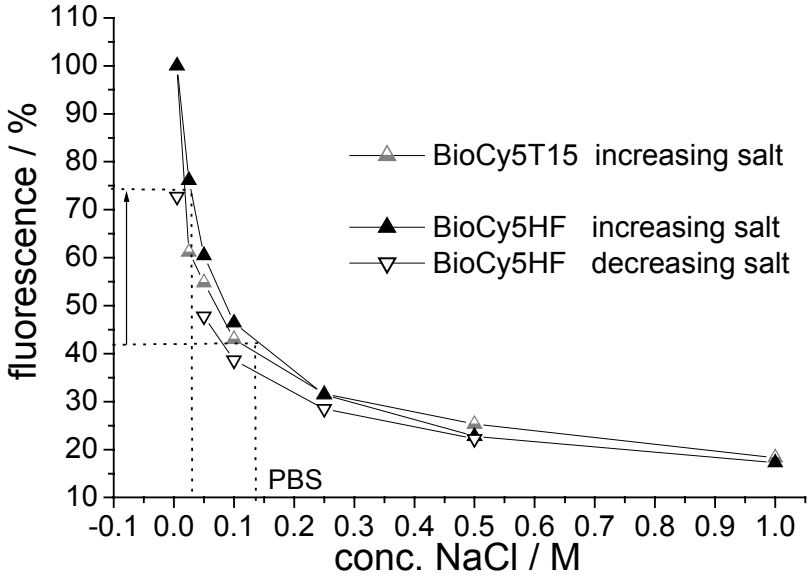

Figure 7.9 : Fluorescence of immobilised hairpin probes BioCy5T15 and hairpin free probes BioCy5HF depending on the NaCl concentration in the medium. The dotted lines mark the relative expected fluorescence intensity in PBS of single and double stranded BioCy5T15.

The decrease in fluorescence with increasing salt concentration can be explained by a higher flexibility of the strands at high ionic strength. This results in a random coil structure which causes the attached dye to be closer to the metal surface. In the low ionic strength limit the persistence length of the probe is increased (equation (7.3)) and the stiff strand separates the attached dye from the surface.

In the hybridisation experiments from 7.3.5 a clear difference between hairpin and random coiled probes was seen with respect to the equilibrium constants and the observed kinetic constants. However, in the ionic strength experiments in Figure 7.9 both probes behaved virtually identical. From this result, one can conclude that the intra-molecular hairpin structure in the hairpin probe BioCy5T15 is already disrupted at low ionic strength. Hence the strand appears as the random coil probe BioCy5HF.

At high salt concentrations the hairpin in BioCy5T15 should be intact and the fluorescence intensity should differ from the one of BioCy5HF. The spacer unit of 15 thymine bases is the same in both probes, but the conformational structure of BioCy5HF and BioCy5T15 in the recognition sequence is not identical. Interestingly, exactly the same relative fluorescence signal of about 18% is obtained in the high salt limit. One possible explanation would be to assume a similar dye-metal distances in both probes (compare distance d_1 in Figure 7.1). The distance d_1 in

the hairpin probe can be estimated since the position of the dye is dictated by the hairpin. The structure of the random coil is not easily predicted. Therefore the assumption of identical distances d_1 is speculative.

In order to evaluate the extent of probe stiffening compared to duplex formation the experimental result of chapter 7.3 are recalled here: the hybridisation experiments in this chapter were carried out in PBS buffer, the NaCl content of which (138 mM) was marked in Figure 7.9. This corresponds to an intensity of ca. 40%. If we assume the typical increase in fluorescence by a factor of 1.75 upon hybridisation, a fluorescence intensity of ~75% would be reached. This value corresponds to a fluorescence signal of a single strand at a NaCl concentration of about 30mM. Thus, one can follow that the conformational changes in the probe due to ionic strength effects are stronger than the "standing-up" effect due to formation of helical structures by hybridisation.

To confirm this assumption, BioCy5T15 probes were immobilised on the streptavidin matrix and hybridised with MM0 unlabelled targets. After duplex formation the PBS buffer was exchanged to a 10mM NaCl solution and the salt concentration was increased stepwise to 1M NaCl. In Figure 7.10 the obtained fluorescence intensities were scaled to maximal intensity at 10mM salt.

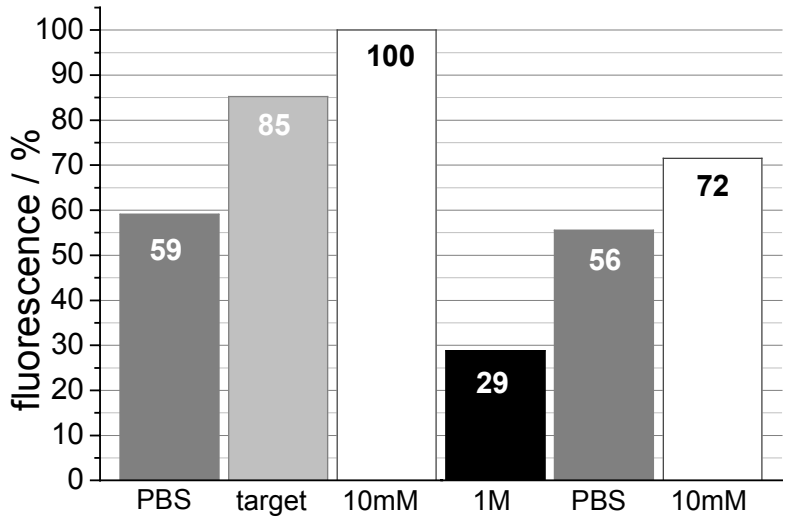

Figure 7.10 : Fluorescence of BioCy5T15 in different buffers as duplex and single strand. All signals were scaled to maximal fluorescence at 10mM NaCl. Immobilised probes in PBS (59%) were hybridised with unlabelled targets (85%). An exchange to 10mM NaCl resulted in a further fluorescence increase (100%). Subsequently the signal was measured in 1M NaCl, PBS and 10mM NaCl. Note that the initial fluorescence of 100% at 10mM could not be recovered.

Upon hybridisation in PBS the expected fluorescence increase from 59% to 85% was seen (compare 7.3.1), although only a factor of 1.5 was observed in this experiment (compared to typically 1.75). The exchange to 10mM salt lead to further signal increase (100%) as predicted by Figure 7.9. It is assumed that due to the low ionic strength the duplex was denatured and the increase was due to the stretched conformation of the single stranded probe. A subsequent stepwise increase to 1M NaCl lead to a similar behaviour as in Figure 7.9 (not shown). In this high salt limit the fluorescence was quenched (29%) as seen before.

However, signals in the high and low salt limit were found to differ only by a factor of 3.44, compared to 5,7 in Figure 7.8. Incomplete dissociation of the target could have influenced the measured value at 10mM.

Finally, the cell was flooded with PBS again and the initial intensity for PBS could be recovered (59%; 56%) This indicated that the duplex was denatured in the previous washing steps. When a final low salt solution of 10mM was applied again, the initial fluorescence (100%) could not be recovered completely. Analogous to the experiment in Figure 7.9, it was not possible to rinse off all salt so that only 70% of the initial signal was obtained.

The absolute fluorescence values in this experiment were not identical to the ionic strength experiment with un-hybridised probes in Figure 7.9. But the assumption of a stronger conformational change by ionic strength compared to duplex formation, could be confirmed clearly. In the next paragraph, the experimental values from Figure 7.9 are used to derive the distance change for different ionic strengths.

7.4.3 Evaluating the Dye-Metal Distance

In order to estimate the dye-metal distance at different ionic strengths and after duplex formation, the data from Figure 7.9 were compared with the theoretical quenching profile of Cy5 from chapter 4.3. This calibration curve is given in Figure 7.11a.

In the range of 7-20nm the expected change in fluorescence signal was calculated for different dye-metal distances and different distance changes Δd. Moving along the calibration curve in Figure 7.11a in different step width Δd resulted in individual curves, some of which are plotted in Figure 7.12b. For example, an increase in the dye-metal distance of Δd=7.75nm to a final distance of d=16nm would correspond to an increase in fluorescence signal of a factor of 5.7. This value is comparable to the measured factor of 5.8 for the transition between the probe

conformation at 10mM and 1M NaCl in Figure 7.9. The experimental enhancement factors that were taken into account are summarised in Table 7.3.

Generally, there are many solutions for d and Δd which lead to the experimental enhancement factors in Table 7.3. But only a few solutions fulfil the following boundary conditions:

- the minimum distance d is 5.5 nm as dictated by the thiol-streptavidin layer thickness
- the maximal distance is about 16 nm. A loose helical structure is assumed for single strands (30bases=10.2nm) and the dye is assumed to be 0.5 nm
- half of the duplex probe in BioCy5T15 exhibits a stiff structure of 5.1 nm (15 bases) length, while the single stranded spacer is still flexible at high salt concentrations
- Due to the hairpin in the probe BioCy5T15, the 3' terminus is folded back to the middle of the probe strand in the high salt limit (see chapter 6.3). This determines the relative position of the attached Cy5 dye.

Since the values in Table 7.3 are not independent, a set of parameters can be found to solve all requirements. The optimised calibration curves are plotted in Figure 7.11b and the estimated values d were used to construct a schematic view of the probe configuration in Figure 7.12.

Table 7.3 : Ratios of fluorescence enhancement for the transitions between conformational states at different ionic strength and duplex formation as derived from Figure 7.9

	1M	**duplex**	**PBS**	**10mM**
10mM	5.8	1.3	2.4	--
1M	--	4.3	2.4	5.8
duplex	4.3	--	1.75	1.3

In addition to the hairpin in the probe BioCy5T15, it is assumed that the single stranded part is flexible in the high salt limit. This allows for a minimal dye-metal distance of about 8nm. In PBS the single stranded spacer may be unfolded, but the hairpin still fixes the fluorophore at a distance with corresponds to one half of the probe length. After duplex formation in PBS the maximal possible distance was not reached due to the flexible of the 15T spacing unit. However, in the low salt limit the entire single strand is stiffened and the Cy5 dye can reach far out into the medium.

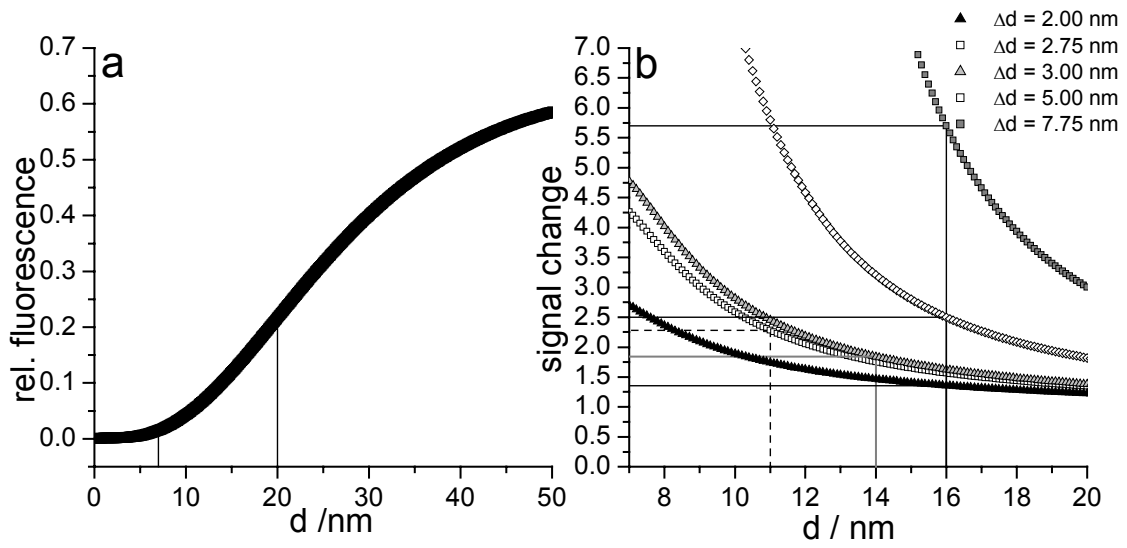

Figure 7.11 : Using the theoretical quenching profile (a) the factorised change in the fluorescence signal was calculated in the interesting range between 7-20 nm (b). Different step-widths Δd resulted in different curves. Only a certain set of curves were consistent with the requirements set by the fluorescence signals in Figure 7.9. For example d=16nm and assuming a distance change Δd= 2nm, 5nm and 7.75 nm predicted acceptable factors for the signal change upon transition from the conformations a-c to the stretched 10mM structure (d) in Figure 7.12d.

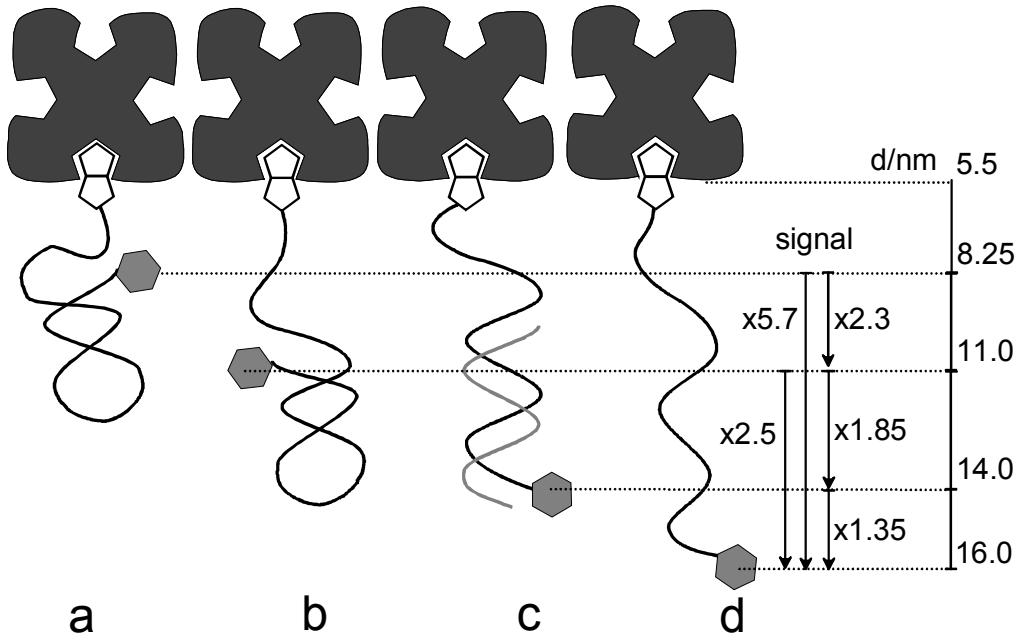

Figure 7.12 : Schematic presentation of the probe conformation at different ionic strength and after duplex formation. a) 1M NaCl, b) PBS, c) duplex, d) 10mM NaCl. As derived from Figure 7.9 the fluorescence signal of the probe changed upon transition between the individual states by the given factors. By comparison with the calibration curves in Figure 7.11 the dye-metal distances were estimated.

7.5 Conclusion

A novel DNA detection scheme capable of detecting unlabelled targets was presented, which is based on monitoring conformational changes in the probe sequence by SPFS. In common detection strategies the targets need to be labelled before the actual hybridisation reaction. The presented technique allows analysis of clinical DNA samples like restriction products without further processing. Moreover, the detection limit of this fluorescence based method exceeds the capability of many label-free detection techniques like SPR. The detection scheme exploits conformational changes from single stranded probe sequences to double stranded helices upon hybridisation. The fluorescence of the used 3' labelled probes is dependent on the quenching profile to the supporting metal surface. Any change of the metal-dye distance due to formation of the stiff helical region can be monitored by Surface Plasmon Fluorescence Spectroscopy (SPFS). Thus, an increase in initial probe fluorescence indicates the binding process between immobilised labelled probe and unlabelled target.

The immobilisation of the probe onto the streptavidin matrix was investigated and the extent of photo bleaching of the bound fluorophore was determined. To minimise bleaching of the labelled probes the excitation source of the SPFS spectrometer had to be chopped to allow the observation of long term kinetics.

The influence of the flexible spacing unit was evaluated by changing the thymine spacer length from 15 to 30 thymine residues. It was found that the maximal fluorescence enhancement of about 75% was seen in the case of the 15T spacer. Only 25% increase was observed by using the long 30T spacer. This behaviour could be satisfactory explained, by taking into account that the stiff helical part occupied half of the length of BioCy5T15, while in BioCy5T30 two third were still be flexible after hybridisation.

It was known from previous studies in chapter 6.4 that the mismatch discrimination ability of the probe is influenced by the secondary structure[152,153]. Therefore sequences which were designed to form intra-molecular hairpins were compared to hairpin free probes sequences. In case of unlabelled probes, the presence of a hairpin enhanced the mismatch discrimination ability as shown in chapter 6.4. The opposite effect was found here in the case of the novel labelled probes. The response of the probes was similar to both the fully complementary and single mismatched targets. This suggests, that the attached Cy5 dye may interfere with a proper hairpin formation in BioCy5T15.

A similar response of the labelled strands was also seen when the ionic strength of the solution was altered. A strong decrease in fluorescence was attributed to a screening of the negative backbone charges and an enhanced flexibility of the strand. The closer distance to the metal surface in the high salt limit led to quenching of the attached dye. The similarity between the hairpin probe BioCy5T15 and the random coil probe could be explained by an early disruption of the hairpin structure at low salt concentrations.

In comparison with the strategy of using unlabelled probes and fluorescent labelled targets as discussed in chapter 6 the introduced novel detection scheme appears to be less sensitive for mismatches in the investigated 15mer targets. However, it is still capable of distinguishing mismatched and complementary sequences. The aim of this study was to prove the principle of the novel DNA probes. It has to be noted, that the experimental conditions have to be optimised, which promises to enhance the mismatch sensitivity by some orders of magnitude.

These optimisations include the choice of an appropriate reaction temperature and ionic strength of the medium as well as the further design of the probe sequences. In order to compare the obtained results with literature values the base sequence of the labelled probes were adapted from the P2 probes in chapter 6.3.2.

The length of the spacing unit should be optimised to obtain a compromise between the enhanced signal increase with short spacers (<=15T) and the reduction of steric hindrances during the hybridisation reaction. It is known that secondary structures in the probe enhance the mismatch discrimination sensitivity. Thus, the number of base pairs in the double stranded stem of the hairpin has to be optimised. It has been reported that optimised competition of secondary structures to target hybridisation in molecular beacons can reduce the binding of mismatched probes drastically. Furthermore, the stronger the quenching of the probe fluorescence is before hybridisation, the stronger the signal enhancement will be upon binding of the target. Thus, an optimised probe will exhibit a secondary structure with appropriate hairpin stability and minimal distance between the attached fluorophore and the metal surface.

As discussed previously, the stability of a hairpin structure is dependent on the loop sequence [150]. This difference was negligible for the investigated probes as pointed out in chapter 6.4.3. In order to design optimised probes according to the conditions mentioned above, it would be appropriate to construct the stem of the hairpin by incorporating the thymine spacing unit. By

simply attaching a Cy5 labelled poly$(A)_n$ residue of certain length to 3' end of the probe recognition sequence a probe of the following form can be used:

Biotin-5'-poly$(T)_m$- (recognition_sequence)-poly$(A)_n$-Cy5-3'

Since long probe sequences are known to result in steric constraints due to crowding [176] one is advised to keep the overall length of the probe short. In future studies the length m and n of the stem part has to be optimised. For molecular beacons an excellent balance has been determined by a 15-25 base recognition sequence together with a 5 base stem.

Summarising, a novel class of DNA probes have been introduced, which can be used on metallic surfaces. The novel probes are easy to use, relatively cheap and most of all not limited to certain fluorophores like in MBs, but can easily adapted to be used with the dye of choice. Labelling of the probes itself make fluorescence labelling of the target redundant. Due to the possibility of sensing unlabelled targets the novel strategy could also be referred to as 'single-fluorescent molecular beacon'.

8 Fluorescence Resonance Energy Transfer Between Oligonucleotide Bound Dyes

The fluorescence resonance energy transfer (FRET) technique is a valuable and powerful tool for monitoring intermolecular interaction distances in the range of 2-10 nm (chapter 2.1.3) and is therefore suitable for recording association and binding reactions between probes and analytes in various bio-assays. FRET has been successfully applied to problems in protein or membrane biophysics and has helped to elucidate the structure and conformation of DNA [177-180]. Also detection schemes for oligonucleotides based on FRET are known [181-186].

FRET detection schemes have been successfully combined with common fluorescence spectroscopy, however no investigations by surface plasmon fluorescence spectroscopy (SPFS) have been reported, yet. Therefore donor-acceptor interaction of a potential Förster pair was investigated by the use of this surface sensitive detection method. The results were compared to corresponding measurements in solution.

8.1 Probe and Target Sequences

In analogy to previous experiments, fully complementary (MM0) and mismatched target sequences (MM1) were investigated in respect to their hybridisation behaviour with immobilised probe sequences. The probe strands were labelled at the 3' end with a chlorinated fluorescein-derivative (6-Carboxy-hexachlorofluorescein HEX) that served as the fluorescence donor. The targets strands were modified with JA270. The spectral properties of this dye make it a suitable system to serve as a Förster acceptor of the HEX emission. The structure formulas of both fluorophores are given in Figure 8.1.

As shown in Table 8.1 the probes are labelled at the 3´end while the targets are modified with the acceptor at the 5´ end. Upon hybridisation the distance between the dyes is expected to fall below the specific Förster radius for this system and hence permits energy transfer. Monitoring changes in the fluorescence signal of both donor and acceptor is therefore expected to permit sensitive recording of hybridisation reactions between surface attached probes and complementary targets in solution. In order to characterise the spectral properties of the labelled oligos hybridisation experiments were carried out in solution first, using standard fluorescence spectroscopy techniques.

Table 8.1: Sequences of the labelled probe and target sequences used as Förster donor-acceptor system in the hybridisation experiments.

type	dye	sequence	mismatch
probe H1	HEX	5´-*Biotin*-T_{15}-TGT ACA TCA CAA CTA-*HEX*-3´	
target J1	JA270	5´- *JA270*-TAG TTG TGA TGT ACA - 3´	MM0
target J2	JA270	5´- *JA270*-TAG TTG TGA *C*GT ACA - 3´	MM1

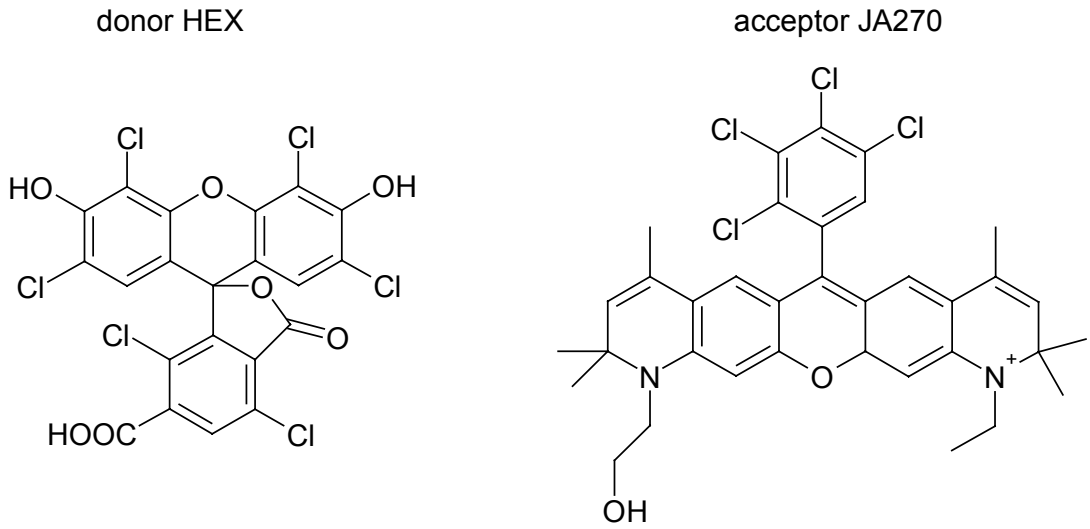

Figure 8.1 : Structure formulas of the Förster donor (HEX) and acceptor (JA270)

8.2 Characterisation of the Dyes by Absorption and Fluorescence Spectroscopy in Solution

Both the acceptor labelled targets and the donor labelled probes were diluted separately to a concentration of c_0=1 µM in phosphate buffer (PBS) and excitation and emission spectra were recorded using standard fluorescence spectrophotometer equipment. The spectra in Figure 8.2 were corrected for the monochromator's throughput function, the emission characteristics of the used lamp and for the wavelength dependent detector. All fluorescence spectra were normalised to unity.

The absorption of HEX and JA270 were measured by UV spectroscopy in solution. The resulting spectra were superimposed to the corresponding excitation spectra and appeared to be virtually identical. Generally, this identity is expected for a given fluorophore in solution under constant conditions. The Stoke´s shift between excitation and emission maximum both in the donor and the acceptor fluorescence is clearly seen. A substantial overlap of the donor emission and the acceptor absorption spectrum is observed. This is the base for successful attempts to

transfer energy from one dye to the other. Table 8.2 summarises the spectral properties of the two dyes:

Table 8.2: Excitation and emission characteristics of the used donor and acceptor used for resonance energy transfer studies between labelled oligonucleotides.

label	excitation max /nm	emission max /nm	ε / (mol cm)$^{-1}$
HEX	535	555	105000
JA270	623	645	84000

The surface plasmon field enhanced fluorescence experiments in 8.3 were performed on silver/gold substrates. Therefore excitation and emission spectra of the donor were recorded on the same kind of samples, additionally. For this purpose, $LaSFN_9$ substrates were evaporation-covered with a fresh layer of 40 nm silver and 5 nm gold. By a self assembly process (SAM) outside the spectroscopic cell a multilayer of the following architecture was prepared:

AgAu / thiols / streptavidin / biotinylated HEX donor probe

Subsequently the samples were transferred into the fluorescence set-up. Excitation and emission spectra of the surface bound donor dye were recorded in reflection using the front face mode of the instrument. In this measurement mode scattered excitation light can disturb the measurement if the difference between excitation and emission wavelength is less than 30 nm. Thus, when using an excitation-wavelength of λ_{ex}=510 nm the emission spectra were recorded starting from λ_{em}=540 nm. An analogous offset holds for the excitation spectrum.

Normalising the obtained reflection spectra to unity reveals the similarity of the surface and the solution based fluorescence characteristics of the donor molecule. Slight deviations were found at the shoulders of the emission/excitation maximum (Figure 8.2) originating presumably from the specific properties of the Au substrate in that spectral range. Hence, results obtained from fluorescence experiments in solution can be directly compared to surface based fluorescence studies. However, it has to be taken into account that the excitation mechanism in surface plasmon enhanced fluorescence experiments is quite different from the front-face illumination applied here. Also, different processes leading to a decay of the fluorescence have to be considered near metallic surfaces.

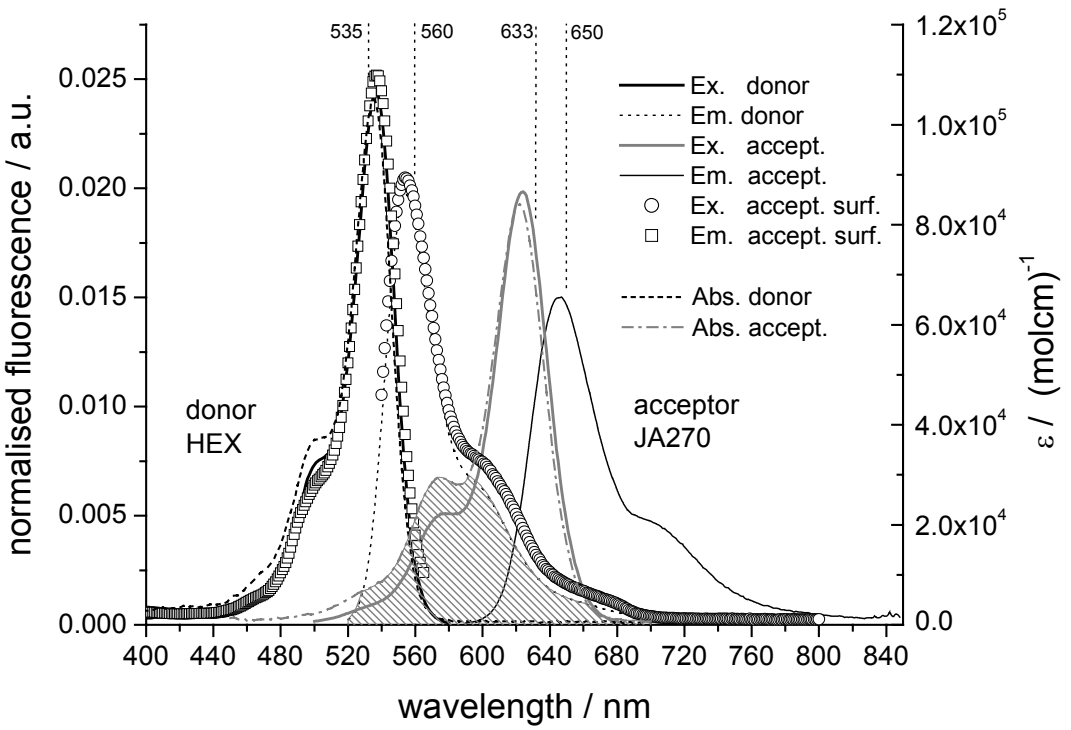

Figure 8.2 : Normalised excitation and emission spectra (lines) of donor (HEX) and acceptor (JA270) bound to probe and target oligonucleotides in solution and reflection spectra on gold surfaces (circles, squares) of the donor fluorophore. The reflection spectra of the donor matched the corresponding measurements in solution. Additionally, the absorption spectra of both strands in solution are superimposed on the excitation spectra and appear to be virtually identical. An overlap (shaded) between the emission spectrum of the donor and the absorption spectrum of the acceptor dye is seen, making this Förster pair suitable for FRET experiments. Emission and excitation wavelengths used for the SPFS experiments are indicated.

8.2.1 Increasing Acceptor Concentration at Fixed Donor Concentration

In order to monitor the influence of the acceptor concentration on the donor fluorescence a 1 μM solution of the HEX labelled probe H1 was prepared in PBS buffer. After recording an emission spectrum at an excitation wavelength of λ_{ex}=510 nm (Figure 8.3a) the fluorescence was observed as a function of time for increasing acceptor concentration in the cell. The kinetics were recorded at an excitation wavelength of λ_{ex}=532 nm and an emission wavelength of λ_{em}=560 nm. These wavelength were chosen to match the laser excitation light and the filter characteristics used in the SPFS experiments (Nd:YAG laser, λ_{ex}=532, bandpass filter λ=560 nm in front of the PMT). The emission spectrum in Figure 8.3a was measured at an excitation wavelength of λ=510 nm in order to observe detect record the entire emission peak. Due to the

different λ_{ex}=532 nm used for the kinetic experiment the fluorescence intensity in Figure 8.3b is higher than the corresponding value at λ_{em}=560 nm in Figure 8.3a.

The kinetics are depicted in Figure 8.3. The acceptor concentration in the cell was increased stepwise by adding small volumes of a concentrated J1 target solution in PBS. As expected, the fluorescence intensity of this wavelength decreases with increasing acceptor concentration. The perturbations of the fluorescence signal seen directly after each injection originate from stirring the solution after new acceptor was added. This stirring with a spatula was done to assure optimal mixing in the cuvette. The first 200 seconds of each step exhibit strong perturbations due to motion in the solvent and are not taken into account. However, one can still observe, that the fluorescence signal at the donor emission wavelength of λ_{em}=560 nm did not equilibrate later than 4 minutes after each injection. For surface based reactions with unlabelled probes and Cy5 labelled targets stabilisation of the signal at comparable target concentrations takes more than half an hour [47]. In our solution experiment the equilibrium is reached almost instantaneously. After an acceptor/target concentration of c_0=1.25 μM was reached the donor emission was recorded again. A clear reduction in the fluorescence intensity (Figure 8.3a) due to the interaction between the two nucleotide coupled dyes was observed.

Stern Volmer Plot

Considering the observed effect to be a simple quenching effect of the donor by the acceptor, it is useful to plot the quenching data in a Stern-Vollmer plot as normalized fluorescence F_0/F versus the concentration C of the quencher. F_0 and F are the intensity in the absence and presence of the quencher, respectively. As seen from Figure 8.3c the obtained curve (black squares) deviates from linearity strongly as we approach higher concentrations of the acceptor and a clear upwards curvature towards the F_0/F axis is observed. Generally, this upwards curvature indicates, that more than one quenching process has to be considered. In addition to collisional deactivation of the donor, the influence of static quenching by formation of a non-fluorescent ground state complex of fluorophore and quencher (acceptor) has to be considered. After all, static quenching seems to be reasonable, since donor and acceptor are bound to two complementary DNA strands. Duplex formation in solution leads to a proximity of both dyes and therefore strong interaction between both fluorophores.

A common method to separate static and collisional quenching is to construct a modified Stern-Volmer plot of $K_{app} = ((F_0/F)-1)/C$ versus C. Generally this permits a graphical separation

by determining the intercept and slope of the linear dependence (chapter 2.1.3). However, in Figure 8.3c a clear deviation of K_{app} (white squares) from linearity is seen for higher concentrations. Thus, the application of a simple quenching theory seams not appropriate to explain the fluorescence decrease. Additional factors have to be considered:

- inner filter effects of the sample and re-absorption of the donor fluorescence by the acceptors in solution due to the spectral overlap of the acceptor absorption and the donor emission
- resonance energy transfer from the donor to the acceptor of strands that are not bound permanently, but come into proximity statistically.

To prove that the strong decrease can be attributed to hybridisation, unlabelled target strands of the same complementary base sequence (MM0) were added. The concentration of the unlabelled targets was chosen to be identical to the one of the acceptor labelled target J1 (c_0=1,25 uM) in solution. Figure 8.4 shows the competitive replacement kinetics of the labelled targets by unlabelled species. These kinetics were monitored at λ_{ex}=532 nm λ_{ex}=560 nm. With time, the labelled targets are replaced resulting in a recovery of the donor fluorescence at λ_{ex}=560 nm. After 10 hours about 60% of the initial donor fluorescence were reached as determined from the emission spectra in Figure 8.3 a.

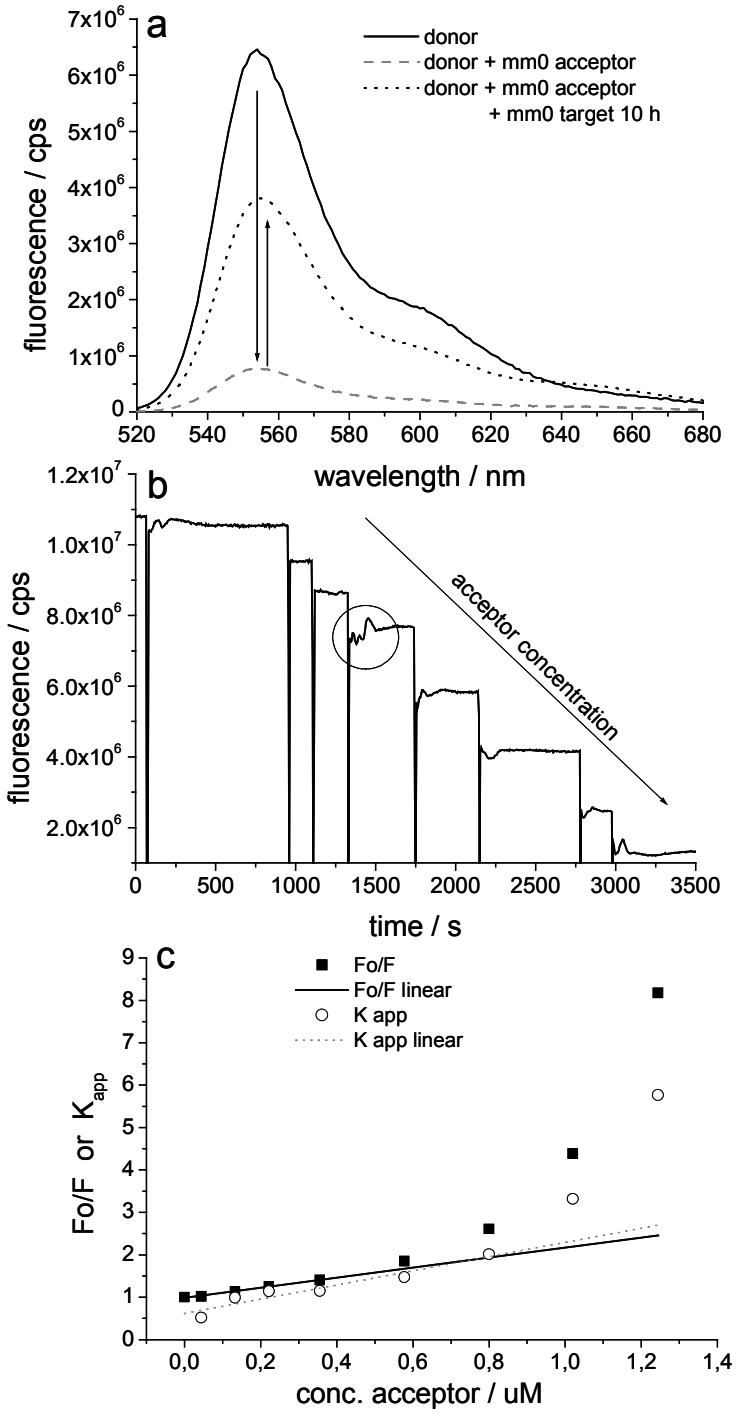

Figure 8.3 : Hybridisation of donor labelled probe H1 at c=1uM in PBS at increasing concentration of the acceptor labelled target J1(0, 0.044, 0.133, 0.222, 0.3555, 0.5777, 0.8, 1.02, 1.244 uM. a) emission spectra (λ_{ex}=510 nm) before and after hybridisation to acceptor labelled target and after replacement reaction with unlabelled target sequences, b) hybridisation kinetics at increasing acceptor concentration monitored at λ_{em}=560 nm and λ_{ex}=532 nm. The perturbations indicated by the circle are to be disregarded. c) Stern-Volmer plots of the fluorescence intensities as a function of the acceptor concentration.

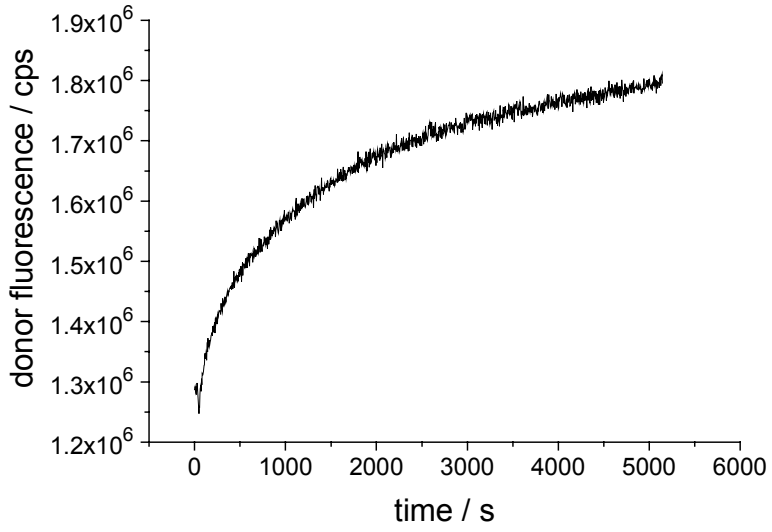

Figure 8.4: Replacement kinetics of labelled MM0 target J1 by unlabelled targets of the same complementary (MM0) as measured at λ_{em}=560 nm and λ_{ex}=532 nm.

Resonant energy transfer from the donor to the acceptor dye is not only characterised by a decreasing of the donor emission. If the acceptor dye is a fluorescent molecule also an increase in the acceptor emission is expected. However, in our solution based hybridisation experiments no such increase was seen when the donor was excited at λ_{ex}=532 nm and the acceptor signal was monitored at λ=650 nm (not shown). Following processes can be envisaged to contribute to the donor fluorescence decay in the presence of the acceptor:

- energy is transferred from the donor to the acceptor by Förster mechanism, but the acceptor is not able to emit fluorescence due to quenching or other deactivation processes.
- both, the donor and the acceptor fluorescence is simply quenched by the proximity of the two dyes due to the formation of non fluorescent ground state complexes (static quenching).

UV Spectroscopy of the Donor at Increasing Acceptor Concentration

In order to search for complexes that might have been formed between donor and acceptor, absorption spectra of the donor at concentration of c_0=1 μM were measured in PBS. The acceptor concentration was increased stepwise and the absorption was measured for wavelengths between λ=425 nm and 700nm for each concentration. The obtained spectra in Figure 8.5 revealed a strong increase in absorbance at λ=628 nm with increasing acceptor concentration.

Compared to this the absorption maximum of a 1uM acceptor solution in PBS was found at λ=621 nm. The position of the maximum of the donor absorption at λ=535 nm is not influenced by the presence of the acceptor. Except for the slight shift in the acceptor maximum no evidence for the formation of a complex between donor and acceptor dye was found by UV spectroscopy.

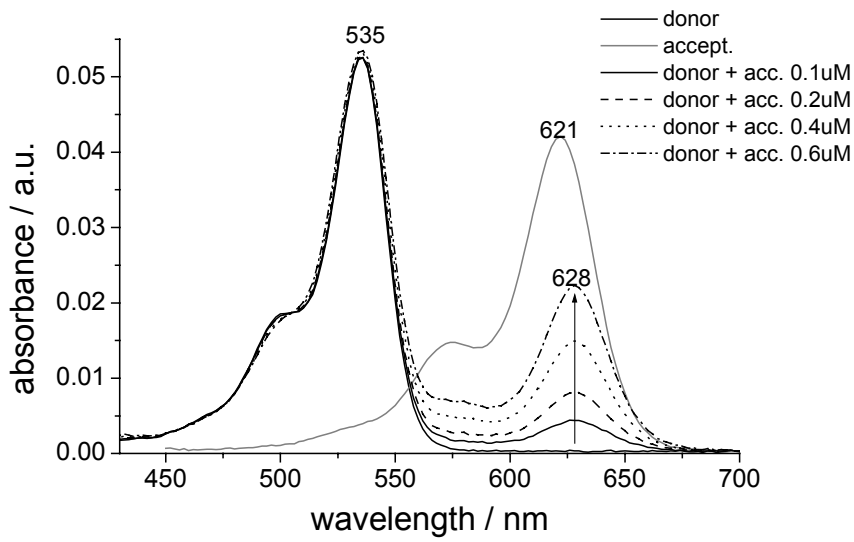

Figure 8.5 : UV absorptions spectra of the probe H1 (c=1μM), acceptor J1 (c=1μM) and mixtures of probe(c=1uM) and increasing target concentration in solution. Except for the increase in absorption at λ=628nm no additional peaks were found upon adding J1.

8.2.2 Increasing Donor Concentration at Constant Acceptor Concentration

It was investigated how the presence of the donor labelled probe influences the emission characteristics of the acceptor. A 1 μM solution of labelled target J1 was prepared in PBS and excited at λ_{ex}=632nm (in analogy to HeNe laser excitation in the SPFS experiments). The H1 donor concentration in the solution was increased stepwise and fluorescence intensity was measured at λ_{em}=650 nm. As show in Figure 8.6 b, a clear decrease of the acceptor fluorescence intensity was seen upon increasing the donor concentration in the cell. The same behaviour is seen in the emission spectra of the acceptor measured before and after hybridisation to the donor labelled probes Figure 8.6 a).

This experiment proves that the acceptors emission is quenched quenching in the presence of the donor. Re-absorption and inner filter effects are not assumed to contribute to the experimental observations, since the donor does not absorb in the wavelength range of the acceptors emission (Figure 8.2). It seems reasonable that static quenching of prevents the

fluorescence of both dyes from being emitted if donor and acceptor are brought into contact by hybridisation.

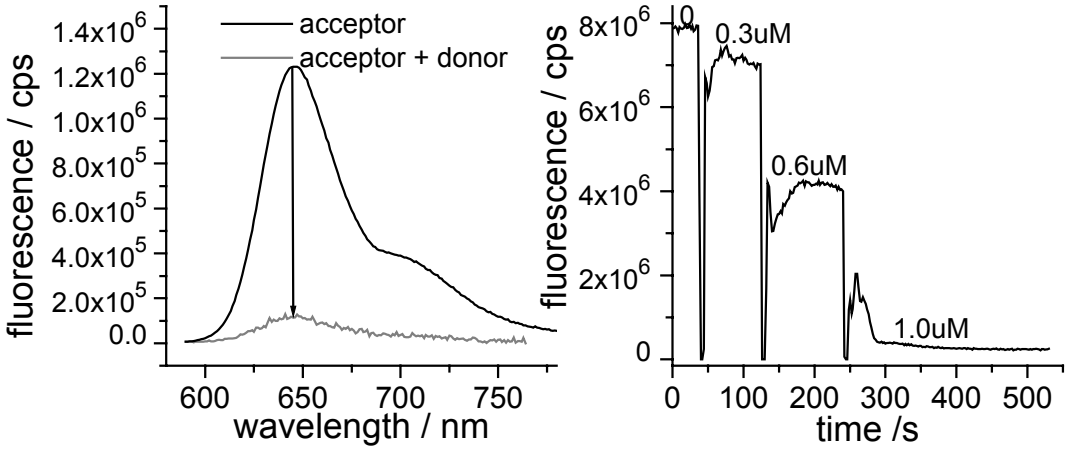

Figure 8.6 : Acceptor and increasing donor concentration, a) emission spectra (excitation 580 nm) before and after hybridisation, b) fluorescence kinetics measured at λ=632nm excitation and λ=650 nm emission wavelength at increasing donor concentration.

8.2.3 Fluorescence Spectroscopy of Immobilised Probes in Reflection

The experiments in solution raised the question about the behaviour of the surface immobilised fluorophores. Differences to the solution based experiments could be caused e.g. by a limited accessibility of the probes for the diffusing targets near the surface. Therefore, hybridisation experiments with the surface immobilised HEX labelled probe H1 were performed. The probe sequences were immobilised via a streptavidin matrix on a Ag-Au substrate as schematically depicted in Figure 8.8. Fluorescence spectra and kinetic measurements were carried out in reflection using of the front face mode of the instrument. The observed excitation and emission spectra of the immobilised donor appeared to be identical to the ones measured in solution (Figure 8.2)

After rinsing the sample with analyte free PBS buffer the acceptor concentration was increased and the fluorescence intensity was measured at λ_{em}=560 nm. Similar to the solution based experiments in chapter 8.2.1, the intensity at this wavelength is decreasing due to the interaction between the dyes (Figure 8.7 b). In contrast to the solution based experiments the donor signal reached a minimal value already at an acceptor concentration of c=0.18 μM. Further addition of acceptor did not reduce the signal anymore.

The amount of surface bound donor molecules in this experiment is small compared to the concentration of donors in the solution based experiments. Therefore a smaller acceptor concentration (c=0.18uM) is sufficient to saturate all donor moieties in the system. This concentration would be too small to bind all donors in the 1uM solution used in Figure 8.3.

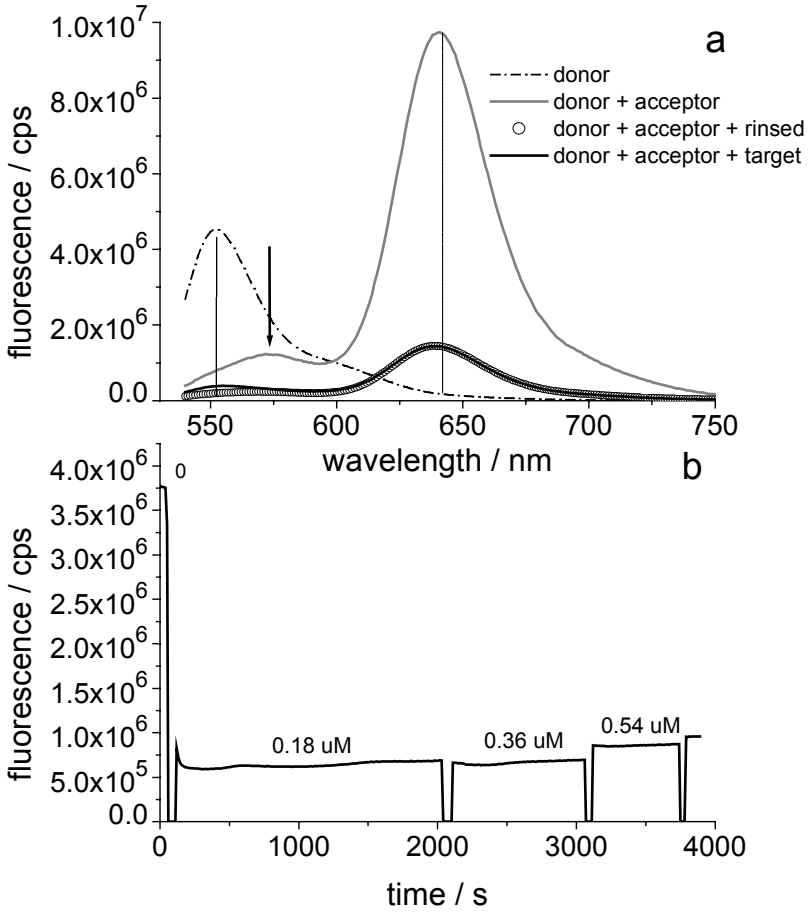

Figure 8.7: a) Emission spectra in reflection at λ_{ex}=510 nm before and after hybridisation of JA270 labelled target to immobilised HEX labelled donor. The large drop in fluorescence after rinsing is due to the removal of bulk acceptor in solution b) fluorescence signal at λ_{em}=560 nm emission at increasing acceptor concentration

When the hybridisation reaction was finished, an emission spectrum was recorded before and after exchanging the acceptor solution in the cell by analyte free PBS buffer. Figure 8.7a a substantial loss in signal at λ_{em}=640 nm was seen upon rinsing due to the removal of acceptor dye in bulk solution. This huge background fluorescence is typical for non-evanescent fluorescence techniques. This proves the advantage of surface-enhanced fluorescence techniques like SPFS. If fluorophores are excited using evanescent fields on surfaces the background fluorescence is almost negligible, as seen in chapter4.

In the kinetic in Figure 8.7b a slight increase in the fluorescence emission at λ_{em}=560 nm was observed for higher acceptor concentrations. This increase is caused by the additional peak at λ_{em}=574 nm the flank of which still seen at the observation wavelength of λ_{em}=560 nm (Figure 8.7 a). This peak was not observed before and does neither belong to the pure donor nor to the acceptor in solution (compare Figure 8.2). Either the acceptor fluorescence was altered due to the proximity to the metal surface or the emission at λ_{em}=574nm is due to fluorescent species formed by donor and acceptor. In none of the solution experiments a maximum at this wavelength was observed. Therefore this peak it is attributed to be presence of the gold surface.

After completed hybridisation reaction the donor emission at λ_{em}=560 nm was found to be quenched. This result was already observed for the solution experiment in 8.2.1. The not vanishing intensity at λ_{em}=640 nm can be attributed to acceptor molecules on the surface.

The obtained experimental results are compared to analogous investigations using excitation evanescent surface plasmon fields in the following chapter.

8.3 Characterisation of the Dyes on the Surface using SPFS

The behaviour of the fluorophores in the surface plasmon enhanced evanescent field near metal surfaces was investigated. The fluorescence signal of the HEX donor labelled probe and the JA270 acceptor labelled target were measured on the surface using surface plasmon fluorescence spectroscopy (SPFS). The donor was excited by NdY:AG laser light of λ_{ex}=535 nm wavelength, while the acceptor was excited using Helium-Neon laser light of λ_{ex}=632.8 nm wavelength. The probe sequences were immobilised onto the streptavidin layer system (Figure 8.8.) in order to obtain following layer architecture:

AgAu / thiols / streptavidin / biotinylated donor probe

The preparation and characterisation of the underlying layers using SPS was already discussed in chapter 6.3.

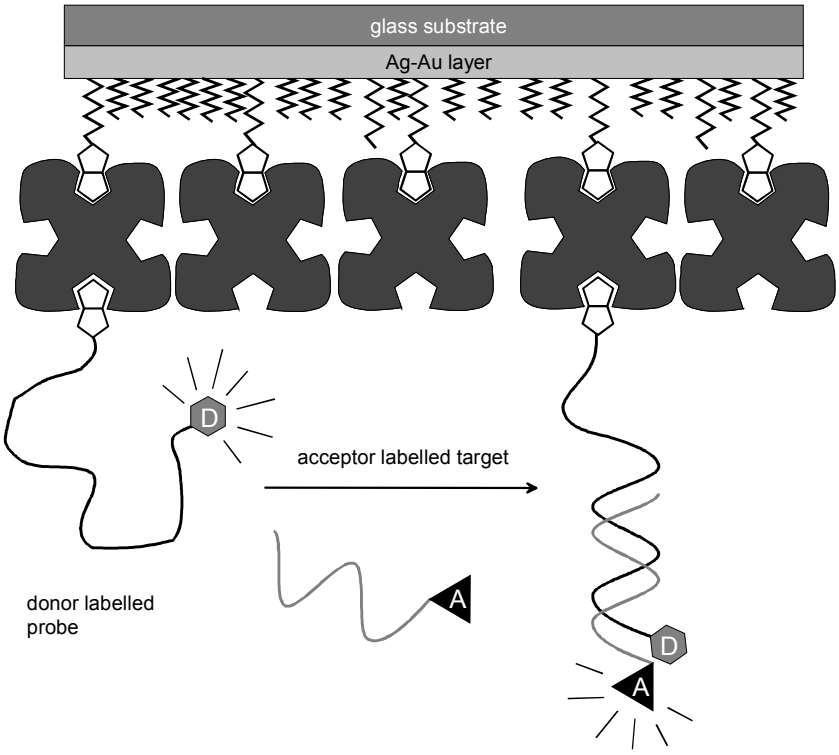

Figure 8.8 : The layer architecture used for FRET experiments on the surface (from top to bottom): LaSFN9 glass substrate, 40 nm silver plus 5 nm gold, thiol layer consistent of biotinylated and hydroxylated thiols, streptavidin layer and HEX donor labelled probe. The fluorescence of donor and acceptor is monitored upon binding of the acceptor labelled targets.

In contrast to the hybridisation experiments with Cy5 labelled targets in chapter 6, gold was not suitable as metallic substrate for the excitation of surface plasmons at λ_{ex}=535 nm. The resonance dip for light of this wavelength appeared very broad (not shown). This resulted in experimental difficulties in recording the entire SPFS fluorescence scan against aqueous solution. In order to keep the half width of the resonance small, a 40 nm thin silver film was used instead. The silver was covered with a 5 nm thin gold film in order to enhance the thiol adsorption ability and to stabilise the film against buffers.

To avoid photo bleaching of the dyes a programmable shutter system was used to block laser irradiation from the sample at times where no data points were taken (every 1-5 min). By a combination of bandpass and edge filters in front of the PMT donor and acceptor fluorescence could be detected almost independent of each other and incident laser light was blocked. Figure 8.9 shows the transmittance of these filter combinations in comparison to the excitation and emission spectra of the donor and acceptor. Only a small part of the donor emission could not be filtered out at λ_{em}=650nm.

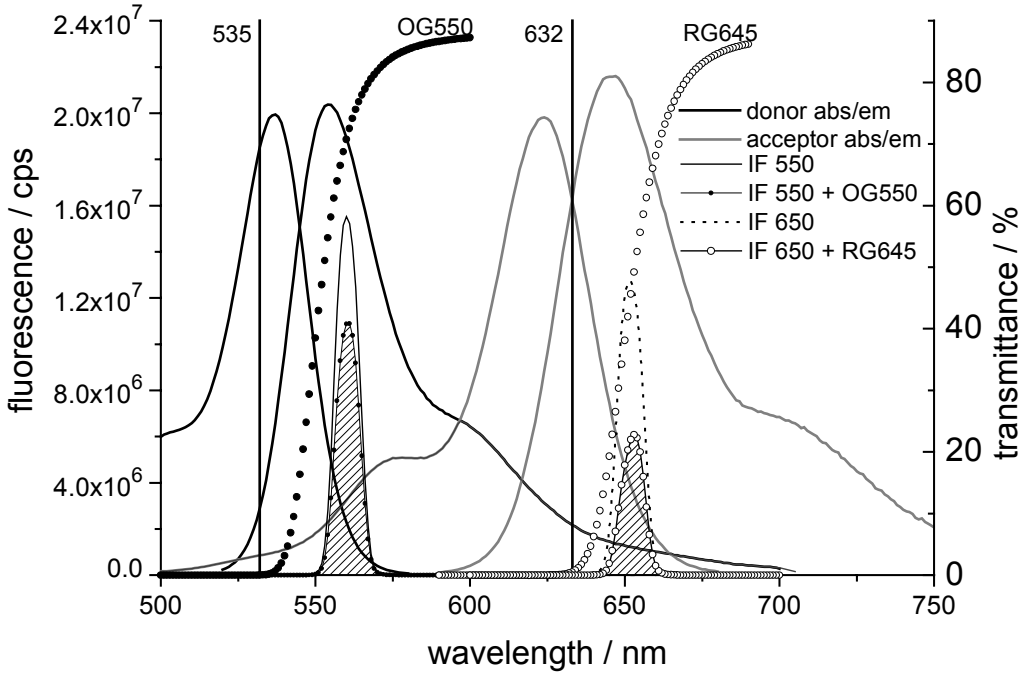

Figure 8.9 : UV spectra of the filter combinations in comparison to the fluorescence spectra of the donor and acceptor dye. The transmittance of bandpass filters IF 550, IF 650 and edge filters OG550, RG645 are shown. The excitation light of HeNe and NdY:AG laser at λ_{ex}=632.8 nm and λ_{ex}=535 nm are indicated as vertical lines.

8.3.1 Hybridisation Between Donor and Acceptor on the Surface

The labelled probe H1 was immobilised by a self assembly process from a 5 µM PBS solution and the process was monitored using SPFS at an excitation wavelength of λ_{ex}= 535 nm and an emission wavelength of λ_{em}=560 nm. After equilibrium was reached the cell was rinsed with analyte free PBS buffer. The rinsing caused a drop in fluorescence (not shown) which is attributed to the desorption of loosely bound probes from the surface. The formation of self annealed probe-probe complexes was already discussed in chapter 1. The hybridisation process was induced by the injection of a 1 µM solution of fully complementary (MM0) acceptor labelled target J1. The reaction was monitored by scan curves recorded at both excitation wavelength (λ_{ex}= 535 nm and λ_{ex}= 632.8 nm) and emission wavelength (λ_{em}=560 nm and λ_{em}=650 nm).

In Figure 8.10a a decrease in the donor fluorescence at λ_{em}=560 nm (excitation at λ_{ex}=535 nm) is clearly seen upon hybridisation. This behaviour is in good comparison to the solution based experiments in chapter 8.2 and can be explained by quenching the donor

fluorescence in the vicinity of the acceptor. An increase in acceptor fluorescence is not detectable at λ_{em}=650 nm (at the same excitation wavelength of λ_{ex}=535 nm) in Figure 8.10 b. Contrastingly, a moderate decrease is found at this wavelength. This was attributed to the fraction of donor fluorescence at 650 nm, which was not blocked out by the filter combination (see Figure 8.9) and hence was representing the quenched donor fluorescence.

When the target J1 was excited directly at λ_{ex}=633 nm, a small emission at λ_{em} =650 nm was observed, indicating the successful binding of the targets to the immobilised probes. Compared to previous SPFS hybridisation experiments using unlabelled probes/labelled targets the observed fluorescence intensity appears small. This is due the quenching of the acceptors in contact to donor molecules as observed in chapter 8.2.2. When the acceptors were removed by denaturation due to three subsequent injections of 0.1M NaOH the donor intensity at λ_{em}=560 nm was recovered to the initial level before hybridisation (Figure 8.10 a).

This experiment demonstrates the potential of monitoring binding events on surfaces by the investigated set of dye molecules. The recovery of the donor emission upon denaturation indicates the reversibility of the hybridisation reaction by harsh conditions and permits recycling of the sensor surface.

In the following paragraph it was investigated if the fluorescence characteristics of donor and acceptor are influenced by the interaction with the oligonucleotide strand of probe and target. This was done by performing hybridisation experiments between Förster labelled sequences and unlabelled complements.

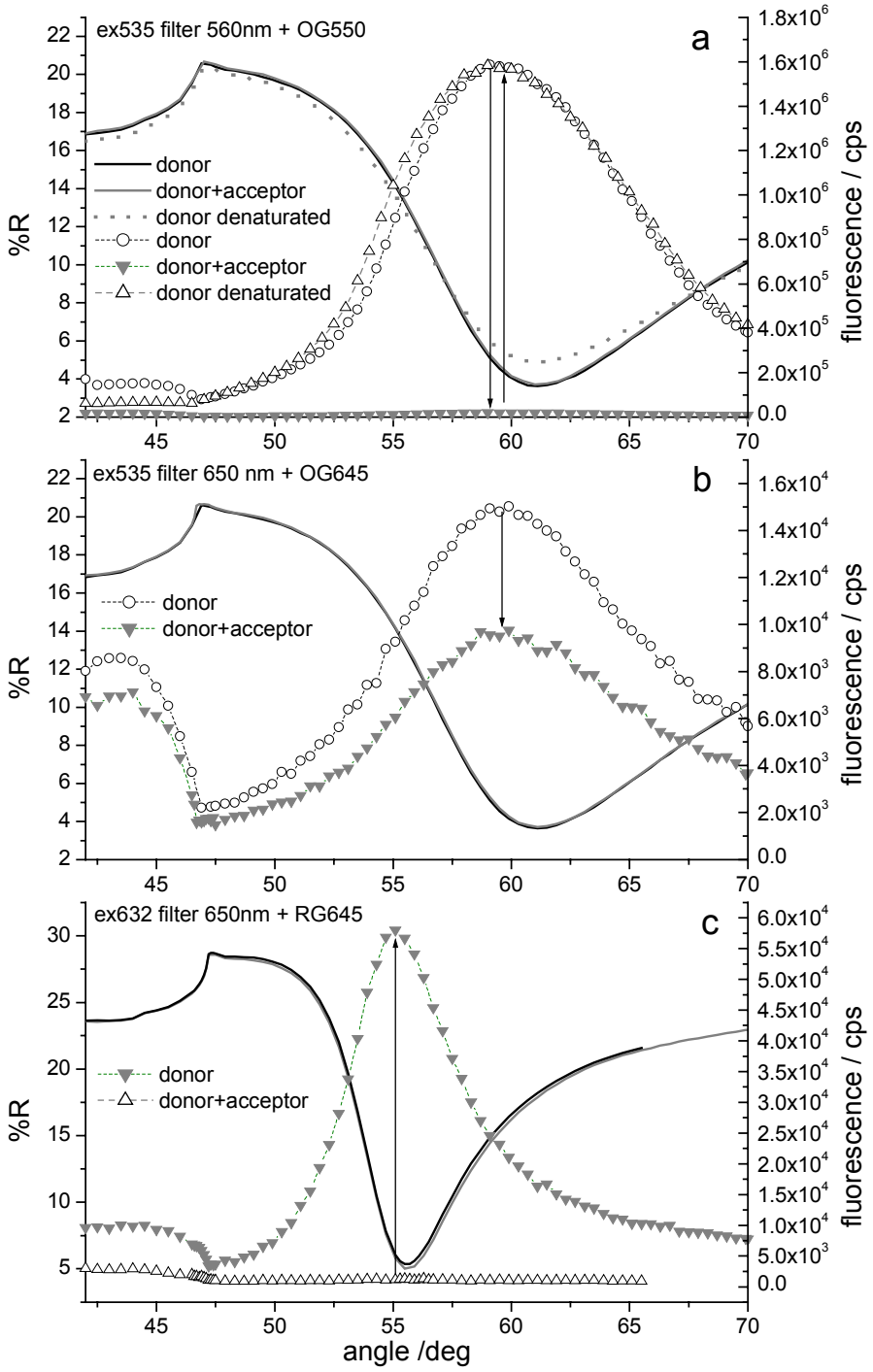

Figure 8.10 : Hybridisation of acceptor labelled target J1 to donor labelled probe H1, immobilised on a streptavidin matrix. a) A substantial decrease in the donor fluorescence at λ_{em}=560 nm is seen upon binding of the acceptor, while subsequent denaturation removes the targets and causes a recovery of the intensity, b) no gain in acceptor fluorescence was observed at λ_{em}=650 nm. The slight decrease at λ_{em}=650 nm upon hybridisation was attributed to the fraction of donor signal which could not be blocked at this wavelength, c) excitation of the acceptor at λ_{ex}=632nm results in a small fluorescence signal, indicative of successful binding to the immobilised probes.

8.3.2 Hybridisation Between Labelled and Unlabelled Strands

The influence of the complementary oligonucleotide strand on the dyes was investigated.

Donor Labelled Probes and Unlabelled Targets

Donor labelled probes H1 were immobilised on the streptavidin monitored at λ_{ex}=535 nm and λ_{em}=560 nm. This led to a fluorescence level of 1.7 Mio cps (Figure 8.11a), a value comparable to the intensities achieved in the last experiment (Figure 8.10a). Subsequent injection of a 1 µM solution of unlabelled MM0 targets caused a noticeable increase in the donor fluorescence (compare Figure 8.11a). This increase in fluorescence was attributed to conformational changes in the single stranded probe upon forming stiff helical duplex structures. This effect was already discussed in chapter 7.

The hybridisation kinetics of the MM0 unlabelled target are shown in Figure 8.11b. The kinetics could be simulated using a regular Langmuir model as introduced in chapter 2.2. After completed hybridisation of the unlabelled targets the flow cell was rinsed with analyte free PBS buffer. Subsequently, acceptor labelled target J1 of the same complementary was added by injecting a 1 µM target solution in PBS. As a result, bound unlabelled targets were replaced competitively by the acceptor labelled targets. This led to a quenching of the donor fluorescence at λ_{em}=560 nm as clearly visible in Figure 8.11a. Direct excitation of the acceptor at λ_{ex}=632.8 nm yield a fluorescence intensity of about 45000 cps at λ_{em}=650 nm. This value is comparable to the previous quenching experiment (Figure 8.10c) and indicates that the acceptor labelled target has replaced the unlabelled by binding to the surface.

Unlabelled Probes and Acceptor Labelled Targets

Unlabelled probe sequences were immobilised and Ja270 labelled MM0 targets hybridised at a target concentration of 1 µM in PBS. The hybridisation kinetics measured at λ_{ex}=632.8 nm and λ_{em}=650 nm are shown in Figure 8.12. The adsorption process could be simulated by a single exponential Langmuir model. The observed high intensity proves that the fluorescence intensity was not influenced by the proximity to the immobilised oligonucleotide strand.

In summary, it was shown that the quenching effect upon hybridisation between donor labelled probe and acceptor labelled target was not caused by the presence of the complementary oligonucleotide strand. In combination with an unlabelled partner each of the labelled strand

exhibited relatively high fluorescence intensity. The corresponding hybridisation kinetics were found to follow regular Langmuir simulations. Therefore any quenching effects and deviation from the Langmuir model between donor labelled probe and acceptor labelled target must be caused by the interaction of the dyes.

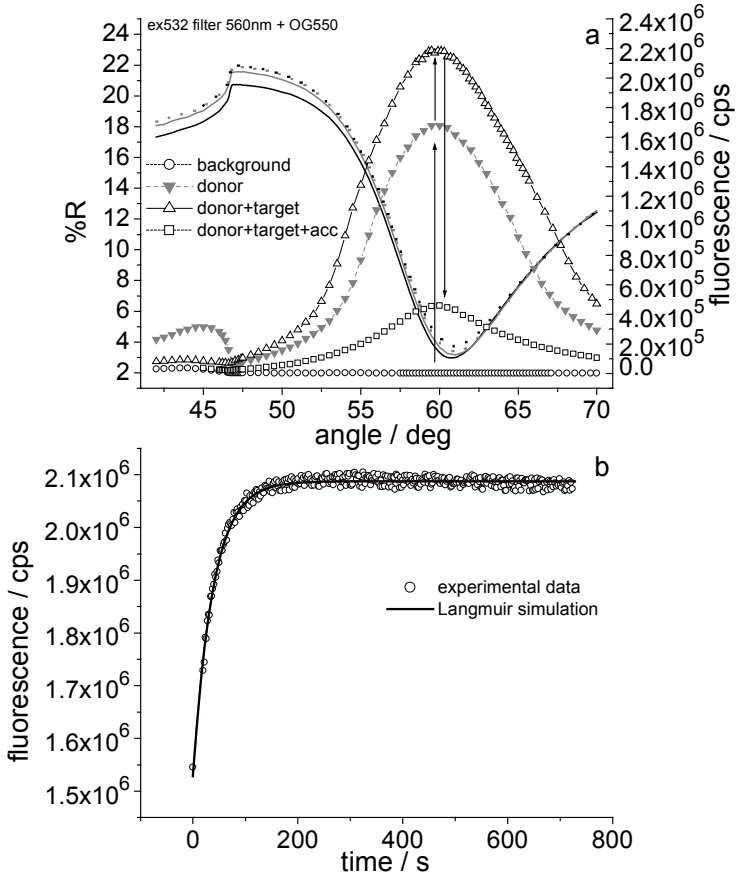

Figure 8.11 : Hybridisation of immobilised donor labelled probe and unlabelled target, a) Scan-curves illustrate the increase in donor fluorescence upon binding of the unlabelled targets followed by a decrease by interaction with additional acceptor, b) hybridisation kinetics of the unlabelled complement to the surface bound donor probes

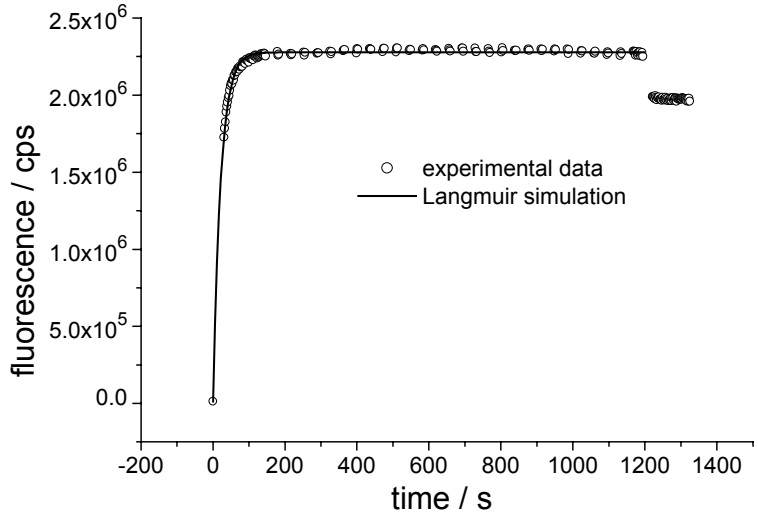

Figure 8.12 : Hybridisation kinetics of JA270 labelled target to unlabelled probe

8.3.3 Detection of Single Base Mismatches using FRET

In DNA sensors fluorescent oligonucleotides are used to sense single base mismatches in target sequences. The mismatch discrimination sensitivity of the set of labelled probes and targets was investigated in the following:

Determination of Equilibrium Constants

It was investigated if the hybridisation between the labelled probes and labelled targets still followed the Langmuir picture. The equilibrium constant of the MM1 system was determined by recording a Langmuir isotherm as described in chapter 2.2. The signal of the immobilised probes was measured at λ_{ex}=535 nm and λ_{em}=560 nm as the target concentration in the cell was increased stepwise. Hybridisation of the target saturated the binding sites on the surface successively, indicated by the quenched donor fluorescence (Figure 8.13a). After complete saturation the measured fluorescence intensities were plotted versus target concentration in Figure 8.13 b. The surface coverage for each saturation step can be calculated to the steady state Langmuir solution in equation (2.18). However, the donor fluorescence decreased with increasing surface coverage. Therefore the equilibrium value for the fluorescence is given by:

$$F = I_{\max} - (I_{\max} - I_0) \cdot \left(\frac{c_0 \cdot K}{1 + c_0 \cdot K} \right) \qquad (8.1)$$

with I_{max} and I_0 being the maximal and minimal fluorescence intensities, respectively, c_0 being the concentration of the target in solution and K being the equilibrium constant of the reaction.

The measured data were fitted according to this equation and the resulting Langmuir isotherm is plotted in Figure 8.13. The equilibrium constant of the MM1 system was determined to $K = 1.3 \cdot 10^8 M^{-1}$ .This value is about one order of magnitude higher than the corresponding value for the system unlabelled probe P2/labelled target from 6.4. The Langmuir model assumes that the individual kinetics for each saturation step can be fitted using the same kinetic constants. This however was not the possible for the measurements in Figure 8.13. Thus, a derivation from the pure Langmuir behaviour is suggested by the measurements.

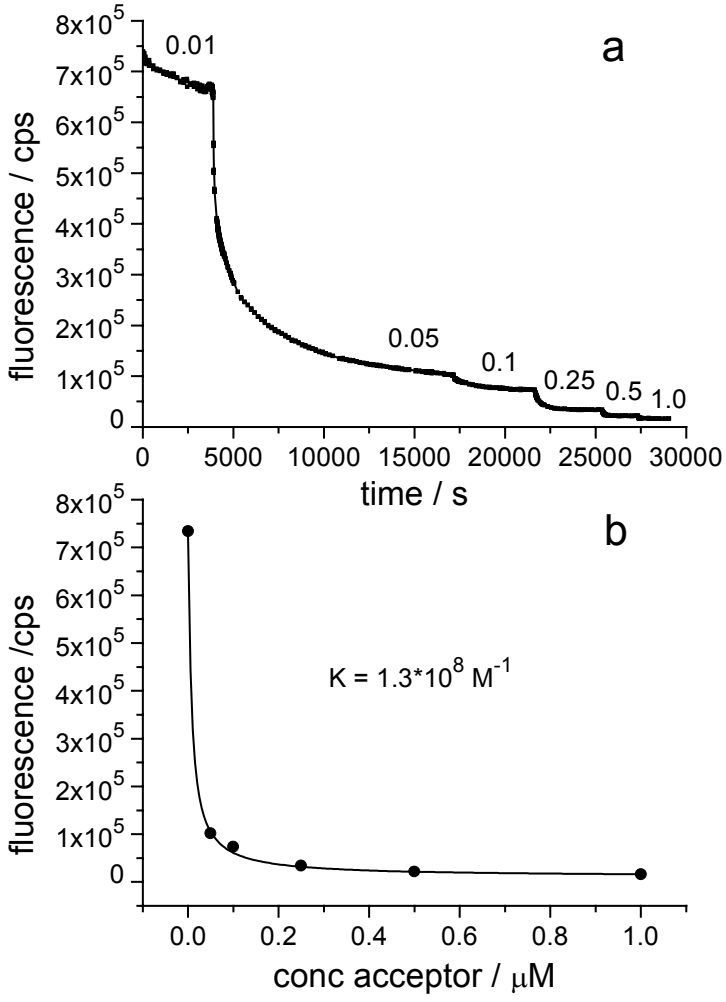

Figure 8.13: Langmuir isotherm of the MM1 system consistent of donor labelled probe H1 and acceptor labelled target J2. a) The fluorescence intensity at λ_{ex}=560 nm decreased with increasing target concentration until the binding places on the surface were all saturated. b) By plotting the fluorescence equilibrium values versus the target concentration the change in intensity was modelled by a Langmuir isotherm, from which the equilibrium constant K could be derived.

Kinetic Constants

In a further experiment the kinetic behaviour of fully complementary and mismatched labelled strands was investigated. The hybridisation kinetics of both targets J1 and J2 to the immobilised probe H1 were recorded at a fixed concentration of c=1μM. Figure 8.14 presents the observed time dependent fluorescence kinetics measured at λ_{ex}=535 nm and λ_{em}=560 nm. The signal drops down to a minimum upon binding of the targets. After 1800 seconds the signal was in stable and the sample was continuously rinsed with pure PBS buffer to desorb the targets from the surface.

As explained in chapter 1, rinsing causes a decrease of the analyte concentration in the solution by some orders of magnitude. Depending on the half-saturation constant of the system the equilibrium at the surface can be shifted towards target desorption. The desorption constant k_{off} was determined by fitting the resulting rinsing kinetics according to equation (2.16). This constant k_{off} used in the calculation of k_{on} by fitting the adsorption process.

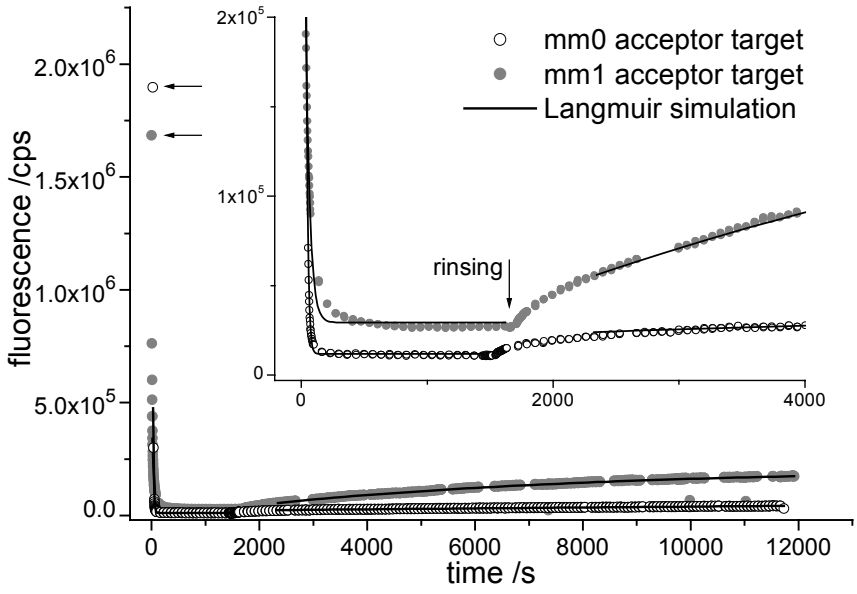

Figure 8.14: Hybridisation kinetics of MM0 and MM1 acceptor labelled target to immobilised donor labelled probe. The fluorescence intensities at the start of the hybridisation and rinsing process are indicated with arrows. Note, that neither of the targets could be rinsed off completely.

Comparing the obtained simulations with the experimental data a virtual agreement is noticeable, but the Langmuir fits were not capable of reflecting the entire kinetics. When the indicated high fluorescence intensities (arrows) were assumed to represented the target surface

coverage of zero, the desorption process could not be fitted by the Langmuir model. The best agreement for both the adsorption and desorption process was obtained by taking into account only the low intensity part of both curves. The kinetic constants derived from these simulations were summarised in Table 8.3. All determined values exhibit a typical error of 10%. The equilibrium constant $K=k_{on}/k_{off}$ of the MM1 system ($K = 1.9 \cdot 10^8 M^{-1}$) was comparable to the one determined from the Langmuir isotherm in Figure 8.13 ($K = 1.3 \cdot 10^8 M^{-1}$).

Additionally, the literature values for the hybridisation between unlabelled probes P2 and labelled targets T1 and T2 [17] on the same streptavidin architectures are given. These sequences are identical to H1, J1 and J2 respectively. MM2 targets to H1 were not available during the experiments and only MM0 and MM1 cases are compared. For fully complementary targets a similar equilibrium constant was found ($K = 6.6 \cdot 10^9 M^{-1}$ $K = 5.3 \cdot 10^9 M^{-1}$). However, the difference to the MM1 sequences in H1 ($K = 1.9 \cdot 10^8 M^{-1}$) was smaller than in the case of P2 ($K = 2.4 \cdot 10^7 M^{-1}$). The MM1 system H1/J2 appeared to be more stable than the analogous combination P2/T1 for unlabelled targets. This was attributed to additional stabilising effects caused by interaction between donor and acceptor dye.

Table 8.3: Kinetic constants determined from Langmuir simulations of MM0 and MM1 hybridisation reactions between Förster dye labelled probes H1 and targets J1 and J2. In comparison the corresponding values for the system P2 from CHAPTER are given.

probe	target	MM	k_{on} / $M^{-1}s^{-1}$	k_{off} / s^{-1}	K / M^{-1}
H1	J1	0	$6.67 \cdot 10^4$	$0.001 \cdot 10^{-3}$	$6.6 \cdot 10^9$
	J2	1	$3.04 \cdot 10^4$	$0.160 \cdot 10^{-3}$	$1.9 \cdot 10^8$
P2	T2	0	$3.69 \cdot 10^4$	$0.007 \cdot 10^{-3}$	$5.3 \cdot 10^9$
	T1	1	$8.94 \cdot 10^3$	$0.370 \cdot 10^{-3}$	$2.4 \cdot 10^7$

Interaction between the labels

In Figure 8.14 a desorption behaviour was found for the MM1 target J2, which was not expected for a mismatched system. In the experiments with P2/T2 (chapter 1), the mismatched targets could be rinsed off with PBS buffer. In our experiments the donor fluorescence could not be recovered by extensive rinsing, indicative of a duplex stabilisation on the surface. This stabilisation is likely to be caused by an interaction between the labels. Note, that the kinetic

constants k_{off} of the J1 target would be much smaller, if the high fluorescence values would be taken into account.

In alternative experiments (not shown) the behaviour of the mismatched system H1/J2 upon competitive treatment with complementary MM0 unlabelled targets T2 was investigated. No difference to the desorption using PBS was observed.

In the used flow cell the target concentration is not reduced to zero in the rinsing step but only reduced by several orders of magnitude. High target concentrations in the hybridisation step could therefore result in target concentration after rinsing still above the half saturation constant of the system. In order to check for saturation of the system hybridisation experiments with J2 were performed at target concentrations of 0.1uM and 0.02uM, respectively. However, a similar stabilisation of the target on the surface was observed. Even an increase in the temperature to 35°C at 0.1uM target concentration did not destabilise the MM1 duplex.

These experiments indicate that strong interaction processes between the dyes stabilise the duplex between the labelled oligonucleotides. The clear difference between MM0 and MM1 observed for the analogous system P2 was not found for the FRET probe H1.

8.4 Conclusion

The use of set donor labelled probes and acceptor labelled target sequences for potential use in DNA hybridisation assays on surfaces was investigated. The labelled sequences were characterised by fluorescence spectroscopy in solution and SPFS on the sensor surface. The spectral properties of the fluorophores were found to be suitable to undergo resonant energy transfer. The partial overlap between the emission of the donor and the excitation of the acceptor permits energy transfer in principle.

In solution a substantial decrease in donor fluorescence was seen upon hybridisation to acceptor labelled targets and a recovery of the signal was obtained by replacing the acceptor labelled targets by unlabelled target of the same complementary.

Surprisingly, the acceptor emission was not increased upon duplex formation. In a separate experiment is could be shown that the acceptor fluorescence was quenched by the presence of the donor. Experiments using unlabelled complements were carried out on the surface using SPFS. These results proved that both the probe H1 and the targets J1 and J2 behaved as expected by the Langmuir model. Furthermore the quenching of donor and acceptor was proven be

caused by donor-acceptor interaction and not by changes in the local environment due to the presence of the oligonucleotide complement.

The potential use of the dyes for mismatch discrimination was investigated by SPFS. A small kinetic difference between MM0 and MM1 targets was observed. However, the discrimination sensitivity of the probe was reduced compared to experiments with the unlabelled probe P2 in 6.3.2. The different stability of MM1 and MM0 duplexes was screened by a stabilisation of the duplex on the surface. This stabilisation was attributed to interactions between both dyes. Changing the experimental conditions like the target concentration and temperature did not reduce this effect remarkably.

Therefore a change in the oligonucleotide structure is recommended. Interactions like π–π–stabilisation between donor and acceptor are only effective at very close distances between the dyes, so that increasing the distance between both dyes could be promising. In further studies it is planned to use target sequences of successive length to define the position of the strands in respect to the labelled end of the probe. By increasing the distance between probe and target energy transfer between the dyes could be still observed without suffering from the stabilising interaction between the chromophores.

If the experimental conditions are optimised the investigated donor-acceptor pair could be applicable for mismatch discrimination in DNA assays. It was shown that resonance energy transfer is a highly sensitive tool for monitoring binding reactions between bio-molecules on surfaces. The FRET detection format known from solution studies could be adapted for surface sensitive detection by SPFS. Since the intrinsic properties of the investigated dye pair complicates the mismatch discrimination the investigation of alternative FRET pairs like CY5/Cy5.5 is recommended.

9 Mismatch Discrimination Using Single Strand Binding Proteins (SSB)

In the last chapters it was demonstrated that the sensitivity of surface plasmon spectroscopy alone is not sufficient to monitor the adsorption of low molecular weight analytes onto immobilised binding partners. In case of the 15 bases long DNA target strands no response in reflectivity was observed upon duplex formation on the surface. This is due to the dilution of the strands on the surface, resulting in a small change in mass upon target hybridisation. Additionally, the hybridisation efficiency was estimated to be far below unity. Hence, various signal enhancement strategies were developed in the past years.

In addition to direct fluorescent labelling of the analytes, a common way to enhance the SPS signal is to form multi-layers in sandwich type assays. Similar to enzyme linked immuno-sorbant assays (ELISA) not the binding of the analyte to the surface itself gives rise to a measurable signal, but an additional agent couples to the bound species and indicates the presence of the analyte by its intrinsic properties. Frequently, antibodies labelled with enzymes (like horseradish peroxidase) are used to identify bound proteins on the surface and subsequent enzymatic reaction leads to detectable products. For bare SPR an increase in adsorbed mass on the surface is sufficient to enhance the signal and hence to follow the immobilisation of the investigated species. In the case of oligonucleotide detection, proteins can be used to enhance the hybridisation signal as shown for biotinylated target sequences and subsequently attached streptavidin [187]. While in this format the streptavidin was just used as an additional bulky mass in order to change the optical properties of the film, other techniques utilise the biological function of the used protein, too. For instance the specificity of MutS, a mismatch repair protein, was used to identify mismatches in target sequences on the surface [188].

In this chapter the use of single strand binding proteins (SSB) for the enhancement of the SPS signal and the simultaneous increase in mismatch sensitivity is investigated. The protein-DNA complex was characterised by common fluorescence spectroscopy in solution and by surface plasmon fluorescence spectroscopy (SPFS) in surface supported hybridisation experiments.

9.1 Structure and Function of SSBs

Single strand binding proteins (SSB) play essential role in DNA replication, recombination and repair [189-191]. They are present in high concentrations in vivo and are presumed to function by binding preferentially to ssDNA. In the process of replication these proteins stabilise the single stranded regions which are formed from a double strand by cooperated action of helicase and Rep-protein in the typical replication fork. More than one single strand binding protein are known, but the one from the bacterium *E.coli* is unique in that it forms homotetramers in solution (4 x 18843 Da) [192]. These tetramers are stable over a wide range of solution conditions[191]. Although the binding of monomers was observed[193] the tetrameric state seemed to be the species that interacts with the oligonucleotide chain. Two different cooperative binding effects can be found between individual SSB tetramers. At low monovalent salt concentrations and a high protein / DNA ratio 'unlimited' cooperative binding results in large protein clusters along the length of ssDNA. However, at high salt concentrations (> 0.2 M NaCl) and low protein /DNA ratio a 'limited' cooperativity is observed. Here only isolated clusters of octamers are observed and the formation of long single cluster along the chain is not possible.

In Figure 9.1 the structure of homo-tetrameric SSB is depicted [194]. The structure of the SSB-DNA complex reveals its perfect D_2 symmetry. A long stretch of ssDNA can by bound and compact by wrapping it extensively around the relatively small protein. The length of the ssDNA bound per tetramer is dramatically effected by the solution conditions and various binding modes can be distinguished [195,196]. These are referred to as $(SSB)_n$, with n=35, 40, 56 or 65 being the average number of DNA bases involved in the binding. At high salt concentration the n=65 mode is dominant, in which all four SSB units are involved in binding the ssDNA strand. In this mode the tetramers are in equilibrium with octamers, thus promoting the 'limited' type of cooperativity and interfering with the formation of a single cluster along the strand. However, at low salt concentration the binding mode $(SSB)_{35}$ is dominant. Due to the strong salt dependent negative intra-molecular cooperativity between the individual SSB subunits [197] the ssDNA strand interacts only with two subunits of the tetramer (Figure 9.1). Due to 'unlimited' positive cooperativity between the tetramers, long SSB clusters along the ssDNA chain are likely to be formed.

SSBs are named due to their preference to bind single stranded DNA. It was investigated if the proteins can be used as transducers for the discrimination of single and double strands in SPS sensor formats. Post hybridisation treatment with SSB proteins can enhance the reflectivity signal

due to the additional mass adsorbed to the sensor surface. The replacement kinetics between SSBs and complementary as well as mismatched fluorescent labelled targets were analysed to estimate the kinetic influence of the proteins. In this model system, the targets were fluorescently labelled to monitor their ad- and desorption. Once the kinetic behaviour of the protein replacement is known, the detection scheme can be extended to unlabelled targets.

Figure 9.1 : Structure of tetrameric E.coli SSB in the the $(SSB)_{35}$ mode, binding a 35 bases long oligonucleotide (black) [194]

9.2 Immobilisation of SSB on the Sensor Surface

In order to investigate the replacement kinetics between SSBs (Pharmacia Biotech) and targets a streptavidin matrix was formed as described in chapter 6.3.1 and as schematically depicted in Figure 9.3. The extend of unspecific binding was determined by applying a 0.1uM *E.coli* SSB solution in PBS buffer to the unloaded streptavidin layer. As shown by the corresponding SPS kinetics in Figure 9.2, a reflectivity jump due to the change in bulk refractive index was observed after injection of the protein solution. However, the initial reflectivity was recovered after rinsing the flow cell with protein-free PBS buffer. Thus, non-specific adsorption of SSBs to the streptavidin surface can be excluded in the further investigation.

Since peptide nucleic acids (PNA) were planned to be used in parallel projects, the binding of SSB on these synthetic molecules was tested, too. In contrast to DNA the backbone of PNA consists of an uncharged quasi-peptide backbone. Biotinylated PNA was immobilised on the streptavidin from a 1uM solution in PBS and the adsorption was investigated by SPS. Figure 9.2 shows the subsequent reaction with SSB at a 0.1uM solution in the same buffer. Similar to the unloaded streptavidin surface the initial reflectivity was recovered after rinsing, indicative of a non evident binding of SSB to PNA. This result seems reasonable, since the backbone of PNA in

uncharged due to the lack of negative phosphate groups. Thus the necessary electrostatic interaction with the protein surface is missing.

In contrast to this, a non vanishing optical thickness is obtained, if SSBs are reacting with immobilised DNA probes P2, the structure of which are given in Table 6.1. Upon rinsing there was a drop in reflectivity seen, similar to that for the PNA and the unloaded streptavidin. This is regarded as a proof that the signal change for PNA and unloaded streptavidin matrix was only due to a bulk refractive index change

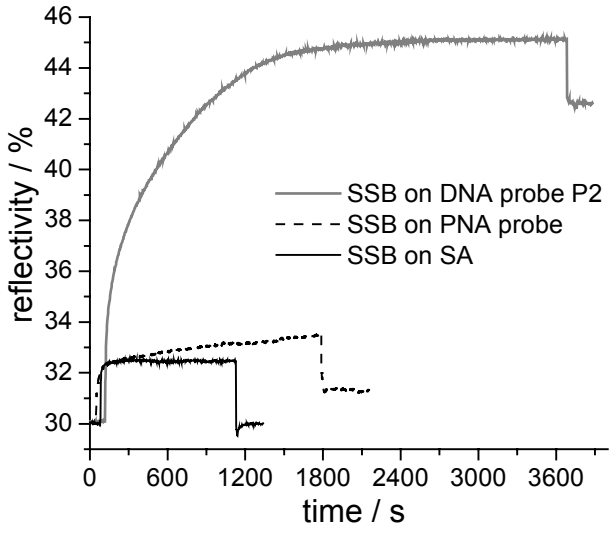

Figure 9.2 : Adsorption kinetics of SSB onto unmodified streptavidin matrix, a PNA probe and the DNA probe P2

Since the used DNA probe has a length of 30 bases in total and the favoured binding mode at low salt conditions in PBS (0.1M NaCl) is the $(SSB)_{35}$ mode only one SSB tetramer can bind to a single probe strand. The expected inter-protein cooperativity along the backbone can be neglected here. However, the adsorption kinetics of SSB on P2 in Figure 9.2 clearly deviate from a single exponential. Thus, the simple Langmuir model does not describe the adsorption of the proteins completely anymore. Effects like cooperative binding effects and steric hindrance between proteins complexes on neighboured probe strands are believed to be responsible for this deviation.

9.3 Replacement between Proteins and Targets

In the last chapter it has been shown that SSBs show no detectable binding to the underlying streptavidin matrix. In contrast, a distinct binding to the 30 bases long P2 sequences was observed. In the following it was investigated how the proteins influence the hybridisation kinetics of complementary and mismatched targets.

Replacement of SSB by Targets

As outlined in chapter 1 fully complementary targets sequences (MM0) differ from mismatched ones (MM1, MM2) in their hybridisation kinetics. Here, it is investigated if the concurrence situation to probe bound proteins can influence the hybridisation reaction.

The immobilised probes were loaded with proteins as described in the last chapter, resulting in a situation as schematically depicted in Figure 9.3a. Subsequently, MM0 and MM1 labelled targets were tested for their ability to replace the proteins from the surface by binding to the probes (Figure 9.3b). The replacement kinetics were monitored by SPFS and both the reflectivity and the corresponding fluorescence signal are plotted in Figure 9.4.

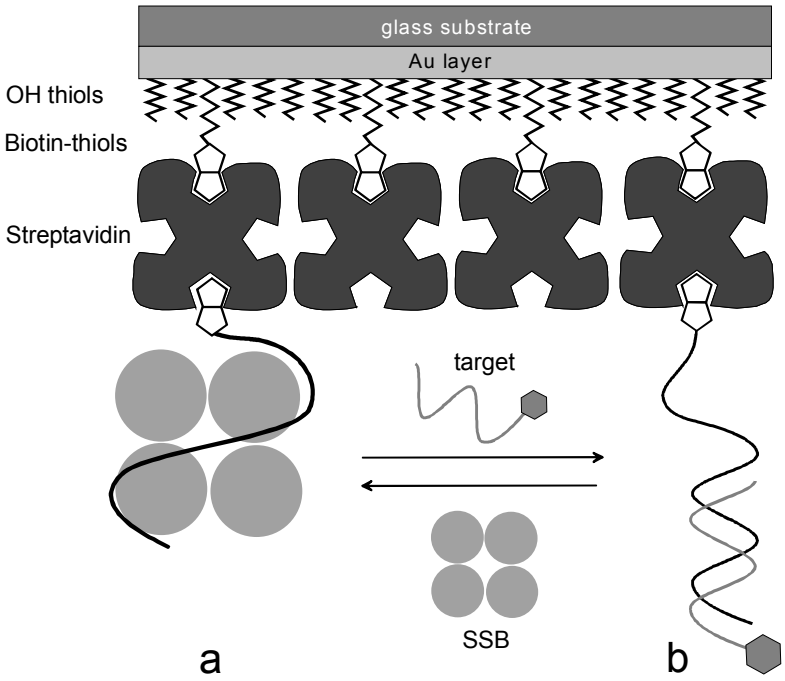

Figure 9.3 : Schematic presentation of the replacement reaction between single strand binding proteins (SSB) and labelled target strands bound to immobilised probes

Upon injection of a 1uM solution of MM0 target in PBS buffer, a substantial decrease in reflectivity was observed. This was attributed to the removal of the SSB tetramers from the surface (Figure 9.4a). Simultaneously, the fluorescence signal increased due to hybridisation of the labelled targets to the immobilised probes. After rinsing with PBS buffer, a 0.1uM solution of

SSB was applied again to check the reversibility of the reaction. The initial reflectivity of about 30% was recovered completely after about 45 min, but the fluorescence signal of the targets was not equilibrated at this time, yet. The replacement of targets by SSB will be discussed in the next paragraph. However, when a SSB loaded surface was treated with a 1uM solution of labelled MM1 target (Figure 9.4b) the change in both reflectivity and fluorescence was negligible compared to the recorded value for fully complementary sequences. An initial signal jump directly upon injection was seen for both the MM0 and MM1 case. It resulted from the changed bulk refractive index and eventually a removal of loosely bound proteins from the surface.

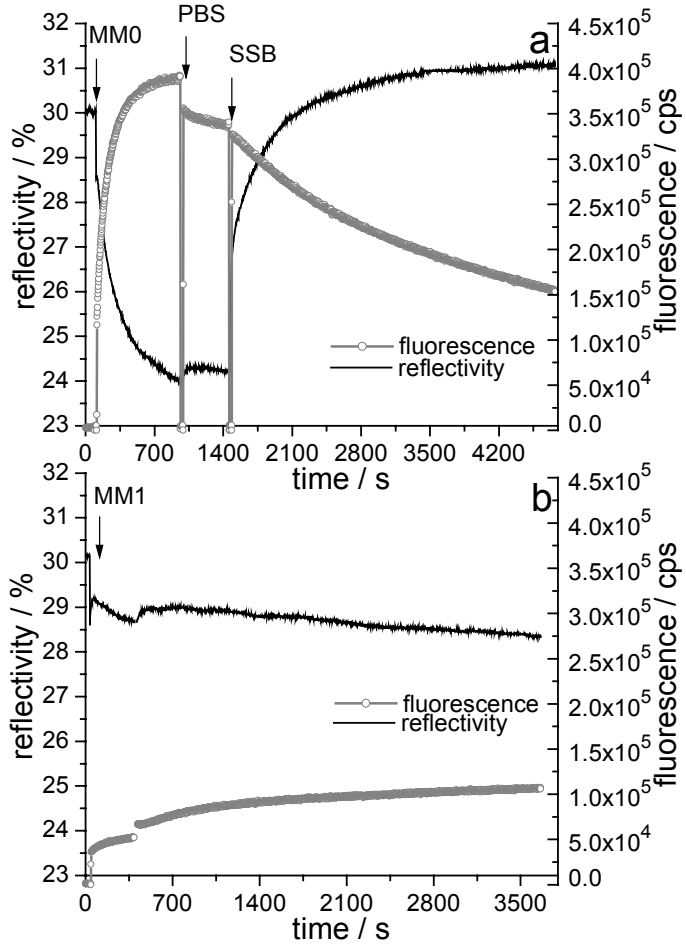

Figure 9.4 : Replacement of SSB by labelled targets. a) Upon injection of MM0 targets the reflectivity decreases while the fluorescence rises; the reverse reaction was obtained by subsequent injection of SSB. b) MM1 targets do barely cause any effect in fluorescence or reflectivity

A clear difference of the hybridisation kinetics to the corresponding measurements for unhindered duplex formation to P2 probes was observed. In chapter 6.4 the complementary MM0 sequence was characterised by a fast adsorption and stable duplexes with the probe (P2), while the MM1 targets could be rinsed off after moderate adsorption. Due to the competition

with the bound proteins, the adsorption of both targets is hindered. Therefore the MM0 hybridisation appeared slower than in the unhindered case and the MM1 target did not bind at all.

MM1 and MM0 targets could easily be distinguished by their interaction kinetics: After 10 minutes already, a clear difference between MM0 and MM1 targets was seen. Preloading of the sensor surface with SSBs thus can be used to increase the mismatch sensitivity of the probe. Due to the distinct mass change upon the protein removal, the fluorescence detection becomes redundant. Unlabelled targets can hence be detected by common surface plasmon resonance.

Replacement of Targets by SSB

The replacement of bound MM0 and MM1 targets by the SSB proteins was investigated now. In two separate experiments labelled MM0 and mismatched MM1 targets were hybridised onto the unlabelled probe P2. In the experiments from chapter 6.4 the hybridised targets were desorbed by extensive rinsing the flow cell with analyte free buffer. In the following experiments, the proteins will compete with the targets for the binding sites on the surface and thus remove them from the probes. After injection of a 0.1uM solution of SSBs in PBS the competition kinetics were followed by SPFS as shown in Figure 9.5.

While a relatively slow decrease in fluorescence was observed in the case of complementary MM0 target the corresponding MM1 signal already reached a stable minimum after 600s. Thus, a clear discrimination between both samples is possible by comparing the fluorescence signal of the labelled targets. The observed trend is consistent with a reduced stability of mismatched sequences as already known from previous hybridisation experiments (chapter 6.4). The target replacement by SSB treatment differs from desorption due to rinsing with PBS by means of the reaction mechanism. In the latter case the kinetics can be perfectly described by Langmuir kinetics by considering the desorption constant $k_{off,T}$ of the targets. Now, the interaction with the competing proteins has to be taken into account.

The surface concentration of initially bound targets is small due to the limited hybridisation efficiency and the dilution of the probes on the surface. Therefore the concentration of the removed targets in solution is negligible. Therefore it is assumed, that re-adsorption of removed strands does not compete with the protein binding. However, a simple two step process consisting of target desorption (rate constant $k_{off,\ T}$) and subsequent protein adsorption (rate constants $k_{on,P}$ and $k_{off,P}$) cannot describe the kinetic differences between MM1 and MM0. The limiting factor would be the desorption of the targets again and the process would be identical to

rinsing. Since the presence of the SSBs appear to destabilise both duplexes, an active replacement mechanism has to be considered, which complicates the analysis of the observed kinetics.

The analysis of the fluorescence signal leads to a clear discrimination between MM0 and MM1 targets. In contrast to this, the change in reflectivity for both cases appeared to be virtually identical and did not allow to distinguish between complementary and mismatched duplexes. In both cases the same amount of protein appeared to be adsorbed. This result is not easily understood in comparison with the experiments in the last paragraph. There the interaction of targets in solution with bound SSB proteins on the surface allowed the discrimination by SPS.

In the following it was investigated if the presence of the SSB proteins can influence the fluorescence signal of the labelled targets by inducing quenching effects.

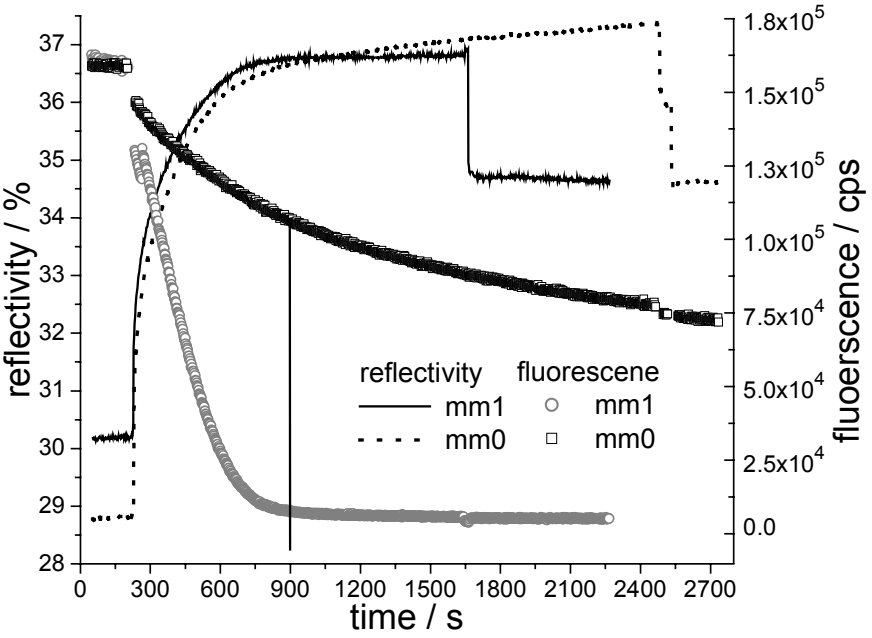

Figure 9.5 : Replacement of complementary and mismatched targets by SSB. Note that after 10 minutes a clear difference was seen in the fluorescence of MM0 and MM1 targets

9.4 Labelled Probes and SSB

In the last paragraph discrepancies between the fluorescence signal and the simultaneously recorded reflectivity was observed when labelled targets were replaced from unlabelled probe sequences by SSB proteins. Therefore, eventual quenching of the fluorescence by SSB proteins was investigated. Instead of labelling the target, the dye was fixed to the surface on the 3' end of the probe sequence. This Cy5 labelled probe sequence BioCy5T15 was introduced already in

chapter 7. Due to the strong streptavidin-biotin binding, the labelled probe sequence is fixed to the surface and cannot be removed by the proteins. Any decrease in the fluorescence upon SSB injection has thus to be attributed to quenching processes.

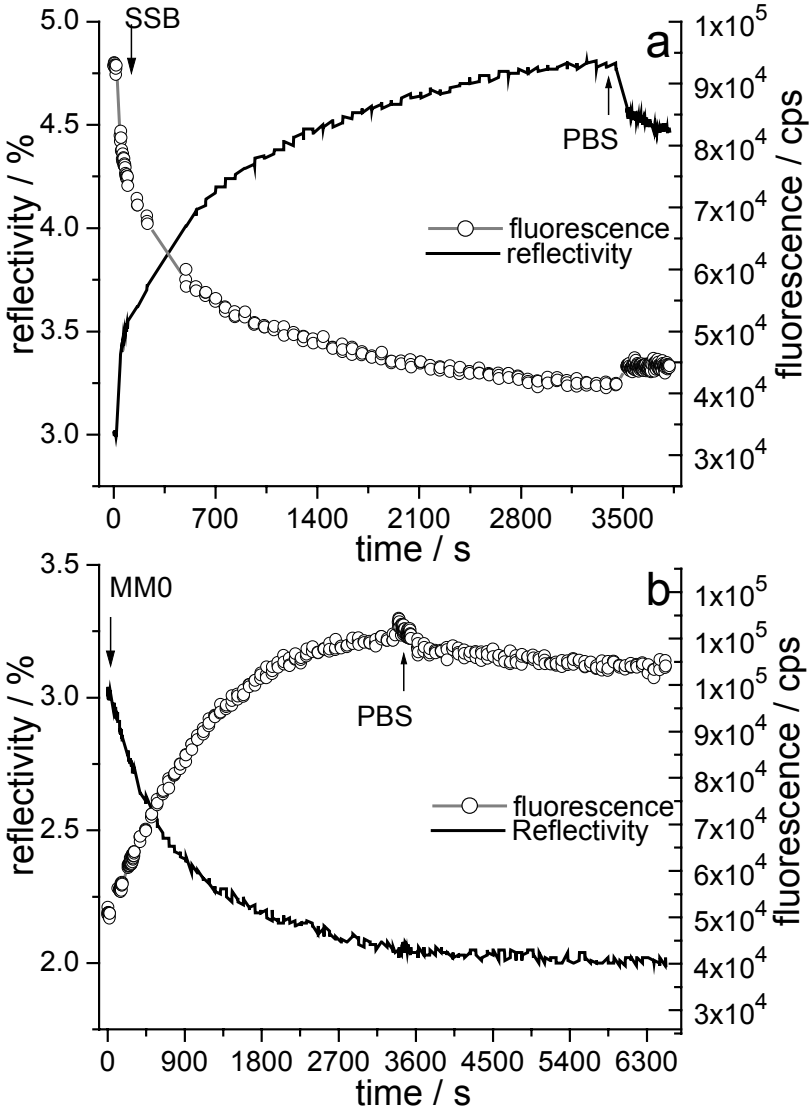

Figure 9.6 : Adsorption of SSB on labelled BioCy5T15 probes (a). Note that the fluorescence is quenched although no desorption of the labelled probes can occur. Subsequent hybridisation with MM0 unlabelled targets resulted in a recovery of the initial fluorescence and a decrease of the reflectivity.

When the immobilised BioCy5T15 probes were treated with SSB the reflectivity increased due to binding of the proteins. The obtained protein thickness of 4nm was identical to the one obtained for unlabelled probes in9.2. However, the fluorescence decreased to half of the initial signal, although the labelled probe strands are not likely to be removed from the streptavidin surface. Therefore the decrease of the fluorescence is attributed to quenching processes induced

by the proximity of the proteins to the dyes. Subsequent injection of complementary targets lead to a recovery of both the fluorescence and the initial layer thickness. The underlying SPFS scan curves (not shown) proved that the 4nm SSB layer could be removed completely by the MM0 target. Thus, the dye at the 3' end of the probe did not influence the de- and adsorption kinetics. Therefore the obtained findings can be adapted to explain the results in the previous paragraph.

From the experimental results we concluded that the presence of the bound proteins caused a strong quenching of the immobilised fluorophores. However, two different quenching mechanisms have to be considered:

- quenching of the fluorescence due to wrapping of the probe strand around the protein complex and thus closer proximity of the immobilised dye to the quenching gold surface (chapter 7)
- static quenching due to the formation of a non fluorescent ground state complex between dye and fluorophore

In order to decide which quenching mechanism is responsible for the observed effects, adsorption reactions in solution were conducted by common fluorescence spectroscopy.

9.5 Adsorption of SSB in Solution

A 1uM solution of BioCy5T15 was diluted in PBS and characterised by common fluorescence spectroscopy. Excitation and emission spectra of the probes were recorded after proteins were added and the SSB concentration in the solution was increased stepwise. After equilibration of the individual adsorption kinetics (not shown) the fluorescence signal was measured and plotted versus the applied SSB concentration as shown in Figure 9.7. The initial fluorescence of the BioCy5T15 probes was quenched upon protein adsorption. Therefore it was concluded, that the quenching effect observed in the previous chapter was not caused by a distance dependent quenching to the gold. More likely the presence of the protein caused static quenching by forming a non fluorescent ground state complex with the oligonucleotides.

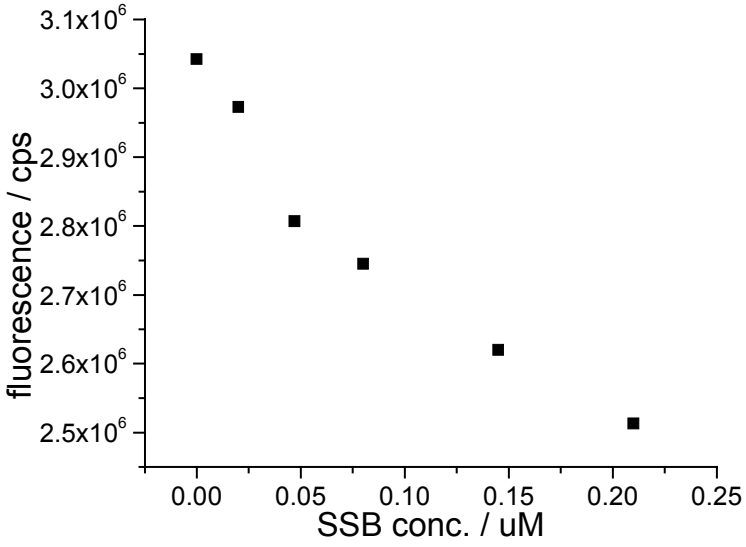

Figure 9.7 : Quenching of fluorescence of labelled probes by SSBs in solution

9.6 Conclusion

The use of single strand binding proteins (SSB) as a novel DNA detection scheme was investigated by surface plasmon fluorescence spectroscopy (SPFS). It has been shown that SSBs bind specifically to immobilised 30mer probe strands and that the SPS background based on unspecific binding to the streptavidin matrix is negligible. Due to the low salt conditions and the short length of the probes, cooperative binding of more than one SSB tetramer on an individual probe strand is not likely. The adsorption kinetics deviate from a pure Langmuir behaviour due to steric effects during the protein adsorption.

In chapter 9.3 the replacement reactions between proteins and targets bound to immobilised probe sequences were investigated. It was shown that the detection limit of the surface plasmon resonance could be enhanced by pre-conditioning the probe surface with SSBs. When the hybridisation reaction was performed with a SSB covered sensor surface, the mass change upon hybridisation was sufficient to obtain a clear resonance minimum shift in the SPS kinetics. Thus, unlabelled low molecular mass targets can be detected without further processing and the expensive and time consuming labelling steps can thus be avoided.

Furthermore, the SSB proteins bound to the probe interfere with the hybridisation reaction, thus enhancing the mismatch discrimination sensitivity of the system. The interaction strength between SSB proteins and the probe caused a complete suppression of the MM1 target binding.

Under the experimental conditions a discrimination between complementary and mismatched sequences was already possible after 10 minutes.

Additionally, the reverse process of denaturing intact duplexes by competitive replacement of the targets by proteins was investigated. The binding of the proteins caused a decrease in the fluorescence signal that can be attributed to two separate effects. One the one hand the targets were removed from the surface with different kinetics depending on their stability. While the signal of mismatched sequences reached a stable minimum right after 10 minutes, complementary targets were found to be more stable. On the other hand, experiments with labelled probes in solution and on the surface revealed a strong fluorescence quenching due to the interaction with the proteins. Therefore, only a part of the fluorescence decrease in Figure 9.5 can be attributed to the replacement by the proteins. Another part is likely to be caused by the quenching of labelled targets that were not removed from the surface. However no difference in the reflectivity change for MM0 and MM1 was seen. Hence, the format of SSB application after completed hybridisation can only be used to improve the mismatch discrimination in the case of labelled targets. A distinction in case of unlabelled targets doesn't seem to be applicable since the reflectivity alone did not allow for a mismatch discrimination.

In summary, a system in which the probe sequences was loaded with SSB proteins before the hybridisation was proven to be a valuable tool for the detection of mismatches in unlabelled targets.

10 Summary

The development and characterisation of DNA sensor formats based on the optical technique Surface Plasmon Fluorescence Spectroscopy (SPFS) was investigated. The study can be divided into two parts of different scope: In the first part the physical behaviour of fluorescent dyes on metallic surfaces was studied. In the second part the results obtained were used for the development of fluorescence detection schemes of oligonucleotides on sensor surfaces.

The excitation and emission of fluorescent molecules on planar metal surfaces was investigated using SPFS in the Kretschmann configuration (prism coupling). Fluorescent molecules could be excited in the evanescent surface plasmon field near the surface and the different decay mechanisms for fluorescence near metallic surfaces were identified. In addition to the free emission of photons the fluorescence emission mediated by plasmon excitation was characterised. For Cy5 dyes on gold the distance dependent quenching profile was determined experimentally and confirmed by model calculations.

The results obtained for the prism set-up were compared to the investigation of fluorescent dyes near blazed metal gratings. Both, free plasmons and coupled resonances were found to mediate the excitation and emission of fluorescence. Analogous to the behaviour on planar surfaces the fluorescence excitation and emission via free resonances was not dependent on the lateral position of the dye on the metal surface. However, coupled surface plasmon resonances lead to a strong localisation of the electric plasmon field on the grating surface. Due to this localisation of the electric field a site-dependent coupling of fluorophores to the field of these coupled resonances was found. This allowed for a site selective excitation and bleaching of the dyes on the metal surface and hence a modulation of the fluorescence intensity along the grating surface could be observed. A potential application of the selective bleaching for a FRAP like diffusion measurement was proposed.

DNA hybridisation could be detected on metallic surfaces using SPFS. The sensor architecture consisted of an unlabelled oligonucleotide probe sequence immobilised on a streptavidin matrix. Cy5 labelled target sequences were hybridised from solution and their fluorescence signal was monitored. The surface sensitive detection of fluorescence permitted the

monitoring of online hybridisation kinetics. The influence of steric factors such as the secondary structure of the oligonucleotides was investigated and thermodynamic considerations were taken into account. Experimental hybridisation kinetics of probes free of secondary structures were compared to previous results for probe sequences capable of forming hairpins. It was found that the introduction of secondary structures could enhance the mismatch sensitivity of the probes.

On the basis of the investigations in the previous chapter a novel detection scheme for unlabelled targets was developed using immobilised Cy5 labelled probe sequences. In the single stranded state the probe sequence exhibited a random coil structure and the fluorescence of the dye bound to the probe was partially quenched by the metal surface. Hybridisation to the unlabelled target sequence caused the formation of stiff helical structures in the probe which separated the dye from the surface. Increasing the dye-metal distance reduced the quenching by the metal surface, such that hybridisation of the unlabelled targets was indicated by an increase in the probe fluorescence. The distance of the dye before and after duplex formation could be estimated by referring to the determined quenching profile for Cy5 on gold. Additionally the influence of the ionic strength in solution on the conformation of the probe was characterised.

The use of a potential Förster donor-acceptor pair for the detection of hybridisation by fluorescence resonance energy transfer (FRET) was investigated. Donor and acceptor dyes were immobilised on the probe and target strands, respectively. The labelled sequences were characterised using fluorescence spectroscopy in solution and SPFS on the sensor surface. The hybridisation between probe and target caused quenching of the donor and acceptor fluorescence. However, a strong interaction between the dyes stabilised the duplex between probe and target and did not allow for a reliable discrimination of complementary and mismatched sequences. Although this particular dye pair was not suitable for detecting binding reactions between oligonucleotides the impact of SPFS for FRET detection schemes was shown.

Finally, the use of single strand binding proteins (SSB) for the enhancement of the mismatch discrimination sensitivity was investigated. Replacement reactions between fluorescently labelled targets and the proteins were studied on the basis of the measured SPS and fluorescence kinetics. It was demonstrated that the competition between SSB's and targets could increase the mismatch sensitivity of the system. The additional mass of the proteins could be sensed by bare surface plasmon resonance and enabled the competitive detection of unlabelled targets.

11 Supplement

11.1 Abbreviations

(k)bp	(kilo) base pairs
[ ]	concentration
3MPT	3-(mercaptopropyl)trimethoxy-silane
CCD	charge coupled device
Cy5	cyanine dye
DNA	deoxyribonucleic acid
dNTP	desoxy-nucleotide-tri-phoshate
ds	double-strand(ed)
EDTA	ethylene diamine tetra acetate
FIA	fluoroimmunoassays
FRAP	fluorescence recovery after photobleaching
FRET	fluorescence resonance energy transfer
h	Planck's constant
HeNe	helium neon (laser)
HEX	fluorescent Förster donor dye
IC	internal conversion
ISC	intersystem crossing
JA270	fluorescent Förster acceptor dye
k	rate constant
k	wave vector
$LaSFN_9$	high refractive index glass
LRSP	long range surface plasmon
mm0, mm1, mm2	number of mismatches between probe and target
n	refractive index
NHS	N-hydroxy-succinimide
OD	optical density
PAGE	poly-acrylamide gel-electrophoresis
PBS	phosphate buffered saline (buffer)
PMT	photo multiplier tube
PVA	poly vinyl alcohol
RNA	ribonucleic acid
S_0, S_1	singlet electronic states of a molecule
SA	streptavidin

SA-F	fluorescently labelled streptavidin
SAM	self assembled monolayer
SPFM	surface plasmon fluorescence microscopy
SPFS	surface plasmon fluorescence spectroscopy
SPM	surface plasmon microscopy
SPS	surface plasmon spectroscopy
SRSP	short range surface plasmon
ss	single-strand(ed)
SSB	single strand binding protein(s)
TE	transversal electric (s-) polarisation
TM	transversal magnetic (p-) polarisation
TMOS	tetramethoxy-silane
ε	dielectric constant
ϕ	quantum yield
κ	absorption coefficient
ν	frequency of light
τ	fluorescence lifetime

11.2 List of Figures

11.3 List of Tables

11.4 Bibliography

1. Lowe, C. R. An introduction to the concepts and technology of biosensors. *Biosensors* **1**, 3-16 (1985).
2. Wingrad, L. B. & Ferrance, J. P. in *Biosensors with Fibreoptics* 1-27 (, 1991).
3. Buckle, M., Williams, R. M., Negroni, M. & Buc, H. *Proc. Natl. Acd. Sci. USA* **93**, 889-894 (1996).
4. Renneberg, R. Molekulare Erkennung mittels Immuno- und Rezeptorsystemen. *Spektrum der Wissenschaft* **9**, 103-108 (1992).
5. Ligler, F. S. & Rabbany, S. Y. in *Synthetic microstructures in biological research* (eds. Schnur, J. M. & Peckerar, M.) 67-75 (Plenum Press, New York, 1992).
6. Turner, A. P. F., Karube, I. & Wilson, G. S. *Biosensors: Fundamentals and Applications* (Oxford University Press, New York, 1987).
7. Hall, E. A. H. *Biosensoren* (Springer, Heidelberg, 1990).
8. Buerk, D. G. *Biosensors* (Technomic Publishing AG, Lancaster, USA, 1992).
9. Guibault, G. G. & Schnidt, R. D. Electrochemical, piezoelectic and fibre-optic biosensors. *Biosensors* **1**, 257-289 (1991).
10. Raether, H. *Surface Plasmon on Smooth and Rough Surfaces and on Gratings* (Springer, Berlin, 1988).
11. Graham, C. R., Leslie, D. & Squirell, D. J. *Biosensors and Bioelectronics* **7**, 487-493 (1992).
12. Piunno, P. A. E., Krull, U. J., Hudson, R. H. E., Damha, M. J. & Cohen, H. *Anal. Chem.* **67**, 2635-2643 (1995).
13. Abel, A. P., Weller, M. G., Duvuneck, G. L., Ehrat, M. & Widmer, W. *Anal. Chem.* **68**, 2905-2912 (1996).
14. Kleinjung, F., Bier, F. F., Warsinke, A. & Scheller, F. W. *Analytica Chimica Acta* **350**, 51-58 (1997).
15. Attridge, J. W., Daniels, P. B., Deacon, J. K., Robinson, G. A. & Davidson, G. P. Sensitivity enhancement of optical immunosensors by the use of a surface plasmon resonance fluoroimmunoassay. *Biosens Bioelectron* **6**, 201-14 (1991).
16. Liebermann, T. & Knoll, W. Surface-plasmon field-enhanced fluorescence spectroscopy. *Colloids and Surfaces a-Physicochemical and Engineering Aspects* **171**, 115-130 (2000).
17. Liebermann, T., Knoll, W., Sluka, P. & Herrmann, R. Complement hybridization from solution to surface-attached probe-oligonucleotides observed by surface-plasmon-field-enhanced fluorescence spectroscopy. *Colloids and Surfaces a-Physicochemical and Engineering Aspects* **169**, 337-350 (2000).
18. O´Donnel, C. M. & Suffin, S. C. Fluorescence Immunoasays. *Anal. Chem.* **51** (1979).
19. Chan, D. W. *Fluorescent Immunoassays. Immunoassays: a practical guide* (ed. Chan, D. W.) (Academic Press, San Diego, 1987).
20. Christopoulos, T. K. & Diamandis, E. P. *Immunoassay* (ed. Chan, D. W.) (Academic Press, San Diego, 1996).
21. Smith, D. J. Enhancement fluoroimmunoassay of thyroxine. *FEBS. Lett.* **77** (1977).

22. Lin, M. & Nielsen, K. J. Binding of the Brucella abortus lipopolysaccharide O-chain fragment to a monoclonal antibody. Quantitative analysis by fluorescence quenching and polarization. *Bioconjugate Chem.* **4** (1997).

23. Chan, I. N., Lin, J. N., Andrade, J. D. & Herron, J. N. Photoaffinity Labeling of Antibodies for Application in Homogenous Fluoroimmunoassays. *Anal. Chem.* **67** (1995).

24. Smith, D. J. Enhancement fluoroimmunoassay of thyroxine. *FEBS. Lett.* **25-27** (1977).

25. Ullman, E. F., Schwarzberg, M. & Rubenstein, K. E. Fluorescent Excitation Transfer Immunoassay : A General Method for Determination of Agents. *J. Biol. Chem.* **251**, 4172-4178 (1976).

26. Lazowski, K. W. & Kaczmarek, L. Highly sensitive detection of hybridization of oligonucleotides to specific sequences of nucleic acids by application of fluorescence resonance energy transfer. *Antisense Nucleic Acid Drud Dev* **10(2)**, 97-103 (2000).

27. Lakowicz, J. R. *Principles of Fluorescence Spectroscopy* (Plenum Press, New York, London, 1983).

28. Berlman, I. B. *Energy Transfer Paramenters of Aromatic Molecules* (Academic Press, London, 1973).

29. Förster, T. Intermolecular energy migration and fluorescence. *Ann. Phys* **2**, 55-75 (1948).

30. Förster, T. *Z. Naturforsch* **4a**, 321 (1949).

31. Steinberg, I. Z. Long-range nonradiative transfer of electronic excitation energy in proteins and polypeptides. *Ann. Rev. Biochem.* **40**, 83-114 (1971).

32. Erikson, J. W., Mittal, R. & Cerione, R. A. Use of Resonance Energy Transfer to Determine the Proximity of the Guanine Nucleotide Binding Site of Transducin Relative to a Conformationally-Sensitive Site on the Subunit of the Cyclic GMP Phosphodiesterase. *Biochemistry* **34**, 8693 (1995).

33. Matyus, L. Fluorescence Resonance Energy Transfer Measurements on Cell Surfaces. *J. Photochem. Photobiol* **B 12**, 323 (1992).

34. Ha, T. Probing the Interaction between Two Single Molecules: Fluorescence Resonance Energy Transfer between a Single Donor and a Singer Acceptor. *Proc. Natl. Acad. Sci USA* **93**, 6264 (1996).

35. Berger, W. Complex Molecular Mechanism for Dihydropyridine Binding to L-Type Ca2+-Channels as Revealed by Fluorescence Resonance Energy Transfer. *Biochemistry* **33**, 11875 (1994).

36. Atkins, P. W. *Physikalische Chemie* (VCH, Weinheim, Germany, 1990).

37. Ulman, A. *An Introduction to Ultrathin Organic Films* (Academic Press, London, 1991).

38. Agranovich, V. M. *Surface Polaritons* (North Holland, Amsterdam, 1982).

39. Yeh, P. *Optical Waves in Layereed Media* (John Wiley & Sons, New York, 1988).

40. Aust, E. F., Ito, S. F., Sadowny, M. & Knoll, W. Investigation of thin films using surface plasmon modes and optical waveguide modes. *Trends in Polymer Science* **2**, 313-323 (1994).

41. Knoll, W. Interfaces and thin films as seen by bound electromagnetic waves. *Annual Review of Physical Chemistry* **49**, 569-638 (1998).

42. Sambles, J. R., Bradberry, G. W. & Yang, F. Optical excitation of surface plasmons: an introduction. *Contemporary physics* **32**, 173-183 (1991).

43. Burstein, E., Chen, W. P. & Hartstein, A. Surface polaritions -propagating electromagnetic modes at surfaces. *Journal of Vacuum Soc.* **11**, 1004-1019 (1974).

44. Otto, A. Excitation of nonradiative surface plasmon waves in silver by the method of frustrated total reflection. *Zritschrift für Physik* **216**, 398-410 (1968).

45. Kretschmann, E. Die Bestimmung optischer Konstanten von Metallen durch Anregung von Oberflächenplasmaschwingungen. *Zeitschrift für Physik* **241**, 313-324 (1971).

46. Karthe, W. & Müller, R. *Integrierte Optik* (Akademische Verlagsgesellschaft Geest und Portig, Leipzig, 1991).

47. Liebermann, T. Oberflächenplasmonen-Fluoreszenzspektroskopie zur Detektion molekularer Erkennungsreaktionen. *Dissertation, University Mainz, Germany* (1998).

48. Axelrod, D., Burghardt, T. P. & Thompson, N. L. *Biophys. Bioeng.* **13**, 247-268 (1984).

49. Johnson, P. B. & Christey, R. W. *Phys. Rev B* **6**, 4370 (1972).

50. Nemetz, A. & Knoll, W. Raman spectroscopy and microscopy with surface plasmon polaritons. *J. Raman Spectrosc.* **27** (1996).

51. Hickel, W., Kamp, D. & Knoll, W. *Nature* **339**, 186 (1989).

52. Rothenhäusler, B. & Knoll, W. Surface-plasmon microscopy. *Nature* **332**, 615-617 (1988).

53. Rothenhäusler, B. & Knoll, W. *Opt. Soc. Am. B* **5**, 1401 (1988).

54. Knoll, W. *Macromol. Chem.* **192**, 2827 (1991).

55. Zizlsperger, M. & Knoll, W. Multispot parallel on-line monitoring of interfacial binding reactions by surface plasmon microscopy. *Progr Colloid Polym Sci* **109**, 204-253 (1998).

56. Piscevic, D. & Knoll, W. Surface Plasmon microscopy of biotin-streptavidin binding reactions on UV-photopatterned alkanethiol self-assembled monolayers. *Supramolecular Science* **2**, 99-106 (1995).

57. Schmitt, F. J. & Knoll, W. Surface-plasmos microscopic observation of site-selective recognition reactions. *Biophys. J.* **60**, 716-720 (1991).

58. Holland, L. *Vacuum Deposition of Thin Films* (ed. Ltd., C. a. H.) (, London, 1966).

59. Bain, C. D. & Witesides, G. M. Modelling organic surfaces with self assembled monolayers. *Adv. Mater.* **4**, 110 (1989).

60. Tovar, G. (University of Mainz, 1995).

61. Tripp, C. P. & Hair, M. L. Reaction of Methylsilanols with Hydrated Silica Surfaces : The Hydrolysis of Trichloro-, Dichloro-, and Monochloromethylsilanes and the Effect of Curing. *Langmuir* **11**, 149ff (1995).

62. Mujumdar, R. B. *Bioconjugate Chemistry* **4**, 105-111 (1993).

63. Yu, H. e. a. *Nucleic Acids Research* **22**, 3226-3232 (1994).

64. Voet, D. & Voet, J. G. *Biochemie* (VCH, Weinheim, 1992).

65. Gilmartin, P. M. *Nucleic Acid Hybridisation* (eds. Rickwood, D. & Hames, B. D.) (John wiley & Sons, Chichester, New York, Brisane, Toronto, Singapore, 1996).

66. Kitson, S. C., Barnes, W. L., Sambles, J. R. & Cotter, N. P. K. Excitation of molecular fluorescence via surface plasmon polaritons. *Journal of modern optics* **43**, 573-582 (1996).

67. Knobloch, H., Brunner, H., Leitner, A., Aussenegg, F. & Knoll, W. Probing the evanescnet field of propagating plasmon surface polaritions by fluorescence and Raman spectroscopies. *J. Chem. Phys.* **98**, 10093-10095 (1993).

68. Eagen, C. F., Weber, W. H., McCarthy, S. L. & Terhune, R. W. Time-dependent decay of surface plasmon coupled molecular fluorescence. *Chemical Physical Letters* **75**, 274-277 (1980).

69. Benner, R. E., Dornhaus, R. & Chang, R. K. *Optics. Commun.* **30**, 145 (1979).

70. Barnes, W. L. Topical review. Fluorescence near interfaces: the role of photonic mode density. *Journal of Modern optics* **45**, 661-699 (1998).

71. Amos, R. & Barnes, W. L. *Phys. Rev. B.* **55**, 7249 (1997).

72. Kuhn, H. *J. chem. phys.* **53**, 101 (1970).

73. Weber, W. & Eagon, C. F. *Optics Lett.* **4**, 236 (1979).

74. Pockrand, I., Brilliante, a. & Mobius, d. *Chem. Phys. Lett.* **69**, 499 (1980).

75. Kreiter, M. Dissertation *University Mainz, Germany* (2000).

76. Kreiter, M., Neumann, T., Mittler, S., Knoll, W. & Sambles, J. R. Fluorescent dyes as a probe for the localised field of coupled surface plasmon-related resonances. *Phys. Rev. B* (2001).

77. Tamir, T. & Peng, S. T. Analysis and design of grating couplers. *Applied Physics* **14**, 235-254 (1977).

78. Sarid, D. *Phys. Rev. Lett* **47**, 1927 (1981).

79. Richie, R. W., Arakawa, E. T., Cowan, J. J. & Hamm, R. N. *Phys. Rev. Lett* **21**, 1530 (1968).

80. Kitson, S. C., Barnes, W. L. & Sambles, J. R. Full Photonic Band GAp for Surface Modes in the Visible. *Phys. REv. Lett* **77**, 2670 (1996).

81. Andrew, P., Kitson, S. C. & Barnes, W. L. Surface-Plasmon energy gaps and photoadsorption. *J. modern optics* **44**, 395-406 (1997).

82. Kitson, S. C., Barnes, W. L. & Sambles, J. R. Surface-plasmon energy gaps and photoluminescence. *Phys. Rev. B.* **52**, 11441-11445 (1995).

83. Barnes, W. L. *et al. Phys. Rev. B* **51**, 11164 (1995).

84. Knoll, W., Philpott, M. R., Swalen, J. D. & Girlando, A. *J. Chem. Phys.* **75**, 4795 (1981).

85. Kitson, S. C., Barnes, W. L. & Sambles, J. R. Photoluminescence from dye molecules on silver gratings. *Optics Communications* **122**, 147-154 (1996).

86. Axelrod, D., Koppel, D. E., Schlessinger, J., Elson, E. & Webb, W. Mobility measurements by analysis of fluorescence photobleaching recovery kinetics. *Biophysics Journal* **16**, 1055-1069 (1976).

87. Cooper, D. N. & Schmidtke, J. Diagnosis of human genetic diseases using recombinant DNA. *Human Genetic* **92**, 211-236 (1993).

88. Culolla, E. & Roshland, D. *Science* **262**, 262 (1958).

89. Adams, R. L. P., Knowler, J. T. & Leader, D. *The Biochemistry of Nucleic Acids* (Chapman & Hall, London, 1992).

90. Saenger, W. *Principles of Nucleic Acid Streucture* (ed. Cantor, C.) (Springer, New York, 1983).

91. Watson, J. D. & Crick, F. H. C. A structure for deoxyribose nucleic acid. *Nature* **171**, 737-738 (1953).

92. Tennover, F. C. in *Manual of Clinical Microbiology* 119-127 (, Washington, 1991).

93. Sanger, F., Nicklen, S. & Coulson, A. R. *Proc. Natl. Acd. Sci. U.S.A* **74**, 5463-5467 (1977).

94. Maxam, A. & Gilbert, W. *Proc. Natl. Acd. Sci. U.S.A* **74**, 560-564 (1977).

95. Bains, S. & Smith, C. G. A novel method for nucleic acid sequence determination. *J. Theor. Biol* **135**, 303-307 (1988).

96. Drmanac, R. & et.al. DNA sequence determination by hybridization: a strategy for efficient large scale sequencing. *Science* **260**, 1649-1652 (1994).

97. Ebersole, R. C., Miller, J. A., Moran, J. R. & WArd, M. D. *J. Am. Chem. Soc.* **112**, 3239 (1990).

98. Okahata, Y. *et al. Anal. Chem.* **70**, 1288-1296 (1998).

99. Nilsson, P., Persson, B., Uhlen, M. & Nygren, P. A. Real-time monitoring of DNA manipulations using biosensor technology. *Analytical Biochemistry* **224**, 400-8 (1995).

100. Gotoh, M., Hasegawa, Y., Shinohara, Y., Shimizu, M. & Tosu, M. A new approach to determine the effect of mismatches on kinetic parameters in DNA hybridization using an optical biosensor. *DNA Research* **2**, 285-93 (1995).

101. Herne, T. M. & Tarlov, M. J. Characterization of DNA probes immobilized on gold surfaces. *Journal of the American Chemical Society* **119**, 8916-8920 (1997).

102. Knoll, W. *et al.* Streptavidin arrays as supramolecular architectures in surface- plasmon optical sensor formats. *Colloids and Surfaces a-Physicochemical and Engineering Aspects* **161**, 115-137 (2000).

103. Piscevic, D. *et al. Appl. Surf. Sci* **90**, 425-436 (1995).

104. Kai, E. *et al.* Detection of PCR Products in Solution Using Surface Plasmon Resonance. *Anal. Chem.* **71**, 796-800 (1999).

105. Nilsson, P., Persson, B., Larsson, A., Uhlen, M. & Nygen, P. Detection of Mutations in PCR Products from Clinical Samples by Surface Plasmon Resonance. *Journal of Molecular Recognition* **10**, 10-17 (1997).

106. Zizlsperger, M. (J.-G. University of Mainz, Mainz, 1998).

107. Bianchi, N. *et al.* Biosensor technology and surface plasmon resonance for real-time detection of HIV-1 genomic sequences amplified by polymerase chain reaction. *Clin. Diag. Virol.* **8**, 199-208 (1997).

108. Bier, F. & Scheller, F. W. *Biosens. Bioelectron.* **11**, 669-675 (1996).

109. Graham, C. R., Leslie, D. & Squirell, D. *Biosens. Bioelectron.* **7**, 487-493 (1996).

110. Hashimoto, K., Mikawa, K., Gotoh, M. & Ishirnori, Y. *Supramol.Chem* **2**, 265-270 (1993).

111. Hashimoto, K., Ito, K. & Ishimori, Y. *Anal. Chim. Acta* **286**, 219-224 (1994).

112. Pinno, P. A. E., Krull, U. J., Hudson, R. H. E., Damha, M. & Cohen, H. *Anal. chem.* **67**, 2635-2643 (1995).

113. Mikkelsen, S. R. *Electroanalysis* **8**, 15-17 (1996).

114. Liebermann, T. Dissertation *University Mainz* (1998).

115. Weber, P. C., Ohlendorf, D. H., Wendoloski, J. J. & Salemme, F. R. Structural origin of High Affinity Biotin Binding to Streptavidin. *Science* **243**, 85-88 (1989).

116. Chilkoti, A. & Stayton, P. S. Molecular-origons of the slow Streptavidin-Biorin Dissocaition Kinetics. *J. Am. Chem. Soc.* **117**, 10622-10628 (1995).

117. Aubry, J. P., Durand, I., Paoli, P. & Bancherea, J. 7-Amino-4-methylcoumarin-3-acetic acid conjugated streptavidin permits simultaneous flow cytometry analysis of either three cell surface antigens or one cell surface antigen as a function of RNA and DNA content. *J. Immun. Method* **165**, 39 (1990).

118. Wilchek, M. & Bayer, A. The Avidin-Biotin complex in bioanalytical applications. *Anal. Biochem.* **184**, 1 (1988).

119. Wilchek, M. & Bayer, E. A. *Methods in enzymology* (Academic Press, San Diego, 1990).

120. Diamandis, T. K. & Christopoulos, K. The Biotin(Strept)Avidin System : Principles and Applications in Biotechnoligy. *Clin. Chem.* **37**, 625 (1991).

121. Hendrickson, W. A. & et.al. *Proc. Natl. Acad. Sci. U.S.A.* **85**, 2190-2194 (1989).

122. Ebersole, R. C., Miller, J. A., Moran, J. R. & Ward, M. d. Spontaneously formed functionally active svidin monolayers on metal surfaces: A strategy for immobilising biological reagents and design of piezoelectric biosensors. *J. Am. Chem. Soc.* **112**, 3239 (1990).

123. Chignell, C. K., Starkweather, d. K. & Sinha, B. K. *J. Biol. Chem.* **250**, 5622-5630 (1975).

124. Weber, P. C., Wendoloski, J. J., Pantoliano, M. W. & Salemme, F. R. *J. Am. Chem. Soc.* **114**, 3197-3200 (1992).

125. Häußling, l., Michel, B., Ringsdorff, H. & Rohrer, H. Rastertunnelmikroskopische Beobachtung von spezifisch adsorbiertem Streptavidin auf Biotinfunktionalisierten selstorganisierten Oberflächen. *Angew. Chem.* **103**, 568 (1991).

126. Spinke, J. *et al.* in *Frontiers of polymers and advanced materials* (Plenum Press, 1994).

127. Müller, W. *et al.* Review-formation of proteinmultilayers and their competetive replacement based on self assembled biotinylated phospholipids. *Biomater. Sci. Polymer Edn.* **6**, 481 (1994).

128. Spinke, J. Dissertation, *University Mainz, Germany* (1992).

129. Piscevic, D. Dissertation *University Mainz, Germany* (1995).

130. Wolcott, M. J. *Clinical Microbiology Reviews* **5**, 370-386 (1992).

131. Shchepinov, M. S., CaseGreen, S. C. & Southern, E. M. Steric factors influencing hybridisation of nucleic acids to oligonucleotide arrays. *Nucleic Acids Research* **25**, 1155-1161 (1997).

132. Day, P. J. R., Flora, P. S., Fox, J. E. & Walker, M. R. Immobilization of Polynucleotides on Magntic Particles - Factors Influencing Hybridization Efficiency. *Biochemical Journal* **278**, 735-740 (1991).

133. Freier, S. M. (ed. Crooke, S. T., Lebleu, B.) 67-82 (CRC Press, Boca Raton, FL., 1993).

134. Johnson, T., Zhu, J. & Wartell, R. M. Differences between DNA base pair stacking energies are conserved over a wide range of ionic conditions. *Biochemistry* **37**, 12343-12350 (1998).

135. Breslauer, K. J., Frank, R., Blöcker, H. & Marky, L. A. *Proc. Natl. Acad. Sci. USA* **83**, 3746-3750 (1986).

136. SantaLucia, J., Allawi, H. T. & Seneviratne, A. Improved nearest-neighbor parameters for predicting DNA duplex stability. *Biochemistry* **35**, 3555-3562 (1996).

137. Gray, M. D. Derivation of Nearest Neighbor Prooerties from Data on Nucleic Acid Oligomers II. Thermodynamic Parameters of DNA-RNA Hybrids and DNA Duplexes. *Biopolymers* **42**, 795-810 (1996).

138. Owczarzy, R. *et al.* Predicting sequence-dependent melting stability of short duplex DNA oligomers. *Biopolymers* **44**, 217-239 (1997).

139. Owczarzy, R., Gallo, F. J. & Benight, A. S. Global comparison of published nearest-neighbor sequence dependent thermodynamic parameters. *Biophysical Journal* **72**, TH429-TH429 (1997).

140. Owczarzy, R., Vallone, P. M., Goldstein, R. F. & Benight, A. S. Studies of DNA dumbbells VII: Evaluation of the next nearest- neighbor sequence-dependent interactions in duplex DNA. *Biopolymers* **52**, 29-56 (1999).

141. Riccelli, P. V. *et al.* Thermodynamic, spectroscopic, and equilibrium binding studies of DNA sequence context effects in six 22-base pair deoxyoligonucleotides. *Biochemistry* **38**, 11197-11208 (1999).

142. SantaLucia, J. A unified view of polymer, dumbbell, and oligonucleotide DNA nearest-neighbor thermodynamics. *Proc. Natl. Acad. USA* **95**, 1460-1465 (1998).

143. Mathews, D. H. & Burkard, M. E.RNA Structure3.5 http://www.rna.chem.rochester.edu (1996-1999).

144. Mathews, D. H., Sabina, J., Zuker, M. & Turner, D. H. Expanded Sequence Dependence of Thermodynamic Paramaters Improves Prediction of RNA Structures. *J. Mol. Biol.* **288**, 911-940 (1999).

145. Grosschedl, R. & Hobom, G. *Nature* **277**, 621-623 (1979).

146. Chraibi, Z., Refregiers, M., Jolles, B. & Laigle, A. Hybridization kinetics of oligodeoxyribonucleotides with a d(GCGAAGC) hairpin at the 3 '-end. *Journal of Biomolecular Structure & Dynamics* **17**, 539-544 (1999).

147. Montanari, A. & Mezard, M. Hairpin formation and elongation of biomolecules. *Physical Review Letters* **86**, 2178-2181 (2001).

148. Amaratunga, M., Snowdenifft, E., Wemmer, D. E. & Benight, A. S. Studies of Dna Dumbbells .2. Construction and Characterization of Dna Dumbbells With a 16-Base-Pair Duplex Stem and Tn End Loops (N = 2, 3, 4, 6, 8, 10, 14). *Biopolymers* **32**, 865-879 (1992).

149. Paner, T. M., Amaratunga, M. & Benight, A. S. Studies of Dna Dumbbells .3. Theoretical-Analysis of Optical Melting Curves of Dumbbells With a 16-Base-Pair Duplex Stem and Tn End Loops (N = 2, 3, 4, 6, 8, 10, 14). *Biopolymers* **32**, 881-892 (1992).

150. Senior, M., Jones, R. A. & Breslauer, K. J. Influence of loop residues on the relative stability of DNA hairpin structures. *Proc. Natl. Acad. Sci. USA* **85**, 6242-6246 (1988).

151. Vallone, P. M. *et al.* Melting studies of short DNA hairpins: Influence of loop sequence and adjoining base pair identity on hairpin thermodynamic stability. *Biopolymers* **50**, 425-442 (1999).

152. Bonnet, G., Tyagi, S., Libchaber, A. & Kramer, F. R. Thermodynamic basis of the enhanced specificity of structured DNA probes. *Proc Natl Acad Sci* **96**, 6171-6176 (1999).

153. Bonnet, G. & Libchaber, A. Optimal sensitivity in molecular recognition. *Physica a* **263**, 68-77 (1999).

154. Tyagi, S. & Kramer, F. R. Molecular Beacons: Probes that Fluoresce upon Hybridization. *Nature Biotech* **14**, 303-308 (1996).

155. Riccelli, P. V. *et al.* Hybridization of single-stranded DNA targets to immobilized complementary DNA probes: comparison of hairpin versus linear capture probes. *Nucleic Acids Research* **29**, 996-1004 (2001).

156. Zizlsperger, M. Dissertation, *University Mainz, Germany* (1998).

157. Allawi, H. T. & SantaLucia, J. Thermodynamics and NMR of internal GC Mismatches. *Biochemistry* **36**, 10581-10594 (1997).

158. Allawi, H. T. & SantaLucia, J. Nearest-neighbor thermodynamics of internal A center dot C mismatches in DNA: Sequence dependence and pH effects. *Biochemistry* **37**, 9435-9444 (1998).

159. Allawi, H. T. & SantaLucia, J. Nearest Neighbor Thermodynamics and NMR of DNA Sequences with internal AA, CC, GG, TT Mismatches. *Biochemistry* **38**, 3468-3477 (1999).

160. Peyret, N. & SantaLucia, J.HyTher, http://jsl1.chem.wayne.edu/ (1999).

161. Peyret, N. *Biochemistry* **38**, 3468-3477 (1999).

162. Kricka, L. J. Nucleic Acid Detection Technologies-Labels, Strategies, and Formats. *Clin. chem.* **45**, 453-458 (1999).

163. Tyagi, S. & Kramer, F. R. Multicolor molecular beacons for allele discrimination. *Nature Biotechnology* **16**, 49-53 (1998).

164. Fang, X., Liu, X., Schuster, S. & Tan, W. Designing a Novel Molecular Beacon for Surface-Immobilized DNA Hybridization Studies. *J. Am. Chem. Soc.* **121**, 2921-2922 (1999).

165. Liu, X. J., Farmerie, W., Schuster, S. & Tan, W. H. Molecular beacons for DNA biosensors with micrometer to submicrometer dimensions. *Analytical Biochemistry* **283**, 56-63 (2000).

166. Tinland, B., Pluen, A., Sturm, J. & Weill, G. Persistance Length of Single Stranded DNA. *Macromolecules* **30**, 5763-5765 (1997).

167. Bednar, J. *et al. J. Mol. Biol.* **254**, 579-594 (1995).

168. Schuerman, G. S. & Meervelt, L. V. Conformational Flexibility of the DNA Backbone. *J. Am. CHem. Soc.* **122**, 232-240 (2000).

169. Lankas, F., Sponer, J., Hobza, P. & Langowski, J. Sequence-dependent elastic properties of DNA. *Journal of Molecular Biology* **299**, 695-709 (2000).

170. Goddard, N. L., Bonnet, G., Krichevsky, O. & Libchaber, A. Sequence dependent rigidity of single stranded DNA. *Physical Review Letters* **85**, 2400-2403 (2000).

171. Marathias, V. M., Bozidar, J., Haricabu, A. & Bolton, P. H. Felxibility and Curvature of Duplex DNA Containing Mismatched Sites as a Function of Temperature. *Biochemitry* **39**, 153-160 (2000).

172. Levicky, R., Herne, T. M., Tarlov, M. J. & Satija, S. K. Using self-assembly to control the structure of DNA monolayers on gold: A neutron reflectivity study. *Journal of the American Chemical Society* **120**, 9787-9792 (1998).

173. Kambhampati, D. (2000).

174. Kuhn, B. & Kollman, P. A. Binding of a diverse set of ligands to avidin and streptavidin. *Journal of Medicinal Chemistry* **43**, 3786-3791 (2000).

175. Buranda, T. *et al.* Ligand Receptor Dynamics at Streptavidin-Coated Particle Surfaces: A Flow Cytrometric and Spectrofluorimetric Study. *J. Phys. Chem. B* **103**, 3399-3410 (1999).

176. Steel, A. B., Levicky, R. L., Herne, T. M. & Tarlov, M. J. Immobilization of nucleic acids at solid surfaces: Effect of oligonucleotide length on layer assembly. *Biophysical Journal* **79**, 975-981 (2000).

177. Mergny, J.-L. Fluorescence Energy Transfer as a Probe for Nucleic Acid Structures and Sequences. *Nucleic Acids Research* **22**, 920 (1994).

178. Hiyoshi, M. & Hosoi, S. Assay of DNA Denaturation by Polymerase Chain Reaction-Driven Fluorescent Label Incorporation and Fluorescence Resonance Energy Transfer. *Anal. Biochem.* **221**, 306 (1994).

179. Toth, K., Sauermann, V. & Langowski, J. DNA Curvature in Solution Measured by Fluorscence Resonance Energy Transfer. *Biochemistry* **37**, 8173 (1998).

180. Charreyre, M. T. Fluorescence Energy Transfer Study of the Conformation of Oligonucleotides Covalently Bound to Polystyrene Latex Particles. *Langmuir* **13**, 3103-3110 (1997).

181. Tyagi, S., Bratu, D. P. & Kramer, F. R. Multicolor Molecular Beacons for Allele Discrimination. *Nature Biotech* **16**, 49 (1998).

182. Tyagi, S. & Kramer, F. R. Molecular Beacons: Probes That Fluoresce upon Hybridization. *Nature Biotech* **14**, 303 (1996).

183. Parkhurst, K. M. & Parkhurst, L. J. Kinetic Studies by Fluorescence Resonance Energy Transfer Employing a Double-Labeled Oligonucleotide: Hybridization to the Oligonucleotide Complement and to Single-Stranded DNA. *Biochemistry* **34**, 285 (1995).

184. Cardullo, R. A. Detection of Nucleic Acid Hybridization by Nonradiative Fluorescence Resonance Energy Transfer. *Proc. Natl. Acad. Sci USA* **85**, 8790 (1988).

185. Lazowski, K. W. & Kaczmarek, L. Highly sensitive detection of hybridization of oligonucleotides to specific sequences of nucleic acids by application of fluorescence resonance energy transfer. *Antisense & Nucleic Acid Drug Development* **10**, 97-103 (2000).

186. Henry, M. R., Winkins Stevens, P., Sun, J. & kelso, D. M. Real-Time Measurements of DNA Hybridization on Microparticles with Fluorescence Resonance Energy Transfer. *Anal. Biochem.* **276**, 204-214 (1999).

187. Jordan, C. E., Frutos, A. G., Thiel, A. J. & Corn, R. M. Surface Plasmon Resonance Imaging Measurements of DNA Hybridization Adsorption and Streptavidin/DNA Multilayer Formation at Chemically Gold Surfaces. *Anal. Chem.*. **69**, 4939-4947 (1997).

188. Babic, I., Andrew, S. E. & Jirik, F. R. MutS interaction with mismatch and alkylated base containing DNA molecules detected by optical biosensor. *Mutation REsearch* **372**, 87-96 (1996).

189. Meyer, R. R. & Leine, P. S. *Microbiol. Rev.* **54**, 342-380 (1990).

190. Lohman, T. M. & Ferrari, M. E. *Annu. REv. Biochem.* **63**, 527-570 (1994).

191. Lohmann, T. M., Bujalowski, W. & Overman, L. B. E.coli single strand binding protein: a new look at helix-destabilizing proteins. *TIBS* **13**, 250-255 (1988).

192. Sancar, A., Willialms, K. R., Chase, J. W. & Rupp, w. D. *Proc. Natl. Acad. Sci. USA* **78**, 4274-4278 (1981).

193. Bujalowski, W. & Lohman, T. M. *J. Mol. Biol.* **217**, 63-74 (1991).

194. Raghunathan, S., Kozlov, A. G., Lohman, T. M. & Waksman, G. Structure of the DNA binding domain of E-coli SSB bound to ssDNA. *Nature Structural Biology* **7**, 648-652 (2000).

195. Bujalowski, W., Overman, L. B. & Lohman, T. M. Binding Mode TRansitions of E.coli SSB SIngle Stranded Complexes. *J. Biol. Chem.* **263**, 4629-4640 (1988).

196. Lohman, T. M. & Overman, L. B. Two Biding Modes in E.coli SSB Single Stranded DNA Complexes. *J. Biol. Chem.* **260**, 3594-3603 (1984).

197. Lohman, T. M. & Bujalowski, W. Negative Cooperativity within Individual Tetramers of E.Coli Single Strand Binding Protein is Responsible for the Transition between the (SSB)35 and (SSB)56 DNA Binding Mode. *Biochemistry* 27, 2260-2265 (1988).